Closed-loop active flow control for road vehicles under unsteady cross-wind conditions

vorgelegt von

Dipl.-Ing.
Jens Pfeiffer
geb. in Traunstein

von der Fakultät III - Prozesswissenschaften
der Technischen Universität Berlin
zur Erlangung des akademischen Grades

Doktor der Ingenieurwissenschaften
- Dr.-Ing. -

genehmigte Dissertation

Promotionsausschuss:

Vorsitzender:	Prof. Dr.-Ing. Matthias Kraume
Gutachter:	Prof. Dr.-Ing. Rudibert King
Gutachter:	Prof. Ph.D. David R. Williams

Tag der wissenschaftlichen Aussprache: 22. Januar 2016

Berlin 2016

Abstract

Many road vehicles can be classified as bluff bodies based on their aerodynamic characteristics. Due to their geometry, the flow separates at the back of the vehicle, leading to a large, turbulent wake and a high drag coefficient. Active flow control (AFC) represents a promising technique for mitigating these detrimental effects. Although this has been successfully demonstrated in various wind tunnel experiments, most of the research has been limited to simplified, generic vehicle shapes under low-turbulent conditions. By contrast, real vehicles experience a significant amount of on-road turbulence, most notably when driving in gusty cross wind. This thesis explores the potential of AFC to adapt to these changing flow conditions by using feedback control. Here, the focus lies on ensuring an efficient drag reduction especially during cross-wind gusts; the effects on lateral vehicle dynamics and driver behavior are considered as well. To this end, further advantages of closed-loop AFC such as disturbance suppression are exploited to reduce the vehicle's cross-wind sensitivity and improve comfort and safety for the driver.

These techniques are first applied to a simple generic 2D bluff body equipped with Coanda actuators. A multivariable robust H_∞ controller is designed based on a set of black-box models identified from experimental data. The controller adjusts the Coanda blowing rates at the two trailing edges simultaneously and achieves an efficient drag reduction of up to 35 %. Additionally, it rapidly suppresses disturbances acting on the yaw moment during cross-wind conditions, which are emulated here by a simple rotation of the bluff body in the wind tunnel.

This approach is extended to a 3D bluff body exposed to more realistic gusts in a special cross-wind facility. A novel support system for wind-tunnel models replicates the lateral vehicle motion during the experiments based on a real-time simulation of lateral vehicle dynamics and driver behavior. This enables an investigation of the various transient effects resulting from unsteady cross-wind gust response, actuated flow dynamics and lateral vehicle response.

A particular goal of this thesis lies on capturing these transient effects better than existing techniques. This is achieved through the application of linear parameter-varying (LPV) modeling and control tools. To this end, a novel approach for the identification of LPV models for unsteady flow dynamics is developed and presented. It exploits the similarity of the nondimensional transient aerodynamic characteristics for varying free-stream velocities. Furthermore, it allows dependencies on additional parameters such as cross-wind angle to be easily taken into account. Here, LPV models are identified for actuated flow dynamics and unsteady cross-wind gust response of the 3D bluff body. These models describe the flow physics more accurately than conventional linear black-box models and allow an improved LPV controller design that takes the parameter dependency of the flow dynamics on varying free-stream velocities and cross-wind angles directly into account. This translates into better performance than conventional robust controllers. Additional LPV feedforward control reduces the cross-wind sensitivity further. In wind-tunnel experiments with cross-wind gusts the controllers achieve an efficient drag reduction of up to 15 % while simultaneously improving the vehicle's side-wind sensitivity significantly.

Last but not least, the LPV models can be scaled easily to different vehicle dimensions and driving velocities. The thesis concludes with a prediction of the dynamic characteristics of unsteady gust response, actuated flow dynamics and controller performance for a real-sized vehicle based on the models identified from wind-tunnel experiments.

Kurzfassung

Straßenfahrzeuge weisen üblicherweise die aerodynamischen Eigenschaften stumpfer Körper auf. Auf Grund ihrer Körpergeometrie löst die Strömung an den Fahrzeughinterkanten ab und bildet ein großes, turbulentes Nachlaufgebiet, das zu einem hohen Widerstandsbeiwert führt. Der Einsatz aktiver Strömungsbeeinflussung stellt eine vielversprechende Möglichkeit dar, dem entgegenzuwirken. Dies wurde in verschiedenen Windkanalexperimenten mit zumeist turbulenzarmen Anströmbedingungen und einfachen, generischen Fahrzeugformen nachgewiesen. Da reale Straßenfahrzeuge jedoch insbesondere bei Fahrten in böigem Seitenwind deutlich höheren Turbulenzgraden ausgesetzt sind, wird in dieser Arbeit untersucht, wie mittels einer Regelung der Strömung gezielt auf veränderliche Anströmbedingungen reagiert werden kann. Hierbei wird über das Ziel einer effizienten Luftwiderstandsreduktion hinaus auch der Einfluss auf Fahrzeugquerdynamik und Fahrerverhalten betrachtet, um durch eine Unterdrückung von Störungen den Fahrer während Seitenwindböen zu entlasten und so Sicherheit und Fahrtkomfort zu erhöhen.

Die Methoden zur aktiven Strömungsbeeinflussung werden zunächst an einem generischen zweidimensionalen stumpfen Körper angewandt, der mit Coanda-Aktuatoren entlang der Körperhinterkanten ausgestattet ist. Ein anhand von experimentell identifizierten Black-Box-Modellen ausgelegter robuster H_∞-Mehrgrößenregler stellt die Ausblasgeschwindigkeiten an den beiden Aktuatoren simultan ein und erzielt eine effiziente Luftwiderstandsreduktion von bis zu 35 %. Zudem werden Störungen des Giermoments bei Schräganströmungsbedingungen schnell ausgeregelt, die hier durch ein einfaches Verdrehen des Versuchskörpers nachgebildet werden.

Dieser Ansatz wird anschließend auf einen dreidimensionalen stumpfen Körper erweitert, der in einem speziellen Seitenwindkanal realitätsnahen Böen ausgesetzt wird. Mittels einer Echtzeitsimulation der Querdynamik und des Fahrerverhaltens wird auch die Fahrzeugquerbewegung berücksichtigt und durch ein neuartiges Verfahrsystem im Windkanal umgesetzt. Dies ermöglicht eine Untersuchung der unterschiedlichen transienten Effekte, die sich aus instationärer Böenantwort, Dynamik der aktuierten Strömung und Fahrzeugquerdynamik ergeben.

Ein wichtiges Ziel dieser Arbeit stellt eine im Vergleich zu herkömmlichen Verfahren verbesserte Erfassung dieser transienten Effekte mittels linear parameter-veränderlicher (LPV) Verfahren dar. Hierzu wird ein neuartiger Ansatz für die Identifikation von LPV-Modellen vorgestellt, der die Ähnlichkeit der transienten Aerodynamik für variierende Anströmgeschwindigkeit ausnutzt. Darüber hinaus können Abhängigkeiten von weiteren Parametern wie dem Schräganströmungswinkel leicht berücksichtigt werden. Für den 3D stumpfen Körper werden entsprechende LPV-Modelle für die Dynamik der aktuierten Strömung und das transiente Seitenwindverhalten identifiziert. Sie beschreiben die Strömungsphysik genauer als herkömmliche lineare Black-Box-Modelle und erlauben einen verbesserten LPV-Reglerentwurf, der die Parameterabhängigkeiten der Strömungsdynamik von variiender Anströmgeschwindigkeit und Schräganströmungswinkel berücksichtigt. Im Vergleich zu konventionellen robusten Reglern wird so eine höhere Performance erzielt, die durch eine LPV-Störgrößenaufschaltung weiter gesteigert werden kann. In Windkanalversuchen mit Seitenwindböen wird so eine effiziente Widerstandsreduktion von bis zu 15 % bei gleichzeitiger Verbesserung der Seitenwindempfindlichzeit erzielt.

Des weiteren können die LPV-Modelle leicht auf andere Fahrzeuggrößen und Fahrtgeschwindigkeiten skaliert werden. Dies wird abschließend anhand der in Windkanalversuchen identifizierten Modelle für eine Abschätzung und Vorhersage der Dynamik der instationären Böenantwort, der aktuierten Strömung und der Reglerperformance für Realfahrzeuggröße vorgenommen.

Vorwort

Die vorliegende Arbeit entstand während meiner Tätigkeit als wissenschaftlicher Mitarbeiter am Fachgebiet Mess- und Regelungstechnik des Instituts für Prozess- und Verfahrenstechnik an der TU Berlin.

Aufbauend auf den wichtigen Grundlagenerkenntnissen, die von meinen Kollegen und Vorgängern im Sonderforschungsbereich 557 „Beeinflussung komplexer turbulenter Scherströmungen“ erarbeitet wurden, entstand die Idee, aktive Strömungsbeeinflussung auch bei realitätsnahen, instationären Anströmbedingungen anzuwenden, denen Kraftfahrzeuge bei Fahrt in böigem Seitenwind ausgesetzt sind. Die entsprechenden Untersuchungen wurden im Rahmen des Forschungsprojekts „Regelung instationärer Strömungen um stumpfe Körper unter Berücksichtigung der Fahrzeugquerdynamik“ durchgeführt, woraus die wesentlichen Ergebnisse dieser Doktorarbeit entstanden. An dieser Stelle sei der deutschen Forschungsgemeinschaft für die Förderung herzlich gedankt.

Mein besonderer Dank gilt meinem Doktorvater Prof. Dr.-Ing. Rudibert King, der mir während der Durchführung stets hilfreich zur Seite stand und immer ein offenes Ohr für Fragen und Diskussionen hatte. Ohne ihn wäre diese Arbeit gar nicht erst zu Stande gekommen. Des weiteren möchte ich ganz herzlich Prof. Ph.D. Dave Williams für die konstruktiven Anmerkungen zu Themen der instationären Aerodynamik und für die Übernahme des Koreferats danken, für das er von Chicago aus den weiten Weg nach Berlin zur mündlichen Aussprache anreiste. Mein Dank geht auch an Herrn Prof. Dr.-Ing. Matthias Kraume für den Vorsitz des Prüfungssausschusses.

Außerdem möchte ich meinen Kolleginnen und Kollegen am Fachgebiet für die gute Zusammenarbeit und die vielen spannenden Diskussionen danken, aus denen sich immer wieder neue Impulse und Inspirationen ergaben. Vielen Dank auch an die am Projekt beteiligten studentischen MitarbeiterInnen, sowie an Joachim Kraatz und Peter Golz, ohne die der Aufbau und der Betrieb der Versuchsstände und der Messtechnik nicht möglich gewesen wäre.

Abschließend danke ich meinen Eltern, die mir diesen Weg erst ermöglicht haben, und meiner Partnerin Clara, die mir ganz besonders beim Abschluss dieser Arbeit und bei der Vorbereitung auf die mündliche Aussprache unermüdliche Unterstützung und Rückhalt gab.

Berlin, 20. Februar 2016 Jens Pfeiffer

Contents

List of symbols and abbreviations

Abbreviations:

2D	Two-dimensional
3D	Three-dimensional
AFC	Active flow control
BRL	Bounded real lemma
Co	Convex hull
DSP	Digital signal processor
LFT	Linear fractional transformation
LMI	Linear matrix inequality
LPV	Linear parameter-varying
MIMO	Multiple-input, multiple-output
MISO	Multiple-input, single-output
MPC	Model predictive control
NP	Nominal performance
PEM	Prediction-Error-Method
RP	Robust performance
RS	Robust stability
PRBS	Pseudo random binary signal
SISO	Single-input, single-output

Latin letters:

a_l	Lateral acceleration
$\boldsymbol{A}$	State matrix
$\boldsymbol{A}^*$	Nondimensional state matrix
$\boldsymbol{A}_i^*$	Nondimensional state matrix for affine dependency on the parameter θ_i
$\boldsymbol{A}(\underline{\theta})$	Parameter-dependent, dimensional state matrix
A_b	Cross-sectional surface of the 2D bluff body
A_B	Cross-sectional surface of the 3D bluff body
$A_{a,i}$	Cross-sectional surface of the slot exit of actuator i
$\boldsymbol{B}$	Input matrix
$\boldsymbol{B}_i^*$	Nondimensional input matrix for affine dependency on the parameter θ_i
$\boldsymbol{B}(\underline{\theta})$	Parameter-dependent, dimensional input matrix
$\boldsymbol{B}^*(\underline{\theta})$	Nondimensional, parameter-dependent input matrix
$\mathcal{B}$	Bounded Real Lemma map
c_D	Drag coefficient
$\hat{c}_D$	Drag coefficient as estimated from pressure measurements
c_{D_0}, $c_{D_{\mathrm{afc}}}$	Drag coefficients for natural and actuated flow
$c_{p,b}$	Base-pressure coefficient
c_{p_j}	Pressure coefficient at position j
$\overline{c}_{p_j}$	Time-averaged pressure coefficient at position j
c'_{p_j}	Fluctuation of the pressure coefficient at position j
c_S	Side force coefficient
$c_{S,raw}$	Raw side-force coefficient without compensation for inertial force

$\hat{c}_S$	Side-force coefficient as estimated from pressure measurements
c_N	Yaw-moment coefficient
$\hat{c}_N$	Yaw-moment coefficient as estimated from pressure measurements
$c_{N,raw}$	Raw yaw-moment coefficient without compensation for inertial moment
c_μ	Overall momentum coefficient
$c_{\mu,i}$	Momentum coefficient of actuator i
$\boldsymbol{C}$	Output matrix
$\boldsymbol{C}^*$	Nondimensional output matrix
$C_{\alpha f}$, $C_{\alpha r}$	Front and rear cornering stiffnesses
$\underline{d}$	Disturbance vector
$\underline{d}^*$	Nondimensional disturbance input vector
d_{CG}	Distance between center of wheelbase and center of gravity
$\underline{d}_{vd,quasi-steady}$	Disturbance input vector of the driver-vehicle system for quasi-steady aerodynamics
$\underline{d}_{vd,unsteady}$	Disturbance input vector of the driver-vehicle system for unsteady aerodynamics
d_w	Wheel diameter
D	Drag
D_0, D_{afc}	Drag forces for natural and actuated flow
$\boldsymbol{D}$	Feedthrough matrix
$\underline{e}$	Vector of control errors
$\boldsymbol{E}$	Disturbance input matrix
$\boldsymbol{E}^*$	Nondimensional disturbance input matrix
$\boldsymbol{E}(\underline{\theta})$	Parameter-dependent, dimensional disturbance input matrix
$\boldsymbol{E}_I$	Input uncertainty
$\boldsymbol{E}_o$	Unstructured multiplicative output uncertainty
f	Frequency
f^*	Reduced, nondimensional frequency
$\underline{f}$	Body force vector
$f_{bw,-3dB}$	Bandwidth
$f(u_i)$	Static nonlinear map for input u_i
f_a	Actuation frequency for pulsed blowing
f_c	Cross-over frequency
$\boldsymbol{F}$	Disturbance feedthrough matrix
$F(s)$	Dynamic reference filter
$F_l(\boldsymbol{P}, \boldsymbol{K})$	Lower linear fractional transformation of $\boldsymbol{P}$ and $\boldsymbol{K}$
$F_u(\boldsymbol{N}, \boldsymbol{\Delta})$	Upper linear fractional transformation of $\boldsymbol{N}$ and $\boldsymbol{\Delta}$
F_y	Side force acting on the center of gravity
$G(s)$	Transfer function
$\boldsymbol{G}(s)$	Matrix of transfer functions
$\boldsymbol{G}(\underline{\theta})$	LPV plant model
$\tilde{\boldsymbol{G}}(\underline{\theta})$	Reduced LPV plant model for feedforward control design
$\boldsymbol{G}_a$	Actuator model
$G_{a_i}(j\omega)$	Transfer function of actuator i
$G_{c_D\beta_w}(j\omega, \mathrm{u}_\infty)$	Transfer function from cross-wind angle to drag coefficient for a given free-stream velocity u_∞
$G_{c_Dp_t}(j\omega, \mathrm{u}_\infty)$	Transfer function from normalized total pressure to drag coefficient for a given free-stream velocity u_∞
$G^*_{c_D\beta_w}(j\omega^*)$	Nondimensional transfer function from cross-wind angle to drag coefficient
$G^*_{c_S\beta_w}(j\omega^*)$	Nondimensional transfer function from cross-wind angle to side-force coefficient

$G^*_{c_N\beta_w}(j\omega^*)$	Nondimensional transfer function from cross-wind angle to yaw-moment coefficient
$G^*_{c_D p_t}(j\omega^*)$	Nondimensional transfer function from normalized total pressure to drag coefficient
$G^*_{c_S p_t}(j\omega^*)$	Nondimensional transfer function from normalized total pressure to side-force coefficient
$G^*_{c_N p_t}(j\omega^*)$	Nondimensional transfer function from normalized total pressure to yaw-moment coefficient
$G_{delay}(s)$	Padé-approximation of the time delay
$G_{\mathrm{a}_l\beta_w}$	Transfer function from cross-wind angle to lateral vehicle acceleration
$\tilde{G}_{\mathrm{a}_l\beta_w(s)}$	Transfer function for the approximated response of lateral acceleration to cross-wind angle
$G_{\mathrm{a}_l c_S}$	Transfer function for the lateral acceleration response a_l to changes in c_S
$G_{\mathrm{a}_l c_N}$	Transfer function for the lateral acceleration response a_l to changes in c_N
$G_{\mathrm{a}_l\delta}(s)$	Transfer function of the vehicle from steering input δ to lateral acceleration a_l
$\boldsymbol{G}_{\mathrm{a}_l\underline{d}}(s)$	Transfer function of the vehicle from disturbances $\underline{d}$ to lateral acceleration a_l
$G_{c_S\beta_w}(j\omega, \mathrm{u}_\infty)$	Transfer function for the unsteady aerodynamic response of c_S to β_w at u_∞
$G_{c_N\beta_w}(j\omega, \mathrm{u}_\infty)$	Transfer function for the unsteady aerodynamic response of c_N to β_w at u_∞
$G_d(\underline{\theta})$	LPV disturbance model
$\boldsymbol{G}_f(s)$	Prefilter for feedforward LPV control design
$\boldsymbol{G}_{flow}$	Model for actuated flow dynamics
$G_{ij}(s, \underline{\theta})$	Dimensional transfer function from input j to output i for a frozen parameter value $\underline{\theta}$
$G^*_{ij}(s^*, \underline{\theta}^*)$	Nondimensional transfer function from input j to output i for a nondimensional frozen parameter value $\underline{\theta}^*$
$G_{LPV,ij}(j\omega, \mathrm{u}_\infty, \beta_w)$	Transfer function of LPV model from input j to output i for frozen values of u_∞ and β_w
$\boldsymbol{G}_n$	Nominal plant model
$\boldsymbol{G}_p$	Uncertain plant model
h	Height of the 2D bluff body
H	Height of the 3D bluff body
i_s	Steering gear ratio
$\boldsymbol{I}$	Identity matrix
J_z	Moment of inertia
k	Discrete time-step
$k_{\delta F_y}$, $k_{\delta M_z}$	Gains for the steering angle δ to compensate for constant side force F_y and yaw moment M_z
$\boldsymbol{K}$	Controller
$\boldsymbol{K}(\underline{\theta})$	LPV controller
$\boldsymbol{K}_d(\underline{\theta})$	Feedforward LPV controller
$\boldsymbol{K}'_d(\underline{\theta})$	Feedforward LPV controller without prefilter
l	Length of the 2D bluff body
l_I	Unstructured multiplicative input uncertainty
l_o	Multiplicative output uncertainty
L	Length of the 3D bluff body
L_f, L_r	Distances from front and rear axles to the center of gravity
L_{real}	Length of real-sized car
L_{wb}	Length of wheelbase
m	Mass
$\dot{m}_{a,i}$	Mass flow of actuator i
$\boldsymbol{M}$	Anti-reset windup compensator
$\boldsymbol{\mathcal{M}}$	Auxiliary matrix for the construction of the Lyapunov matrix $\boldsymbol{X}_{cl}$

$\boldsymbol{M}_d(s)$	Transfer function for the feedforward part of the driver
$M_R(s)$	Transfer function for the feedback part of the driver
M_z	Yaw moment acting on the center of gravity
$\underline{n}$	Measurement noise
N	Yaw moment
$\boldsymbol{N}$	Nominal system
$\boldsymbol{\mathcal{N}}$	Auxiliary matrix for the construction of the Lyapunov matrix $\boldsymbol{X}_{cl}$
n_x	Model order
p	Pressure
$\underline{p}_{act}$	Pressures inside the actuator ducts
$p_{a,i}$	Supply pressure for actuator i
$\underline{p}_{des}$	Setpoints for the pressure regulators
p_j	Pressure reading at position j
p_s	Static pressure
$\overline{p}_s$	Time-averaged, nominal static pressure
p_t	Total pressure
$\overline{p}_t$	Time-averaged, nominal total pressure
p'_t	Unsteady component of total pressure
$\hat{\overline{p}}_t$	Time-averaged estimated total pressure
$\hat{p}'_t$	Unsteady component of estimated total pressure
$\boldsymbol{P}$	Generalized plant
$\boldsymbol{P}(\underline{\theta})$	Generalized LPV plant
$\tilde{\boldsymbol{P}}(\underline{\theta})$	Generalized plant for feedforward LPV control
$\mathcal{P}$	Generalized LPV plant in polytopic form
P_0, P_{afc}	Powers to overcome drag for natural and actuated flow
$P_{a,i}$	Power of actuator jet i
q	Dynamic pressure
$\overline{q}$	Time-averaged, nominal dynamic pressure
$\underline{r}$	Reference variables
$\boldsymbol{\mathcal{R}}$	LMI solution for the LPV controller synthesis
Re	Reynolds number
Re_w	Reynolds number with respect to body width w
Re_L	Reynolds number with respect to body length L
s	Laplace variable
s^*	Nondimensional Laplace variable
S	Side force
$\boldsymbol{S}$	Sensitivity
$\boldsymbol{\mathcal{S}}$	LMI solution for the LPV controller synthesis
$S_{c'_{p_j}c'_{p_j}}$	Power spectral density of pressure coefficient fluctuations at position j
$\boldsymbol{S}_{p,H_\infty}$	Worst-case sensitivity for the robust controller
$\boldsymbol{S}_{LPV}$	Worst-case sensitivity for the LPV controller
St	Strouhal number
$St_{a,w}$	Strouhal number of the actuation frequency f_a for body width w
St_w	Strouhal number for body width w
t	Dimensional time
t^*	Nondimensional or convective time
t_{real}	Dimensional time for real-sized car
$\boldsymbol{T}$	Complementary sensitivity
T_0^*	Input delay in convective time
T_s	Sampling time
T_I	Time constant of the feedback part of the driver model
T_P	Prediction time of the driver model

$\boldsymbol{T}_R$	Transformation matrix for nondimensionalization
T_S	Time constant of the feedforward part of the driver model
u	Velocity in x-direction
$\underline{u}$	Input vector
$\tilde{\underline{u}}$	Input variable compensated for static nonlinearities
$\underline{u}^*$	Nondimensional control input vector
$\underline{u}_\Delta$	Input signal to the generalized plant $\boldsymbol{P}$ from the normalized uncertainty $\boldsymbol{\Delta}$
$\mathrm{u}_{a,i}$	Mean blowing velocity at the slot exit of actuator i
$\mathrm{u}^*_{a,i}$	Mean dimensionless blowing velocity at the slot exit of actuator i
$\tilde{\underline{\mathrm{u}}}^*_a$	Vector of surrogate variables for blowing rates compensated for static nonlinearities
$\underline{\mathrm{u}}_{a,des}$	Desired dimensional blowing velocities of the actuators
$\underline{\mathrm{u}}^*_{a,des}$	Desired nondimensional blowing velocities of the actuators
$\underline{\mathrm{u}}_{a,jet}$	Instantaneous actuator jet velocities
$\underline{\mathrm{u}}^*_{a,jet}$	Nondimensional instantaneous actuator jet velocities
$\mathrm{u}^*_{a_i,des}$	Desired nondimensional blowing velocity of actuator i
$\mathrm{u}^*_{a_i,jet}$	Instantaneous nondimensional jet velocity of actuator i
$\mathrm{u}_{\mathrm{ref}}$	Reference velocity for the boundary layer profile
u_∞	Free-stream velocity
$\overline{\mathrm{u}}_\infty$	Time-averaged, nominal free-stream velocity
$\overline{\mathrm{u}}_{\infty,i}$	Time-averaged, nominal free-stream velocity of experiment i
u(y)	Velocity in the boundary layer at position y
U	Reference velocity for nondimensionalization
v_v	Driving speed of the vehicle
$\underline{\mathrm{v}}_v$	Vector of the vehicle's velocity
v	Velocity in y-direction
$\underline{v}$	Measured outputs from generalized plant $\boldsymbol{P}$
$\underline{\mathrm{v}}_v^-$	Vector of the wind due to the vehicle's motion
$\underline{v}_i$	Vertex i of the parameter polytope Θ
v_l	Lateral velocity
v_l^-	Velocity component due to lateral vehicle motion
$\mathrm{v}_{v,\mathrm{real}}$	Driving speed of real-sized car
$\underline{\mathrm{v}}_{res}$	Resulting overall velocity vector
v_w	Cross-wind velocity
$V(\underline{x})$	Lyapunov function
V_M	Gain of the driver model
w	Width of the 2D bluff body
w	Velocity in z-direction
$\underline{w}$	External inputs to the generalized plant P
w_{c_S}, w_{c_N}	Constant weighting factors for the effects of c_S and c_N on a_l
w_I	Scalar weight for unstructured input uncertainty
w_o	Scalar weight for the multiplicative output uncertainty
w_s	Width of the actuator exit slots
$w_S(s)$	Scalar weight for the sensitivity
$\tilde{w}_{S_d}(s)$	Scalar weight for the disturbance sensitivity
W	Width of the 3D bluff body
$W_{c_S}(s)$, $W_{c_N}(s)$	Frequency-dependent weighting factors for the effects of c_S and c_N on a_l
$\boldsymbol{W}_P$, $\boldsymbol{W}_U$, $\boldsymbol{W}_T$	Matrices of frequency-dependent weights for sensitivity, control effort and complementary sensitivity
$\tilde{\boldsymbol{W}}_U(\underline{\theta})$	Parameter- and frequency-dependent weight for feedforward LPV control effort
x	Longitudinal position in the aerodynamic coordinate system

x^*	Nondimensional longitudinal position in aerodynamic coordinates
$\underline{x}$	Dimensional state vector
$\underline{x}^*$	Nondimensional state vector
x_0	Longitudinal position in inertial coordinates
x_{CG}	Longitudinal position in the coordinate system for vehicle dynamics
$\mathrm{x}_{\mathrm{real}}$	Longitudinal position for real-sized car dimensions
$\boldsymbol{X}$	Lyapunov matrix
y	Lateral position in the aerodynamic coordinate system
$\underline{y}$	Output vector
y^*	Nondimensional lateral position in aerodynamic coordinates
y^*	Nondimensional output variable
y_0	Lateral position in inertial coordinates
y_{CG}	Lateral position in the coordinate system for vehicle dynamics
$\underline{y}_\Delta$	Output signal from the generalized plant P to the normalized uncertainty Δ
y_l	Lateral displacement
$\underline{y}_m$	Measured output vector
$y_{w_{c_S c_N}}$	Surrogate variable for the combined influence of c_S and c_N on a_l
z	Vertical position in the aerodynamic coordinate system
z^*	Nondimensional vertical position in aerodynamic coordinates
z_0	Vertical position in inertial coordinates
z_{CG}	Vertical position in the coordinate system for vehicle dynamics
$\underline{z}$	Weighted outputs from P
$\underline{z}_k$	State vector in discrete time

Greek letters:

α_i	Polytopic coordinates
β	On-road side-slip angle
β	Side-slip angle
β_w	Cross-wind angle
$\beta_{w,m}$	Effective cross-wind angle as seen by moving wind-tunnel model
$\beta_{w,res}$	Effective cross-wind angle as seen by moving car
$\hat{\beta}_w$	Cross-wind angle as estimated from surface-pressure measurements
$\overline{\beta}_{w,i}$	Time-averaged cross-wind angle of experiment i
δ	Steering wheel angle
δ_f	Turning angle of the front wheel
δ_2	Momentum thickness of the boundary layer
δ_{99}	Boundary layer thickness
$\Delta P/P_0$	Normalized net power savings
Δ	Difference from baseline or reference value
$\boldsymbol{\Delta}$	Normalized uncertainty
$\hat{\boldsymbol{\Delta}}$	Block-diagonal structured uncertainty comprising $\boldsymbol{\Delta}$ and $\boldsymbol{\Delta}_P$
$\boldsymbol{\Delta}_I$	Normalized input uncertainty
$\boldsymbol{\Delta}_o$	Normalized output uncertainty
$\boldsymbol{\Delta}_P$	Fictitious unstructured uncertainty for testing of robust performance
γ	Quadratic H_∞ performance
μ	Dynamic viscosity
μ_Δ	Structured singular value with respect to a given uncertainty Δ
ν	Kinematic viscosity
ω	Radial frequency
ω^*	Reduced radial frequency
ω_v	Undamped eigenfrequency of the single-track model
$\boldsymbol{\Omega}(\underline{\theta})$	LPV controller in state-space representation

Π_I	Set of identified models for input uncertainty (2D bluff body)
Π_o	Set of identified models for output uncertainty (3D bluff body)
ϕ_r	Phase reserve
ψ	On-road yaw angle
ψ_m	Wind-tunnel model yaw angle
ρ	Density
$\sigma(t^*)$	Step response in convective time
$\sigma_{c_D\beta_w}(t, \mathrm{u}_\infty)$	Step response of $G_{c_D\beta_w}$ for a given free-stream velocity u_∞
$\sigma_{c_Dp_t}(t, \mathrm{u}_\infty)$	Step response of $G_{c_Dp_t}$ for a given free-stream velocity u_∞
σ_{max}, σ_{min}	Maximum and miminum singular value
σ_v	Decay constant of the single-track model
$\underline{\theta}$	Vector of external, time-varying parameters
$\underline{\vartheta}$	Vector of LPV model coefficients
Θ	Parameter polytope

Subscripts and superscripts:

$()_0$	Inertial coordinates
$()_a$	Actuator dynamics
$()_{a,des}$	Desired value for the actuator jet velocity
$()_{a,jet}$	Instantaneous value of the actuator jet velocity
$()_{\mathrm{afc}}$	Actuated flow dynamics
$()_{c_Sc_N}$	Model for transient gust response of side-force and yaw-moment coefficients
$()_{cl}$	Closed-loop system
$()_{\mathrm{cwg}}$	Cross-wind gust response
$()_{drv}$	Virtual driver model
$()_K$	Controller
$()_{K_i}$	Controller at vertex $\underline{v}_i$ of the parameter polytope Θ
$()_{max}$	Maximum value
$()_{min}$	Minimum value
$()_R$	Reference variable for nondimensionalization
$()_{v_i}$	State-space system at vertex $\underline{v}_i$ of the parameter polytope Θ
$()_v$	Single-track model
$()_{vd}$	Driver-vehicle system
$\|\|\dots\|\|_\infty$	H_∞-norm
$\|\|\dots\|\|_2$	H_2-norm
$\dot{()}$	Derivative with respect to dimensional time
$\hat{()}$	Estimated variable
$()^*$	Nondimensional variable
$\overline{()}$	Time-averaged value of a variable
$()'$	Time-varying component of a variable
$()^-$	Wind velocity due to vehicle motion

Chapter 1

Introduction

1.1 Overview

Research and development in road vehicle aerodynamics is largely driven by the continuous need to increase fuel efficiency. In the automobile industry this objective is mostly pursued by reducing the aerodynamic drag through conventional methods such as shape optimization or other passive means. However, the margin of further improvement through geometry changes is restricted by several aspects: In the case of passenger cars in particular the design needs to appeal to customer expectations, whereas commercial vehicles such as trucks and buses have to provide sufficient loading capacity within a confined set of outer dimensions. This is why most road vehicles have a shape representing a bluff body. According to Hucho [57], bluff bodies are characterized by flow separation, which is induced by geometric properties such as a large ratio of body width to length. This leads to a large wake behind the body and significant pressure losses, which result in a high drag coefficient. These negative effects can be only partially alleviated by passive means such as boat-tailing, spoilers or vortex generators.

A promising, relatively new technology is active flow control (AFC), which uses actuation methods such as pulsed or steady blowing, synthetic jets, microjets or fluidic actuators to favourably influence flow. In the case of bluff bodies, this is usually applied to delay flow separation or to control the wake directly, the goal being to reduce the drag coefficient [30]. So far, however, this has been mostly studied for relatively simple, generic vehicle shapes under well-controlled laboratory conditions in wind tunnel experiments.

By contrast, real vehicles show more complicated flow phenomena and experience a significant amount of on-road turbulence due to the wakes of other vehicles and natural wind gusts. Lately there has been growing interest in understanding and modeling the influence of these unsteady flow conditions on road vehicle aerodynamics, especially with regard to cross-wind gusts [120]. Yet the application of AFC in this context has received little attention, even though it offers a way for adapting to changing flow conditions, in particular when used in a feedback control loop.

This thesis seeks to extend existing approaches for closed-loop active flow control for simple generic vehicles under low-turbulence, straight flow conditions to include more realistic vehicle shapes under unsteady flow conditions. Here, the focus lies on ensuring an efficient drag reduction, especially during cross-wind gusts. Further advantages of closed-loop AFC such as disturbance suppression are exploited to reduce the cross-wind sensitivity of the vehicle to increase safety and comfort for the driver.

These techniques are first applied to a simple generic 2D bluff body. A suitable actuation concept and an appropriate strategy for multivariable feedback control of drag and yaw-moment coefficients is developed and presented. Here, the closed-loop controller has to suppress cross-wind disturbances that are emulated by a simple rotation of the vehicle model in the wind tunnel.

This approach is subsequently extended to a 3D bluff body exposed to more realistic gusts in a special cross-wind facility. Here, the effects on lateral vehicle dynamics and driver behavior are also considered. To this end, a novel wind tunnel model support system replicates the lateral

vehicle motion during the experiments based on a real-time simulation of the driver-vehicle system. This setup enables the investigation of possible additional unsteady aerodynamic effects arising from lateral vehicle motion.
A particular focus of this thesis lies on modeling the transient actuated flow characteristics and the aerodynamic cross-wind gust response better than existing techniques. This is achieved through the application of linear parameter-varying (LPV) modeling and control tools. A novel and practical approach for the identification of gray-box LPV models for unsteady flow dynamics is presented that exploits the similarity of the nondimensional transient aerodynamic characteristics for varying free-stream velocities. This approach allows dependencies on additional parameters such as cross-wind angle to be easily taken into account.
This is used to identify gray-box models for unsteady cross-wind gust responses and for actuated flow dynamics, which describe the flow physics more accurately than conventional linear black-box models. This answers some open questions in the literature regarding the relative importance of various transient effects by assessing their nondimensional frequency characteristics and evaluating their effect on the characteristics of lateral vehicle dynamics. The LPV approach also allows for improved controller design, which achieves better performance than conventional robust controllers by taking into account the parameter dependency of the flow dynamics on varying free-stream velocities and cross-wind angles. This translates into a higher closed-loop bandwidth, which helps to ensure an efficient drag reduction under unsteady flow conditions while simultaneously improving the vehicle's cross-wind sensitivity.
This thesis builds on and extends findings and methods from the fields of unsteady vehicle aerodynamics, active flow control, lateral vehicle dynamics, system identification and control design. The relevant current state of research in these disciplines is briefly summarized in the sections below. It is followed by an overview of the open questions identified in the research and a statement of the objectives and goals addressed by this thesis.

1.2 State of research

1.2.1 Unsteady aerodynamics of road vehicles and cross-wind sensitivity

Unsteady flow phenomena affect the aerodynamics of road vehicles in many different ways. The effects can be classified by three different types of situations: The first are time-varying external flow conditions such as those caused by cross-wind gusts; the second are unsteady effects created by lateral or vertical vehicle motion; and the third are self-excited flow characteristics such as wake instabilities. This section focuses on the first two categories; the wake characteristics and the possibilities of controlling it by passive and active means are discussed in section 1.2.2.
External unsteady flow conditions on the road have a multitude of sources. According to the overview article published by Sims-Williams [120], vehicles experience turbulent flow due to natural wind, because of unsteady wakes by other vehicles and as they pass through regions of constant cross-wind between road side obstacles. The last case is particularly important, as it can create gusts of a significant amplitude, affecting driving comfort and safety. Gusts with a scale of 2 to 20 vehicle lengths are the most critical, because they occur frequently at considerable amplitudes. The resulting flow characteristics can differ significantly from quasi-steady conditions, and lateral vehicle dynamics and driver behavior are particularly sensitive to disturbances in this frequency range [120].
Extensive measurements of the turbulent on-road flow conditions for a driving speed of 100 km/h have been carried out by Wordley and Saunders [147, 148]. Depending on the terrain and traffic conditions, the identified turbulence intensities and length scales range widely. Driving in smooth terrain is mostly characterized by low turbulence levels with long length scales, whereas the wakes of other vehicles in highway traffic lead to a high vertical turbulence intensity with very short length scales. The highest level of lateral turbulence occurs with a mean intensity of 4.7 % for driving in an environment with roadside obstacles, at an average length scale of 2.4 m

as determined based on the von Kármán spectral fitting method. In contrast to Wordley and Saunders [147, 148], whose focus lies on determining the average turbulent conditions to provide guidelines for wind tunnel design, Wojciak et al. [143, 145] put an emphasis on identifying and characterizing individual, strong cross-wind gusts from on-road measurements. Their results show that the most frequently occurring cross-wind gusts during driving at a velocity of 140 km/h have an amplitude of 5° to 7° at a frequency of 1.0 Hz to 1.5 Hz. Assuming a vehicle length of 4 m, this corresponds to a gust wavelength of about 6.5 to 10 vehicle lengths, which lies in the range stated by Sims-Williams, where unsteady aerodynamic effects can play a significant role [120].

As pointed out by Wordley and Saunders [148], full-scale automotive wind tunnels are not capable of reproducing the turbulence characteristics experienced by vehicles in on-road conditions. Passive techniques such as grids at the test-section inlet may be used to increase the turbulence intensity to some degree, but these methods cannot reproduce lateral wind gusts at sufficient amplitude. Therefore, the cross-wind sensitivity is conventionally assessed by exposing the vehicle model to a series of constant cross-wind angles by rotating it on a turntable. The response to unsteady cross-wind conditions is evaluated only later in drive-by tests on tracks equipped with cross-wind fans [47]. At this point of the design process, however, few changes can be applied to the vehicle, and on-track testing does not allow for a thorough investigation of the flow phenomena. Thus, different test methods have been developed to study unsteady flow conditions in wind-tunnel experiments.

According to the overview articles published by Széchényi [123] and by Sims-Williams [120], setups in which a stationary model is exposed to a time-varying flow are best suited to represent the on-road conditions. For this purpose, oscillating wings are often installed at the outlet of the wind tunnel nozzle [82, 99, 114]. These facilities can generate a stochastic distribution of the unsteady lateral velocity component with a realistic range of yaw angles and turbulence levels. Corresponding experiments are carried out by Schröck et al. [113, 114] for different SAE reference vehicle models. Depending on the shape of the back, the vehicle models experience increased amplitudes of unsteady side force and yaw moment in the range $0.06 \leq f^* \leq 0.12$, where the reduced frequency is defined as $f^* = f L_{wb}/\mathrm{u}_\infty$ for the length of the wheelbase L_{wb} and the free-stream velocity u_∞. The largest amplifications are reported for a squareback geometry, with yaw moments exceeding the quasi-steady prediction by up to 100 %. Furthermore, the increased aerodynamic admittance of side force and yaw moment coefficients lies in a frequency range that is relevant for the lateral vehicle dynamics and driver behavior.

Similar observations are also made for vehicle models exposed to single, large-amplitude gusts. These can be generated in special cross-wind tunnels consisting of a blowing axial wind tunnel and an additional cross-wind fan and shutter system along an open test section. Opening the shutters consecutively creates a cross-wind gust that realistically convects over the wind tunnel model and simulates a vehicle driving into a region of constant side-wind. This concept was introduced by Dominy et al. [32, 33] and is also used by Volpe et al. [134]. The experiments carried out by these authors with vehicle models exposed to cross-wind gusts show an overshoot of the transient yaw moment by up to 20 % above the corresponding steady-state values [106, 107, 133].

Oscillating models in an otherwise constant external flow have been frequently studied [38, 41, 50, 63, 83, 124, 144]. Most of these experiments were limited to a few, specific frequencies. Especially in the case of oscillating rotation, yaw moments are often reported that significantly exceed the quasi-steady values and those obtained with externally varying flow conditions. As discussed by Watkins et al. [138], however, it must be pointed out that pure oscillation does not represent flow conditions experienced on-road, where gusts convect over the vehicle. The discrepancy between the published experimental results for oscillating models and for externally varying flow conditions is also mentioned by Sims-Williams [120]. He concludes that further research is necessary to explain these differences, since the various experiments differ significantly in model geometry and applied test method.

On-road measurements investigating transient aerodynamic effects are carried out by Oettle et al. [93]. According to the authors, the pressure fluctuations in the sideglass region can be accurately predicted over a large range of reduced frequencies from quasi-steady wind tunnel measurements if the effects of self-excited unsteadiness are separated from the data. But their study is focused on local flow phenomena, for which strong transient effects may not play an important role. By contrast, the overall aerodynamic response of side force and yaw moment as estimated from surface-pressure measurements is studied by Okada et al. [94] for sinusoidal steering input at high-speed driving. Here, the high-speed stability and maneuverability of a production-type mid-sized sedan vehicle is compared with and without aerodynamic add-on parts such as side skirts, front and rear tire deflectors and an underbody cover. For the aerodynamically optimized vehicle the authors report smaller side-wake structures with a faster aerodynamic response and shorter time lag. This helps increase aerodynamic dampening and improve high-speed stability. The results are confirmed in a corresponding numerical simulation by Tsubokura et al. [128].

As emphasized by Huemer [58] and Wagner [136], the cross-wind sensitivity of vehicles cannot be assessed exclusively on the basis of steady and transient aerodynamic characteristics, since the effect on lateral vehicle dynamics and on driver behavior has to be taken into account. Wagner thus develops an empirical dynamic model for a virtual driver. This model is extended and improved by Krantz [72] on the basis of on-road measurements under turbulent flow conditions.

The transient characteristics of unsteady aerodynamic effects are usually assessed on the basis of admittance or transfer functions, whose frequency response is directly determined from experiments via the power-spectral densities of the input and output signals [113]. Approaches to model the measured response are rarely presented, however. Krantz [72] suggests simple transfer-functions with first-order time lag, but the time constants are not stated and it is unclear how they are determined. Furthermore, the model is given in dimensional time and can thus only capture the flow dynamics at a single free-stream velocity. An interesting theoretical model for the aerodynamic admittance of the side force and yaw moment of road vehicles is proposed by Filippone [39]. It is based on the indicial method, which is summarized by Leishman [77] and goes back to Theodorsen [125], Wagner [137] and Küssner [74]. These authors derived analytical expressions for the unsteady aerodynamic response of airfoils to oscillating motion [125], impulsive changes in angle of attack [137] and sharp edged gusts [74], respectively. Filippone shows that this approach can be extended to road vehicles, provided that the flow remains attached to the sides [39], which is a valid assumption for the most commonly encountered on-road flow conditions. The derived expressions for the aerodynamic response to sinusoidal gusts match well with experimental results. The main parameters affecting the unsteady aerodynamic characteristics are the mean vehicle length relative to the wave length of the gust, the traveling speed of the sharp-edged gust and the vehicle's streamwise elongation along the vertical cross-section.

A model for the unsteady aerodynamic loads arising from lateral and vertical vehicle motion is presented by Kawakami et al. [63]. It is based on a quasi-steady aerodynamic assumption that assumes that the instantaneous aerodynamic forces and moments are identical to those in a steady flow at the same relative inflow angle. Nevertheless, a dynamic model is obtained as the rates of change of displacement and rotation angle as well as the acceleration of the wind tunnel model are taken into account. These terms are not considered in the other publications about rotational oscillation cited above. This may explain the discrepancies between transient and quasi-steady forces and moments often observed in these experiments already at very low frequencies, since the quasi-steady prediction is commonly and mistakenly based on nominal instead of relative side-wind angle. By contrast, the linear transfer functions derived by Kawakami et al. [63] accurately approximate the transient forces and moments measured in experiments with sinusoidal translation and rotation of a bluff body.

Methods for improving the cross-wind sensitivity of vehicles are mostly focused on form optimization. A comprehensive overview of the different options is given by Hucho [56], who observes that the problem is most pronounced for buses, vans and small trucks. This is studied in CFD-simulations for a double-decker bus exposed to cross-wind gusts by Hemida and Krajnović [51], who conduct a successive shape optimization to reduce the transient aerodynamic yaw moment [71]. Other methods for reducing the cross-wind sensitivity of road vehicles include add-on parts such as aerodynamic separation edges or a tail fin as proposed by Schröck et al. [114]. Although small improvements can be achieved by these passive means, their overall potential is limited and may have other disadvantages in terms of increased aerodynamic drag under normal driving conditions without side-wind.

Active steering or breaking systems have been developed that allow the effect of cross-wind gusts on lateral vehicle dynamics to be reduced by feedback control. An overview of these methods is given by Isermann [60]; examples of specific applications and methods were published by Ackermann et al. [1, 2], Sackmann and Trächtler [108] or Schorn et al. [112]. The importance of cross-wind sensitivity for comfort and safety of vans and small trucks is also addressed in commercially available vehicles, such as by the "cross-wind assistant" by Daimler AG [31]. It is based on a disturbance observer which processes sensor information from the system for Electronic Stability Control (ESC) to estimate the aerodynamic disturbance, and creates a counter-moment by regulating the suspension strut forces or by asymmetric breaking [9, 64].

These solutions intervene in the driving dynamics only after these have been affected by the gust, but it is desirable to reduce the effects of unsteady cross-wind on the aerodynamics directly. Ideas based on active flow control have been proposed by Englar [34, 35] and Sumitani and Yamada [122], and are discussed in the next section.

1.2.2 Passive and active flow control for bluff bodies

Most road vehicles exhibit aerodynamic characteristics which correspond to bluff bodies. Their flow is dominated by separation, which is usually induced by the rear geometry of the body [57]. This leads to large, turbulent wakes with significant pressure losses, which contribute to a large drag coefficient of bluff bodies. These negative consequences can be mitigated by passive or active flow control (AFC) methods.

An overview of the various techniques applied to bluff bodies is provided by Choi et al. [30]. Most of the research is conducted for generic bodies under low-turbulent, steady wind tunnel conditions with the objective of reducing drag and explaining the related mechanisms. Earlier studies focus predominantly on simple, two-dimensional bluff bodies. These are characterized by a two-sided flow separation with mutually interacting shear layers. Wake instabilities lead to large, alternating vortices that induce a low pressure on the base of the bluff body.

A relatively simple way to reduce drag is thus to prevent or delay the interaction of the two shear layers. This can be achieved by passive means such as a splitter plate or by active base bleed, as shown by Bearman [17, 18]. Another method involves introducing three-dimensional disturbances that break the large-scale coherent two-dimensional flow structures and thus suppress alternating vortex shedding. This has been successfully demonstrated by using a wavy trailing edge [126], by installing small tabs on the trailing edge [97], by spanwise distributed continuous blowing and suction [67] or by spanwise distributed, pulsed suction [88, 89].

The wake instability of 2D bluff bodies can also be mitigated by enhancing the symmetry of the wake. Periodic open-loop actuation with synthetic jets as described by Henning and King [55] forces a synchronous vortex shedding and results in a lock-on of the wake in phase with the actuation frequency. This can also be achieved by direct opposition control through anti-cyclically generated control forces [119, 44], or through phase control with synthetic jet actuation only on one side, as demonstrated by Pastoor et al. [100]. These results show how the application of feedback control strategies can contribute to more energy-efficient drag reduction.

However, most of the aforementioned mechanisms for bluff body drag reduction are only applicable to two-dimensional bodies, which exhibit an unstable wake with large, alternating, coherent vortices at characteristic frequencies. If the location of separation is not fixed by the body geometry, the drag of bluff bodies can also be significantly reduced by delaying the separation. To this end, different passive or active means can be applied such as vortex generators [4], rotating cylinders on the rear edge [20], combined suction and pulsed blowing [115] or synthetic jets with zero-net-mass-flux actuation [8, 75]. Based on the mechanism of delaying the separation, considerable advances have recently also been made in the application of flow control to three-dimensional bluff bodies. Most researchers focus on the Ahmed body [3] with a rear slant angle of 25° or 35° as a generic vehicle model. Delaying the separation on the rear slant leads to a significant drag reduction. This can be achieved by using pulsed jets [27, 46], vortex generators [4] or steady microjets [16].

By contrast, flow control for the drag reduction of 3D bluff bodies with a square back is more challenging, since the location of separation is fixed and their wake is highly turbulent without large, coherent vortices. Successful applications of AFC are mostly based on steady blowing at relatively high momentum coefficients, for example in the region of the upper rear trailing edge [78], or along all four trailing edges, by exploiting the Coanda effect as described by Englar [34, 35]. He also demonstrates that the aerodynamic yaw moment can be influenced by asymmetric Coanda blowing to counter the effects of side wind. Another possibility for improving cross-wind sensitivity is suggested by Sumitani and Yamada [122], who use blowing on the front leeward side to trigger flow separation and reduce the yaw moment. This technique is associated with an increase in drag, however.

Active flow control offers the potential to adapt to changing flow conditions, which is especially important given the turbulent flow encountered by vehicles on the road. This can be achieved through the application of closed-loop active flow control. Various methods have been developed for this approach. An online optimization can be carried out with extremum or slope seeking controllers, which do not require a dynamic model of the flow. A sinusoidal perturbation is applied to the plant input to estimate the gradient of a cost functional via an adequate filtering of the measurement variables. This approach has been successfully applied to various configurations, such as flow control for a backward-facing step and the suppression of combustion instabilities [70] or a high-lift configuration [23], for which slope-seeking control yields higher lift values than open-loop active flow control. In applications to 2D bluff bodies [53] and to the 3D Ahmed body [26] the drag is reduced by up to $13\,\% - 15\,\%$ through an optimization of the actuation amplitude.

Although a significant speed-up can be achieved by estimating the gradient with an Extended Kalman Filter as proposed by Henning et al. [53], slope-seeking controllers do not provide a sufficient bandwidth to react to fast disturbances such as cross-wind gusts. For this purpose, model-based controllers are better suited, as they offer better performance for disturbance suppression and additional benefits such as reference variable tracking. To this end, robust control strategies represent a powerful tool. They are able to handle the uncertainties arising from the often nonlinear or parameter-dependent behavior of the actuated flow, and their design can be carried out with standard methods, as described by Skogestad and Postlethwaite [121]. Within the context of AFC, the required uncertain plant model is usually derived from a set of black-box models that describe the input/output plant dynamics for the complete range of operating conditions. Well-established system identification algorithms are available for the identification of these models from experimental data such as the Prediction-Error-Method or the Subspace method, see e.g. Ljung [79]. Successful applications of robust controllers for AFC of bluff bodies are described for the 2D case by Henning and King [55] and Pastoor et al. [100], and for the 3D Ahmed body by Muminović et al. [87]. Extensions of these approaches to the multivariable case with simultaneous control of drag or base-pressure and yaw-moment coefficient have been published by the author prior to this thesis in Pfeiffer and King [103, 101] for 2D and 3D bluff bodies, respectively.

An online optimization of fast processes such as turbulent flows can be achieved with model predictive control (MPC). An overview of the different methods used for AFC is given by King et al. [68]. For systems without saturated input or state variables, linear unconstrained MPC can be used to control flows at very high sampling rates, as demonstrated by Gelbert et al. [43] for the suppression of thermoacoustic instabilities and by Goldin et al. [48] for the active

dampening of Tollmien-Schlichting waves. Active-Set-Methods allow a real-time application of MPC in the presence of actuator saturation and have been applied to 2D and 3D bluff bodies by Muminović et al. [87, 90, 88]. Model uncertainties can be taken into account by robust MPC approaches [90, 89], but these methods require a relatively large computational effort.
If a nonlinear, theoretical model for flow dynamics is available, advanced nonlinear control methods such as sliding mode control, backstepping or nonlinear MPC can be applied [5, 6]. Appropriate low-order models can be derived as Galerkin-models directly from the Navier-Stokes-Equations or as Generalized-Mean-Field models calibrated to experimental data [80]. Of particular interest for this thesis are linear parameter-varying (LPV) approaches, as they allow the parameter-dependent behavior of the actuated flow for external variables such as varying free-stream velocity to be taken into account directly. Such LPV gain-scheduling controllers are described by Ali et al. [7] for transition control in plane Poiseuille flow or by Fitzpatrick et al. [40] for flow control in a driven cavity. However, the application of these approaches has so far been limited to very simple canonical configurations. This is because the required LPV models are derived with low-order modeling methods, which are not yet applicable to more complicated flows such as the wakes of 3D bluff bodies.
Although active flow control offers potential benefits particularly in changing flow conditions, this has rarely been studied and most experiments have been carried out in a well-defined, low-turbulent laboratory environment. Recent research has been increasingly turning its attention to realistic flow conditions. For example, Müller-Vahl et al. [86] use adaptive, open-loop blowing to reduce unsteady aerodynamic loads acting on wind turbines, and Troshin et al. [127] describe a closed-loop controller to compensate for a slow performance degradation of soiled wind turbine blades. The performance of combined feedforward and robust feedback AFC at suppressing disturbances on the lift of a wing during longitudinal gusts is demonstrated from wind tunnel experiments by Williams et al. [141] and Kerstens et al. [66, 65]. Last but not least, the applicability of closed-loop AFC in real-world conditions is proven in flight tests by King et al. [69].

1.2.3 Linear parameter-varying system identification and control theory

This section briefly summarizes publications from the field of system identification and control theory that are relevant for the methods applied in this thesis. Here, the identification of linear dynamic models with the Prediction-Error-Method represents a well-established standard approach, see for example Ljung [79]. A comprehensive overview of the methods for modeling uncertainty and the corresponding design of multivariable robust H_∞ controllers is given by Skogestad and Postlethwaite [121].
The dynamics of the actuated flow and other unsteady flow characteristics such as the transient gust response usually show a nonlinear behavior that depends on external parameters such as free-stream velocity or cross-wind angle. A conventional approach for coping with such parameter dependencies is the use of gain-scheduling controllers, in areas such as flight control, where the airplane dynamics depend on Mach number. Here, plant dynamics are linearized for a range of different operating points for which individual linear controllers are designed. During operation, an online interpolation between these controllers is carried out based on one or several scheduling parameters. As discussed by Shamma and Athans in [116, 117, 118], however, it is difficult or impossible to prove stability and performance of these approaches, and they may fail in the presence of fast parameter variations. The authors thus introduce the class of linear parameter-varying (LPV) systems [117], whose dynamics depend on external, measurable parameters, and for which stability, robustness and performance conditions of the closed-loop can be stated. Successful and widely used design methods for LPV H_∞ gain scheduling controllers are presented by Packard [95], Apkarian and Gahinet [13], Gahinet et al. [42] and Becker et al. [22]. In these studies the control synthesis problem is formulated via linear matrix inequalities (LMI) that can be solved numerically with efficient algorithms [25, 42]. This yields a fixed, parameter-independent Lyapunov function on whose basis stability and performance of

the closed-loop can be shown. The resulting LPV controllers can achieve a higher performance than conventional robust H_∞ controllers, as their dynamics are adapted online to the plant characteristics from measurements of the current parameter value.
According to Wu et al. [149], however, the use of a fixed Lyapunov function can still lead to a conservative control design, as it allows for arbitrarily fast parameter variations. Wu et al. [149] and Apkarian and Adams [11] thus propose a parameter-dependent Lyapunov function that takes into account the maximal rates of change of the parameters. But controller synthesis is computationally intensive, relying on a gridding of the parameter space to obtain a finite number of LMIs.
Further extensions for mixed H_2/H_∞ LPV control problems allow the energy content of a signal to be minimized over the entire frequency range [15, 28]. Prime et al. [104] use such an approach to suppress the aeroelastic vibrations of a wing exposed to vertical gusts at time-varying free-stream velocities.
The LPV models for the controller design are often derived from physical first-order principles, see Tóth [129] for an overview. When this is not easy to perform, LPV models can also be identified from experimental data. Verdult et al. [130, 131, 135], Felici et al. [37] and Wingerden and Verhaegen [142] propose subspace methods for the identification of LPV state-space models; Boonto and Werner [24] present an approach for the closed-loop LPV identification of input/output models. However, some of these methods are not applicable to larger data sets as they suffer from a "curse of dimensionality" resulting in a high computational burden [132]. What is more, they are given in discrete time and a conversion to continuous time is complicated due to the parameter dependency of the models [129]. Many LPV control synthesis algorithms such as the one by Apkarian et al. [12, 13, 14] used in this thesis are implemented in continuous time. Hence, a custom LPV identification algorithm for output error models is developed and presented here. Its model structure is tailored to the typical parameter dependencies of the flow dynamics. Details are given in sections 2.2.2 and 2.2.3.

1.3 Problem statement and outline

The main objective of this thesis is the development of a closed-loop active flow control strategy for road vehicles to efficiently reduce drag coefficient and cross-wind sensitivity under unsteady flow conditions. This requires the interaction between transient aerodynamics in terms of the unsteady gust response and the actuated flow dynamics, as well as the lateral vehicle dynamics and the driver behavior to be taken into account. To achieve this goal, various approaches and results from the current state of research summarized in the previous section are brought together and extended where necessary. In particular, the following questions and objectives are addressed:

- The characterization of the unsteady aerodynamic response to cross-wind gusts, to active blowing and to the lateral vehicle motion;
- the identification of dynamic models for these effects in a way that takes into account their dependence on the most relevant parameters such as the free-stream velocity;
- a derivation of their nondimensional characteristics and a prediction of the behavior at realistic driving velocities and vehicle sizes;
- an investigation of the interaction between unsteady aerodynamics, lateral vehicle dynamics and driver response, with a characterization and comparison of the relative importance and bandwidth of the transient effects for various driving speeds;
- the development of a suitable closed-loop active flow control strategy based on the dynamic models;
- better accounting for the parameter-dependent flow dynamics than provided by existing robust controllers; and
- an efficient drag reduction under unsteady flow conditions while simultaneously improving cross-wind sensitivity.

For this purpose, existing approaches for the design of LPV controllers [14], for the modeling of the lateral vehicle dynamics [85, 108] and for the driver behavior [105, 85] are applied. These methods are summarized in chapter 2, together with a brief overview of similarity laws in aerodynamics. Based on these, a novel procedure for the identification of LPV models for flow dynamics is introduced in sections 2.2.2 and 2.2.3.

Chapter 3 describes the development of a multivariable closed-loop AFC strategy for a generic 2D bluff body. Its actuation concept with Coanda blowing is adapted from Englar [34, 35] and is described in section 3.1 together with the experimental setup. The natural and actuated flow characteristics are discussed in sections 3.2 and 3.3, respectively. For the model identification and control design procedure described in sections 3.4 and 3.5 existing single-input single-output (SISO) approaches for 2D bluff bodies [54] are extended to the multivariable case to simultaneously regulate drag and yaw-moment coefficients under cross-wind conditions. To this end, a set of linear black-box models is identified from experiments to derive an uncertain model on whose basis a robust H_∞ controller is designed. In section 3.6 the closed-loop performance is discussed for experiments in which the bluff body is rotated on a turntable. This is a simplified way to simulate cross-wind disturbances.

These preliminary experiments with the 2D bluff body form a starting point for the development of a similar control strategy for a more realistic 3D bluff body, which is presented in chapter 4. The body geometry and actuation concept are adapted from the publications by Englar [34, 35], but its length is reduced to correspond to a small truck or delivery van. The experimental setup described in section 4.1 also involves a special cross-wind tunnel to create realistic gusts

according to the approach proposed by Dominy and Ryan [33]. Furthermore, the setup features a novel dynamic model support system for a real-time replication of the lateral vehicle motion during the wind tunnel experiments.
The natural flow is characterized in section 4.2, with a focus on the cross-wind gust response and its representation via a linear parameter-varying model. This method is applied here for the first time to a gray-box modeling of unsteady flow phenomena from experimental data, and allows dependencies on external parameters such as free-stream velocity or varying cross-wind angle to be taken into account explicitly. In section 4.3 this LPV modeling approach is also used to identify the actuated flow dynamics and compared with the conventional method, which is based on identifying a set of linear black-box models at various cross-wind angles and free-stream velocities.
The characteristics of the models for lateral dynamics [85, 108] and driver behavior [85, 105] are discussed in section 4.5. Here, a scaling method is proposed to convert these models so that their dynamics match wind tunnel dimensions and velocity. This is necessary to enable a real-time simulation during the experiments, and special care has to be taken for a correct replication of the vehicle motion in the wind tunnel. As described in section 4.5.3, this setup and the identified LPV models for the unsteady gust response allow the interaction between transient aerodynamics and lateral vehicle dynamics to be investigated for various driving velocities.
The design of robust and linear parameter-varying feedback controllers is presented in section 4.6, together with a dynamic reference filter that helps to reduce drag efficiently and improve cross-wind sensitivity. Additionally, an LPV feedforward controller is proposed that provides additional disturbance suppression during cross-wind gusts.
In section 4.7 the performance of these controllers is tested and compared in cross-wind gust experiments with real-time replication of the lateral vehicle dynamics and driver behavior. The proposed LPV approach is then used to estimate the closed-loop performance for a real-sized vehicle at realistic driving velocities. Chapter 5 concludes with a summary and a brief evaluation of the obtained results.

Chapter 2

Fundamentals of applied methods

2.1 Linear parameter-varying H_∞ control

A linear parameter-varying (LPV) system can be described in state-space form by

$$\underline{\dot{x}}(t) = \boldsymbol{A}(\underline{\theta}(t))x(t) + \boldsymbol{B}(\underline{\theta}(t))\underline{u}(t), \tag{2.1}$$

$$\underline{y}(t) = \boldsymbol{C}(\underline{\theta}(t))\underline{x}(t) + \boldsymbol{D}(\underline{\theta}(t))\underline{u}(t). \tag{2.2}$$

Its state-space matrices are functions of a vector of varying parameters $\underline{\theta}$. Following standard notation, state, input and output vectors are denoted by $\underline{x}$, $\underline{u}$ and $\underline{y}$, respectively.
A conventional approach to control this class of systems is to design so-called gain-scheduling controllers. To this end, Eq. (2.1) and (2.2) are evaluated for a range of frozen parameter values $\underline{\theta}$ to obtain a set of linear time-invariant (LTI) models. The overall control law is obtained by interpolating between several linear controllers that are designed separately for each LTI system corresponding to the respective operating point. However, stability or performance cannot be guaranteed for this kind of gain-scheduling controllers unless the parameters are slowly time-varying [14]. If the parameters can be measured or estimated online, this problem can be circumvented by designing a time-varying controller

$$\underline{\dot{x}}_K(t) = \boldsymbol{A}_K(\underline{\theta}(t))\underline{x}_K(t) + \boldsymbol{B}_K(\underline{\theta}(t))\underline{v}(t), \tag{2.3}$$

$$\underline{u}(t) = \boldsymbol{C}_K(\underline{\theta}(t))\underline{x}_K(t) + \boldsymbol{D}_K(\underline{\theta}(t))\underline{v}(t), \tag{2.4}$$

whose state-space matrices depend on the same parameters as the plant [14]. Here, the vectors $\underline{x}_K$ and $\underline{v}$ denote the controller state and input variables, respectively. In a typical feedback control configuration for tracking setpoints $\underline{r}$, the controller inputs are chosen as $\underline{v} = \underline{r} - \underline{y}$ [121].

2.1.1 Control synthesis for polytopic LPV systems

The control synthesis approach summarized in the following is proposed by Apkarian et al. [12, 13, 14]. It is implemented in the `MATLAB`-command "`hinfgs.m`" in the Robust Control Toolbox [84]. Proofs are omitted here and all formulations and theorems are described only for the continuous-time case.
The derivation is based on the Bounded Real Lemma (**BRL**), which is valid only for linear time-invariant (**LTI**) systems and is given in the following theorem.

Theorem 2.1.1 (**Bounded Real Lemma [14]**). *Given a continuous-time transfer function $\boldsymbol{G}(s)$ of (not necessarily minimal) realization $\boldsymbol{G}(s) = \boldsymbol{D} + \boldsymbol{C}(s\boldsymbol{I} - \boldsymbol{A})^{-1}\boldsymbol{B}$ and a positive scalar γ, the following statements are equivalent:*

- *$\boldsymbol{A}$ is stable and $\left\|\boldsymbol{D} + \boldsymbol{C}(s\boldsymbol{I} - \boldsymbol{A})^{-1}\boldsymbol{B}\right\|_\infty < \gamma$*
- *there exists a positive definite solution $\boldsymbol{X}$ to the matrix inequality*

$$\boldsymbol{\mathcal{B}}_{[\boldsymbol{A},\boldsymbol{B},\boldsymbol{C},\boldsymbol{D}]}(\boldsymbol{X}, \gamma) < 0, \tag{2.5}$$

*with the Bounded Real Lemma (**BRL**) map*

$$\boldsymbol{\mathcal{B}}_{[\boldsymbol{A},\boldsymbol{B},\boldsymbol{C},\boldsymbol{D}]}(\boldsymbol{X},\gamma) := \begin{bmatrix} \boldsymbol{A}^T\boldsymbol{X}+\boldsymbol{X}\boldsymbol{A} & \boldsymbol{X}\boldsymbol{B} & \boldsymbol{C}^T \\ \boldsymbol{B}^T\boldsymbol{X} & -\gamma\boldsymbol{I} & \boldsymbol{D}^T \\ \boldsymbol{C} & \boldsymbol{D} & -\gamma\boldsymbol{I} \end{bmatrix}. \tag{2.6}$$

■

In [14], the authors extend the Bounded Real Lemma (**BRL**) to linear parameter-varying (**LPV**) systems with the notion of Quadratic H_∞ Performance.

Definition 2.1.1 (Quadratic H_∞ Performance [14]). *The LPV system (2.1, 2.2) has quadratic H_∞ performance γ if and only if there exists a single matrix $\boldsymbol{X} > 0$ such that*

$$\boldsymbol{\mathcal{B}}_{[\boldsymbol{A}(\underline{\theta}),\boldsymbol{B}(\underline{\theta}),\boldsymbol{C}(\underline{\theta}),\boldsymbol{D}(\underline{\theta})]}(\boldsymbol{X},\gamma) < 0 \tag{2.7}$$

for all admissible values of the parameter vector $\underline{\theta}$.
Then the Lyapunov function $V(\underline{x}) = \underline{x}^T\boldsymbol{X}\underline{x}$ establishes (global) stability and the $\mathcal{L}_2$ gain of the input/output map is bounded by γ. That is,

$$\left\|\underline{y}\right\|_2 < \gamma \left\|\underline{u}\right\|_2 \tag{2.8}$$

along all possible parameter trajectories $\underline{\theta}$.

■

Definition 2.1.1 for Quadratic H_∞ Performance implies the existence of a fixed Lyapunov function for the entire operating range [14]. Condition (2.7) is difficult to evaluate, however, since it imposes an infinite number of constraints. This problem can be circumvented for LPV systems whose state-space matrices depend affinely on a parameter vector $\underline{\theta}(t)$, which varies in a polytope Θ

$$\underline{\theta}(t) \in \Theta := \mathrm{Co}\{\underline{\theta}_1, \underline{\theta}_2, \ldots, \underline{\theta}_r\}. \tag{2.9}$$

Here, the vertices $\underline{\theta}_1, \underline{\theta}_2, \ldots, \underline{\theta}_r$ correspond to the extremal parameter values. A matrix polytope is defined as the convex hull

$$\mathrm{Co}\{\boldsymbol{N}_i : i = 1, \ldots, r\} := \left\{ \sum_{i=1}^{r} \alpha_i \boldsymbol{N}_i : \alpha_i \geq 0, \sum_{i=1}^{r} \alpha_i = 1 \right\} \tag{2.10}$$

of a finite number r of matrices $\boldsymbol{N}_i$ with the same dimension. Here, the polytopic coordinates of the convex hull are denoted by α_i, with $i = 1, \ldots, r$. Following this notation, Apkarian et al. define “polytopic” LPV plants as state-space systems with affine dependence of the matrices $\boldsymbol{A}(\underline{\theta}), \boldsymbol{B}(\underline{\theta}), \boldsymbol{C}(\underline{\theta}), \boldsymbol{D}(\underline{\theta})$ on the parameter vector $\underline{\theta}$, which ranges over a fixed polytope. This leads to the following theorem for the Quadratic H_∞ Performance of polytopic LPV systems.

Theorem 2.1.2 (Vertex Property [14]). *Consider a polytopic LPV plant described in state-space form by*

$$\dot{\underline{x}} = \boldsymbol{A}(\underline{\theta})\underline{x} + \boldsymbol{B}(\underline{\theta})\underline{u} \tag{2.11}$$
$$\underline{y} = \boldsymbol{C}(\underline{\theta})\underline{x} + \boldsymbol{D}(\underline{\theta})\underline{u} \tag{2.12}$$

with

$$\begin{bmatrix} \boldsymbol{A}(\underline{\theta}) & \boldsymbol{B}(\underline{\theta}) \\ \boldsymbol{C}(\underline{\theta}) & \boldsymbol{D}(\underline{\theta}) \end{bmatrix} \in \mathcal{P} := Co\left\{ \begin{bmatrix} \boldsymbol{A}_i & \boldsymbol{B}_i \\ \boldsymbol{C}_i & \boldsymbol{D}_i \end{bmatrix} := \begin{bmatrix} \boldsymbol{A}(\underline{\theta}_i) & \boldsymbol{B}(\underline{\theta}_i) \\ \boldsymbol{C}(\underline{\theta}_i) & \boldsymbol{D}(\underline{\theta}_i) \end{bmatrix} : i = 1, \ldots, r \right\}. \tag{2.13}$$

The following statements are equivalent:

- *the LPV system (2.11, 2.12) is stable with Quadratic H_∞ Performance γ,*
- *there exists a single matrix $\boldsymbol{X} > 0$ such that for all $\begin{bmatrix} \boldsymbol{A}(\underline{\theta}) & \boldsymbol{B}(\underline{\theta}) \\ \boldsymbol{C}(\underline{\theta}) & \boldsymbol{D}(\underline{\theta}) \end{bmatrix} \in \mathcal{P}$,*

$$\boldsymbol{\mathcal{B}}_{[\boldsymbol{A}(\underline{\theta}),\boldsymbol{B}(\underline{\theta}),\boldsymbol{C}(\underline{\theta}),\boldsymbol{D}(\underline{\theta})]}(\boldsymbol{X},\gamma) < 0 \tag{2.14}$$

- *there exists $\boldsymbol{X} > 0$ satisfying the system of LMIs:*

$$\boldsymbol{\mathcal{B}}_{[\boldsymbol{A}_i,\boldsymbol{B}_i,\boldsymbol{C}_i,\boldsymbol{D}_i]}(\boldsymbol{X},\gamma) < 0, \quad i = 1, 2, \ldots, r. \tag{2.15}$$

■

This theorem implies that the infinite number of constraints imposed by Eq. (2.7) can be reduced to a finite set of LMIs in the special case of polytopic systems.
Similar to LTI plants, the H_∞ control synthesis problem for polytopic LPV systems is formulated by augmenting the plant (2.1,2.2) with adequate loopshaping weights [14]. This results in a generalized plant description

$$\dot{\underline{x}} = \boldsymbol{A}(\underline{\theta})\underline{x} + \boldsymbol{B}_1(\underline{\theta})\underline{w} + \boldsymbol{B}_2(\underline{\theta})\underline{u}, \tag{2.16}$$
$$\underline{z} = \boldsymbol{C}_1(\underline{\theta})\underline{x} + \boldsymbol{D}_{11}(\underline{\theta})\underline{w} + \boldsymbol{D}_{12}(\underline{\theta})\underline{u}, \tag{2.17}$$
$$\underline{v} = \boldsymbol{C}_2(\underline{\theta})\underline{x} + \boldsymbol{D}_{21}(\underline{\theta})\underline{w} + \boldsymbol{D}_{22}(\underline{\theta})\underline{u}, \tag{2.18}$$

with exogenous inputs $\underline{w}$, control inputs $\underline{u}$, weighted outputs $\underline{z}$, measured outputs $\underline{v}$ and the dimensions

$$\boldsymbol{A}(\underline{\theta}) \in \mathbb{R}^{n\times n}, \boldsymbol{D}_{11}(\underline{\theta}) \in \mathbb{R}^{p_1\times m_1}, \boldsymbol{D}_{22}(\underline{\theta}) \in \mathbb{R}^{p_2\times m_2}. \tag{2.19}$$

The matrices of the generalized plant vary in a polytope

$$\begin{bmatrix} \boldsymbol{A}(\underline{\theta}) & \boldsymbol{B}_1(\underline{\theta}) & \boldsymbol{B}_2(\underline{\theta}) \\ \boldsymbol{C}_1(\underline{\theta}) & \boldsymbol{D}_{11}(\underline{\theta}) & \boldsymbol{D}_{12}(\underline{\theta}) \\ \boldsymbol{C}_2(\underline{\theta}) & \boldsymbol{D}_{21}(\underline{\theta}) & \boldsymbol{D}_{22}(\underline{\theta}) \end{bmatrix} \in Co \left\{ \begin{bmatrix} \boldsymbol{A}_i & \boldsymbol{B}_{1i} & \boldsymbol{B}_{2i} \\ \boldsymbol{C}_{1i} & \boldsymbol{D}_{11i} & \boldsymbol{D}_{12i} \\ \boldsymbol{C}_{2i} & \boldsymbol{D}_{21i} & \boldsymbol{D}_{22i} \end{bmatrix}, i = 1, 2, \ldots, r \right\}. \tag{2.20}$$

Here, the extremal matrices $\boldsymbol{A}_i$, $\boldsymbol{B}_{1i}\ldots$ correspond to the values of $\boldsymbol{A}(\underline{\theta})$, $\boldsymbol{B}_1(\underline{\theta}), \ldots$ at the vertices $\underline{\theta} = \underline{\theta}_i$ of the parameter polytope. The controller to be synthesized is of the form

$$\dot{\underline{x}}_K = \boldsymbol{A}_K(\underline{\theta})\underline{x}_K + \boldsymbol{B}_K(\underline{\theta})\underline{v} \tag{2.21}$$
$$\underline{u} = \boldsymbol{C}_K(\underline{\theta})\underline{x}_K + \boldsymbol{D}_K(\underline{\theta})\underline{v}, \tag{2.22}$$

with dimension $\boldsymbol{A}_K(\underline{\theta}) \in \mathbb{R}^{k\times k}$. It is denoted in the following by

$$\boldsymbol{\Omega}(\underline{\theta}) := \begin{bmatrix} \boldsymbol{A}_K(\underline{\theta}) & \boldsymbol{B}_K(\underline{\theta}) \\ \boldsymbol{C}_K(\underline{\theta}) & \boldsymbol{D}_K(\underline{\theta}) \end{bmatrix}. \tag{2.23}$$

With $\underline{x}_{cl} = \begin{bmatrix} \underline{x}^T & \underline{x}_K^T \end{bmatrix}^T$, the closed-loop system can be described by state-space equations

$$\dot{\underline{x}}_{cl} = \boldsymbol{A}_{cl}(\underline{\theta})\underline{x}_{cl} + \boldsymbol{B}_{cl}(\underline{\theta})\underline{w}, \tag{2.24}$$
$$\underline{z} = \boldsymbol{C}_{cl}(\underline{\theta})\underline{x}_{cl} + \boldsymbol{D}_{cl}(\underline{\theta})\underline{w}, \tag{2.25}$$

with

$$\boldsymbol{A}_{cl}(\underline{\theta}) = \boldsymbol{A}_0(\underline{\theta}) + \boldsymbol{\mathcal{B}}\boldsymbol{\Omega}(\underline{\theta})\boldsymbol{\mathcal{C}}, \qquad \boldsymbol{B}_{cl}(\underline{\theta}) = \boldsymbol{B}_0(\underline{\theta}) + \boldsymbol{\mathcal{B}}\boldsymbol{\Omega}(\underline{\theta})\boldsymbol{\mathcal{D}}_{21}, \tag{2.26}$$
$$\boldsymbol{C}_{cl}(\underline{\theta}) = \boldsymbol{C}_0(\underline{\theta}) + \boldsymbol{\mathcal{D}}_{12}\boldsymbol{\Omega}(\underline{\theta})\boldsymbol{\mathcal{C}}, \qquad \boldsymbol{D}_{cl}(\underline{\theta}) = \boldsymbol{D}_{11}(\underline{\theta}) + \boldsymbol{\mathcal{D}}_{12}\boldsymbol{\Omega}(\underline{\theta})\boldsymbol{\mathcal{D}}_{21}, \tag{2.27}$$

and

$$\boldsymbol{A}_0 = \begin{bmatrix} \boldsymbol{A}(\underline{\theta}) & \boldsymbol{0} \\ \boldsymbol{0} & \boldsymbol{0}_{k\times k} \end{bmatrix}, \quad \boldsymbol{B}_0 = \begin{bmatrix} \boldsymbol{B}_1(\underline{\theta}) \\ \boldsymbol{0} \end{bmatrix}, \quad \boldsymbol{C}_0 = \begin{bmatrix} \boldsymbol{C}_1(\underline{\theta}) & \boldsymbol{0} \end{bmatrix}, \tag{2.28}$$

$$\boldsymbol{\mathcal{B}} = \begin{bmatrix} \boldsymbol{0} & \boldsymbol{B}_2 \\ \boldsymbol{I}_k & \boldsymbol{0} \end{bmatrix}, \quad \boldsymbol{\mathcal{C}} = \begin{bmatrix} \boldsymbol{0} & \boldsymbol{I}_k \\ \boldsymbol{C}_2 & \boldsymbol{0} \end{bmatrix}, \quad \boldsymbol{\mathcal{D}}_{12} = \begin{bmatrix} \boldsymbol{0} & \boldsymbol{D}_{12} \end{bmatrix}, \quad \boldsymbol{\mathcal{D}}_{21} = \begin{bmatrix} \boldsymbol{0} \\ \boldsymbol{D}_{21} \end{bmatrix}. \tag{2.29}$$

For the control synthesis approach by Apkarian et al. [14] three assumptions have to be made on the plant:

(A1) $\boldsymbol{D}_{22}(\underline{\theta}) = \boldsymbol{0}$ or equivalently $\boldsymbol{D}_{22i} = \boldsymbol{0}$ for $i = 1, 2, \ldots, r$,

(A2) $\boldsymbol{B}_2(\underline{\theta}), \boldsymbol{C}_2(\underline{\theta}), \boldsymbol{D}_{12}(\underline{\theta}), \boldsymbol{D}_{21}(\underline{\theta})$ are parameter-independent or equivalently,

$$\boldsymbol{B}_{2i} = \boldsymbol{B}_2, \boldsymbol{C}_{2i} = \boldsymbol{C}_2, \boldsymbol{D}_{12i} = \boldsymbol{D}_{12}, \boldsymbol{D}_{21i} = \boldsymbol{D}_{21}, \quad \text{for } i = 1, 2, \ldots, r. \tag{2.30}$$

(A3) The pairs $(\boldsymbol{A}(\underline{\theta}), \boldsymbol{B}_2)$ and $(\boldsymbol{A}(\underline{\theta}), \boldsymbol{C}_2)$ are quadratically stabilizable and quadratically detectable over Θ, respectively.

If assumptions 1 or 2 are not satisfied, **(A1)** can often be fulfilled by redefining the plant output, whereas assumption **(A2)** can be achieved by pre- or postfiltering the plant inputs or outputs $\underline{u}$ and $\underline{y}$, respectively, as described by Apkarian et al. [14]. This leads to parameter-free control and measurement matrices. Assumption **(A3)** is sufficient and necessary for quadratic stabilization of the polytopic LPV plant by output feedback [14]. Given these conditions, the following theorem states the notion of an interpolating LPV controller.

Theorem 2.1.3 ([14])**.** *Consider a continuous LPV polytopic plant and assume **(A1)-(A3)**. Given some positive scalar γ, the following statements are equivalent:*

1. *there exists a k-th order LPV controller solving the Quadratic H_∞ Performance problem with bound γ,*
2. *there exist some $(n+k)\times(n+k)$ positive definite matrix $\boldsymbol{X}_{cl}$ and k-th order LTI controllers $\boldsymbol{\Omega}_i = \begin{bmatrix} \boldsymbol{A}_{Ki} & \boldsymbol{B}_{Ki} \\ \boldsymbol{C}_{Ki} & \boldsymbol{D}_{Ki} \end{bmatrix}$ such that*

$$\boldsymbol{\mathcal{B}}_{[\boldsymbol{A}_{cl}(\underline{\theta}_i),\boldsymbol{B}_{cl}(\underline{\theta}_i),\boldsymbol{C}_{cl}(\underline{\theta}_i),\boldsymbol{D}_{cl}(\underline{\theta}_i)]}(\boldsymbol{X}_{cl}, \gamma) < 0 \quad (i = 1, 2, \ldots, r), \tag{2.31}$$

where $\underline{\theta}_1, \ldots, \underline{\theta}_r$ are the vertices of the parameter polytope and $\boldsymbol{A}_{cl}(\underline{\theta}_i) = \boldsymbol{A}_0(\underline{\theta}_i) + \boldsymbol{\mathcal{B}}\,\boldsymbol{\Omega}_i\boldsymbol{\mathcal{C}}, \ldots$ with the notation (2.26, 2.27).

If 1 or 2 is satisfied, a possible choice of LPV controller is the polytopic controller in state-space form by

$$\boldsymbol{\Omega}(\underline{\theta}) := \sum_{i=1}^{r} \alpha_i \boldsymbol{\Omega}_i = \sum_{i=1}^{r} \alpha_i \begin{bmatrix} \boldsymbol{A}_{Ki} & \boldsymbol{B}_{Ki} \\ \boldsymbol{C}_{Ki} & \boldsymbol{D}_{Ki} \end{bmatrix} \tag{2.32}$$

where $(\alpha_1, \ldots, \alpha_r)$ is any solution of the convex decomposition problem:

$$\underline{\theta} = \sum_{i=1}^{r} \alpha_i \underline{\theta}_i \tag{2.33}$$

■

Thus, the control synthesis problem involves computing a single Lyapunov matrix $\boldsymbol{X}_{cl}$ and vertex controllers $\boldsymbol{\Omega}_i$ fulfilling the LMIs (2.31). The solvability conditions are as follows:

Theorem 2.1.4 (Convex Solvability Conditions [14])**.** *Consider a continuous LPV polytopic plant and assume **(A1)-(A3)**. Let $\boldsymbol{\mathcal{N}}_R$ and $\boldsymbol{\mathcal{N}}_S$ denote bases of the null space of $(\boldsymbol{B}_2^T, \boldsymbol{D}_{12})^T$ and $(\boldsymbol{C}_2, \boldsymbol{D}_{21})$, respectively. There exists an LPV controller guaranteeing Quadratic H_∞ Performance γ along all parameter trajectories in the polytope*

$$\Theta = \left\{ \sum_{i=1}^{r} \alpha_i \underline{\theta}_i : \quad \alpha_i \geq 0; \quad \sum_{i=1}^{r} \alpha_i = 1 \right\} \tag{2.34}$$

if and only if there exist two symmetric matrices $(\boldsymbol{\mathcal{R}}, \boldsymbol{\mathcal{S}})$ in $\mathbb{R}^{n \times n}$ satisfying the system of $2r+1$ LMIs:

$$\left[\begin{array}{c|c} \boldsymbol{\mathcal{N}}_R & \boldsymbol{0} \\ \hline \boldsymbol{0} & \boldsymbol{I} \end{array}\right]^T \left[\begin{array}{cc|c} \boldsymbol{A}_i\boldsymbol{\mathcal{R}} + \boldsymbol{\mathcal{R}}\boldsymbol{A}_i^T & \boldsymbol{\mathcal{R}}\boldsymbol{C}_{1i}^T & \boldsymbol{B}_{1i} \\ \boldsymbol{C}_{1i}\boldsymbol{\mathcal{R}} & -\gamma\boldsymbol{I} & \boldsymbol{D}_{11i} \\ \hline \boldsymbol{B}_{1i}^T & \boldsymbol{D}_{11i}^T & -\gamma\boldsymbol{I} \end{array}\right] \left[\begin{array}{c|c} \boldsymbol{\mathcal{N}}_R & \boldsymbol{0} \\ \hline \boldsymbol{0} & \boldsymbol{I} \end{array}\right] < 0 \quad (i = 1, \ldots, r), \tag{2.35}$$

$$\left[\begin{array}{c|c} \boldsymbol{\mathcal{N}}_S & \boldsymbol{0} \\ \hline \boldsymbol{0} & \boldsymbol{I} \end{array}\right]^T \left[\begin{array}{cc|c} \boldsymbol{A}_i\boldsymbol{\mathcal{S}} + \boldsymbol{\mathcal{S}}\boldsymbol{A}_i^T & \boldsymbol{\mathcal{S}}\boldsymbol{B}_{1i} & \boldsymbol{C}_{1i}^T \\ \boldsymbol{B}_{1i}^T\boldsymbol{\mathcal{S}} & -\gamma\boldsymbol{I} & \boldsymbol{D}_{11i}^T \\ \hline \boldsymbol{C}_{1i} & \boldsymbol{D}_{11i} & -\gamma\boldsymbol{I} \end{array}\right] \left[\begin{array}{c|c} \boldsymbol{\mathcal{N}}_S & \boldsymbol{0} \\ \hline \boldsymbol{0} & \boldsymbol{I} \end{array}\right] < 0 \quad (i = 1, \ldots, r), \tag{2.36}$$

$$\begin{bmatrix} \boldsymbol{\mathcal{R}} & \boldsymbol{I} \\ \boldsymbol{I} & \boldsymbol{\mathcal{S}} \end{bmatrix} \geq 0. \tag{2.37}$$

Moreover, there exist k-th order LPV controllers solving the same problem if and only if $\boldsymbol{\mathcal{R}}, \boldsymbol{\mathcal{S}}$ further satisfy the rank constraint

$$rank(\boldsymbol{I} - \boldsymbol{\mathcal{R}}\boldsymbol{\mathcal{S}}) \leq k. \tag{2.38}$$

■

In the full-order case ($k = n$) the rank constraint (2.38) is readily satisfied and $\boldsymbol{\mathcal{R}}, \boldsymbol{\mathcal{S}}$ are only constrained by the LMIs (2.35 - 2.37). Minimizing γ subject to (2.35 - 2.37) and computing a feasible solution for $\boldsymbol{\mathcal{R}}, \boldsymbol{\mathcal{S}}$ represents a convex problem that can be solved efficiently with convex optimization algorithms [14]. The Lyapunov matrix $\boldsymbol{X}_{cl}$ is constructed from $\boldsymbol{\mathcal{R}}, \boldsymbol{\mathcal{S}}$ with the following steps [14]:

- compute full-rank matrices $\boldsymbol{\mathcal{M}}, \boldsymbol{\mathcal{N}} \in \mathbb{R}^{n \times k}$ such that

$$\boldsymbol{\mathcal{M}}\boldsymbol{\mathcal{N}}^T = \boldsymbol{I} - \boldsymbol{\mathcal{R}}\boldsymbol{\mathcal{S}}, \tag{2.39}$$

- compute $\boldsymbol{X}_{cl}$ as the unique solution of the linear matrix equation $\boldsymbol{\Pi}_2 = \boldsymbol{X}_{cl}\boldsymbol{\Pi}_1$, where

$$\boldsymbol{\Pi}_2 := \begin{bmatrix} \boldsymbol{\mathcal{S}} & \boldsymbol{I} \\ \boldsymbol{\mathcal{N}}^T & \boldsymbol{0} \end{bmatrix}; \quad \boldsymbol{\Pi}_1 := \begin{bmatrix} \boldsymbol{I} & \boldsymbol{\mathcal{R}} \\ \boldsymbol{0} & \boldsymbol{\mathcal{M}}^T \end{bmatrix}. \tag{2.40}$$

Once $\boldsymbol{X}_{cl}$ is found, the vertex controllers $\boldsymbol{\Omega}_i = \begin{bmatrix} \boldsymbol{A}_{Ki} & \boldsymbol{B}_{Ki} \\ \boldsymbol{C}_{Ki} & \boldsymbol{D}_{Ki} \end{bmatrix}$ can be computed by solving the matrix inequality

$$\boldsymbol{\mathcal{B}}_{[\boldsymbol{A}_{cl}(\underline{\theta}_i), \boldsymbol{B}_{cl}(\underline{\theta}_i), \boldsymbol{C}_{cl}(\underline{\theta}_i), \boldsymbol{D}_{cl}(\underline{\theta}_i)]}(\boldsymbol{X}_{cl}, \gamma) < 0. \tag{2.41}$$

The time-varying controller matrices are obtained by interpolation between the vertex controllers by

$$\boldsymbol{\Omega}(\underline{\theta}) = \sum_{i=1}^{r} \alpha_i \boldsymbol{\Omega}_i = \sum_{i=1}^{r} \alpha_i \begin{bmatrix} \boldsymbol{A}_{Ki} & \boldsymbol{B}_{Ki} \\ \boldsymbol{C}_{Ki} & \boldsymbol{D}_{Ki} \end{bmatrix}, \tag{2.42}$$

with the polytopic coordinates $(\alpha_1, \ldots, \alpha_r)$ defined by the convex decomposition

$$\underline{\theta} = \sum_{i=1}^{r} \alpha_i \underline{\theta}_i : \alpha_i > 0, \sum_{i=1}^{r} \alpha_i = 1. \tag{2.43}$$

2.1.2 Implementation and discretization of LMI-synthesized LPV controllers

The control synthesis algorithm by Apkarian et al. [14] and its `Matlab`-implementation in the "`hinfgs.m`"-function are given in continuous time. For real-time control, the controller matrices resulting from the current measurement of the time-varying parameter $\underline{\theta}$ are updated in each sampling step by interpolation between the vertex controllers following the scheme given in Eq. (2.42). The corresponding state-space equations of the LPV controller (2.3, 2.4) may be solved by numerical integration on a digital signal processor (DSP).
However, the continuous-time LPV H_∞ controllers synthesized with the algorithm described in the previous section usually contain fast Eigenmodes. Due to the limited maximum sampling rates in real-time applications on a DSP, this often leads to unstable results with the commonly available integration schemes.
This problem may be circumvented by different control synthesis algorithms that restrict the pole locations of the controller to the stable region [109], or by an adequate order reduction of the LPV controller state-space equations to eliminate the fast modes, see e.g. Wood et al. [146]. In this thesis, a different approach proposed by Apkarian in [10] is applied. It involves discretizing the continuous-time state-space equations of the LPV controller

$$\dot{\underline{x}}_K(t) = \boldsymbol{A}_K(\underline{\theta}(t))\underline{x}_K(t) + \boldsymbol{B}_K(\underline{\theta}(t))\underline{v}(t), \tag{2.44}$$
$$\underline{u}(t) = \boldsymbol{C}_K(\underline{\theta}(t))\underline{x}_K(t) + \boldsymbol{D}_K(\underline{\theta}(t))\underline{v}(t), \tag{2.45}$$

via the LPV counterpart of the Tustin or bilinear transformation. Here, Apkarian [10] assumes that the parameter and the measurement vectors on the time interval $[kT_s, (k+1)T_s]$ can be approximated by

$$\underline{\theta}(t) \approx \underline{\theta}_k, \quad \underline{v}(t) \approx \underline{v}_k, \quad \text{for } kT_s \leq t < (k+1)T_s, \tag{2.46}$$

where the index k denotes the corresponding value at time kT_s. The LPV trapezoidal approximation is then formalized by the following theorem:

Theorem 2.1.5 (Trapezoidal Approximation [10]). *Consider the LPV controller governed by (2.44, 2.45) and assume the sampling period is T_s. A trapezoidal approximation of the sampled dynamics of the system can be described in state space by the following discrete time LPV system*

$$\underline{z}_{k+1} = \left(\boldsymbol{I} - \frac{T_s}{2}\boldsymbol{A}_K(\underline{\theta}_k)\right)^{-1}\left(\boldsymbol{I} + \frac{T_s}{2}\boldsymbol{A}_K(\underline{\theta}_k)\right)\underline{z}_k + \sqrt{T_s}\left(\boldsymbol{I} - \frac{T_s}{2}\boldsymbol{A}_K(\underline{\theta}_k)\right)^{-1}\boldsymbol{B}_K(\underline{\theta}_k)\underline{v}_k, \tag{2.47}$$

$$\begin{aligned}\underline{u}_k =& \sqrt{T_s}\boldsymbol{C}_K(\underline{\theta}_k)\left(\boldsymbol{I} - \frac{T_s}{2}\boldsymbol{A}_K(\underline{\theta}_k)\right)^{-1}\underline{z}_k \\ &+ \left(\frac{T_s}{2}\boldsymbol{C}_K(\underline{\theta}_k)\left(\boldsymbol{I} - \frac{T_s}{2}\boldsymbol{A}_K(\underline{\theta}_k)\right)^{-1}\boldsymbol{B}_K(\underline{\theta}_k) + \boldsymbol{D}_K(\underline{\theta}_k)\right)\underline{v}_k.\end{aligned} \tag{2.48}$$

Proof: See Apkarian [10].

■

Carrying out the bilinear transformation given in theorem 2.1.5 in each sampling step k results in a relatively large computational effort due to the required matrix inversions in Eq. (2.47, 2.48). However, Apkarian shows in [10] that an LTI controller obtained by evaluating the LPV controller matrices at a frozen parameter value $\underline{\theta}_0 := \underline{\theta}(t)$ maintains stability and performance in the vicinity of $\underline{\theta}_0$. As a result, the update of the discrete-time LPV controller matrices in Eq. (2.47, 2.48) may be performed at certain multiples of the sampling period, given a sufficiently slow variation of $\underline{\theta}(t)$ in the neighborhood of $\underline{\theta}_0$. The associated computational benefits help the real-time applicability of the proposed method.

2.2 Aerodynamics

2.2.1 Nondimensional incompressible Navier-Stokes equation

The Navier-Stokes equation for an incompressible Newtonian Fluid is given in dimensional form by

$$\rho\left(\frac{\partial \underline{u}}{\partial t} + \underline{u}\cdot\nabla\underline{u}\right) = -\nabla p + \mu\nabla^2\underline{u} + \underline{f}, \tag{2.49}$$

with the velocity vector $\underline{u}$, the density ρ and dynamic viscosity μ of the fluid, the pressure p and the body force $\underline{f}$, see e.g. White [140]. Introducing nondimensional scales for length, velocity and time as described by Schlichting and Gersten in [110] results in the dimensionless variables as given in table 2.1. For the assumption of an incompressible fluid, density ρ and viscosity μ are

Dimensional variable	**Scale**	**Dimensionless variable**
Location: x, y, z	Reference length: L	$\mathrm{x}^* = \frac{\mathrm{x}}{L}, \mathrm{y}^* = \frac{\mathrm{y}}{L}, \mathrm{z}^* = \frac{\mathrm{z}}{L}$
Velocity: u, v, w	Reference velocity: U	$\mathrm{u}^* = \frac{\mathrm{u}}{\mathrm{U}}, \mathrm{v}^* = \frac{\mathrm{v}}{\mathrm{U}}, \mathrm{w}^* = \frac{\mathrm{w}}{\mathrm{U}}$
Time: t	Reference time: $\frac{L}{\mathrm{U}}$	$t^* = \frac{t\mathrm{U}}{L}$
Pressure: p	$\rho\mathrm{U}^2$	$p^* = \frac{p-p_R}{\rho\mathrm{U}^2}$

Table 2.1: Nondimensional variables and corresponding scales for the dimensionless representation of the incompressible Navier-Stokes equation

constant, and thus no reference scales need to be introduced for these variables. Furthermore, the pressure p only appears in derivative terms in Eq. (2.49). Therefore, the difference from a reference pressure p_R can be used in the dimensionless variable p^*.
Substituting the variables in Eq. (2.49) for their dimensionless counterparts yields the nondimensional incompressible Navier-Stokes equation

$$\frac{\partial \underline{u}^*}{\partial t^*} + \underline{u}^*\cdot\nabla^*\underline{u}^* = -\nabla^* p^* + \frac{1}{Re}\nabla^{*2}\underline{u}^* + \underline{f}\frac{L}{\rho U^2}. \tag{2.50}$$

Here, the last term can be neglected if the body forces are small. This can be assumed in many practical applications such as road vehicle aerodynamics [110]. In Eq. (2.50) the Reynolds number

$$Re = \frac{\rho \mathrm{U} L}{\mu} \tag{2.51}$$

appears as an dimensionless parameter. It describes the ratio between inertial and viscous forces [140] and is often also defined with respect to the kinematic viscosity $\nu = \mu/\rho$. Another important nondimensional characteristic number is the Strouhal number

$$St = \frac{fL}{\mathrm{U}} = f^*, \tag{2.52}$$

which corresponds to a reduced frequency f^* and is commonly used to describe the characteristics of periodic time-varying flow phenomena such as the von Kármán Vortex street [140].

2.2.2 LPV model for dimensional flow dynamics

In this thesis a nondimensional form of dynamic state-space models is proposed to describe the characteristics of unsteady flow phenomena. The nondimensionalization and choice of scales is carried out in an analogous manner as described in the previous section for the Navier-Stokes equation. The structure of the dimensionless state-space models is chosen as

$$\frac{d\underline{x}^*}{dt^*} = \boldsymbol{A}^*\underline{x}^* + \boldsymbol{B}^*\underline{u}^* + \boldsymbol{E}^*\underline{d}^*, \tag{2.53}$$

$$\underline{y}^* = \boldsymbol{C}^*\underline{x}^* + \boldsymbol{D}^*\underline{u}^* + \boldsymbol{F}^*\underline{d}^*, \tag{2.54}$$

with nondimensional vectors of the state variables $\underline{x}^*$, control inputs $\underline{u}^*$, disturbance inputs $\underline{d}^*$ and measurement or output variables $\underline{y}^*$. Here, the time derivative $d\underline{x}^*/dt^*$ is defined with respect to nondimensional or convective time

$$t^* = \frac{t\,\mathrm{u}_\infty}{L}. \tag{2.55}$$

However, all dynamic processes in the actual experiment or on-road application elapse in physical, dimensional time t. Thus, for model identification or control purposes the nondimensional state-space model defined in equations (2.53) and (2.54) has to be converted to an at least partially dimensional form in physical time. With the diagonal matrix

$$\boldsymbol{T}_R = diag(x_{1,R}, x_{2,R}, \ldots x_{n_x,R}) \tag{2.56}$$

of reference variables $x_{1,R} \ldots x_{n_x,R}$ for the n_x dimensional state variables in vector

$$\underline{x} = \left[x_1 \ldots x_{n_x}\right]^T, \tag{2.57}$$

the nondimensional state vector can be expressed as

$$\underline{x}^* = \boldsymbol{T}_R^{-1}\underline{x}. \tag{2.58}$$

Expanding its derivative with respect to nondimensional time according to

$$\frac{d\underline{x}^*}{dt^*} = \frac{d\underline{x}^*}{dt}\frac{dt}{dt^*}, \text{ with } \frac{d\underline{x}^*}{dt} = \boldsymbol{T}_R^{-1}\frac{d\underline{x}}{dt}, \text{ and } \frac{dt}{dt^*} = \frac{L}{\mathrm{u}_\infty}, \tag{2.59}$$

results in

$$\frac{d\underline{x}^*}{dt^*} = \boldsymbol{T}_R^{-1}\frac{d\underline{x}}{dt}\frac{L}{\mathrm{u}_\infty} = \frac{L}{\mathrm{u}_\infty}\boldsymbol{T}_R^{-1}\underline{\dot{x}}. \tag{2.60}$$

Substituting Eq. (2.55), (2.58) and (2.60) into Eq. (2.53) and (2.54) yields

$$\underline{\dot{x}} = \underbrace{\frac{\mathrm{u}_\infty}{L}\boldsymbol{T}_R\boldsymbol{A}^*\boldsymbol{T}_R^{-1}}_{\boldsymbol{A}(\theta)}\underline{x} + \underbrace{\frac{\mathrm{u}_\infty}{L}\boldsymbol{T}_R\boldsymbol{B}^*}_{\boldsymbol{B}(\theta)}\underline{u}^* + \underbrace{\frac{\mathrm{u}_\infty}{L}\boldsymbol{T}_R\boldsymbol{E}^*}_{\boldsymbol{E}(\theta)}\underline{d}^*, \tag{2.61}$$

$$\underline{y}^* = \underbrace{\boldsymbol{C}^*\boldsymbol{T}_R^{-1}}_{\boldsymbol{C}}\underline{x} + \underbrace{\boldsymbol{D}^*}_{\boldsymbol{D}}\underline{u}^* + \underbrace{\boldsymbol{F}^*}_{\boldsymbol{F}}\underline{d}^*, \tag{2.62}$$

which represents a linear parameter-varying (LPV) model with one parameter $\theta = \mathrm{u}_\infty$ and the parameter-dependent matrices $\boldsymbol{A}(\theta)$, $\boldsymbol{B}(\theta)$ and $\boldsymbol{E}(\theta)$. A model in this partially dimensional form allows the flow dynamics at different free-stream velocities u_∞ to be described and gives an estimate of how the frequency characteristics change with length scale L. Note that the control and disturbance input variables $\underline{u}^*$ and $\underline{d}^*$ and the output variables $\underline{y}^*$ do not have to be converted to dimensional variables from a control systems point of view. This results in models with varying dynamics but constant gains. These are independent of free-stream velocity u_∞ and length scale L and therefore facilitate the control synthesis procedure.

If the model (2.61,2.62) is identified from experimental data, as is the case for this thesis, the state variables do not necessarily have a physical meaning. Thus, there is no obvious choice for the reference state variables $x_{1,R} \dots x_{n_x,R}$. Accordingly, the matrix $\boldsymbol{T}_R$ is set equal to the identity matrix here. This simplifies Eq. (2.61,2.62) to

$$\underline{\dot{x}} = \underbrace{\frac{\mathrm{u}_\infty}{L}\boldsymbol{A}^*}_{\boldsymbol{A}(\theta)} \underline{x} + \underbrace{\frac{\mathrm{u}_\infty}{L}\boldsymbol{B}^*}_{\boldsymbol{B}(\theta)} \underline{u}^* + \underbrace{\frac{\mathrm{u}_\infty}{L}\boldsymbol{E}^*}_{\boldsymbol{E}(\theta)} \underline{d}^*, \text{ for } \boldsymbol{T}_R = \boldsymbol{I}, \tag{2.63}$$

$$\underline{y}^* = \underbrace{\boldsymbol{C}^*}_{\boldsymbol{C}} \underline{x} + \underbrace{\boldsymbol{D}^*}_{\boldsymbol{D}} \underline{u}^* + \underbrace{\boldsymbol{F}^*}_{\boldsymbol{F}} \underline{d}^*, \text{ for } \boldsymbol{T}_R = \boldsymbol{I}, \tag{2.64}$$

which is the basis of the model structure used for the LPV identification scheme presented in the next section.

2.2.3 LPV model identification

For the identification of the LPV state-space models introduced in the previous section, a custom algorithm is applied here. Only single-input, single-output (SISO) or multiple-input, single-output (MISO) models are considered, as they can be easily combined into full multiple-input, multiple-output (MIMO) models. Furthermore, the matrices D and F are set to zero, as physical processes usually do not posess a direct feedthrough. In order to be able to account for gain variations of the flow dynamics with respect to additional parameters $\tilde{\theta}_2 \dots \tilde{\theta}_p$ such as cross-wind angle, the equations (2.63) and (2.64) are expanded according to an LPV state-space model in output error structure

$$\underline{\dot{x}} = \underbrace{\frac{\mathrm{u}_\infty}{L}\boldsymbol{A}^*}_{\boldsymbol{A}(\underline{\theta})} \underline{x} + \underbrace{\frac{\mathrm{u}_\infty}{L}\left(\boldsymbol{B}_1^* + \tilde{\theta}_2\boldsymbol{B}_2^* \dots \tilde{\theta}_p\boldsymbol{B}_p^*\right)}_{\boldsymbol{B}(\underline{\theta})} \underline{u}^* + \underbrace{\frac{\mathrm{u}_\infty}{L}\left(\boldsymbol{E}_1^* + \tilde{\theta}_2\boldsymbol{E}_2^* \dots \tilde{\theta}_p\boldsymbol{E}_p^*\right)}_{\boldsymbol{E}(\underline{\theta})} \underline{d}^*, \tag{2.65}$$

$$y^* = \underbrace{\underline{c}^{*T}}_{\underline{c}^T} \underline{x} + e, \tag{2.66}$$

with the output error e and the parameter vector

$$\underline{\theta} = \begin{bmatrix}\theta_1 & \theta_2 & \dots & \theta_p\end{bmatrix}^T = \begin{bmatrix}\mathrm{u}_\infty & \mathrm{u}_\infty\tilde{\theta}_2 & \dots & \mathrm{u}_\infty\tilde{\theta}_p\end{bmatrix}^T. \tag{2.67}$$

The identification of the LPV model in Eq. (2.65, 2.66) from experimental data is carried out in several steps outlined in Fig. 2.1. The algorithm begins with the identification of an initial linear black-box model with a suitable model order n_x using the standard Prediction-Error-Method (PEM), see e.g. Ljung [79]. This is carried out for one single data set recorded from an identification experiment at a fixed parameter value. The input/output variables are chosen as nondimensional coefficients to avoid dependencies of the model gains on the free-stream velocity. In step 2, the identified initial model is converted to continuous time, followed by the nondimensionalization in step 3. This is carried out according to Eq. (2.65) and (2.66) to obtain the state-space matrices

$$\boldsymbol{A}^*_{init} = \frac{L}{\mathrm{u}_\infty}\boldsymbol{A}_{init}, \quad \boldsymbol{B}^*_{1,init} = \frac{L}{\mathrm{u}_\infty}\boldsymbol{B}_{1,init}, \quad \boldsymbol{E}^*_{1,init} = \frac{L}{\mathrm{u}_\infty}\boldsymbol{E}_{1,init}, \quad \underline{c}^{*T}_{init} = \underline{c}^T_{init}, \tag{2.68}$$

of an initial, dimensionless model in convective time. Dependency on the other parameters $\theta_2 \dots \theta_p$ is not yet taken into account, and the corresponding matrices $\boldsymbol{B}^*_{2,init} \dots \boldsymbol{B}^*_{p,init}$ and $\boldsymbol{E}^*_{2,init} \dots \boldsymbol{E}^*_{p,init}$ are initialized with zero. This initial model is subsequently transformed into

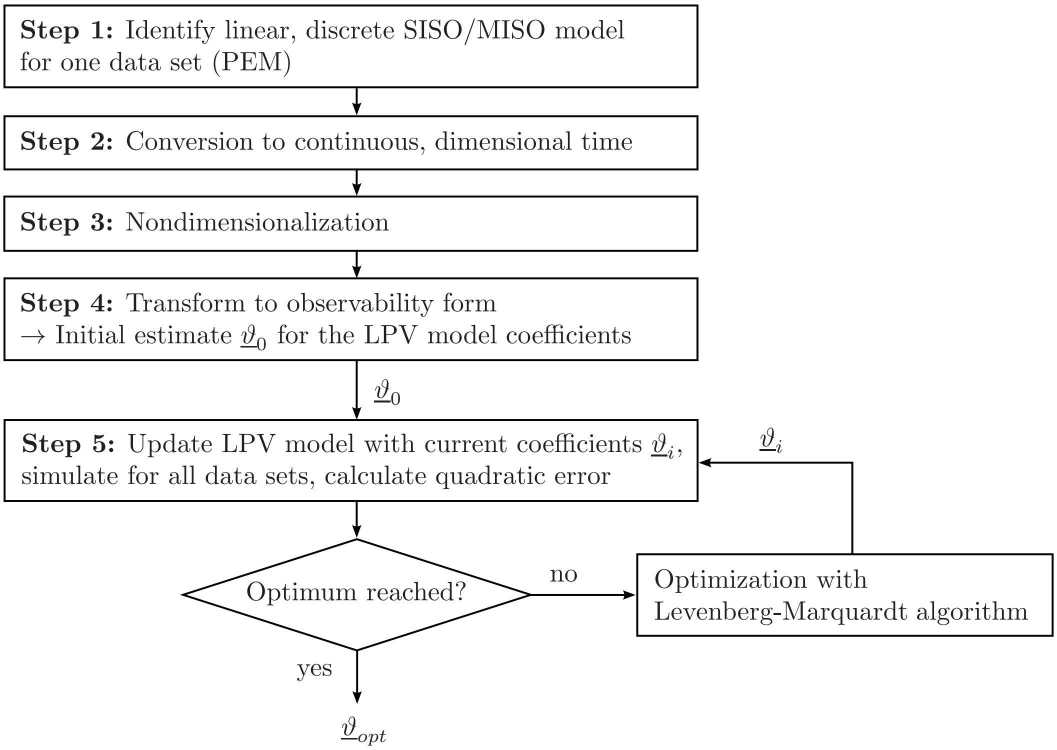

Figure 2.1: LPV model identification procedure

observable canonical form via a state transformation as described by Luenberger [81], with the matrices

$$\boldsymbol{A}^*_{obs} = \begin{bmatrix} 0 & 0 & \dots & 0 & -a^*_0 \\ 1 & 0 & \dots & 0 & -a^*_1 \\ 0 & 1 & \dots & 0 & -a^*_2 \\ & & \ddots & & \\ 0 & 0 & \dots & 1 & -a^*_{n_x-1} \end{bmatrix}, \tag{2.69}$$

$$\boldsymbol{B}^*_{j,obs} = \begin{bmatrix} b^*_{j_{0,1}} & b^*_{j_{0,2}} & \dots & b^*_{j_{0,n_u}} \\ b^*_{j_{1,1}} & b^*_{j_{1,2}} & \dots & b^*_{j_{1,n_u}} \\ & & \vdots & \\ b^*_{j_{n_x-1,1}} & b^*_{j_{n_x-1,2}} & \dots & b^*_{j_{n_x-1,n_u}} \end{bmatrix}, \text{ for } j = 1 \dots p, \tag{2.70}$$

$$\boldsymbol{E}^*_{j,obs} = \begin{bmatrix} e^*_{j_{0,1}} & e^*_{j_{0,2}} & \dots & e^*_{j_{0,n_d}} \\ e^*_{j_{1,1}} & e^*_{j_{1,2}} & \dots & e^*_{j_{1,n_d}} \\ & & \vdots & \\ e^*_{j_{n_x-1,1}} & e^*_{j_{n_x-1,2}} & \dots & e^*_{j_{n_x-1,n_d}} \end{bmatrix}, \text{ for } j = 1 \dots p, \tag{2.71}$$

$$\underline{c}^{*T}_{obs} = \begin{bmatrix} 0 & \dots & 0 & 1 \end{bmatrix}. \tag{2.72}$$

This corresponds to a state-space realization with a minimum number of coefficients $a^*_0 \dots a^*_{n_x-1}$, $b^*_{j_{0,1}} \dots b^*_{j_{n_x-1,n_u}}$, $e^*_{j_{0,1}} \dots e^*_{j_{n_x-1,n_d}}$, for $j = 1 \dots p$, which are gathered in a coefficient vector $\underline{\vartheta}$. The identification of the LPV model coefficients is carried out via nonlinear least-squares minimization with the Levenberg-Marquardt algorithm as implemented in the `MATLAB`-command "`lsqnonlin.m`". Each evaluation of the cost function in step 5 involves updating the LPV model with the current coefficient vector $\underline{\vartheta}_i$, simulating the model for all data sets and calculating the quadratic error between measured and simulated output variable. This process is repeated until an optimal coefficient vector $\underline{\vartheta}_{opt}$ is obtained.

2.3 Driving dynamics

2.3.1 Single-track model for lateral vehicle dynamics

The main characteristics of lateral vehicle dynamics can be described by the single-track model, see e.g. Mitschke and Wallentowitz [85]. Hereby, the entire undercarriage is replaced by single wheels located at the center of the front and rear axle, respectively. Additionally, the vehicle's center of gravity is assumed to be located at road-level, such that vertical motion as well as rolling and pitching can be neglected. Fig. 2.2 shows the corresponding definitions of the variables.

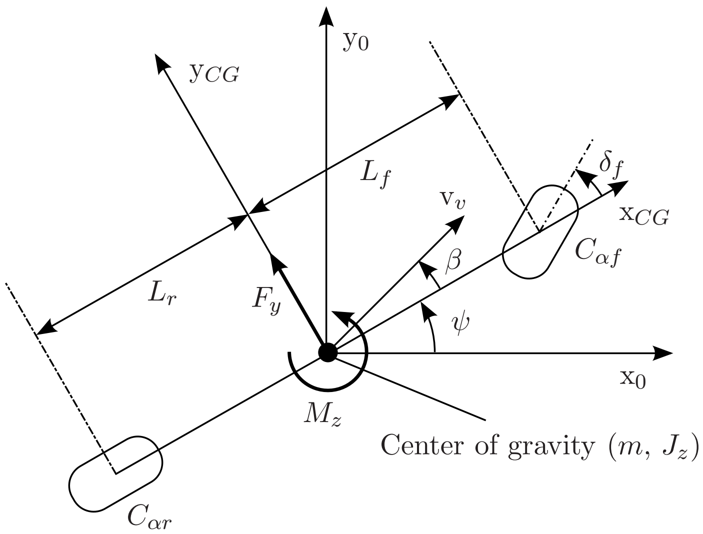

Figure 2.2: Single-track model, adapted from Mitschke and Wallentowitz [85] and Sackmann and Trächtler [108].

The x_{CG}-y_{CG}-coordinate system is fixed in both origin and rotation to the body frame, whereas the index 0 denotes the inertial reference frame.
As described by Sackmann and Trächtler [108], the standard single-track model is augmented here by additional inputs F_y and M_z for the cross-wind excitation that act on the vehicle's center of gravity. Assuming a planar motion in the horizontal plane, a constant driving velocity v_v and linearizing for small angles, the momentum balances for transversal and rotational motion yield the differential equations

$$\dot{\beta} = a_{11}\beta + a_{12}\dot{\psi} + b_1\delta + e_1 F_y, \tag{2.73}$$

$$\ddot{\psi} = a_{21}\beta + a_{22}\dot{\psi} + b_2\delta + e_2 M_z, \tag{2.74}$$

for the side-slip angle β and the yaw angle ψ. Here, the steering angle δ of the driver is transferred to the turning angle δ_f of the front wheel via the steering gear ratio

$$i_s = \frac{\delta}{\delta_f}. \tag{2.75}$$

The coefficients

$$\begin{aligned} a_{11} &= -\frac{C_{\alpha r} + C_{\alpha f}}{m v_v},\; a_{12} = \frac{C_{\alpha r} L_r - C_{\alpha f} L_f}{m v_v^2} - 1, \\ a_{21} &= \frac{C_{\alpha r} L_r + C_{\alpha f} L_f}{J_z},\; a_{22} = -\frac{C_{\alpha r} L_r^2 + C_{\alpha f} L_f^2}{J_z v_v}, \\ b_1 &= \frac{C_{\alpha f}}{i_s m v_v},\; b_2 = \frac{C_{\alpha f} L_f}{i_s J_z},\; e_1 = \frac{1}{m v_v},\; e_2 = \frac{1}{J_z}, \end{aligned} \tag{2.76}$$

depend on the front and rear cornering stiffnesses $C_{\alpha f}$ and $C_{\alpha r}$, the driving speed v_v, the vehicle mass m and moment of inertia J_z, the steering gear ratio i_s and the distances L_f and L_r from the front and rear axle to the center of gravity, respectively. Assuming small angles ψ and β, the lateral velocity v_l and acceleration a_l in the inertial coordinate system can be calculated by

$$\mathrm{v}_l \approx (\psi + \beta)\mathrm{v}_v, \tag{2.77}$$

$$\mathrm{a}_l \approx (\dot{\psi} + \dot{\beta})\mathrm{v}_v. \tag{2.78}$$

Transferring Eq. (2.73), (2.74) and (2.78) into the Laplace domain results in

$$\mathrm{a}_l(s) = G_{\mathrm{a}_l\delta}(s)\,\delta(s) + \boldsymbol{G}_{\mathrm{a}_l\underline{d}}(s)\,\underline{d}, \text{ with } \underline{d} = \begin{bmatrix} F_y(s) & M_z(s) \end{bmatrix}^T, \tag{2.79}$$

with the Laplace variable s. Here, $G_{\mathrm{a}_l\delta}(s)$ and $\boldsymbol{G}_{\mathrm{a}_l\underline{d}}(s)$ represent the transfer functions for the vehicle's lateral acceleration response to the steering input δ and to the disturbance input vector $\underline{d}$, respectively.

2.3.2 Virtual driver model

As pointed out by Wagner [136] and Schröck [113] the behavior of the driver plays an important role when assessing the cross-wind sensitivity of a vehicle. The single-track model described in the previous section is augmented here by a virtual driver based on the models suggested by Risse [105] and Mitschke and Wallentowitz [85]. Fig. 2.3 shows the corresponding driver-vehicle

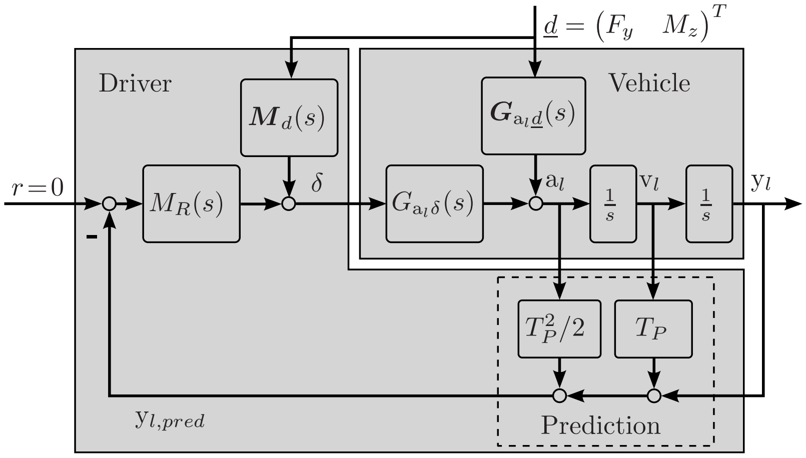

Figure 2.3: Driver-vehicle control-loop for disturbance compensation, adapted from Risse [105] and Mitschke and Wallentowitz [85]

feedback loop. The driver perceives the lateral deviation y_l, velocity v_l and acceleration a_l and estimates a future vehicle trajectory $\mathrm{y}_{l,pred}$ with a prediction time T_P. For the task of pure lane keeping under side-wind disturbances the reference variable r is zero. According to Risse [105] the feedback part of the driver can be modeled by the transfer function

$$\tilde{M}_R(s) = V_M \frac{1}{1 + T_I s} e^{-s\tau}. \tag{2.80}$$

The time constant T_I and the reaction time τ are largely independent of the vehicle type and the individual driver, with values of about 0.2 s. However, the gain V_M and the prediction time T_P are adapted by the driver to the vehicle characteristics in order to achieve a cross-over frequency 0.3 Hz $< f_c <$ 0.5 Hz and a phase reserve $30° < \phi_r < 40°$ of the open driver-vehicle feedback loop. The time delay is replaced by a second-order Padé approximation

$$e^{-s\tau} \approx G_{delay}(s) = \frac{1 - \frac{\tau}{2}s + \frac{\tau^2}{12}s^2}{1 + \frac{\tau}{2}s + \frac{\tau^2}{12}s^2}, \tag{2.81}$$

to obtain a linear transfer function

$$M_R(s) = V_M \frac{1}{1+T_I s} G_{delay}(s) \tag{2.82}$$

for the feedback part of the driver. The prediction block can be represented by a transfer function

$$G_{pred}(s) = \frac{1 + T_P s + \frac{T_P}{2} s^2}{s^2}, \tag{2.83}$$

with the lateral acceleration a_l as input variable, as described by Mitschke and Wallentowitz [85]. Setting all external input variables r and $\underline{d}$ to zero and moving the prediction block to the upper part of the feedback loop in Fig. 2.3, results then in the open-loop transfer function

$$G_0(s) = M_R(s) \cdot G_{\mathrm{a}_l\delta}(s) \cdot G_{pred}(s) \tag{2.84}$$

of the driver-vehicle system. For a given phase reserve ϕ_r and cross-over angular frequency $\omega_c = 2\pi f_c$ the prediction time T_P can be calculated by

$$T_P = \frac{1}{\omega_c}\left(-\frac{1}{A_1} + \sqrt{\frac{1}{A_1^2} + 2}\right), \text{ with}$$

$$A_1 = \tan\left\{-\pi + \frac{\pi}{180^\circ}\phi_r + \tan^{-1}(T_I\omega_c) - \tan^{-1}\left(\frac{\frac{L_r}{\mathrm{v}_v}\omega_c}{1 - \frac{J_z}{C_{\alpha r}L_{wb}}\omega_c^2}\right) + \tan^{-1}\left(\frac{\sigma_v\frac{\omega_c}{\omega_v^2}}{1 - \frac{\omega_c^2}{\omega_v^2}}\right) + \omega_c\tau\right\}. \tag{2.85}$$

Apart from the desired phase reserve and cross-over angular frequency, Eq. (2.85) additionally depends on the given driver time constant T_I and time delay τ, as well as several parameters of the single-track model. The vehicle's decay constant σ_v is given by

$$\sigma_v = \frac{m(C_{\alpha f}L_f^2 + C_{\alpha r}L_r^2) + J_z(C_{\alpha f} + C_{\alpha r})}{2J_z m\mathrm{v}_v}, \tag{2.86}$$

and the undamped eigenfrequency ω_v by

$$\omega_v = \sqrt{\frac{C_{\alpha f}C_{\alpha r}L_{wb}^2 + m\mathrm{v}_v^2(C_{\alpha r}L_r - C_{\alpha f}L_f)}{J_z m\mathrm{v}_v^2}}. \tag{2.87}$$

Based on the condition

$$|G_0(j\omega_c)| = 1 \tag{2.88}$$

for the magnitude of the open-loop driver-vehicle transfer function G_0 at the cross-over frequency ω_c, the driver gain V_M can be calculated by

$$V_M = \frac{\sqrt{1 + T_I^2\omega_c^2}}{|G_{\mathrm{a}_l\delta}(j\omega_c)| \cdot |G_{pred}(j\omega_c)|}. \tag{2.89}$$

The parameters of the prediction block $G_{pred}(s)$ and the feedback part $M_R(s)$ of the driver are now fully determined.

For disturbance compensation and zero steady-state error during constant cross-wind, the virtual driver is augmented by a feedforward part

$$\boldsymbol{M}_d(s) = \left[\frac{k_{\delta F_y}}{1+T_S s}e^{-s\tau} \quad \frac{k_{\delta M_z}}{1+T_S s}e^{-s\tau}\right], \tag{2.90}$$

as suggested by Mitschke and Wallentowitz [85]. Again, the feedforward part of the driver is modeled by a first-order transfer function with the same time delay τ as in the feedback part. The parameters

$$k_{\delta F_y} = -\frac{C_{\alpha r}L_r - C_{\alpha f}L_f}{L_{wb}C_{\alpha f}C_{\alpha r}}i_s, \quad \text{and} \quad k_{\delta M_z} = -\frac{C_{\alpha r} + C_{\alpha f}}{L_{wb}C_{\alpha f}C_{\alpha r}}i_s \tag{2.91}$$

represent the gains for the steering angle δ to compensate for constant side force F_y and yaw moment M_z, respectively. The time constant T_S is usually chosen to be around 0.7 s [85]. Replacing the time delay by the second-order Padé approximation $G_{delay}(s)$ according to Eq. 2.81 results in the overall control law of the driver model

$$\delta = \begin{bmatrix} \frac{-V_M}{1+T_I s} & \frac{-V_M}{1+T_I s} T_P & \frac{-V_M}{1+T_I s} \frac{T_P^2}{2} \end{bmatrix} G_{delay}(s) \begin{bmatrix} \mathrm{y}_l \\ \mathrm{v}_l \\ \mathrm{a}_l \end{bmatrix} + \begin{bmatrix} \frac{k_{\delta F_y}}{1+T_S s} & \frac{k_{\delta M_z}}{1+T_S s} \end{bmatrix} G_{delay}(s) \begin{bmatrix} F_y \\ M_z \end{bmatrix} . \qquad (2.92)$$

For implementation and real-time simulation in the wind tunnel experiments, the overall driver-vehicle model is converted to state-space form, see Appendix A. Furthermore, its coefficients are scaled online to match the smaller model dimensions and the current free-stream velocity in the wind tunnel, as described in section 4.5.2.

Chapter 3

2D bluff body

3.1 Experimental setup

The experiments are conducted in an Eiffel-type wind tunnel with a maximum free stream velocity of approximately 20 m/s and a maximum turbulence level of less than 0.5 %. The closed test section has a length of 2500 mm, a width of 545 mm and a height of 490 mm. A Prandtl tube located 200 mm downstream of the test section entrance monitors the dynamic pressure q and free stream velocity u_∞. The 2D bluff body investigated here is shown in Fig. 3.1 and has the dimensions $l = 181\,\text{mm}$, $h = 474\,\text{mm}$ and $w = 50\,\text{mm}$. It is mounted at a distance of 620 mm downstream of the test section entrance and has an elliptic nose with an aspect ratio of 1:4 to prevent laminar separation bubbles. Here, the Reynolds number $Re_w = u_\infty w/\nu$ is defined with respect to the body width w and the kinematic viscosity ν. Most of the experiments are carried out in a range $30000 < Re_w < 60000$. The cross-wind is characterized by the yaw

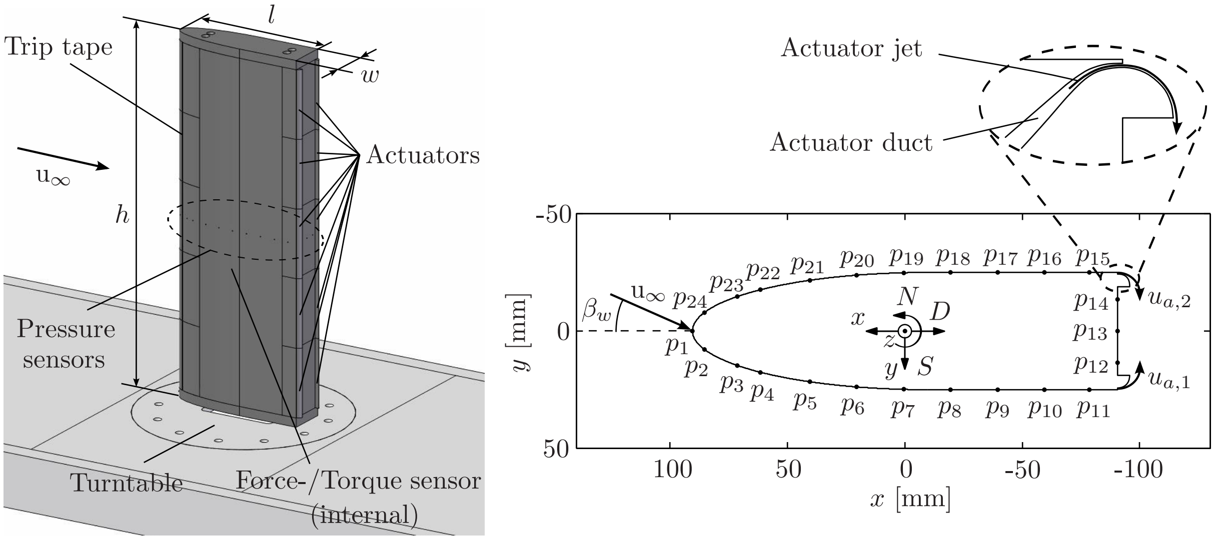

Figure 3.1: Experimental setup and cross-section of the 2D bluff body showing the definition of cross-wind angle, forces and moments for the coordinate system as well as illustrating the positions of pressure sensors and actuators.

angle β_w between the free-stream velocity u_∞ and the driving direction x. As common in vehicle aerodynamics, the forces and moments are measured in the body-fixed coordinate system, which is located here at the center of the body's mean section, 90.5 mm behind the nose. The drag force D faces in negative x-direction, the side force S in positive y-direction and the yaw moment N is defined around the upward facing z-axis. The corresponding nondimensional coefficients are given by

$$c_D = \frac{D}{qhw}, \quad c_S = \frac{S}{qhw}, \quad c_N = \frac{N}{qhwl}, \tag{3.1}$$

for drag, side-force and yaw-moment coefficients, respectively. Pressurized air can be blown through actuator slots located along both trailing edges. The slot exits are parallel to the body's side walls and have a width of 0.3 mm. Rounded surfaces adjacent to the slots redirect the actuator jets towards the base of the bluff body by means of the Coanda effect [34, 35] and allow for an efficient control of the bluff body's wake. The supply pressures $p_{a,1}$ and $p_{a,2}$ of the actuators are adjusted for each trailing edge separately using Piezo pressure regulators (Hoerbiger, Tecno Basic PRE-U). Fast solenoid switching valves (Festo, MHE4) installed on either side between the pressure regulators and the actuator slots allow steady blowing or pulsed blowing at different frequencies. During the experiments, the actuators are driven by the system shown in Fig. 3.2. The desired nondimensional blowing rates $\underline{\mathrm{u}}^*_{a,des}$ are converted to dimensional

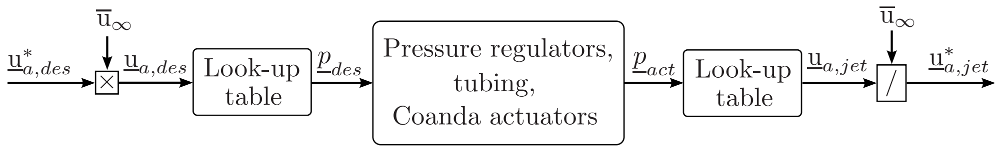

Figure 3.2: Schematic sketch of the actuator system.

velocities $\underline{\mathrm{u}}_{a,des}$ based on the mean free-stream velocity $\overline{\mathrm{u}}_\infty$. A set of look-up tables, determined from flow meter readings in a series of steady-state measurements, is used to calculate the corresponding setpoints $\underline{p}_{des}$ for the piezo pressure regulators. The instantaneous pressures $\underline{p}_{act}$ are monitored by transducers installed inside the actuator ducts from which the instantaneous blowing velocities $\underline{\mathrm{u}}_{a,jet}$ can be determined via a second set of look-up tables. The actuation amplitude is characterized in terms of the momentum coefficient

$$c_{\mu,i} = \frac{A_{a,i}\mathrm{u}_{a,i}^2}{hw\mathrm{u}_\infty^2}, \text{ for } j = 1, 2\,, \tag{3.2}$$

where $A_{a,i}$ denotes the cross-sectional area of all actuator slots on side i, and $\mathrm{u}_{a,i}$ stands for the corresponding blowing velocity at the slot exit. The drag force and yaw moment acting on the bluff body are measured using a six component force/torque balance (ATI, FTD-Gamma SI-32-2.5, absolute measurement accuracy better than 1 % of full scale span) that is sufficiently stiff to capture transient forces and moments. 24 miniature pressure sensors (Sensortechnics, HCLA12X5B, measurement uncertainty due to hysteresis and nonlinearity less than 0.25 % of full scale span) along the mean section of the bluff body monitor the pressure distribution. The pressure coefficients

$$c_{p_j} = \frac{p_j - p_s}{q}, \text{ for } j = 1 \ldots 24, \tag{3.3}$$

are calculated from the corresponding pressure reading p_j at each position j. Here, p_s and q denote the static and dynamic pressures as measured by the Prandtl probe. The pressure coefficient $c_{p,b}$ at the body's base is obtained by averaging the readings of sensors 12, 13 and 14. A turntable driven by a stepper motor is used to rotate the body around its vertical axis, thus enabling measurements at different cross-wind angles. The setup also allows transient cross-wind angles to be studied. However, it is not capable of accurately reflecting the unsteady aerodynamics of a real car driving into a cross-wind gust, since a side-wind gust simulated by turning the body acts simultaneously on the whole body. Furthermore, the drag and yaw-moment measurements will include inertial forces. In spite of these limitations, the setup offers the possibility of testing the control performance under well-defined, reproducible disturbances.

3.2 Natural flow characteristics

The flow characteristics of the wind-tunnel model correspond to a typical two-dimensional bluff body. Due to the trip tapes installed on either side of the elliptic front of the body, the transition to a turbulent boundary layer is fixed to a location 11 mm downstream of the nose. For the range of small to medium cross-wind angles $-5° < \beta_w < 5°$ investigated here, the flow stays attached along the sides of body and separates at the trailing edges. A smoke wire visualization of the wake for the natural flow at $\beta_w = 0°$ is shown in the upper picture of Figure 3.3. The

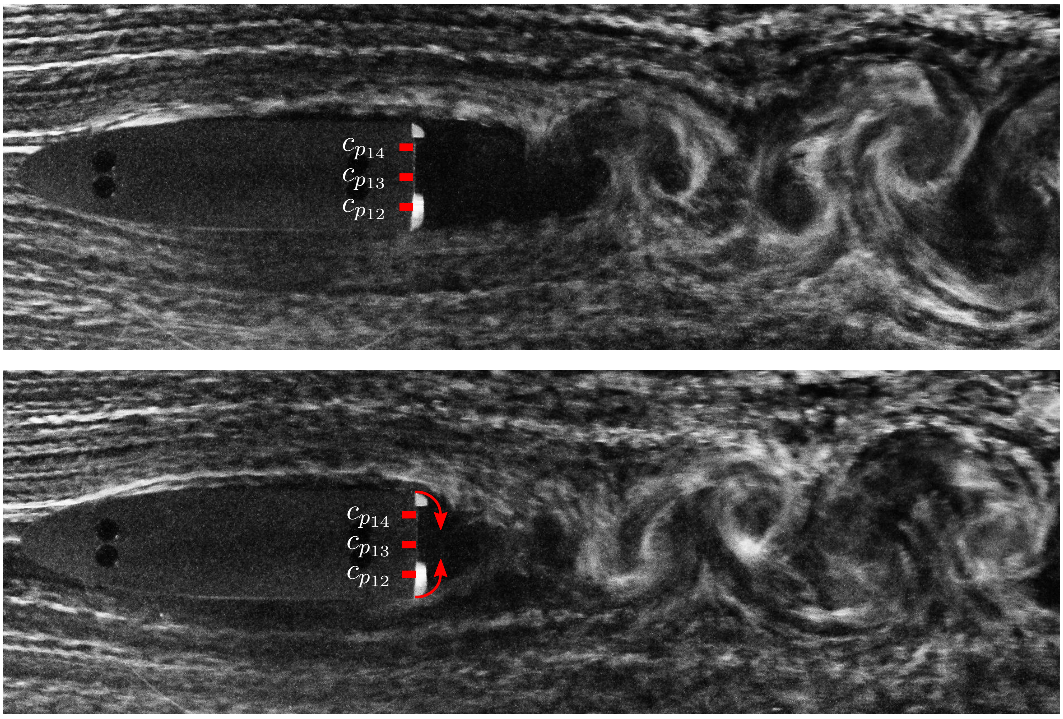

Figure 3.3: Smoke wire flow visualization of the wake behind the 2D bluff body for natural (upper photo) and symmetrically actuated flow (lower photo) at $Re_w = 15000$ and $\beta_w = 0°$.

two shear layers roll up towards the base of the bluff body, interact mutually and form large, alternating vortices. The flow is governed by a global wake instability that results in the typical von Kármán vortex street observed behind two-dimensional bluff bodies [59]. The vortices induce a low pressure in the near wake of the bluff body. This leads to a low time-averaged base-pressure coefficient of $\bar{c}_{p,b} \approx -0.62$ and a high time-averaged drag coefficient of $\bar{c}_D \approx 0.57$. These results agree well with the values reported for the base-pressure coefficient of similar 2D bluff bodies [17, 18, 19, 96, 97, 126].

Furthermore, the alternating shedding of the vortices lead to large, periodic pressure fluctuations on the base of the bluff body. Their power spectral densities for the three sensor positions 12, 13 and 14 are shown in Fig. 3.4. The spectra coincide well for all investigated Reynolds numbers in the range $3 \cdot 10^4 \leq Re_w \leq 6 \cdot 10^4$, with stronger fluctuations at the lowest Reynolds number $Re_w = 3{\cdot}10^4$. Sensors 12 and 14, located near the trailing edges on the base, show a distinct peak at a Strouhal number $St_w = fw/\mathrm{u}_\infty \approx 0.29$, representing the characteristic reduced frequency of the von Kármán vortex street. For all three sensor positions a second, wider peak at a higher frequency is visible in the power spectral density, with a maximum at about twice the vortex shedding frequency. These observations correspond well to the results of Henning et al. [54], Pastoor et al. [100] and Muminović et al. [88, 89], who conducted experiments with similar 2D bluff bodies. However, they report slightly lower characteristic frequencies of the wake pressure fluctuations in the range $0.23 \leq St_w \leq 0.25$, and significantly higher drag coefficients in the range $0.91 \leq \bar{c}_D \leq 0.98$, compared with a value of $\bar{c}_D \approx 0.57$ of the bluff body presented in this thesis. The differences are likely due to its more streamlined elliptic nose. The front of the bluff

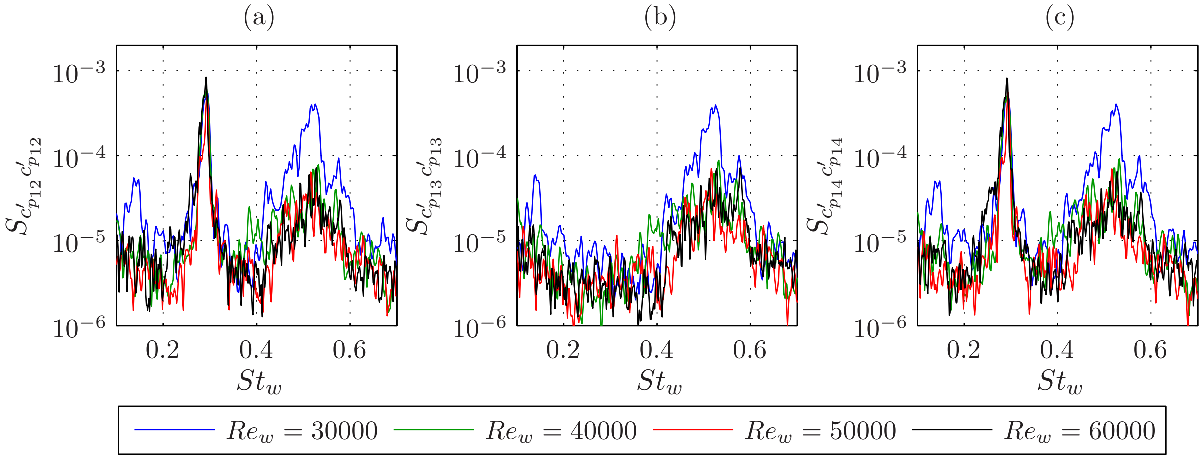

Figure 3.4: Power spectral density of pressure coefficient fluctuations on the base of the bluff body for the natural flow at $3 \cdot 10^4 \leq Re_w \leq 6 \cdot 10^4$ at zero yaw angle.

bodies used in [54, 88, 89, 100] has a blunter shape with a fairly small rounding radius of the leading edges. This leads to laminar separation bubbles on the sides and a higher contribution of the frontal body part to the overall drag. Furthermore, thicker boundary layers develop along the sides of the body due to its blunter shape, which explains the lower characteristic frequencies reported in [54, 88, 89, 100]. Also, the flow visualization in Fig. 3.3 suggests that, even without actuation, the Coanda surfaces installed at the base lead to an effect similar to parallel extension plates [62]. This reduces the wake width and pushes the formation of the vortices further downstream, thus reducing their negative impact on the base pressure.
Tombazis and Bearman [126] and Park et al. [97] report that the drag coefficient for simple, streamlined 2D bluff bodies with blunt trailing edges can be approximated by $c_D \approx -c_{p,b}$. This is also the case for the 2D bluff body investigated here. However, this is only true for nominally straight flow conditions, as can be seen from the steady-state maps in Fig. 3.5. At a zero degree yaw angle, the bluff body has a drag coefficient of $\overline{c}_D \approx 0.57$ and a base-pressure coefficient $\overline{c}_{p,b} \approx -0.62$, as seen in Fig. 3.5 (a) and (f). For increasing cross-wind angles β_w, the drag coefficient decreases more and more, whereas the base pressure remains almost unaffected. However, the pressure coefficients c_{p_1} at the center of the nose and c_{p_2} and $c_{p_{24}}$ at the frontal sides change significantly, which reflects a shift of the stagnation point to the windward side and a suction peak on the leeward side. Together with the elliptical shape of the frontal part of the body, this leads to a decrease in drag with raising yaw angle. The pressure coefficients $c_{p_{11}}$ and $c_{p_{15}}$ at the rear wind- and leeward sides are also affected by cross-wind, but less than the frontal pressure distributions. This leads to an almost linear increase in side-force and yaw-moment coefficients, as can be seen in Fig. 3.3 (b) and (c).
Here, the goal of the application of AFC with Coanda actuation is to reduce the detrimental effects of cross-wind on the flow around the bluff body while maintaining an efficient reduction of the drag coefficient. The corresponding characteristics of the actuated flow are discussed in the next section.

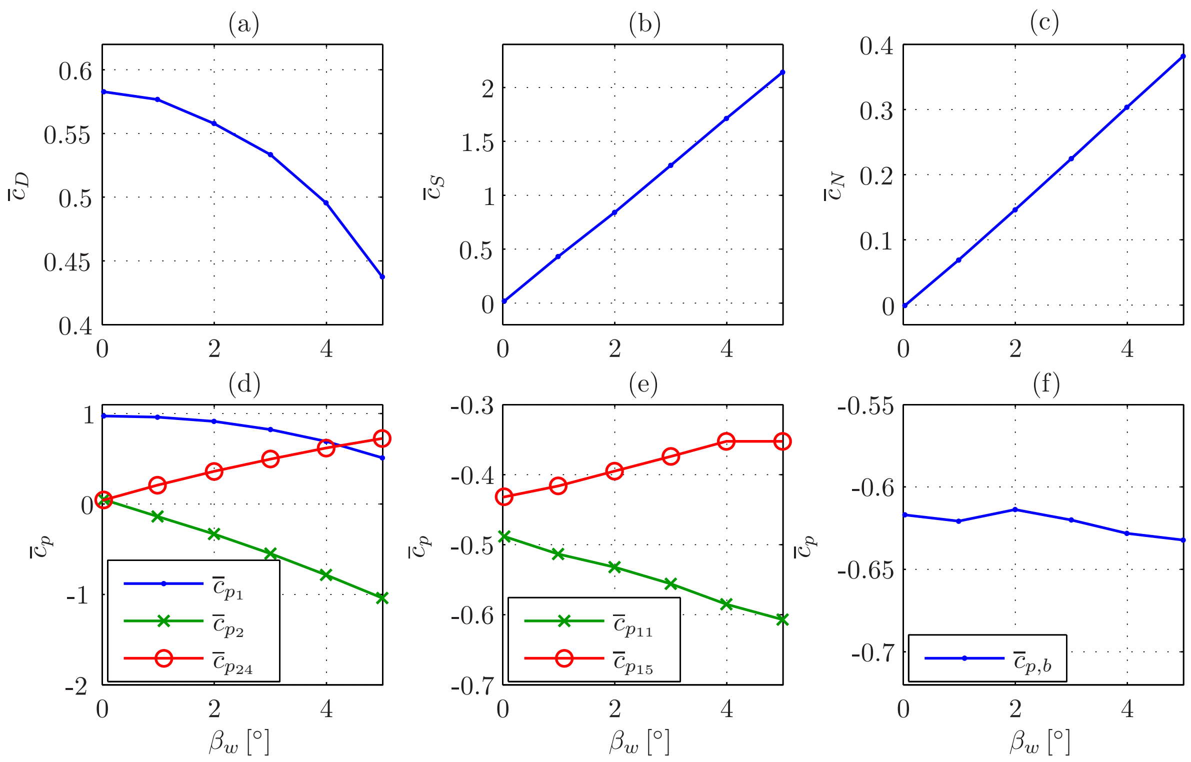

Figure 3.5: Steady-state maps for drag, side-force and yaw-moment coefficients, as well as selected pressure coefficients for the natural flow at cross-wind angles $0° \leq \beta_w \leq 5°$ and $Re_w = 4 \cdot 10^4$.

3.3 Actuated flow characteristics

As presented in section 1.2.2, the application of passive and active control for the drag reduction of 2D bluff bodies has been extensively studied for many years. The various methods can be classified by the physical mechanism of the wake manipulation:

- Delay of separation: For bodies without a fixed separation point, such as cylinders or bluff bodies with rounded trailing edges, the base pressure can be increased by keeping the flow attached for a longer distance at the rear end of the body. This can be achieved by increasing the mixing of the shear layer with higher momentum fluid by passive means such as vortex generators or by active means such as rotating cylinders at the trailing edge [20], combined suction and pulsed blowing [115] or synthetic jets with zero-net-mass-flux actuation [8, 75].

- Prevention of the interaction of the shear layers: Installing splitter plates [17] or applying active base bleed [18] stabilizes the near wake by delaying the interaction of top and bottom shear layers. This attenuates the vortex strength close to the body and increases the base pressure.

- Breaking of large-scale coherent 2D flow structures by 3D disturbances: Spanwise distributed forcing can be used to generate three-dimensional disturbances that break up the large, alternating two-dimensional vortex shedding responsible for the high drag coefficient of many 2D bluff bodies. This can be achieved by passive means such as a wavy trailing edge [126] or installing small tabs on the trailing edges [97]. Active methods include spanwise distributed continuous blowing and suction [67], spanwise distributed, pulsed suction [88, 89] or energized shear layers to attenuate the formation of large-scale 2D vortices by high-frequency forcing [29].

- Enhancing the symmetry of the wake: Forcing a synchronous shedding of smaller vortices from both trailing edges leads to a base-pressure increase relative to the uncontrolled case characterized by large, alternating vortices. This can be achieved via open-loop periodic actuation with synthetic jets, because the wake locks on in phase to the forcing frequency [55]. A more energy efficient drag reduction can be achieved via direct opposition control by generating anti-cyclic control forces [119, 44] or phase control by feedback active flow control with synthetic jet actuation only on one side [100].

Many of the aforementioned control methods are only applicable to 2D bluff bodies since they build on an attenuation or elimination of the alternating, two-dimensional vortex shedding. However, the goal of the 2D bluff body experiments presented in this thesis is to provide a starting point and a set of guidelines for a successive application of AFC to 3D bluff bodies as the one presented in section 4. Hence, steady blowing using the Coanda effect is chosen here as an active flow control method. Geropp and Odenthal [45] apply this control strategy to a simplified 2D car model and achieve a significant base-pressure increase of almost 50 %, which leads to a drag reduction of about 10 % in their experiment. Although large blowing rates in the range of the free-stream velocity are required, the authors achieve overall net power savings even if the compressor power needed for generating the actuator jets is taken into account. Furthermore, Coanda blowing is also applicable for the drag reduction of cars and trucks with blunt backs as demonstrated in experiments by Englar [34, 35]. He also points out the potential for yaw-moment reduction under side-wind conditions. In view of these results, blowing with Coanda jets represents a well-suited actuation method for developing a multivariable closed-loop active flow strategy with the goal of reducing cross-wind sensitivity while providing efficient drag reduction. In the following sections the most relevant flow phenomena are discussed to gain insight into the steady and transient characteristics of the actuated flow. This forms the basis for identifying a dynamic model that is suitable for the control design.

3.3.1 Symmetric actuation by continuous blowing

Steady blowing through the Coanda actuators at the trailing edges leads to deflection of the jets towards the base of the bluff body [45]. This also accelerates the boundary layer upstream of the actuators and reduces the velocity deficit in the two shear layers. These effects cause a deflection of high momentum free-stream fluid into the near wake behind the body as shown in the flow visualization in the lower picture of Fig. 3.3. The circulation bubble is significantly reduced compared with the natural flow, and a free stagnation point forms closely behind the bluff body. This shields the base from the large, alternating vortices that form further downstream. Thus, the effect of Coanda blowing on the wake arises from a combination of several physical mechanisms: The flow stays attached to the rounded Coanda surfaces, thus delaying the separation and deflecting high-momentum fluid towards the base. Furthermore, the jets defer the interaction of the shear layers resulting in a symmetrization of the near wake.
All of these effects combined lead to a substantial base-pressure increase of $\Delta\overline{c}_{p,b} \approx 0.2$ and to a drag reduction of $\Delta\overline{c}_D \approx 0.2$ or by more than 35 %, as shown in the steady-state maps in Fig. 3.6. The coefficients for drag and base pressure slightly depend on the Reynolds number, but the overall characteristics coincide well. For small momentum coefficients $\overline{c}_\mu \leq 0.018$ only a small drag reduction is achieved. Increasing the momentum coefficient in the range $0.018 \leq \overline{c}_\mu \leq 0.038$ leads to significant base pressure recovery and a large drag reduction. For larger momentum coefficients the drag coefficient reaches a saturation.
These characteristics qualitatively match the results reported by Henning et al. [54, 52], Pastoor et al. [100], and Muminović et al. [89, 88, 90], but the momentum coefficients required for a significant drag reduction by Coanda blowing are about one order of magnitude higher than those in the cited experiments. In [54, 52, 100] zero-net-mass-flux actuation by Synthetic Jets is applied at an outward facing angle of 45° to the main flow direction, whereas Muminović et al. use pulsed suction at the same angle [89, 88, 90]. In particular the latter experiments

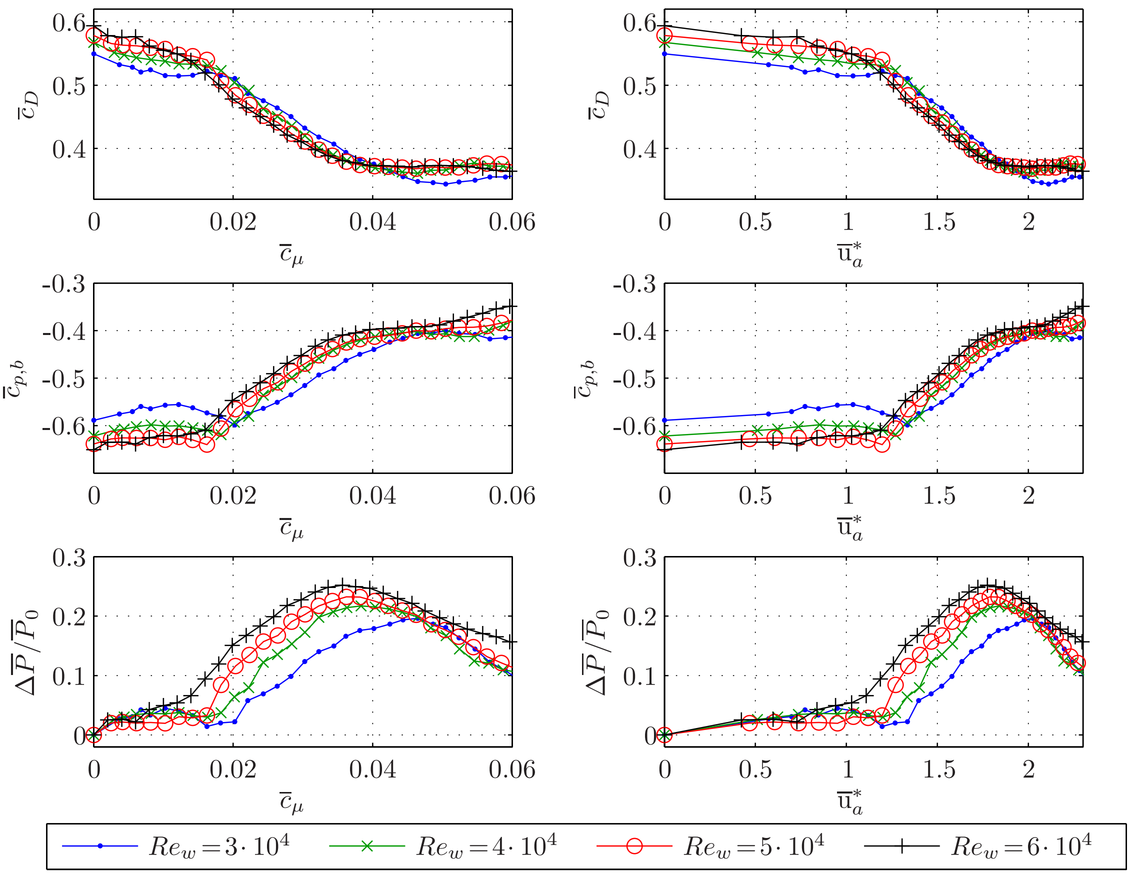

Figure 3.6: Steady-state maps for the drag coefficient $\overline{c}_D$, base-pressure coefficient $\overline{c}_{p,b}$ and time-averaged, normalized power savings $\Delta\overline{P}/\overline{P}_0$ for symmetric actuation with steady Coanda jets at $3 \cdot 10^4 \leq Re_w \leq 6 \cdot 10^4$ and $\beta_w = 0°$.

suggest that the suction part of periodic actuation is effective at modifying the wake at very low momentum coefficients. However, steady or pulsed suction is hard to generate and would require a significant amount of power in a real vehicle application. By contrast, steady blowing with Coanda jets can be applied easily by using pressurized air from a compressor [34, 35]. Furthermore, the achieved drag reduction is with up to 35 % much larger than the ones achieved by Synthetic Jet actuation or pulsed suction. This suggests that the mechanism of base-pressure recovery by Coanda blowing is not only related to the suppression of the influence of the alternating vortex shedding on the near wake, but also has a significant effect on the mean base flow. In order to rate the efficiency of the AFC strategy by Coanda blowing, the normalized net power savings are calculated here with a method proposed by Krentel et al. [73]. At driving velocity u_∞ the powers P_0 and P_{afc} needed to overcome the drag D_0 and D_{afc} of the natural and controlled flow, respectively, are given by

$$P_0 = D_0 u_\infty = \frac{\rho}{2} A_b c_{D_0} u_\infty^3 \,, \tag{3.4}$$

$$P_{\text{afc}} = D_{\text{afc}} u_\infty = \frac{\rho}{2} A_b c_{D_{\text{afc}}} u_\infty^3 \,, \tag{3.5}$$

where c_{D_0} and $c_{D_{\text{afc}}}$ denote the baseline and the actuated drag coefficient, respectively. The power of the air blown through the actuator slot i can be calculated by

$$P_{a,i} = \frac{\rho}{2} A_{a,i} u_{a,i}^3, \ \text{ for } i = 1, 2, \tag{3.6}$$

and has to be subtracted from the power saved due to the drag reduction. This results in the equation

$$\frac{\Delta P}{P_0} = \frac{P_0 - P_{\text{afc}} - P_{a,1} - P_{a,2}}{P_0} = \frac{c_{D_0} - c_{D_{\text{afc}}}}{c_{D_0}} - \frac{c_{\mu,1} u_{a,1}}{c_{D_0} u_\infty} - \frac{c_{\mu,2} u_{a,2}}{c_{D_0} u_\infty} \tag{3.7}$$

for overall net power savings. As shown in the lower left plot of Fig. 3.6, normalized net power savings of up 25% can be achieved by Coanda blowing. The obtained maximum values vary slightly, mostly because the baseline drag coefficient used for normalization changes with the Reynolds number.
As pointed out by Geropp and Odenthal [45], the ratio $u_a^* = u_a/u_\infty$ of Coanda jet velocity to free-stream velocity has to be in the range $1.5 \leq u_a^* \leq 2.5$ to achieve an effective drag reduction. This is shown in the right column of Fig. 3.6. The drag coefficient is reduced significantly only when the blowing velocity exceeds the free-stream velocity by more than 20 %. This suggests that the velocity deficit in the shear layer has to be refilled by Coanda blowing, before a significant effect on the wake is obtained. The largest net power savings are achieved for a blowing ratio $\overline{u}_a^* \approx 1.8$, which agrees well with the effective range published by Geropp and Odenthal [45].
The effect of Coanda blowing with different momentum coefficients on the power spectral density of fluctuations of the pressure coefficients on the base is depicted in Fig. 3.7. For the pressure sensors 12 and 14 located near the trailing edges on the base, a large peak at $St_w \approx 0.29$ is visible for the natural flow. This corresponds to the characteristic reduced frequency of the von Kármán vortex street. Actuation at the threshold of $\overline{c}_\mu = 0.018$, where Coanda blowing starts to become effective, slightly increases both the magnitude and the characteristic frequency. For increasing momentum coefficients, the peaks are pushed towards higher frequencies and become smaller and smaller, until they almost disappear for actuation with $\overline{c}_\mu = 0.042$ in the fully saturated range of the drag reduction. For the fluctuation $c'_{p_{13}}$ of the pressure coefficient in the center of the base, no significant differences are visible between natural and actuated flow. This shift to higher Strouhal numbers of the vortex shedding is also reported by Bearman [18], who applied base bleed to a 2D bluff body. He concluded that the base pressure is directly related to the distance l_f of vortex formation behind the base. The latter is in turn a function of the angle γ between the shear layers and of the ratio θ/w between shear layer thickness θ and the spacing of the shear layers, which here equals the body width w. Coanda blowing reduces the

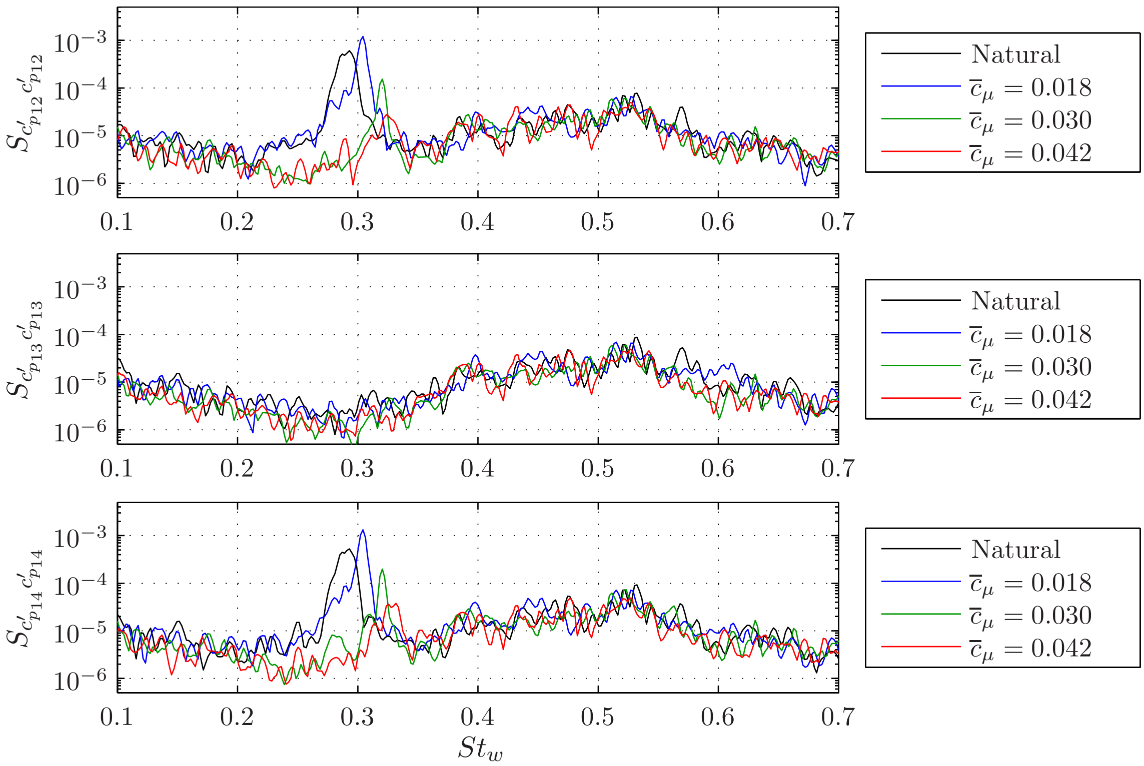

Figure 3.7: Power spectral density of pressure coefficient fluctuations on the base of the bluff body for the natural flow and for the actuated flow with steady Coanda blowing at different momentum coefficients for $Re_w = 4 \cdot 10^4$ at zero yaw angle.

thickness of the shear layers and also deflects them inwards. This results in the formation of smaller vortices further downstream, which explains the shift to higher Strouhal numbers and smaller amplitudes of base pressure fluctuations when the flow is fully actuated.
Examples of the transient evolution of the selected pressure coefficients on the base are shown in Fig. 3.8. For the natural flow, see plots (a-c), the base-pressure coefficient changes at long, seemingly random time intervals between a state with a lower mean level of about $\overline{c}_{p,b,min} \approx -0.7$ and a higher mean level around $\overline{c}_{p,b,max} \approx -0.6$. A close-up view of the pressure coefficients c_{p12} and c_{p14} located towards the sides of the base shows large oscillations with a phase shift of about 180° when the wake is in the first state, as shown in Fig. 3.8 (b). Smaller, almost synchronized fluctuations occur when the wake is in the second state, see Fig. 3.8 (c). This indicates that the distance at which the shear layers interact varies randomly in the longitudinal direction. Actuation at a medium c_μ-level of 0.03, shown in the middle row of Fig. 3.8, increases the mean base pressure. The switching between alternating and synchronized vortex shedding in the near wake still occurs, but the magnitude of the anti-cyclical oscillations is much smaller. For the fully actuated flow with $\overline{c}_\mu = 0.042$ shown in plots (g-f) the near wake spends almost its entire time in the synchronized state, and almost no alternating vortex shedding is detected by pressure sensors 12 and 14.

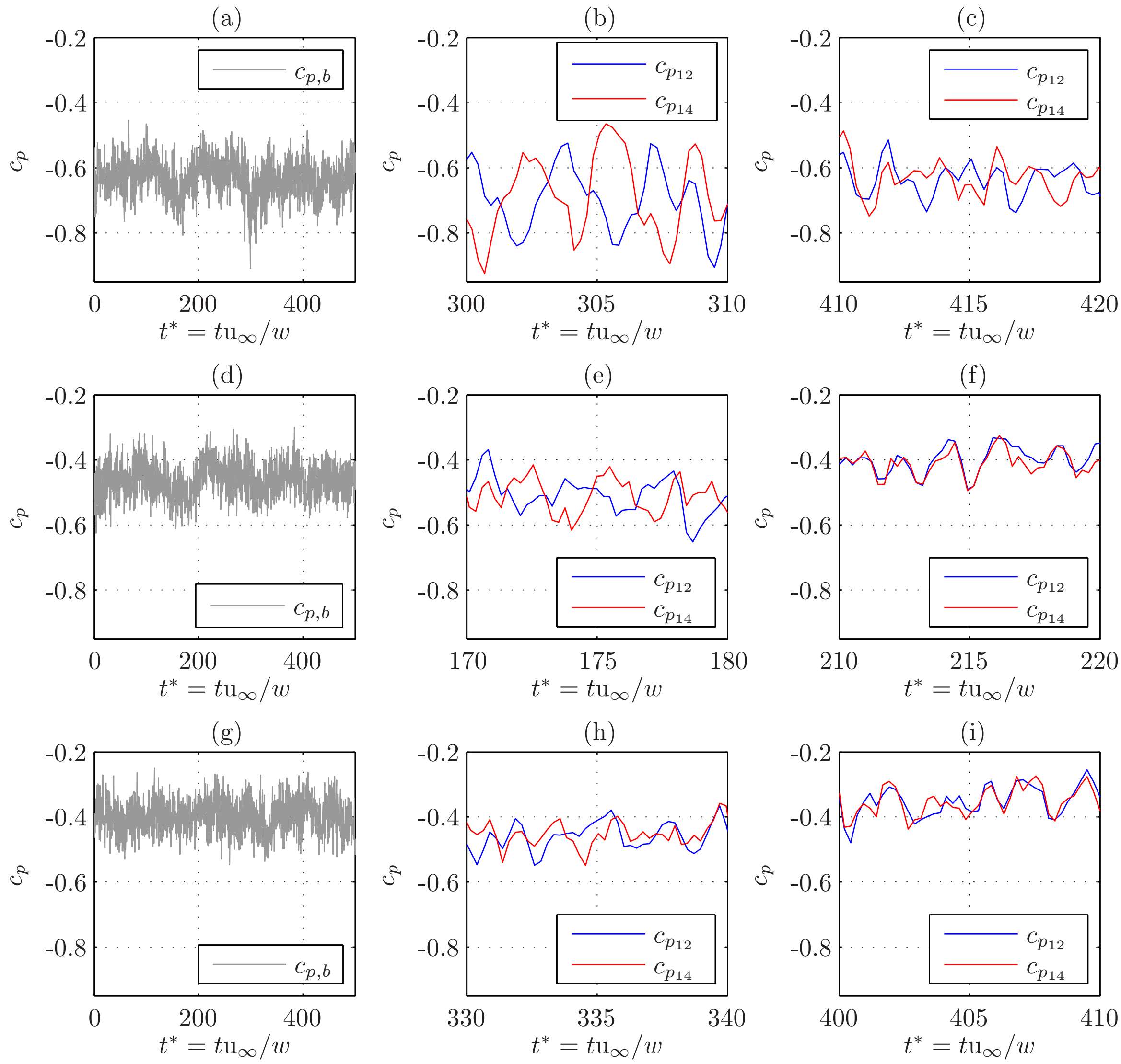

Figure 3.8: Transient evolution of pressure coefficients on the base for natural flow (a-c) and actuated flow at $c_\mu = 0.03$ (d-f) and at $c_\mu = 0.042$ (g-f), for $Re_w = 4 \cdot 10^4$ and $\beta_w = 0°$.

3.3.2 Symmetric actuation by pulsed blowing

In the experiments by Henning et al. [54, 52] and Pastoor et al. [100] periodic actuation with synthetic jets is applied at the rear edges of a D-shaped two-dimensional bluff body. By contrast, Muminović et al. [89, 88, 90] use pulsed suction for a smaller bluff body of the same shape. The authors obtain a substantial base-pressure recovery for periodic actuation at Strouhal numbers $St_a = 0.15$ and $St_a = 0.17$ for the first and second experiment, respectively. In both cases, the most effective drag reduction is obtained for reduced actuation frequencies about 20 % to 40 % below the characteristic frequency of the natural flow instability.

Although the physical mechanism of drag reduction by Coanda blowing is different to the aforementioned actuation methods, a series of experiments was conducted to test if a more efficient drag reduction can be obtained for pulsed instead of continuous Coanda blowing. Here, the pulsed actuation is carried out with fast switching solenoid valves, as described in section 3.1. Before the experiments, look-up tables of the effective blowing velocity were determined via hot-wire anemometry at the Coanda slot exits for a large range of supply pressures and actuation frequencies $10\,\mathrm{Hz} \leq f_a \leq 200\,\mathrm{Hz}$.

Based on these look-up tables the momentum coefficient can be kept constant while testing various actuation frequencies. The results of these measurements are given in Fig. 3.9, which shows the time-averaged, normalized drag coefficient $\overline{c}_D/\overline{c}_{D_0}$ for pulsed actuation at a momentum coefficient $\overline{c}_\mu = 0.04$ with reduced frequencies in the range $0.05 \leq St_{a,w} \leq 1.2$ at several Reynolds numbers. Similar to the experiments cited above, a large drag reduction by about 30

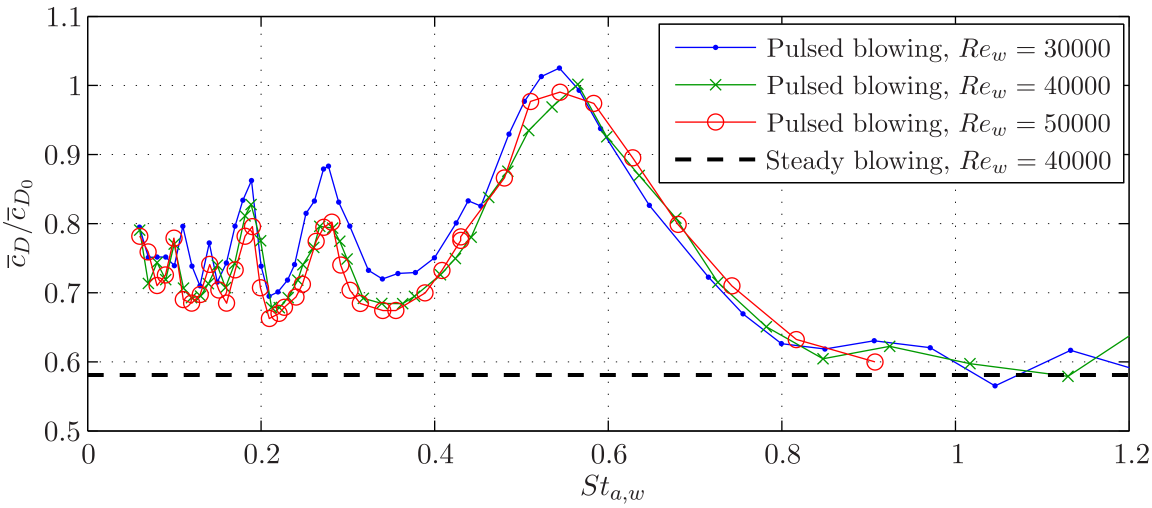

Figure 3.9: Comparison of the drag reduction for steady versus pulsed Coanda blowing at different reduced frequencies with a momentum coefficient $\overline{c}_\mu = 0.04$ for a Reynolds number range $30000 \leq Re_w \leq 50000$ at a zero yaw angle.

% is obtained for pulsed actuation at $St_{a,w} \approx 0.21$, below the frequency $St_w \approx 0.29$ of the von Kármán vortex street. Several peaks are visible in the steady-state maps, indicating the less effective or detrimental forcing frequencies. This is the case for actuation at the same frequency as the natural wake instability – and even more so at twice this frequency. For significantly larger pulsation frequencies $St_{a,w}$ the actuation appears to have a quasi-steady effect on the wake. In this regime, a similar drag reduction of about 40% is achieved both for pulsed and steady blowing at the same momentum coefficient.

This suggests that open-loop pulsed actuation with Coanda jets is not more effective than steady blowing for this body geometry. Thus, only continuous Coanda blowing is considered here further for actuation of the flow around the 2D bluff body.

3.3.3 Boundary layer profiles for natural and actuated flow

Coanda blowing at the trailing edges not only increases the pressure in the near wake of the bluff body; it also accelerates the boundary layer close to the actuators. This is shown in Fig. 3.10 for symmetric and asymmetric Coanda blowing relative to the natural flow at $Re_w = 4 \cdot 10^4$. Here, the velocities u(y) were measured with a hot-wire at the rear edge of the bluff body, next

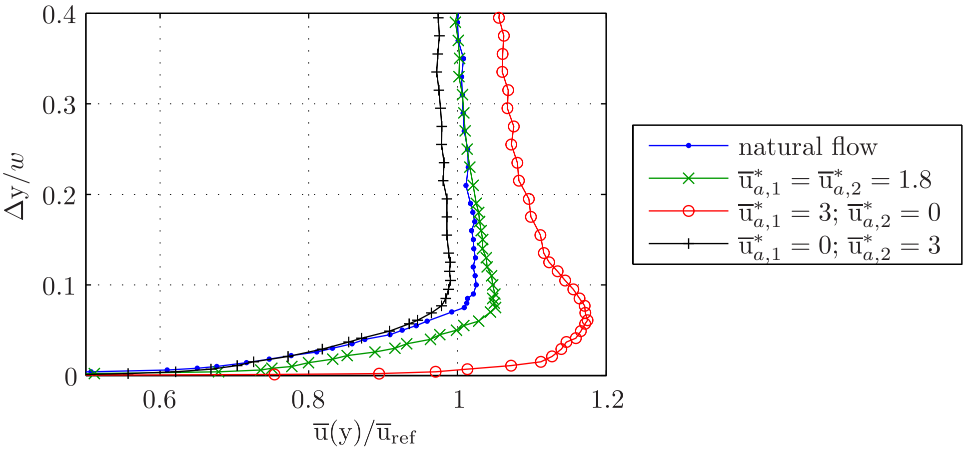

Figure 3.10: Boundary layer profiles for natural and actuated flows at $Re_w = 4 \cdot 10^4$ and $\beta_w = 0°$ at the rear edge of the bluff body ($x = -l/2$, $z = h/2$ and $\Delta y = y - w/2$). The time-averaged hot-wire measurements for the velocities $\overline{u}(y)$ are normalized with the mean reference velocity $\overline{u}_{ref}$ measured outside the natural boundary layer.

to the slot exit of actuator 1. The distance Δy from the surface of the bluff body is defined as $\Delta y = y - w/2$. The profiles are nondimensionalized for the time-averaged reference velocity $\overline{u}_{ref}$ measured outside the natural boundary layer at $\Delta y/w = 0.4$. Due to blockage effects in the closed test section, this velocity is higher than the free-stream velocity, with $\overline{u}_{ref} \approx 1.17\,\overline{u}_\infty$.
The shape of the velocity profile measured for natural flow corresponds to a turbulent boundary layer. A boundary layer thickness of $\delta_{99}/w = 0.0693$ is obtained for the natural flow, and the corresponding momentum thickness is determined to be $\delta_2/w = 5.6 \cdot 10^{-3}$. These values are less than half of those reported by Henning [52] and Muminović [90], who studied D-shaped two-dimensional bluff bodies with a blunter front and much thicker boundary layers. This effect is circumvented by the elliptic nose of the bluff body studied here. Similar to the results published by these authors [52, 90], the velocity profile for the natural flow in Fig. 3.10 shows a region with $\overline{u}(y)/\overline{u}_{ref} > 1$ for $0.07 \leq \Delta y/w \leq 0.35$. According to Becker [21] and Leder [76] this is due to the acceleration of the mean external flow along the boundary of the time-averaged dead-water zone behind the bluff body.
As discussed in section 3.3.1, symmetric actuation with $\overline{u}^*_{a,1} = \overline{u}^*_{a,2} = 1.8$ leads to the most efficient drag reduction under straight flow conditions. This results in a thinner boundary layer with higher velocities relative to the natural flow, as can be seen in Fig. 3.10. When strong one-sided blowing with $\overline{u}^*_{a,1} = 3$ and $\overline{u}^*_{a,2} = 0$ is applied, the boundary layer acceleration is even faster. This also increases the velocity further away from the bluff body and leads to lower surface-pressures upstream of the actuators. For one-sided Coanda actuation on the opposite trailing edge with $\overline{u}^*_{a,1} = 0$ and $\overline{u}^*_{a,2} = 3$, the boundary layer slows and the pressure increases. These well-known effects have been extensively studied in the context of circulation control to modify drag, lift and pitching moment of thick airfoils, see e.g. [61, 36, 92, 139]. Here, they are used to change the pressure distribution around the bluff body to reduce yaw moment under cross-wind conditions. The related flow characteristics are discussed in the next section.

3.3.4 Asymmetric actuation by continuous blowing

As discussed for the natural flow characteristics in section 3.2, cross-wind conditions have a strong influence on the pressure distribution around the front of the 2D bluff body. Asymmetric actuation with Coanda blowing at the rear edges can counteract these changes to some degree. Figure 3.11 shows the corresponding steady-state maps of the actuated flow for a cross-wind angle $\beta_w = 5°$. Here, the nondimensional blowing rates $u^*_{a,1}$ and $u^*_{a,2}$ at the lee- and windward

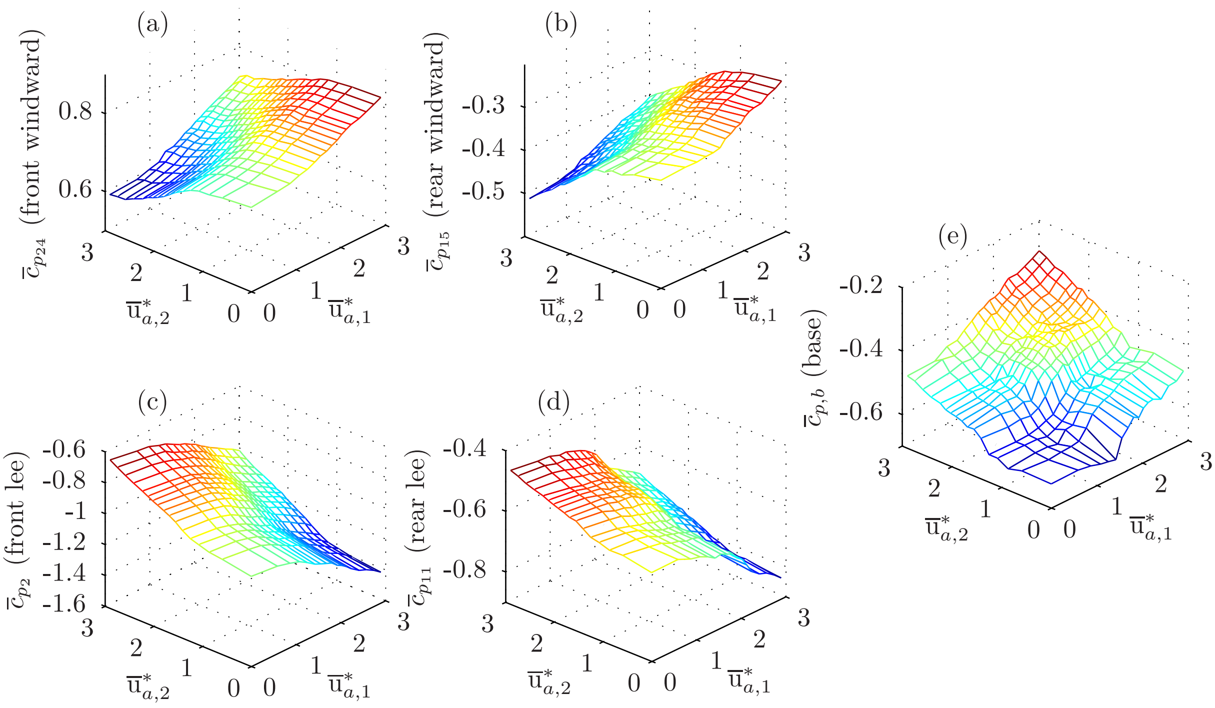

Figure 3.11: Steady-state maps of selected pressure coefficients for asymmetric actuation under cross-wind conditions at $\beta_w = 5°$ and $Re_w = 4 \cdot 10^4$.

side, respectively, are varied independently. The largest increase in base pressure is obtained for symmetric blowing, but one-sided actuation also has a positive effect, as shown in Fig. 3.11 (e). Furthermore, Coanda blowing accelerates the boundary layer upstream of the actuator slots, which decreases the pressure coefficient in the rear region close to the actuators. This can be seen from the steady-state map in plot (d) with blowing $u^*_{a,1}$ at the leeward side alone. Furthermore, the jet from one-sided actuation also obstructs the shear layer on the opposite side. This increases the pressure coefficient there, as shown in Fig. 3.11 (b). A pressure difference between the rear lee- and windward sides can thus be generated by asymmetric actuation, reducing yaw moment under cross-wind conditions. However, the local effects of Coanda blowing on the flow around the rear part of the bluff body carry on upstream and change the pressure distribution around the nose significantly. This reduces the control authority for the yaw moment slightly. Furthermore, side force and yaw moment can only be modified in opposite directions for the given actuator location.

The overall time-averaged effect of asymmetric actuation on the force and moment coefficients is depicted in Fig. 3.12. For straight oncoming flow, see plots (a-c), the map of the drag coefficient is symmetric but nonlinear with respect to the amplitude of the input variables. By contrast, the maps of side-force and yaw-moment coefficients are almost linear when the threshold of $\bar{u}^*_{a,1} > 1.2$ and $\bar{u}^*_{a,2} > 1.2$ is exceeded. This falls in line with observations made for symmetric blowing, which has to be at least 20 % faster than the free-stream velocity to be effective.

When the cross-wind angle is increased to $\beta_w = 5°$ the maps for side-force and yaw-moment coefficients do not change their shape significantly . Rather, they are shifted by a constant bias.

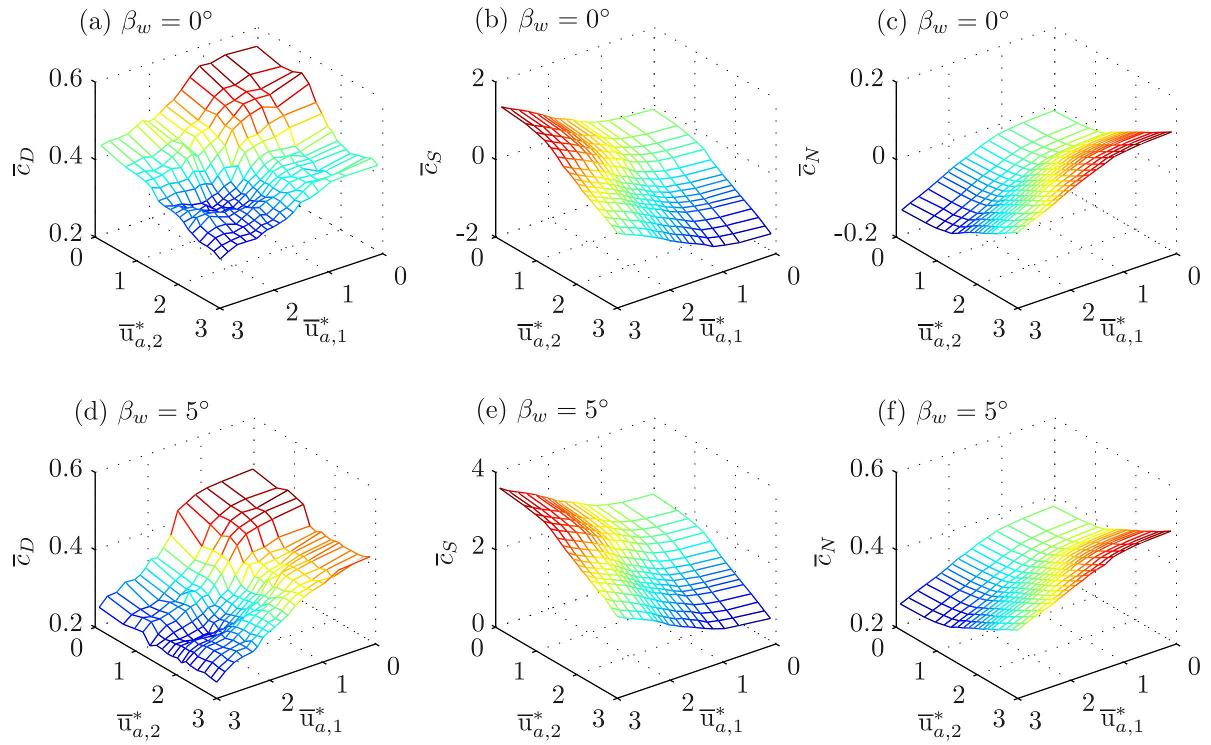

Figure 3.12: Steady-state maps of the force and moment coefficients for asymmetric actuation at $Re_w = 4 \cdot 10^4$ and $\beta_w = 0°$ (top) or $\beta_w = 5°$ (bottom).

By contrast, the map for the drag coefficient becomes asymmetric, as seen in Fig. 3.12 (d). This parameter-dependent behavior is mostly due to changed pressure distribution around the nose under side-wind conditions, whereas the characteristics of the wake and base pressure are not significantly affected by small to moderate cross-wind angles. As discussed for the natural flow characteristics, the stagnation point moves to the windward side and a suction peak forms on the leeward side of the nose. One-sided blowing $u^*_{a,1}$ on the rear leeward side accelerates the flow and increases the suction peak. This explains the higher effectiveness of this actuator at drag reduction for positive cross-wind angles.
These nonlinear, parameter-dependent characteristics have to be taken into account during the model identification and control design.

3.3.5 Transient response of the actuated flow

In this section the transient response of the pressure distribution around the bluff body to stepwise changes in Coanda blowing amplitude is briefly discussed. This helps develop an understanding of the plant dynamics and lays the foundation for identifying suitable models.
In order to evaluate actuator and flow dynamics separately, the instantaneous blowing velocity $u^*_{a,jet}$ at the actuator exit slots must be known. This velocity is determined from pressure readings inside the actuator ducts with the method described in section 3.1. Fig. 3.13 shows the transient response $\Delta c_{p,b}$ of the base-pressure coefficient to stepwise changes in actuation amplitude for symmetric, continuous Coanda blowing.
In all cases, the instantaneous dimensionless jet velocity $u^*_{a,jet}$ rises after a short time delay of about 7 ms, overshoots and settles quickly to the desired value $u^*_{a,des}$. For step inputs in the range $1.3 \leq u^*_{a,des} \leq 2.0$ where the largest drag reduction is achieved, the base-pressure coefficient shows slow transient characteristics, see plots (a) and (c). The response becomes faster with increasing free-stream velocity. This suggests that the dynamics in this range of actuation amplitudes are dominated by slow fluid-dynamic processes related to the suppression of the large, alternating vortices of the wake instability. For higher blowing velocities $2.0 \leq u^*_{a,des} \leq 2.7$

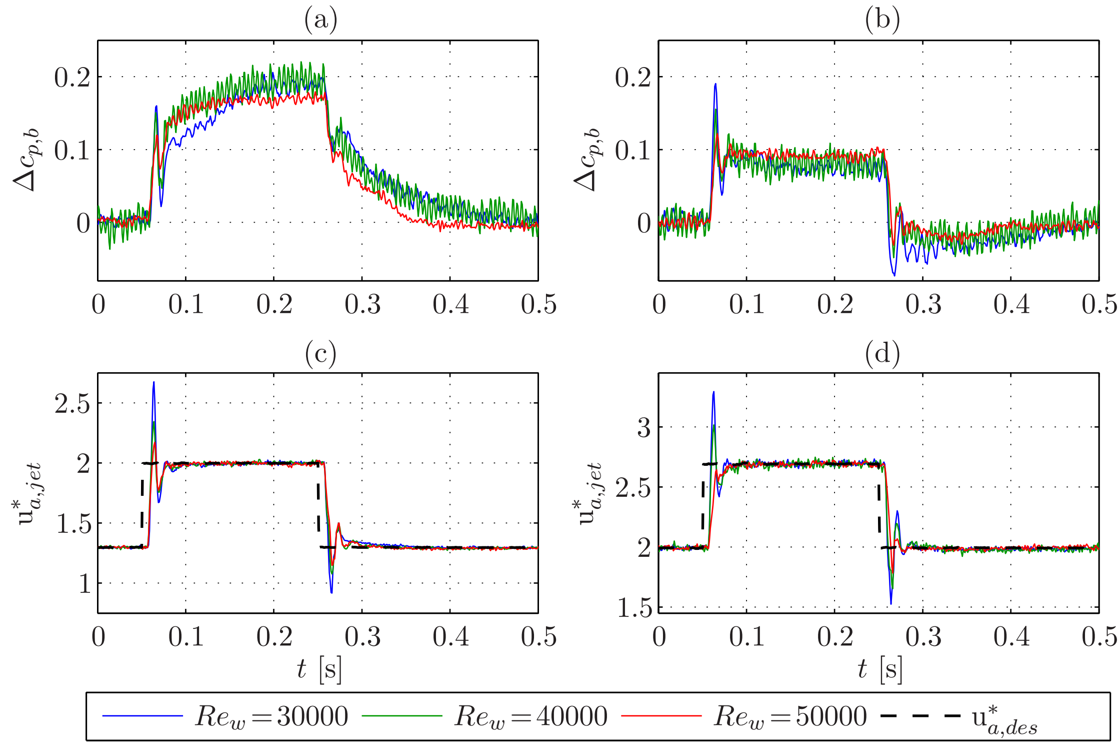

Figure 3.13: Phase-averaged response of the base-pressure coefficient to symmetric actuation at different amplitudes and at different Reynolds numbers $30000 \leq Re_w \leq 50000$

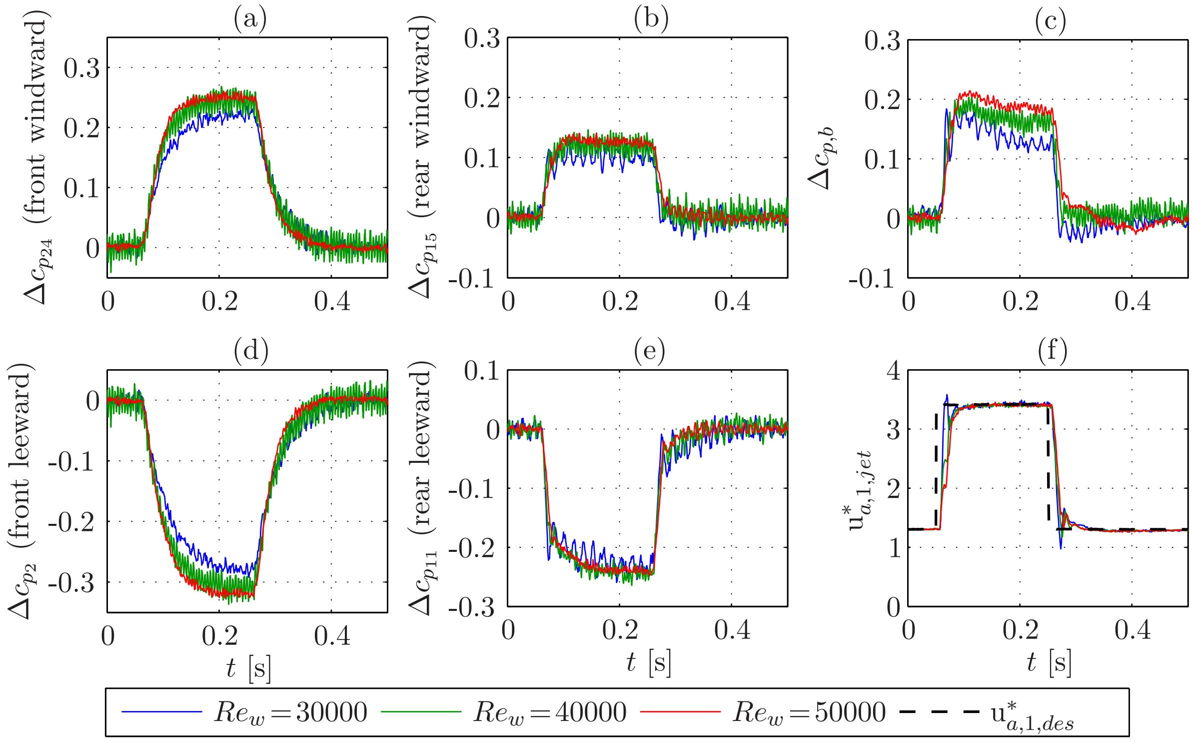

Figure 3.14: Phase-averaged response of several pressure coefficients to one-sided Coanda blowing at different Reynolds numbers $30000 \leq Re_w \leq 50000$

the response is significantly faster and changes almost immediately with the instantaneous jet velocity.
Similar characteristics are observed for one-sided actuation at large amplitudes, as can be seen in Fig. 3.14. Here, the pressure coefficients $c_{p_{11}}$, $c_{p_{15}}$ and $c_{p,b}$, all located on the rear part of the bluff body, also show a very fast response. This can be explained from their proximity to the Coanda jets, so that changes in instantaneous blowing velocity almost immediately translate into changes in local pressure distribution. By contrast, the pressure coefficients $c_{p_{24}}$ and c_{p_2} at the nose of the body respond significantly slower. Furthermore, their response time varies with free-stream velocity, which again indicates dominant fluid-dynamic processes. These dependencies can be accurately described by linear parameter-varying models, as applied for actuated flow dynamics of the 3D bluff body in section 4.4. To stress again, however, the dynamics of the wake of the 2D bluff body show significantly more nonlinear behavior with time constants that change with actuation amplitude. Therefore, LPV modeling for the 2D bluff body is not carried out here. Instead, the dynamics of the actuated flow are described by a set of linear black-box models as discussed in the following section.

3.4 Model identification

The investigation of the actuated flow characteristics in the previous section indicates a nonlinear plant behavior that has to be taken into account in the design of the feedback controller for drag and yaw-moment coefficients. One way proven to be successful in many other applications of closed-loop active flow control, see e.g. [54, 88, 73], is to design a linear H_∞ controller that is robust for a set of linear models identified at different operating points.
An overview of the model structure for the 2D bluff body and the successive steps in deriving a plant model with a suitable uncertainty description are shown in Fig. 3.15. Here, the actuator and actuated flow dynamics are identified and modeled separately. The actuators behave similar under all operating conditions and can be accurately approximated by single linear models. By contrast, the flow dynamics are nonlinear and parameter-dependent. The steady-state part of the nonlinearities can be partly represented by a nonlinear map located at the input of the model for the flow dynamics. Remaining unmodeled dynamic nonlinearities and parameter-dependencies are taken into account by identifying a set of linear black-box models for the flow dynamics at

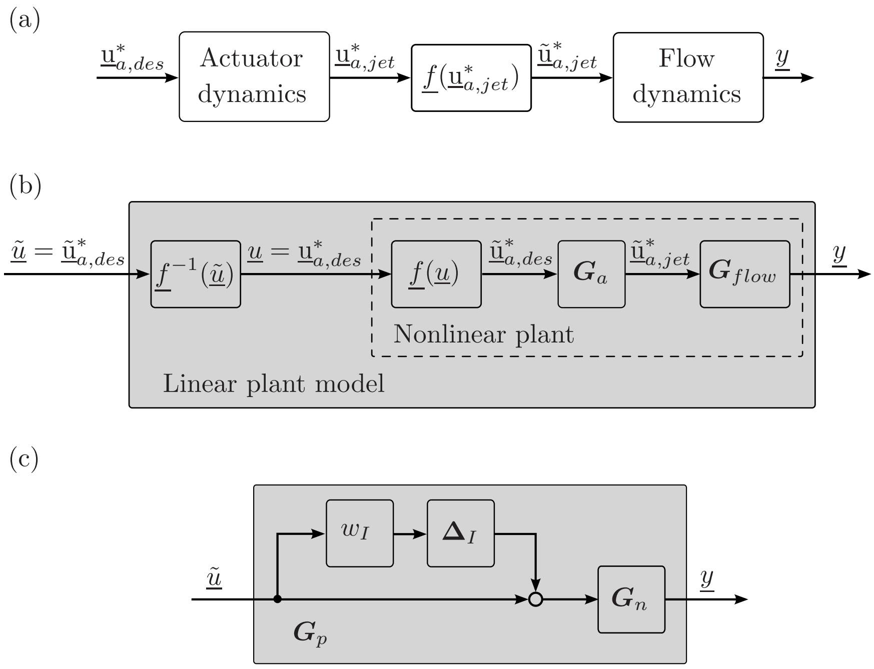

Figure 3.15: Schematic model structure for the actuators and the actuated flow dynamics.

a range of different operating points that comprise several cross-wind angles $-5^\circ \leq \beta_w \leq 5^\circ$, Reynolds numbers $40000 \leq Re_w \leq 60000$ and different actuation amplitudes. This approach is applied in a similar way by Henning and King [54].

From a physical point of view, the static nonlinear map $\underline{f}(\underline{\mathrm{u}}^*_{a,jet})$ should depend on the instantaneous jet velocities $\underline{\mathrm{u}}^*_{a,jet}$ at the actuator exits, see Fig. 3.15 (a). Modeling the plant in this way, however, would make it impossible to compensate for the static nonlinearities via an inverted nonlinear map at the plant input. To circumvent this problem, the nonlinear map $\underline{f}(\underline{u})$ is placed here at the plant input and depends on the control input $\underline{u} = \underline{\mathrm{u}}^*_{a,des}$ as shown in Fig. 3.15 (b). The compensation is carried out prior to the identification of the linear dynamic models. To this end, fictitious compensated desired and instantaneous blowing rates $\underline{\tilde{\mathrm{u}}}^*_{a,des} = \underline{f}(\underline{\mathrm{u}}^*_{a,des})$ and $\underline{\tilde{\mathrm{u}}}^*_{a,jet} = \underline{f}(\underline{\mathrm{u}}^*_{a,jet})$ are calculated based on the static nonlinear map. The actuator model $\boldsymbol{G}_a$ is then identified for inputs $\underline{\tilde{\mathrm{u}}}^*_{a,des}$ and outputs $\underline{\tilde{\mathrm{u}}}^*_{a,jet}$. The errors arising from this approach are negligible, as the plant spends most of its time in a regime where $\underline{f}(\underline{\mathrm{u}})$ is linear. Most importantly, this approach allows the nonlinearity to be pre-compensated by its inverse as shown in Fig. 3.15 (b). The compensation results in a family of linear plant models that describe the dynamic response of $\underline{y}$ to the compensated input variable $\underline{\tilde{u}}$. This set of linear models $\boldsymbol{G}_p$ can then be approximated by a nominal model $\boldsymbol{G}_n$ with an unstructured multiplicative input uncertainty as shown in Fig. 3.15 (c). The individual steps of the model identification are described in the following sections.

3.4.1 Actuator dynamics

The actuator models describe the dynamic response of the instantaneous, compensated blowing rates $\tilde{\mathrm{u}}^*_{a,1,jet}$ and $\tilde{\mathrm{u}}^*_{a,2,jet}$ to changes in the desired, compensated blowing rates $\tilde{\mathrm{u}}^*_{a,1,des}$ and $\tilde{\mathrm{u}}^*_{a,2,des}$. To this end, individual black-box models G_{a_1} and G_{a_2} are identified for actuators 1 and 2 from experiments in which the input variables are varied with pseudo-random binary signals. The structure of the models is chosen as discrete-time state-space models

$$\underline{x}(k+1) = \boldsymbol{A}\underline{x}(k) + \underline{b}\, u(k-n_0), \quad \underline{x}(0) = \underline{x}_0, \tag{3.8}$$

$$y(k) = \underline{c}^T \underline{x}(k), \tag{3.9}$$

with $u = \tilde{\mathrm{u}}^*_{a,i,des}$, $y = \tilde{\mathrm{u}}^*_{a,i,jet}$ for $i = 1, 2$, respectively. The order of each model is set to 2, i.e. $\underline{x} \in \mathbb{R}^2$, and an input delay of $n_0 = 6$ is chosen for a sampling time $T_s = 1\,\mathrm{ms}$. The identification is carried out with the Prediction-Error-Method (PEM) as implemented in the “System Identification Toolbox” in `MATLAB` [84], and the actuator dynamics are well described by the identified linear models over the entire operating range. Transferring the resulting state-space models into the frequency domain yields discrete-time transfer functions $G_{a_1}(z)$ and $G_{a_2}(z)$. Their frequency responses for $z = e^{j\omega T_s}$ are shown in Fig. 3.16. The magnitude response of both models indicates a fast actuator bandwidth larger than 50 Hz, with slightly faster characteristics of the first actuator. The phase response is dominated by the input time-delay, which leads to a large phase shift at higher frequencies.

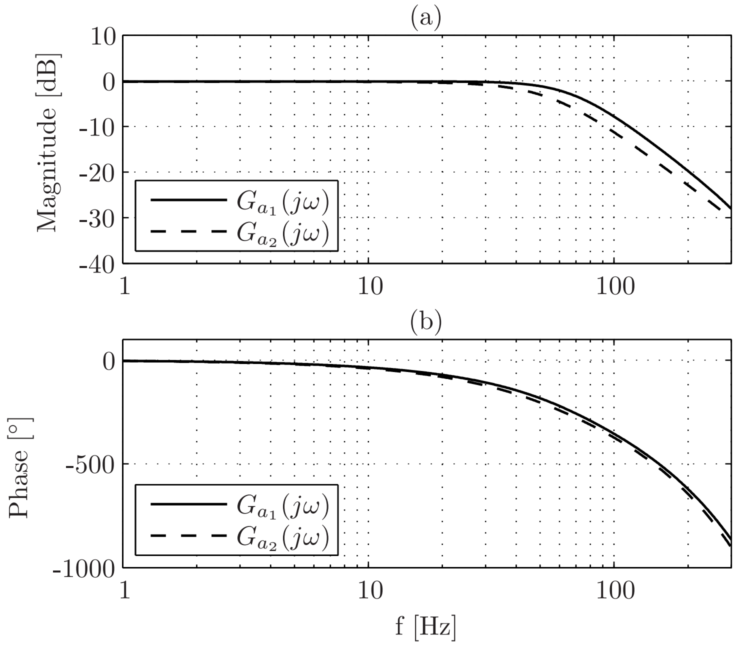

Figure 3.16: Magnitude (a) and phase (b) response of the identified actuator models.

3.4.2 Compensation of static nonlinearities

As discussed with regard to the actuated flow characteristics in section 3.3, the blowing velocity at the actuator exit slot has to exceed the free-stream velocity by about 20 % to have a significant effect on the flow around the 2D bluff body. Therefore, the steady-state maps of drag, side-force and yaw-moment coefficients show a partially similar nonlinear behavior with respect to the nondimensional Coanda blowing rates $\mathrm{u}_{a,1}^*$ and $\mathrm{u}_{a,2}^*$ of the two actuators, respectively. This can

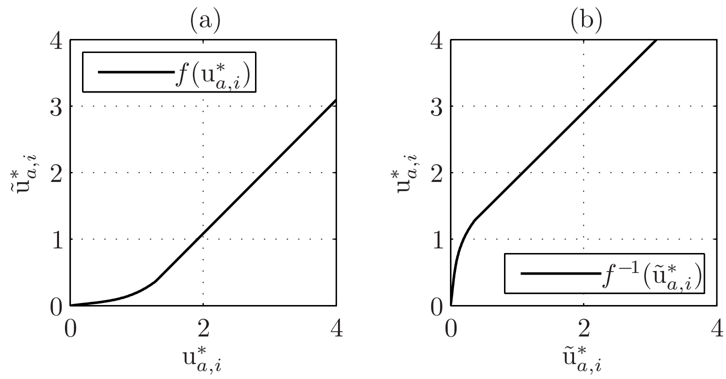

Figure 3.17: Look-up table for the static input nonlinearity (a) of the actuated flow model and the inverted map (b) used for compensation.

be modeled by the nonlinear map shown in Fig. 3.17. Here, the same map $f(\mathrm{u}_{a,i}^*)$ is used for both actuator channels to obtain the compensated input variables

$$\underline{\tilde{\mathrm{u}}}_a^* = \left[f(\mathrm{u}_{a,1}^*) \quad f(\mathrm{u}_{a,2}^*)\right]^T = \underline{f}(\underline{\mathrm{u}}_a^*). \tag{3.10}$$

In the lower range of blowing ratios $0 \leq \mathrm{u}_a^* \leq 1.3$ the map is derived from the steady-state characteristics of the side-fore coefficient for one-sided actuation, followed by a linear increase with a unity slope for $\mathrm{u}_a^* \geq 1.3$. The inverse

$$\underline{f}^{-1}(\underline{\tilde{\mathrm{u}}}_a^*) = \left[f^{-1}(\tilde{\mathrm{u}}_{a,1}^*) \quad f^{-1}(\tilde{\mathrm{u}}_{a,2}^*)\right]^T \tag{3.11}$$

is used for compensating these static nonlinearities, as indicated in Fig. 3.17 (b). A comparison

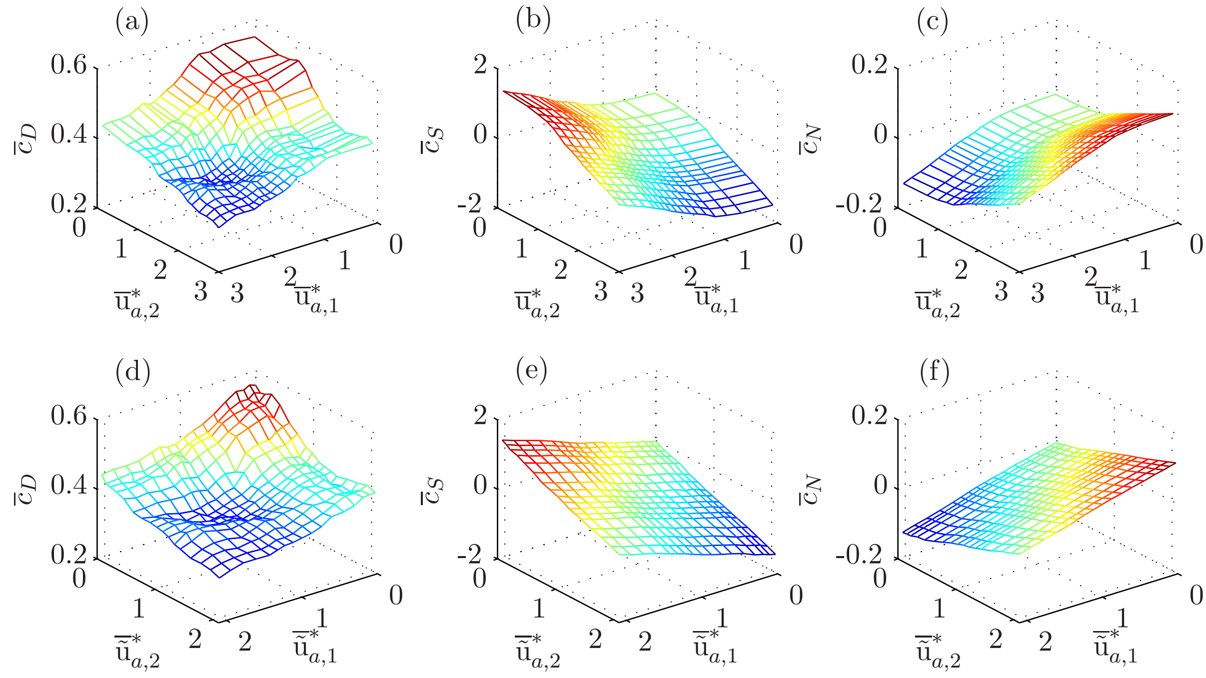

Figure 3.18: Original (upper row) and compensated (lower row) steady-state maps of drag, side-force and yaw-moment coefficients for asymmetric Coanda blowing at $Re_w = 4 \cdot 10^4$ and $\beta_w = 0°$.

of the original maps of the force and moment coefficients with the compensated ones is shown in Fig. 3.18 for a cross-wind angle $\beta_w = 0$ at $Re_w = 40000$. As can be seen from maps (e) and (f), the time-averaged characteristics of side-force and yaw-moment coefficients are almost perfectly linear for the compensated input variables $\tilde{u}^*_{a,1}$ and $\tilde{u}^*_{a,2}$. The compensation also significantly reduces the nonlinearities in the steady-state map of the drag coefficient. This lowers the uncertainty of the overall dynamic model for control design.

3.4.3 Surrogate output variables for force and moment coefficients based on surface-pressure measurements

When applying closed-loop AFC to a real vehicle, the actual force and moment coefficients are hard to measure. Instead, adequate surrogate output variables can be determined from a weighted sum of pressure coefficients. To this end, the bluff body is subjected to a range of asymmetric and symmetric, constant actuation amplitudes at different cross-wind angles and free-stream velocities. The weighting coefficients for the individual pressure coefficients are determined from these steady-state measurements via a linear least squares optimization, see Appendix B for more details.

The surrogate variable $\hat{c}_D$ for the drag coefficient is calculated from a weighted sum of the base-pressure coefficient $c_{p,b}$ and the front respective wind- and leeward pressure coefficients, $c_{p_{24}}$ and c_{p_2}. As indicated by the investigation of the actuated flow characteristics, see section 3.3, asymmetric actuation changes not only the base-pressure coefficient, but also the pressure distribution around the rear sides and the front of the bluff body. Furthermore, changes in cross-wind angle also have a significant impact on the flow around the nose. Thus, the frontal pressure distribution must also be taken into account in the calculation of the surrogate variable for the drag coefficient. In a similar way, the surrogate side-force and yaw-moment coefficients $\hat{c}_S$ and $\hat{c}_N$ can be determined by a weighted sum of the front wind- and leeward pressure coefficients $c_{p_{24}}$ and c_{p_2} and the rear luv- and leeward pressure coefficients $c_{p_{15}}$ and $c_{p_{11}}$. For more details, see Appendix B.

A comparison of drag, side-force and yaw-moment coefficients with their surrogate variables is

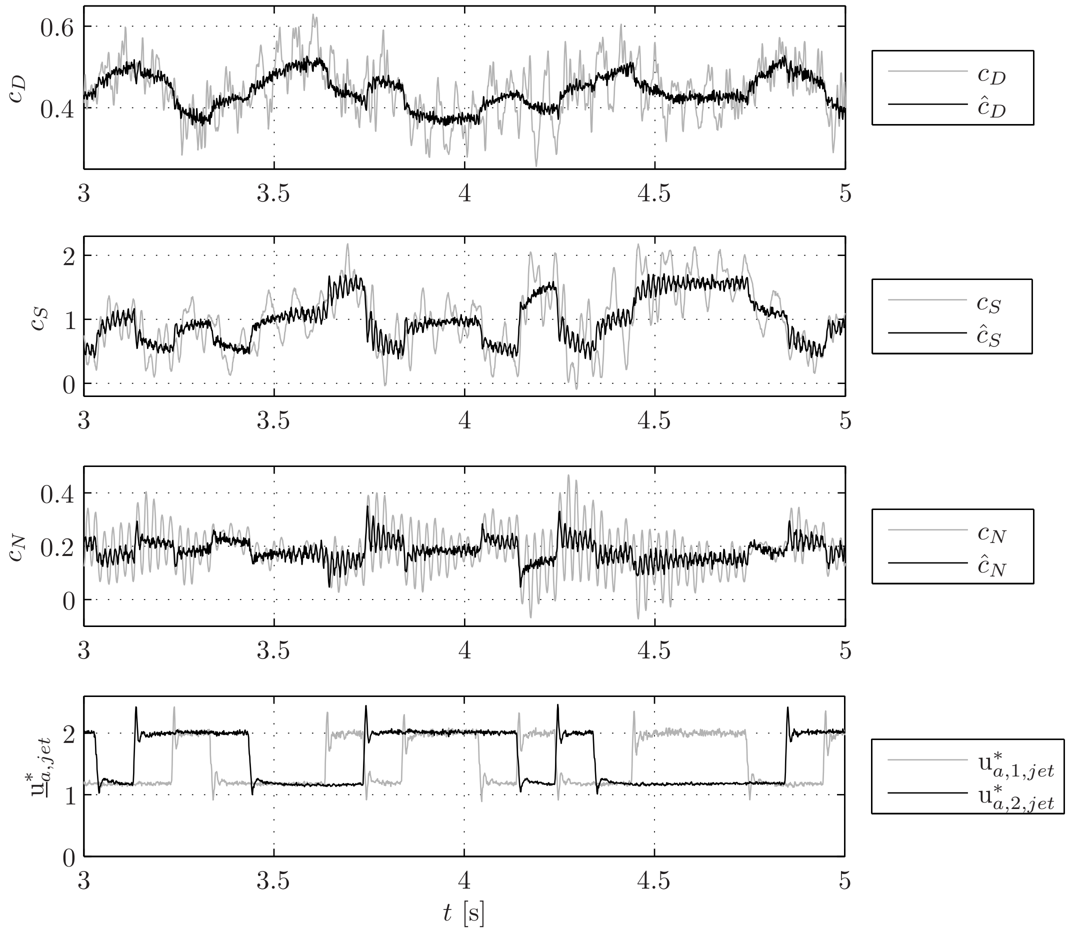

Figure 3.19: Transient evolution of drag, side-force and yaw-moment coefficients as determined from force and moment measurements in comparison with their surrogate variables based on a weighted sum of pressure coefficients. During the experiment the nondimensional actuator blowing ratios are varied with a pseudo-random binary signal at $Re_w = 40000$ and $\beta_w = 5°$.

given in Fig. 3.19. Although the weighting coefficients are determined from a series of steady-state measurements, the surrogate variables $\hat{c}_D$, $\hat{c}_S$ and $\hat{c}_N$ capture the transient evolution very well. Furthermore, the actual force and moment coefficients as determined from the balance readings are superimposed by large oscillations due to the limited stiffness of the model support and the force/torque sensor. This makes the surrogate variables more suitable as output variables for the control design, since they capture the flow behavior at a higher bandwidth without being superimposed by disturbances from mechanical oscillations.

3.4.4 Linear black-box model identification for the actuated flow

For the actuated flow around the bluff body, individual linear black-box models are identified for several operating points covering the Reynolds number range $40000 \leq Re_w \leq 60000$, cross-wind angles $-5° \leq \beta_w \leq 5°$ and different actuation amplitudes. To this end, the desired Coanda blowing rates $\underline{\mathrm{u}}^*_{a,des}$ are varied with pseudo-random binary signals (PRBS). The maximal PRBS frequency covers a range $30\,\mathrm{Hz} \leq f_{PRBS} \leq 45\,\mathrm{Hz}$ and is adjusted proportionally to the Reynolds number of the respective experiment. This ensures that a similar range of nondimensional frequencies is excited in each identification experiment of the actuated flow dynamics. The structure of the models is chosen as discrete-time MIMO models in state-space form

$$\underline{x}(k+1) = \boldsymbol{A}\underline{x}(k) + \boldsymbol{B}\,\underline{u}(k), \quad \underline{x}(0) = \underline{x}_0, \tag{3.12}$$

$$\underline{y}(k) = \boldsymbol{C}\underline{x}(k), \tag{3.13}$$

with $\underline{x} \in \mathbb{R}^6$ and a sampling time $T_s = 1\,\mathrm{ms}$. Here, the compensated nondimensional instantaneous Coanda blowing rates are chosen as input variables $\underline{u} = \underline{\tilde{u}}^*_{a,jet}$. The output variable vector

$$\underline{y} = \begin{bmatrix} \hat{c}_D & \hat{c}_N \end{bmatrix}^T \tag{3.14}$$

consists of the surrogate variables for drag and yaw-moment coefficients as calculated from a weighted sum of pressure coefficients. In total, 54 black-box models are identified from the experiments using the Prediction-Error-Method from the "System Identification Toolbox" in `Matlab` [84].

Transferring these models into the Laplace domain results in matrices of transfer functions $\boldsymbol{G}_{\text{flow}}$, which describe the dynamics of the actuated flow at the range of operating points covered by the identification experiments. Pre-multiplying these transfer functions with the actuator model $\boldsymbol{G}_a$ yields models for the overall plant. A comparison of the nondimensional frequency characteristics is shown in Fig. 3.20. Here, only the SISO submodels for actuation at the first

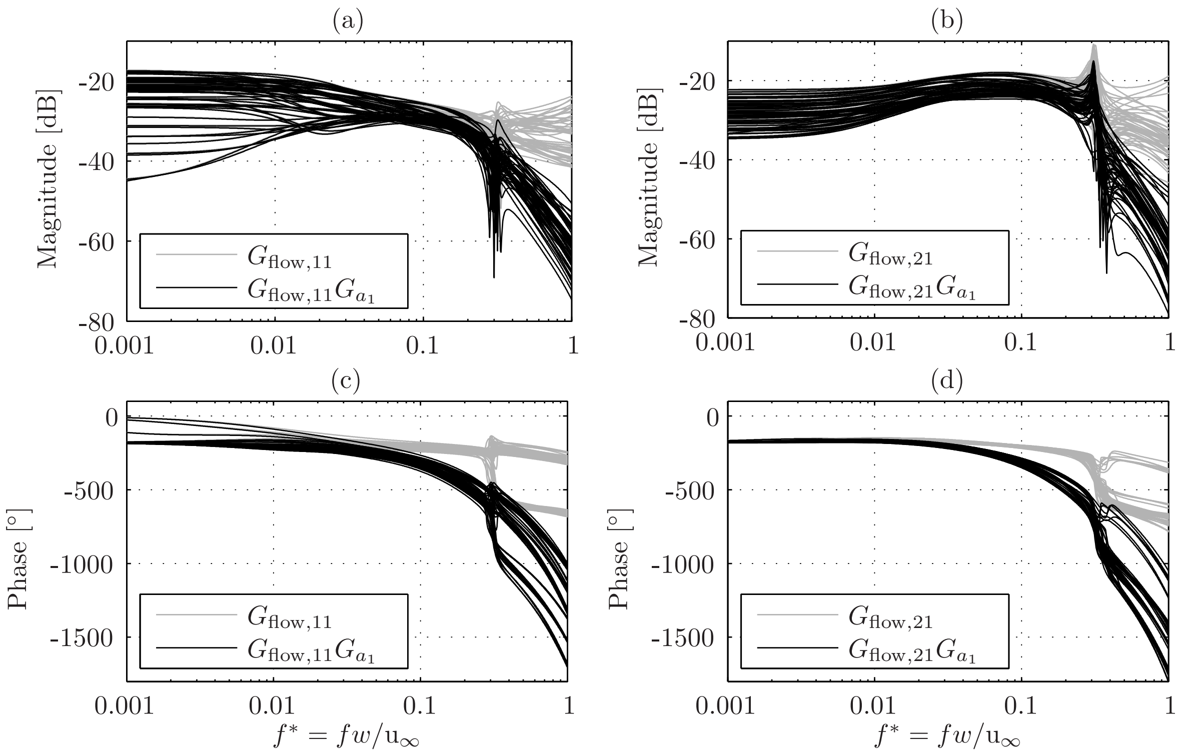

Figure 3.20: Comparison of the actuated flow model and the overall plant model, including actuator dynamics, in terms of the nondimensional frequency responses of the drag coefficient (a and c) and the yaw-moment coefficient (b and d) to Coanda blowing with actuator 1, respectively.

input are evaluated. The submodels for the second actuator channel have similar characteristics and are therefore not included in the plots.
The transfer function $G_{\text{flow},11}$ describes the response of the drag coefficient to inputs in terms of the compensated instantaneous blowing rate at actuator slot exit 1, whereas the product $G_{\text{flow},11}G_{a_1}$ relates to the overall plant including actuator dynamics. The magnitude response of these transfer functions, see Fig. 3.20 (a), coincides up to the actuator bandwidth, which lies in the range of reduced frequencies $0.2 < f^* < 0.3$ depending on the free-stream velocity of the respective experiment. At low frequencies the actuated flow dynamics $G_{\text{flow},11}$ exhibit a large gain variation. This is related to the parameter-dependent behavior of the actuated flow for cross-wind conditions, which is also observed in the steady-state maps of the drag coefficient for asymmetric actuation as discussed in section 3.3.4. For reduced frequencies $f^* > 0.03$ the magnitude response of the drag coefficient starts to fall off. The nondimensional bandwidth coincides well with the results for a similar bluff body as published by Henning [52]. However, for the Coanda actuation applied here, the amplitude response rolls off much slower. Thus, the range in which the drag coefficient can be influenced extends to a reduced frequency $f^* \approx 0.3$, at which point the limited actuator bandwidth starts to have an impact. The phase response shown in Fig. 3.20 (c) varies at low frequencies between $-180°$ and $0°$, indicating that, under certain conditions with strong cross-wind, the drag coefficient is increased because of the actuation. At higher frequencies the phase response of the overall plant is dominated by a large lag due to the input time-delay of the actuators.
Much smaller variations are observed with the frequency response of the transfer function $G_{\text{flow},21}$ for the yaw-moment coefficient, as shown in Fig. 3.20 (b). At a reduced frequency $f^* \approx 0.007$ the magnitude response starts to rise slightly and has a higher gain in the range $0.02 \leq f^* < 0.2$. This is related to the fact that the pressure distribution around the rear sides of the bluff body can be influenced at a higher bandwidth than the frontal pressure distribution. Furthermore, a clear peak at a reduced frequency $f^* \approx 0.3$ is visible, indicating that one-sided actuation amplifies and triggers the natural wake-instability under certain conditions. This is then registered by the pressure sensors on the rear sides and expressed in the magnitude response of the yaw-moment coefficient transfer function.
The transfer functions $G_{\text{flow},11}$ and $G_{\text{flow},21}$ for the actuated flow dynamics of drag and yaw-moment coefficients show a relatively large variation of the magnitude response for reduced frequencies above the characteristic vortex-shedding frequency of the natural flow. A more sophisticated modeling and identification approach would be necessary for this higher frequency range. This could be accomplished with more advanced models capable of tracing individual vortex footprints, as presented by Pastoor et al. [100]. Since the actuator bandwidth is limited to reduced frequencies $f^* \leq 0.3$ anyway, this is not necessary for the robust control approach chosen here. Nevertheless the variation of frequency response over the set of models due to nonlinearities and parameter-dependencies must be taken into account and modeled adequately. This is addressed in the next section.

3.4.5 Overall plant model and uncertainty description

A set of models for the overall plant is obtained by pre-multiplying the black-box models $\boldsymbol{G}_{\text{flow}}$ for the flow dynamics with the actuator models $\boldsymbol{G}_a$ and adding the nonlinear map $\underline{f}(\underline{u})$ at the input. This results in nonlinear Hammerstein models as shown by the dashed box in Fig. 3.15 (b). Each of them describes the dynamic response of the output variable vector $\underline{y} = \begin{bmatrix}\hat{c}_D & \hat{c}_N\end{bmatrix}$ to the input variables $\underline{u} = \begin{bmatrix}\mathrm{u}^*_{a,1,des} & \mathrm{u}^*_{a,2,des}\end{bmatrix}^T$ at a specific operating point. A comparison of the simulated output for one of these models with the measured output from the experiment is shown in Fig. 3.21. Here, very high fits are achieved for the data from the original identification

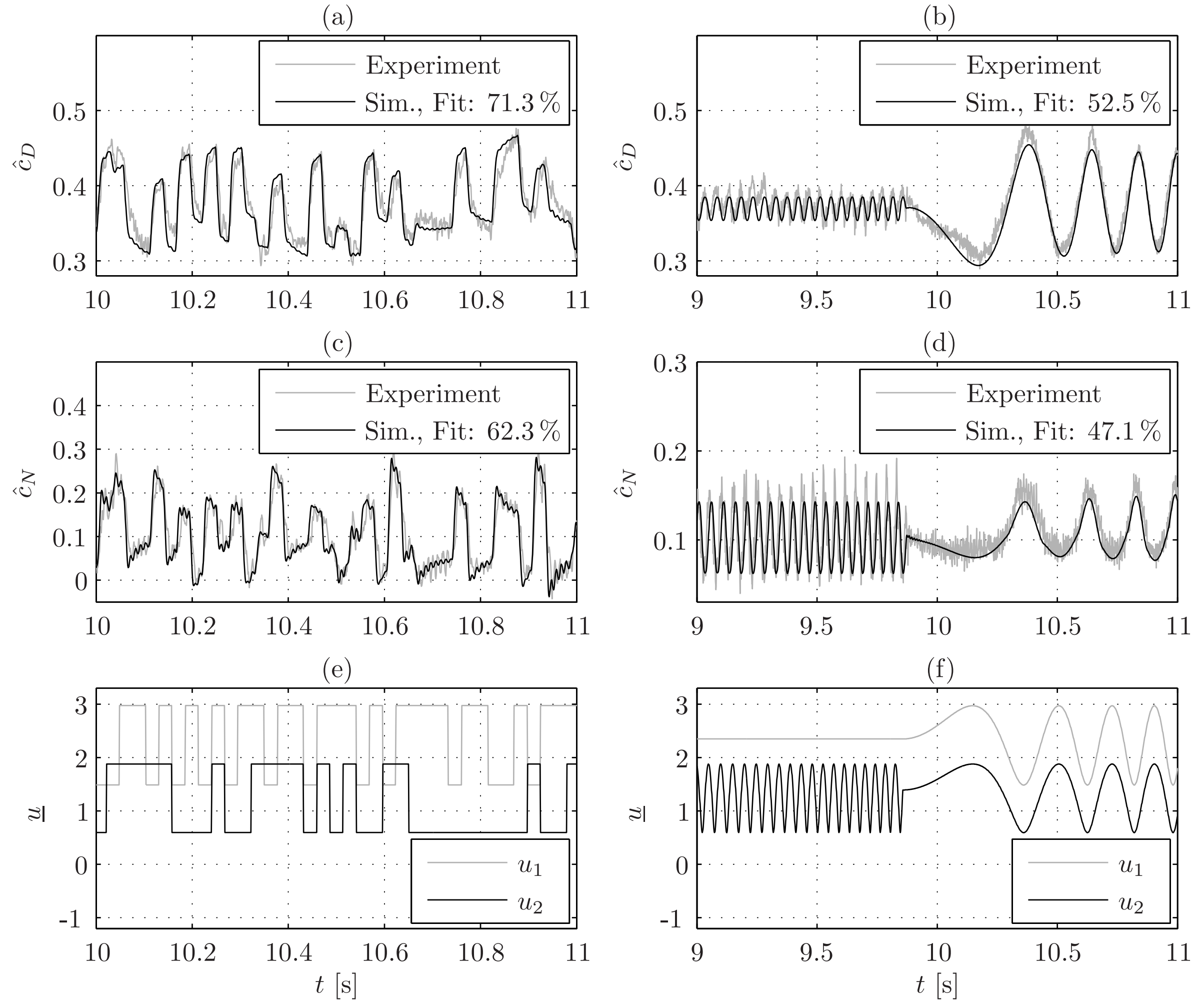

Figure 3.21: Comparison of the measured and the simulated outputs of one of the models identified for the overall plant dynamics at $Re_w = 50000$ and $\beta_w = 5°$. The left column corresponds to the data from the identification experiment itself, whereas the right column shows a cross-validation experiment at the same Reynolds number and cross-wind angle.

experiment as well as for a cross-validation experiment, see left and right columns of Fig. 3.21, respectively.

As a basis for the robust control design, these nonlinear models for the overall plant dynamics are pre-compensated with the inverse $\underline{f}^{-1}(\underline{\tilde{u}})$ of the nonlinear static input map. This yields a set of linear plant models with inputs $\underline{\tilde{u}}$ and outputs $\underline{y}$ that can be approximated by a nominal model $\boldsymbol{G}_n$ and an uncertainty description as shown in Fig. 3.15 (c). Here, one of the identified plant models that yields a small uncertainty is chosen as the nominal model. It corresponds to the plant characteristics at $Re_w = 50000$ at a cross-wind angle $\beta_w = 0$. Hence, its operating point lies in the middle of the range covered by the identification experiments, which helps ensure a "symmetric" performance of the controller for negative and positive cross-wind angles.

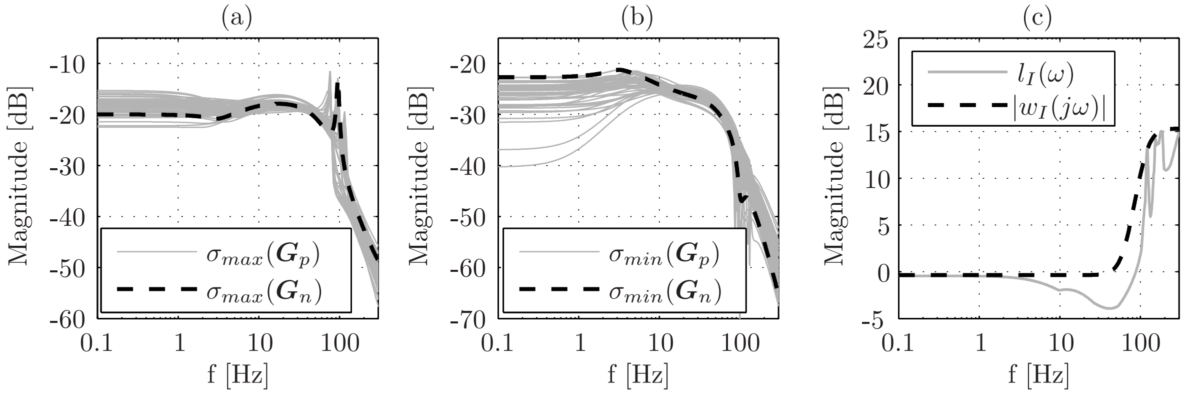

Figure 3.22: Maximal (a) and minimal (b) singular values of the set of models $\boldsymbol{G}_p$ and of the nominal model $\boldsymbol{G}_n$; multiplicative input uncertainty $l_I(\omega)$ with the amplitude response of its upper bound $w_I(j\omega)$ (c).

The maximal and minimal singular values, which describe the largest and smallest gain of the plant at a given frequency, are shown in Fig. 3.22 (a) and (b) for the complete set of identified models and for the nominal plant. A model family Π_I can then be defined by

$$\Pi_I : \boldsymbol{G}_p = \boldsymbol{G}_n(\boldsymbol{I} + \boldsymbol{E}_I), \quad \boldsymbol{E}_I = w_I \boldsymbol{\Delta}_I, \quad \|\boldsymbol{\Delta}_I\|_\infty \leq 1, \tag{3.15}$$

where $\boldsymbol{G}_p$ denotes the uncertain plant model. As discussed by Skogestad and Postlethwaite [121], uncertainties of multivariable plants with strong directional behavior resulting in large condition numbers $\gamma(\boldsymbol{G}) = \sigma_{max}(\boldsymbol{G})/\sigma_{min}(\boldsymbol{G})$ can be better approximated by a multiplicative uncertainty at the plant input instead of the output. As this is the case for the 2D bluff body, an input uncertainty $\boldsymbol{E}_I$ is used here, with a normalized uncertainty $\boldsymbol{\Delta}_I$ and a scalar weight w_I. It places an upper bound on the unstructured multiplicative input uncertainty

$$l_I(\omega) = \max_{\boldsymbol{G}_p \in \Pi_I} \overline{\sigma}\left(\boldsymbol{G}_n^{-1}\left(\boldsymbol{G}_p - \boldsymbol{G}_n\right)\right), \quad |w_I(j\omega)| \geq l_I(\omega), \forall\omega, \tag{3.16}$$

which represents the maximal deviation from the nominal plant $\boldsymbol{G}_n$ for each angular frequency ω. For more information on this standard approach, see e.g. Skogestad and Postlethwaite [121]. Here, the scalar weight for the input uncertainty is chosen as a 3rd order transfer function

$$w_I(s) = 0.96 \frac{\frac{1}{\omega_{I,1}^3}s^3 + \frac{2}{\omega_{I,1}^2}s^2 + \frac{2}{\omega_{I,1}}s + 1}{\frac{1}{\omega_{I,2}^3}s^3 + \frac{2}{\omega_{I,2}^2}s^2 + \frac{2}{\omega_{I,2}}s + 1}, \tag{3.17}$$

with $\omega_{I,1} = 40 \cdot 2\pi \frac{\text{rad}}{\text{s}}$ and $\omega_{I,2} = 73 \cdot 2\pi \frac{\text{rad}}{\text{s}}$. Its magnitude response is shown in Fig. 3.22 (c) together with the multiplicative input uncertainty $l_I(\omega)$. As discussed in the next section, the design of the robust controller is carried out such that robust stability is guaranteed for the uncertain plant model of the 2D bluff body.

3.5 Control design

The multivariable feedback controller for the 2D bluff body is designed via the standard mixed-sensitivity H_∞ approach as described by Skogestad and Postlethwaite [121]. Figure 3.23 (a) shows the controller architecture with the uncertain plant $\boldsymbol{G}_p$ identified in the previous section for the actuated flow and actuator dynamics of the 2D bluff body. In the nominal case the

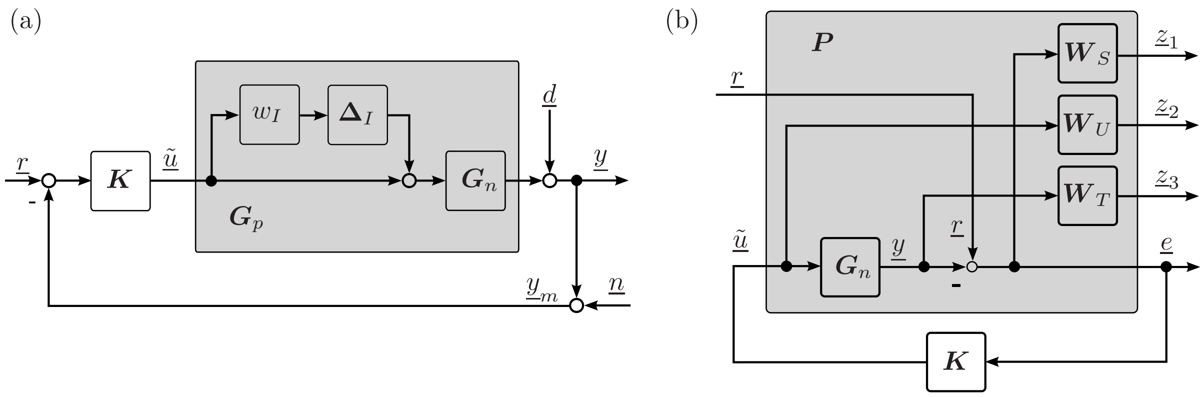

Figure 3.23: Controller architecture with the uncertain plant $\boldsymbol{G}_p$ (a) and generalized plant (b) with weights $\boldsymbol{W}_S$, $\boldsymbol{W}_U$ and $\boldsymbol{W}_T$ for the mixed sensitivity H_∞ control design.

output of the controlled plant is given by

$$\underline{y} = \boldsymbol{T}\underline{r} + \boldsymbol{S}\underline{d} - \boldsymbol{T}\underline{n}, \tag{3.18}$$

with the complementary sensitivity

$$\boldsymbol{T} = (\boldsymbol{I} + \boldsymbol{G}_n\boldsymbol{K})^{-1}\,\boldsymbol{G}_n\boldsymbol{K}, \tag{3.19}$$

representing the closed-loop transfer function from the reference variables $\underline{r}$ and from measurement noise $\underline{n}$ to the outputs. The performance at suppressing disturbances $\underline{d}$ acting on the output of the controlled plant is described by the sensitivity function

$$\boldsymbol{S} = (\boldsymbol{I} + \boldsymbol{G}_n\boldsymbol{K})^{-1}, \tag{3.20}$$

and the necessary control effort is characterized by the product $\boldsymbol{KS}$. Requirements for these closed-loop transfer functions can be specified by augmenting the nominal plant $\boldsymbol{G}_\text{n}$ with frequency-dependent weights $\boldsymbol{W}_S$, $\boldsymbol{W}_U$ and $\boldsymbol{W}_T$ to obtain the generalized plant P as shown in Fig. 3.23 (b). Here, the weight for sensitivity is chosen as a diagonal matrix of transfer functions

$$\boldsymbol{W}_S(s) = \begin{bmatrix} 1 & 0 \\ 0 & 1 \end{bmatrix} w_S(s), \text{ with } w_S(s) = \frac{\frac{1}{M_S}s + \omega_S}{s + A_S\omega_S}, \tag{3.21}$$

with $M_S = 2$, $A_S = 1 \cdot 10^{-3}$ to suppress disturbances up to a desired bandwidth $\omega_S = 6 \cdot 2\pi\frac{\text{rad}}{\text{s}}$. The allowed control effort is limited by the weight

$$\boldsymbol{W}_U(s) = \begin{bmatrix} 1 & 0 \\ 0 & 1 \end{bmatrix} w_u(s), \text{ with } w_u(s) = 0.05\frac{s + \omega_u}{A_u s + \omega_u}, \tag{3.22}$$

with $A_u = 1 \cdot 10^{-3}$ and $\omega_u = 50 \cdot 2\pi\frac{\text{rad}}{\text{s}}$ to avoid control input at high frequencies beyond the actuator bandwidth. For the complementary sensitivity a weighting function

$$\boldsymbol{W}_T(s) = \begin{bmatrix} 1 & 0 \\ 0 & 1 \end{bmatrix} w_T(s), \text{ with } w_T(s) = \left(\frac{s + \frac{\omega_T}{M_T^{1/n}}}{A_T^{1/n}s + \omega_T}\right)^n, \tag{3.23}$$

is selected with $M_T = 1$, $A_T = 1 \cdot 10^{-3}$ and $\omega_T = 45 \cdot 2\pi \frac{\text{rad}}{\text{s}}$. Here, a high order $n = 10$ is necessary to ensure a step roll-off of T at high frequencies so that robust stability can be achieved. This will be discussed below.
All weighting functions are converted to discrete-time transfer functions so that the controller can be synthesized in discrete time. This facilitates the handling of the time delays at the inputs of the plant model. The controller is obtained by minimizing

$$\min_{\boldsymbol{K}} \|\boldsymbol{N}(\boldsymbol{K})\|_\infty, \text{ with } \boldsymbol{N}(\boldsymbol{K}) = \begin{bmatrix} \boldsymbol{W}_S\boldsymbol{S} \\ \boldsymbol{W}_U\boldsymbol{K}\boldsymbol{S} \\ \boldsymbol{W}_T\boldsymbol{T} \end{bmatrix}, \tag{3.24}$$

with the control synthesis algorithm implemented in the `Matlab`-command "`mixsyn.m`" [84]. The frequency responses of the resulting closed-loop transfer functions are shown in Fig. 3.24 (a-c) together with those of the chosen weights. Here, a nominal bandwidth of $\omega_{bw} \approx 7.4 \cdot 2\pi$ rad/s is obtained with respect to the suppression of disturbances acting on the controlled output $\underline{y} = \begin{bmatrix} \hat{c}_D & \hat{c}_N \end{bmatrix}^T$. The time delay of 6 ms at the input of the actuators causes a Waterbed-effect, which results in a small amplification of disturbances in the frequency range $10\,\text{Hz} < f < 70\,\text{Hz}$. This and the uncertainty arising from the nonlinear, parameter-dependent dynamics of the actuated flow limit the achievable closed-loop performance. However, the controller guarantees robust stability for the entire set of identified models. The necessary criterion

$$\|w_I \boldsymbol{T}_I\|_\infty < 1, \text{ with } \boldsymbol{T}_I = \boldsymbol{K}\left(\boldsymbol{I} + \boldsymbol{G}_n\boldsymbol{K}\right)^{-1}\boldsymbol{G}_n \tag{3.25}$$

for scalar weights and multiplicative input uncertainty [121] is fulfilled for the controlled plant, as can be seen in Fig. 3.24 (d).

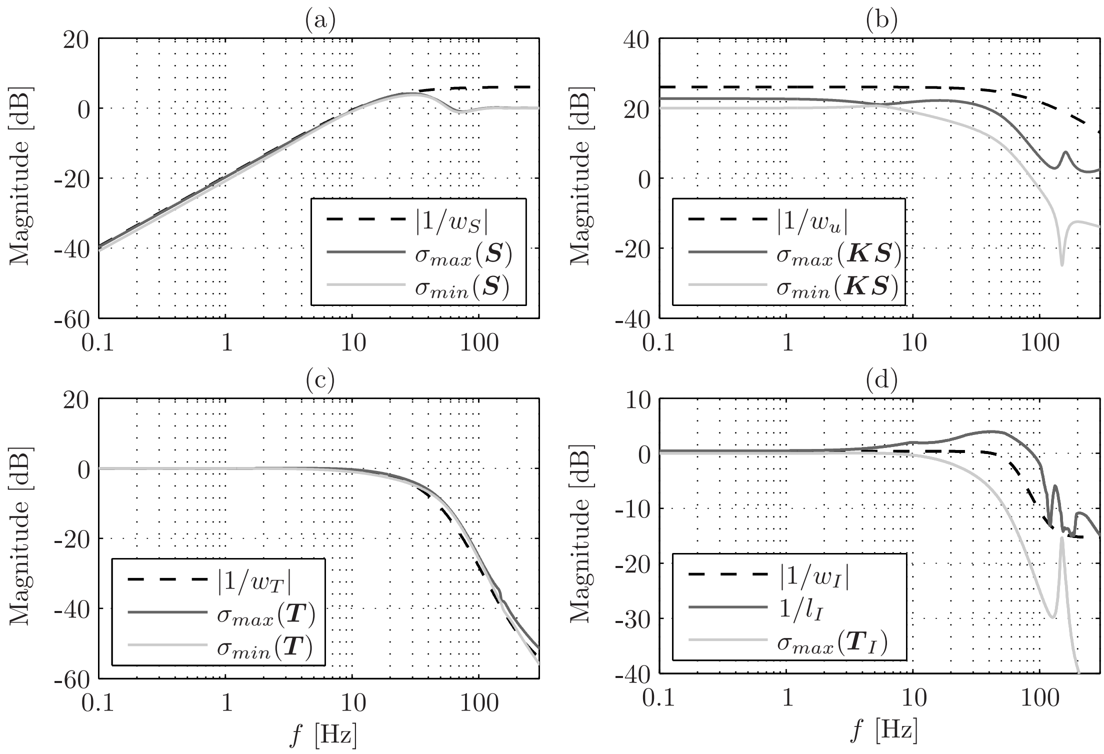

Figure 3.24: Maximal and minimal singular values of the sensitivity $\boldsymbol{S}$ (a), the control effort $\boldsymbol{KS}$ (b) and the complementary sensitivity $\boldsymbol{T}$ (c), as well as the frequency response of the corresponding weight used in the mixed-sensitivity H_∞ control design. The criterion for robust stability for unstructured multiplicative input uncertainty is shown in plot (d).

Reference variable calculation and controller implementation

The robust H_∞ controller is implemented on a digital signal processor for real-time testing in wind tunnel experiments. Figure 3.25 shows the implemented controller architecture. In order

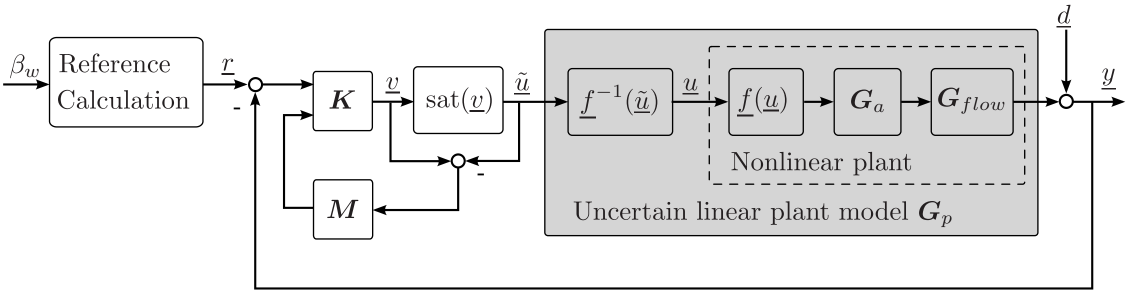

Figure 3.25: Implemented architecture of the robust H_∞ controller for the 2D bluff body.

to account for actuator saturation due to limited supply pressure, the controller is augmented by a dynamic anti-reset windup compensator $\boldsymbol{M}$ according to the method proposed by Park and Choi [98]. The calculated control input $\tilde{\underline{u}}$ is converted via the inverted map $f^{-1}(\tilde{\underline{u}})$ to the desired nondimensional blowing ratios $\underline{u} = \begin{bmatrix} \mathrm{u}^*_{a,1,des} & \mathrm{u}^*_{a,2,des} \end{bmatrix}^T$, which are applied to the nonlinear plant model of the 2D bluff body indicated by the dashed box in Fig. 3.25. Based on a weighted sum of pressure coefficients, the surrogate output variables $\underline{y} = \begin{bmatrix} \hat{c}_D & \hat{c}_N \end{bmatrix}^T$ for drag and yaw-moment coefficients are measured, fed back and compared with their setpoints $\underline{r}$ to form the control error $\underline{e}$. Here, suitable values for the reference variables are calculated based on the current cross-wind angle β_w. Full suppression of disturbances acting on the yaw moment requires large control inputs, which would make an efficient drag reduction under cross-wind conditions impossible. Therefore, the setpoint r_2 is calculated via a low-pass filter $F(s)$ by

$$r_2 = \underbrace{\frac{k}{Ts+1}}_{F(s)} \beta_w, \text{ with } k = \frac{\partial \hat{c}_N}{\partial \beta_w} = 7.44 \cdot 10^{-2} \text{ and } T = 0.2\,\mathrm{s}. \tag{3.26}$$

Its gain k is chosen equal to the steady-state derivative of the natural yaw-moment coefficient with respect to the cross-wind angle β_w. A rather long time constant $T = 0.2\,\mathrm{s}$ is selected, such that the reference value r_2 is slowly increased to the value of the natural steady-state gust response, whereas fast variations are to be suppressed by the controller. This requires smaller control inputs under constant cross-wind conditions. Suitable reference values for the most efficient drag coefficient are calculated by means of a look-up table. It is derived from a series of steady-state measurements under various constant side-wind conditions in which the setpoint $r_1(\beta_w)$ yielding the largest net power savings is determined. As can be seen from Fig. 3.26 (a), a significant drag reduction can be achieved for the range of cross-wind angles investigated here.

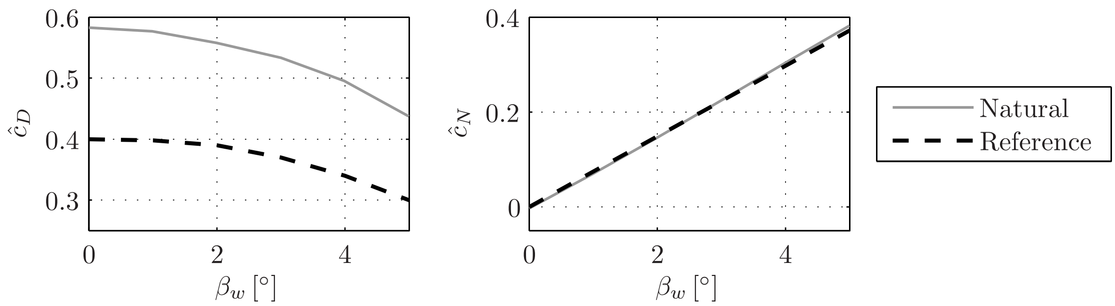

Figure 3.26: Look-up tables for the reference variables for $\hat{c}_D$ (a) and $\hat{c}_N$ (b), relative to the natural flow values for various cross-wind angles $0° \leq \beta_w \leq 5°$.

3.6 Experimental results for the controlled flow

The performance of the designed multivariable robust H_∞ controller is tested in wind tunnel experiments in which cross-wind gusts are simulated by turning the bluff body. The phase-averaged results for ten experiments carried out under equivalent conditions for natural and controlled flow are shown in Fig. 3.27. Here, the goal is to control the drag and yaw-moment

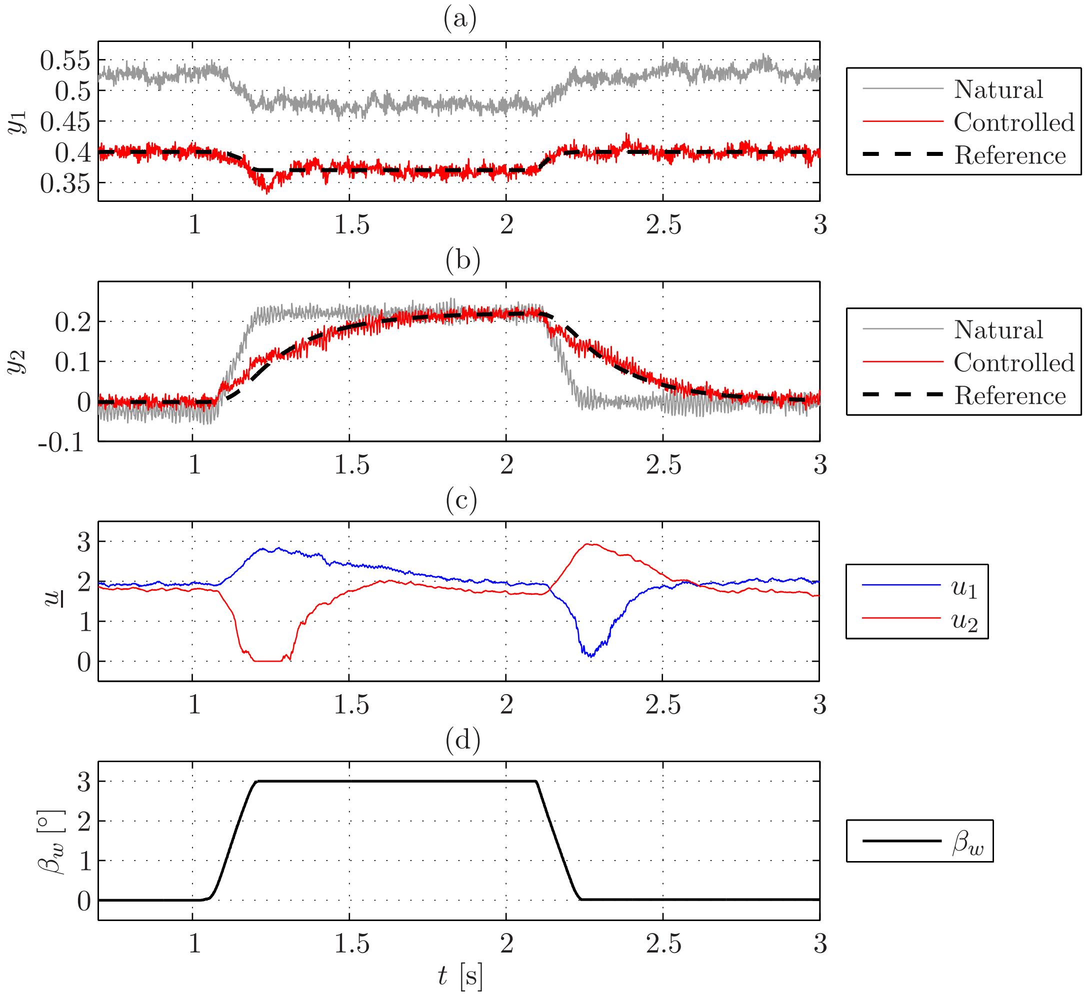

Figure 3.27: Phase-averaged results for ten experiments under equivalent conditions for the natural and the controlled flow at $Re_w = 5 \cdot 10^4$ for a simulated cross-wind gust with a maximum angle $\beta_w = 3°$.

coefficients y_1 and y_2 as closely as possible to their reference variables, both under straight-flow conditions as well as during the simulated gust. The controller shows very good performance in reference tracking and disturbance suppression. Only during fast variations of the cross-wind angle at the beginning and the end of the gust are small deviations visible, most notably for the controlled drag coefficient y_1 around $t = 1.2\,\mathrm{s}$, when the control input u_2 cannot be decreased below zero. Nevertheless, the controller ensures a significant drag reduction at all times and suppresses fast variations of the yaw-moment coefficient successfully. The closed-loop AFC strategy developed here thus represents a good starting point for the design of a similar controller that can handle the more complicated flow around the 3D bluff body. This is the subject of the next chapter.

Chapter 4

3D bluff body

4.1 Experimental setup

4.1.1 Cross-wind tunnel

The experiments are conducted in a special cross-wind tunnel whose concept is partially adapted from the setup used by Dominy and Ryan [33]. Fig. 4.1 shows a schematic view of the test bench used at TU Berlin. It consists of a standard axial blowing wind tunnel and an additional cross-wind tunnel with a lower and an upper outlet equipped with a shutter system. Before creating a gust, the shutters in the upper section are open to prevent the cross-wind tunnel fan from stalling. In order to create a side-wind gust within the test section, the shutters at the lower outlet are opened consecutively by means of pneumatic cylinders driven by solenoid valves. A microprocessor is used to trigger each shutter with a time delay matching the axial velocity component of the wind tunnel jet in order to simulate a car driving into a region of cross-wind. The nozzle exit of the axial wind tunnel has a dimension of 700 mm × 500 mm, whereas the

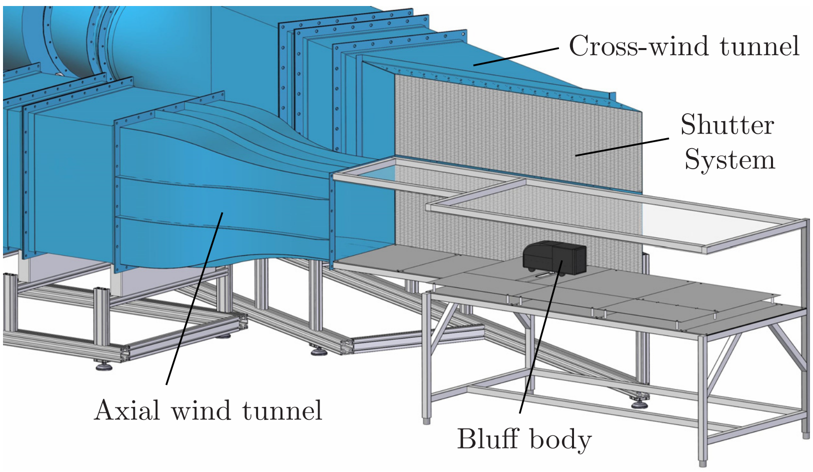

Figure 4.1: Cross-wind facility at TU Berlin

lower and upper outlets of the cross-wind tunnel extend over a length of 1900 mm. A splitter plate 50 mm above the test-section floor is used to reduce the wind tunnel boundary layer as a simple way to approximately simulate on-road boundary layer conditions. Furthermore, the test section is equipped with a roof plate to separate the two cross-wind tunnel outlets. The vehicle is installed at the intersection of the axes of the main and the cross-wind tunnel at a distance of 0.64 times the vehicle length behind the beginning of the raised floor. A 5-hole probe (*Aeroprobe, PC5-TIP-2-5-C240-152-025*, absolute accuracy better than 0.4°) located at the test section ceiling above the front of the model monitors the cross-wind angle β_w, as well as the static and dynamic pressures p_s and q.

4.1.2 Bluff body

The 3D bluff body examined here is depicted in Fig. 4.2. Its geometry and actuation concept are partially adapted from Englar [34, 35], but the vehicle length was reduced to represent a generic model of a small truck or delivery van. The dimensions of the model are $L = 406.5\,\text{mm}$, $W = 115\,\text{mm}$ and $H = 160\,\text{mm}$, with a wheelbase $L_{wb} = 260\,\text{mm}$ and a wheel diameter $d_w = 44\,\text{mm}$. Here, the Reynolds number $Re_L = \text{u}_\infty L/\nu$ is defined for the vehicle length L and kinematic viscosity ν. The wind tunnel experiments are carried out in a range $3 \cdot 10^5 \leq Re_L \leq 6 \cdot 10^5$, which corresponds to a free-stream velocity $11.4\,\text{m/s} \leq \text{u}_\infty \leq 22.8\,\text{m/s}$. Trip tapes ensure

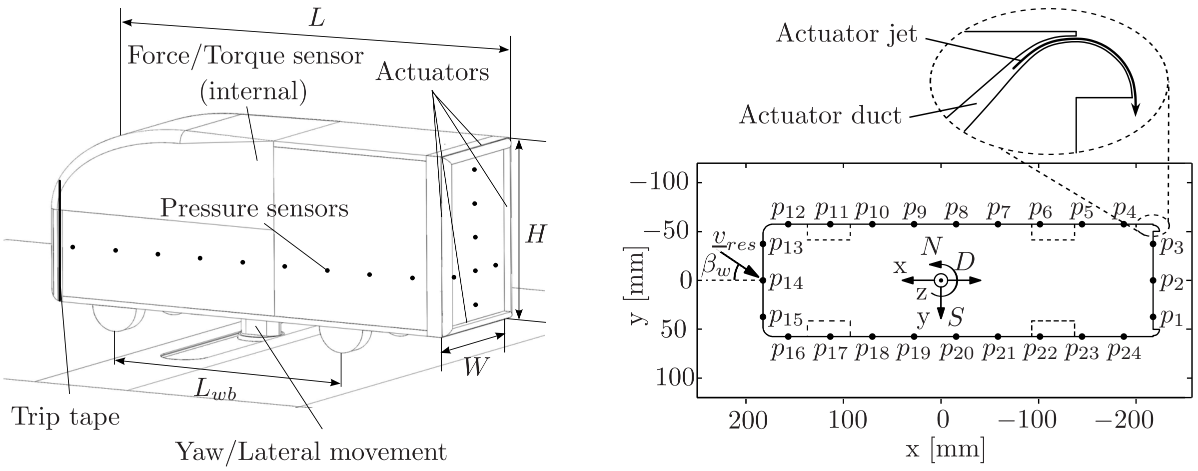

Figure 4.2: Schematic view of the bluff body (left) with a cross-section (right) depicting the coordinate system, the location of the pressure sensors, as well as a close-up view of the Coanda actuator geometry.

a transition from laminar to turbulent boundary layer at a fixed location 10 mm behind the front of the model. The coordinate system is defined with respect to the body frame and is located at the center between front and rear axles. The pressure distribution around the bluff body is monitored by 24 sensors (*Sensortechnics, HCLA02X5B,* measurement uncertainty due to hysteresis and nonlinearity less than 0.25% of full scale span) located at a cross-section 72 mm above the floor. The pressure coefficient at each location j is calculated by

$$c_{p_j} = \frac{p_j - \overline{p}_s}{\overline{q}}, \tag{4.1}$$

where $\overline{p}_s$ and $\overline{q}$ denote the mean static and dynamic pressures under nominal, straight-flow conditions as measured by the 5-hole probe. The base pressure coefficient $c_{p,b}$ is calculated from a spatial average over the readings of 7 sensors located on the base of the bluff body, as shown in Fig. 4.2. Forces and moments acting on the bluff body are measured using a 6-component-balance (*ATI, FTD-Gamma SI-32-2.5*, absolute measurement accuracy better than 1% of full scale span), which is installed inside the model. The aerodynamic drag D always faces opposite to the driving direction x, whereas the side force S is defined in the positive y-direction and the yaw moment N is measured around the upward pointing z-axis. The corresponding non-dimensional coefficients are defined by

$$c_D = \frac{D}{\overline{q} A_B}, \quad c_S = \frac{S}{\overline{q} A_B}, \quad c_N = \frac{N}{\overline{q} A_B L_{wb}}, \tag{4.2}$$

respectively, where A_B denotes the cross-sectional surface of the bluff body.

Pneumatic AFC actuators are installed along all four rear edges of the vehicle. A close-up view of their geometry is shown in Fig. 4.2. The blown air is accelerated via an actuator duct with a slot width of $w_s = 0.3\,\text{mm}$ at the exit. The actuator jet stays attached to a rounded surface with a radius of 6 mm by means of the Coanda effect. This deviates the blown air towards the base of the bluff body. The supply pressures of the actuators are controlled by three fast Piezo pressure regulators (*Hoerbiger, tecno basic PRE-U*). To this end, the right and left actuator supply pressures $p_{a,r}$ and $p_{a,l}$ are regulated separately, whereas the upper and lower actuators are supplied with the same pressure $p_{a,ul}$. Pulsed blowing can be performed with the help of fast solenoid switching valves (*Festo, MHE4*). Under steady-state conditions the mean jet velocities u_r, u_l and u_{ul} at the actuator slot exits can be computed from the flow rate measured by flow meters (*Festo, SFAB-200U*, accuracy ±3% of mean value + 0.3% of full span). The actuation amplitude at each actuator i is characterized by the nondimensional momentum coefficient

$$c_{\mu,i} = \frac{A_{a,i}\mathrm{u}_{a,i}^2}{A_B \mathrm{u}_\infty^2}. \tag{4.3}$$

Here, $A_{a,i}$ and $\mathrm{u}_{a,i}$ represent the cross-sectional slot exit surface and the effective jet velocity at the corresponding actuator i, respectively. To enable a time-resolved assessment of the jet velocities, each actuator is equipped with a piezo pressure transducer inside the actuator duct (*Sensortechnics, HCLA12X5B*, measurement uncertainty due to hysteresis and nonlinearity less then 0.25% of full scale span). Correlating the pressure readings with the steady-state flow rate measurements for various supply pressures yields a look-up table for the jet velocity of each actuator. This allows for estimating the actuator dynamics separately from the flow dynamics in the model identification, as described in section 4.4. A digital signal processor (*dSpace, DS 1005 PPC*) running at a sampling frequency of 1 kHz is used for data acquisition and control of the actuators.

4.1.3 Dynamic model support system for lateral dynamics replication

Apart from the possibility of creating realistic cross-wind gusts, the experimental setup also features a novel model suspension enabling the real-time investigation of additional unsteady aerodynamic effects due to lateral vehicle dynamics. To this end, the model can be traversed and rotated dynamically by a pair of electromagnetic linear servo motors (*Linmot, PS01-37x120/180x260*). The slot in the raised wind tunnel floor, see Fig. 4.2, is covered by a telescopic sliding mechanism to minimize interference with the underbody flow. Furthermore, the bluff body is supported by a slender hollow beam through which the actuator pressure supply tubes and the sensor cables enter the model. When yawing or traversing the model dynamically in the running wind tunnel, the forces and moments measured by the 6-component balance include the model's inertia. In order to separate inertial effects from the external transient aerodynamic forces and moments, two 3-axis accelerometers (*Pololu, MMA7361L*, nonlinearity less than ±1 % of full scale output, cross-axis sensitivity less than ±5 %) are installed inside the model at the front and rear axle locations. They monitor the model's angular and lateral acceleration in order to compensate the balance readings for the inertial forces and moments during dynamic movements. The model's mass and moment of inertia necessary for converting the accelerometer readings to inertial forces and moments are determined beforehand from identification experiments in which the model is moved laterally and rotated in the switched-off wind tunnel.

4.2 Natural flow characteristics

4.2.1 Steady-state flow characteristics

The vehicle model investigated here represents a typical 3D bluff body. At zero yaw the flow separates at the trailing edges and forms a large, three-dimensional wake. This leads to a low time-averaged base-pressure coefficient $\overline{c}_{p,b} \approx -0.12$ and a high time-averaged drag coefficient of about $\overline{c}_D \approx 0.43$ at $Re_L = 4 \cdot 10^5$. Exposing the bluff body to cross-wind increases the drag coefficient further, as can be seen from the steady-state maps in Fig. 4.3. Here, the focus lies on small to medium side-wind angles $0° < \overline{\beta}_w < 10°$, since this is the most common range found in on-road conditions at larger driving speeds [114, 113]. The asymmetric flow conditions lead to significant pressure changes around the front of vehicle, as can be seen from the steady-state maps for the pressure coefficients $\overline{c}_{p_{11}}$ and $\overline{c}_{p_{17}}$ for sensor locations at the front wind- and leeward side, respectively. By contrast, the pressure coefficients $\overline{c}_{p_4}$ and $\overline{c}_{p_{24}}$ at the rear luv and lee sides of the bluff body vary only very little. These changes in the pressure distribution result in an almost linear increase of side-force and yaw-moment coefficient with cross-wind angle.

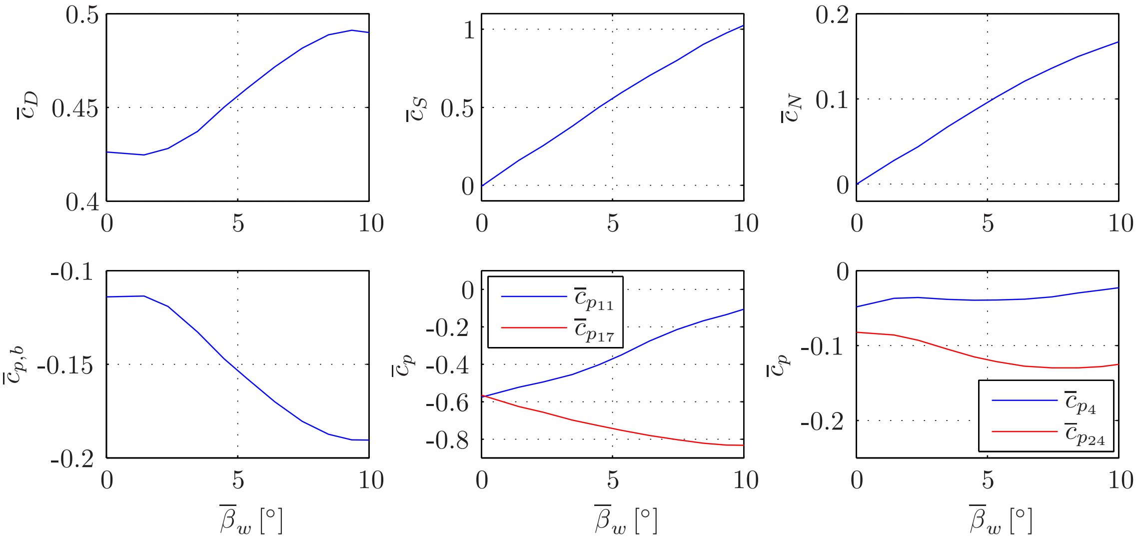

Figure 4.3: Steady-state maps for drag, side-force and yaw-moment coefficients, as well as selected pressure coefficients for natural flow at cross-wind angles $0° \leq \overline{\beta}_w \leq 10°$ and $Re_L = 4 \cdot 10^5$.

4.2.2 Transient cross-wind gust response

Fig. 4.4 shows the transient aerodynamic characteristics for a cross-wind gust with a maximum cross-wind angle $\beta_w \approx 11°$. The blue and green lines correspond to the measured variables in terms of force and moment coefficients (a, c, e), selected pressure coefficients (b, d, f), cross-wind angle (g) and total pressure fluctuation (h) as measured by the 5-hole probe. The red lines correspond to surrogate variables. These are explained further down.

The depicted time series are phase-averaged over 10 identical experiments. At $t^* = t\,\mathrm{u}_\infty/L = 0$ the gust reaches the front of the model, followed by an increase in normalized total pressure fluctuation $p_t'/\overline{p}_t$, see Fig. 4.4 (h). Here, the time-varying total pressure

$$p_t(t) = \overline{p}_t + p_t'(t) \tag{4.4}$$

is decomposed into an unsteady component $p_t'(t)$ and a steady mean component $\overline{p}_t$, which corresponds to nominal, straight-flow conditions. The unsteady total pressure reaches a maximum at a convective time $t^* \approx 3$, when the cross-wind angle β_w starts to increase. The drag coefficient

c_D, see Fig. 4.4 (a), is superimposed by fluctuations caused by mechanical oscillations due to the limited stiffness of the force/torque balance. However, its transient evolution correlates very well with the base-pressure coefficient as can be seen in Fig. 4.4 (b), indicating that the change in drag is mostly caused by a modification of the wake during the gust. After the beginning of the gust, the base-pressure coefficient $c_{p,b}$ starts to decrease with a delay of about 1 convective time unit after the increase in unsteady total pressure. This is probably due to the longitudinal pressure gradient caused by the change in flow speed during the gust, which elongates the wake in the longitudinal direction and causes the base pressure to drop. This results in a first peak

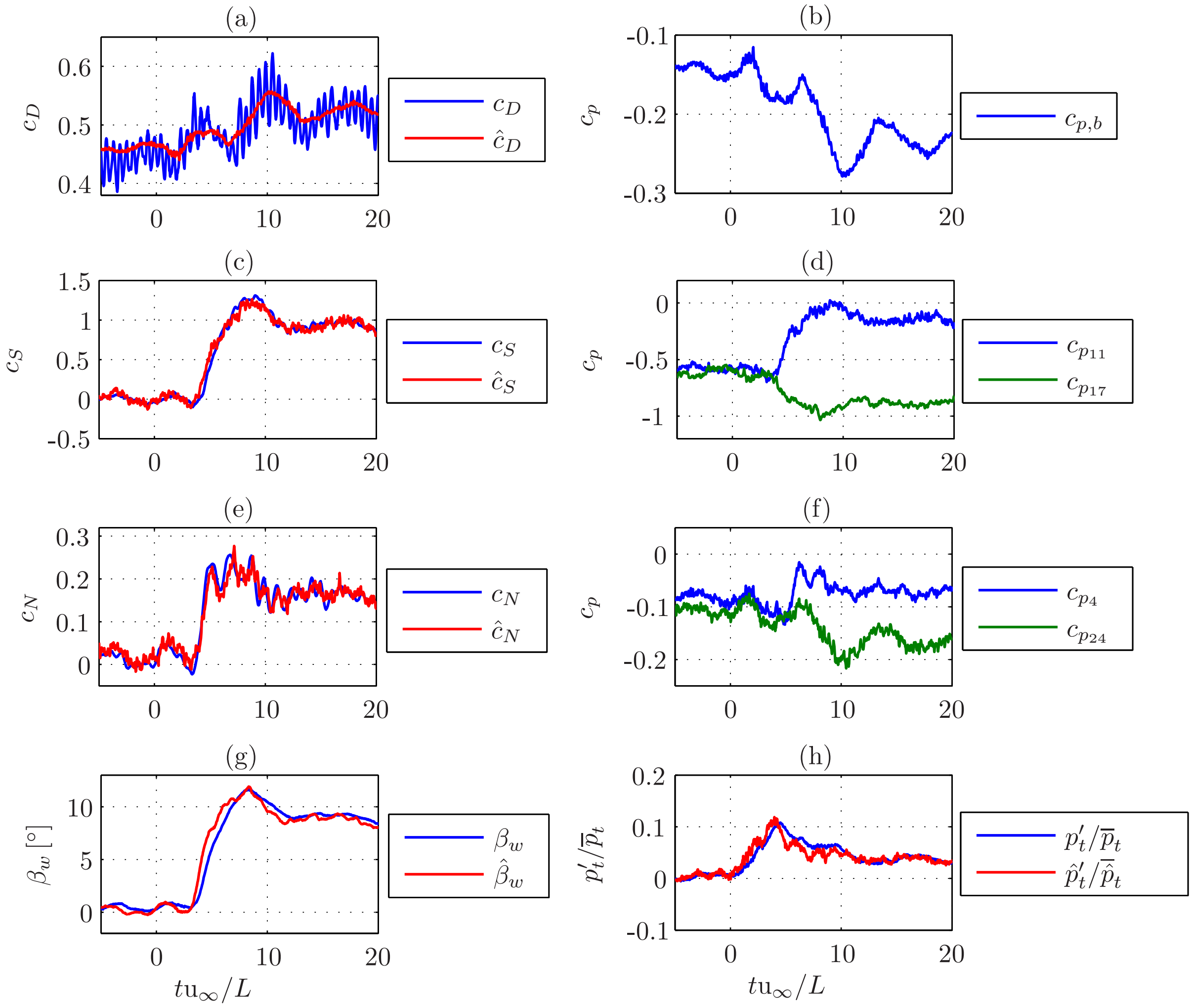

Figure 4.4: Phase-averaged time series of transient force and moment coefficients (left column) and of selected pressure coefficients (right column) for a gust with a maximum cross-wind angle $\beta_w \approx 11°$ at $Re_L = 4 \cdot 10^5$. Measurement variables are plotted in blue and green; surrogate variables calculated from surface-pressure measurement are depicted in red.

in the transient evolution of the drag coefficient, followed by an even larger increase in drag and decrease in base pressure in response to the increasing cross-wind angle β_w. All in all, the wake response is characterized by significant time delays and relatively slow dynamics.

By contrast, the side-force coefficient and even more so the yaw-moment coefficient react significantly faster to the gust compared with the drag coefficient. As already discussed for the steady-state cross-wind characteristics, the flow along the bluff body's sides is dominated by pressure changes in the frontal region. Here, the pressure coefficients $c_{p_{11}}$ and $c_{p_{17}}$ on the wind- and leeward side, respectively, change almost instantaneously with the cross-wind angle β_w. In comparison, the response of the pressure readings c_{p_4} and $c_{p_{24}}$ at the rear sides is significantly smaller and is delayed by approximately 1 convective time unit. This causes a small delay in

the build-up of the side-force coefficient during the gust and an overshoot of the yaw-moment coefficient relative to the cross-wind angle.
In an application of closed-loop active flow control to a real vehicle, the force and moment coefficients would not be available as on-road measurement variables. However, the steady-state and transient characteristics shown in Fig. 4.3 and 4.4 (b, d, f) indicate that the main effects can be estimated from surface-pressure measurements. To this end, the surrogate measurement variables $\hat{c}_D$, $\hat{c}_S$ and $\hat{c}_N$ are calculated from a weighted sum of the base-pressure coefficient $c_{p,b}$, the front wind- and leeward pressure coefficients $c_{p_{11}}$ and $c_{p_{17}}$ and the rear wind- and leeward pressure coefficients c_{p_4} and $c_{p_{24}}$, respectively. The corresponding parameters for the respective weights were determined by linear regression from a series of steady-state measurements for several Reynolds numbers, cross-wind angles and actuation amplitudes. Similar to the surrogate variables for force and moment coefficients, an estimate $\hat{\beta}$ for the cross-wind angle β is obtained based on the nondimensional pressure difference $c_{p_{13}} - c_{p_{15}}$ at the front of the vehicle model, whereas the total pressure estimate $\hat{p}_t$ is calculated from the sum of the dimensional pressure readings $p_{13} + p_{15}$. More details about the determination of the surrogate variables are given in the Appendix C.
As can be seen from Fig. 4.4 the surrogate variables (plotted in red) match the transient evolution of the measurement variables (plotted in blue) very well. Apart from the availability for online measurement in an on-road application, using surrogate input and output variables based on surface-pressure measurements avoids potential problems during model identification arising from different sensor dynamics. All pressure sensors inside the bluff body are connected to the pressure taps with a short piece of flexible tubing with an identical length of 2 cm, respectively. This ensures that all sensor readings possess the same frequency characteristics at a bandwidth as high as possible. As shown in Fig. 4.4 (g) and (h), changes in cross-wind angle $\hat{\beta}_w$ and normalized total pressure $\hat{p}_t'/\overline{p}_t$ are significantly faster detected from surface-pressure measurements (red lines) when compared with the values β_w and $p_t'/\overline{p}_t$ measured by the 5-hole probe (blue lines). Furthermore, the surrogate output variable $\hat{c}_D$ for the drag coefficient remains largely unaffected by mechanical oscillations relative to the balance readings c_D. Most importantly, filtering all input and output variables through the same sensor transfer function forms the basis for a reliable identification of models for transient aerodynamic phenomena. The related procedure is described in the following section.

4.2.3 Model identification for the transient aerodynamic cross-wind gust response

The cross-wind tunnel allows the effects of side-wind gusts on the vehicle model to be studied at different Reynolds numbers $3{\cdot}10^5 \leq Re_L \leq 6{\cdot}10^5$. Adjusting the speeds of the axial and the cross-wind fan such that similar gust amplitudes are achieved for each flow speed, and matching the time delay at which the shutters are opened with the current free-stream velocity creates a similar nondimensional evolution of cross-wind angle and total pressure fluctuation. Also, the resulting transient responses of the surrogate variables for drag, side-force and yaw-moment coefficients to these identical gusts at different flow speeds match very well when plotted against convective time, as seen in Fig. 4.5. Hence a model for the transient cross-wind aerodynamics should be in nondimensional form, too. The nondimensional state-space model introduced in section 2.2.2 yields a linear parameter-varying model when converted to dimensional time. This forms the basis for a novel model identification procedure for unsteady aerodynamic phenomena, which is described in section 2.2.3. Here, separate multiple-input single-output (MISO) LPV models are identified for the dynamics of drag, side-force and yaw-moment coefficients, respectively.

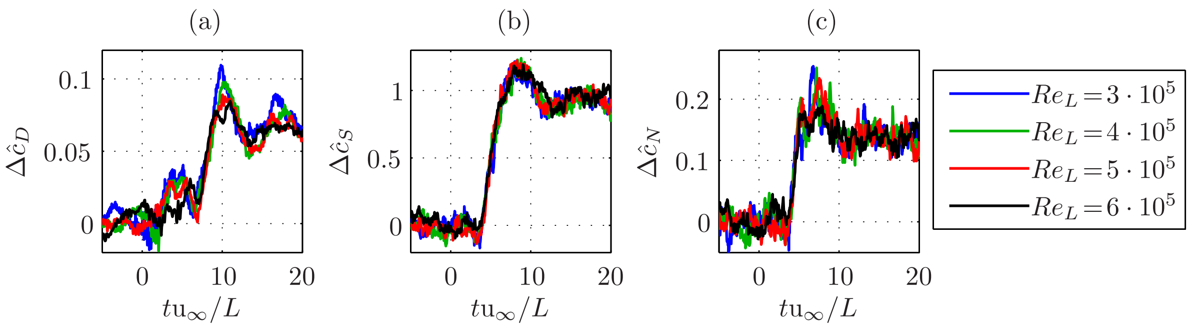

Figure 4.5: Dimensionless transient characteristics of estimated drag (a), side-force (b) and yaw-moment (c) coefficients for similar cross-wind gusts at several Reynolds numbers $3 \cdot 10^5 \leq Re_L \leq 6 \cdot 10^5$

Drag and wake dynamics

The surrogate variable $\hat{c}_D$ is exclusively calculated from the base-pressure coefficient $c_{p,b}$ as outlined in appendix C. The transient characteristics of the estimated drag coefficient $\hat{c}_D$ are thus equivalent to the dynamics of the wake response to cross-wind gusts.
As already discussed in the previous section 4.2.2, changes in cross-wind angle β_w as well as total pressure fluctuations p_t' have a significant influence on base pressure. The disturbance input variables are thus chosen as

$$\underline{d}^* = \left[\hat{\beta}_w \quad \hat{p}_t'/\overline{\hat{p}_t}\right]^T. \tag{4.5}$$

Following the steps outlined in section 2.2.3, the model identification procedure is initialized by estimating a linear, discrete-time model from an experimental data set at a single Reynolds number $Re_L = 3 \cdot 10^5$, corresponding to a free-stream velocity $u_\infty = 11.4\,{}^{\mathrm{m}}\!/\mathrm{s}$. Here, the cross-wind angle β_w was varied with a pseudo-random binary signal (PRBS) with a maximum frequency of 15 Hz. This means that a time-shifted version of the same PRBS sequence is applied consecutively to open and close each shutter. The opening time of each shutter determines the frequency of the cross-wind angle variation and thus the individual length of each gust, whereas the time delay between each shutter is adjusted according to the free-stream velocity of each experiment. This creates realistic cross-wind gusts that convect over the bluff body at free-stream velocity but vary in length scale.
A model order of $n_x = 2$ is sufficient to provide a good fit of the experimental data. Considering an input delay of $T_0^* \approx 1$ in convective time improves the fit significantly. This corresponds to the time it takes for a cross-wind disturbance to convect one vehicle length L downstream and affect the wake after it has been registered by the pressure sensors at the vehicle's front. Based on the LPV structure proposed in section 2.2.2 the LPV model for the dynamics of the drag coefficient is chosen as

$$\dot{\underline{x}}(t) = \underbrace{\frac{u_\infty(t)}{L}\boldsymbol{A}^*}_{\boldsymbol{A}(\theta)}\underline{x}(t) + \underbrace{\frac{u_\infty(t)}{L}\boldsymbol{E}^*}_{\boldsymbol{E}(\theta)}\underline{d}^*(t - \underbrace{T_0^* L/u_\infty(t)}_{T_0(1/\theta)}), \tag{4.6}$$

$$y^*(t) = \underbrace{\underline{c}^{*T}}_{\underline{c}^T}\underline{x}(t), \tag{4.7}$$

$$\theta(t) = u_\infty(t). \tag{4.8}$$

Its coefficients are initialized based on the identified linear model and then optimized over four data sets recorded at different Reynolds numbers $3 \cdot 10^5 \leq Re_L \leq 6 \cdot 10^5$, with the algorithm outlined in section 2.2.3. Here, the matrices $\boldsymbol{A}(\theta)$ and $\boldsymbol{E}(\theta)$ depend on the parameter $\theta = u_\infty$, whereas the dimensional time-delay T_0 depends on $(1/\theta)$. This dependency on the inverse of the parameter would increase of the complexity of the LPV control design and can be avoided

by approximating the nondimensional time-delay with an all-pass transfer function such as the Padé-approximation. This additional step is omitted, however, because the model for the gust response of the drag coefficient is not used for control design in this thesis. The feedforward LPV control design presented in section 4.6.4 takes into account only the models for side-force and yaw-moment coefficients.
Fig. 4.6 shows the simulated output of the identified LPV model in comparison with the output of the initial model and the response of the drag coefficient for cross-validation experiments with cross-wind gusts at two different Reynolds numbers. For $Re_L = 3 \cdot 10^5$, at which the linear model was identified, both models yield approximately the same fit of the measured surrogate drag coefficient. At the larger Reynolds number $Re_L = 6 \cdot 10^5$, however, the linear model's

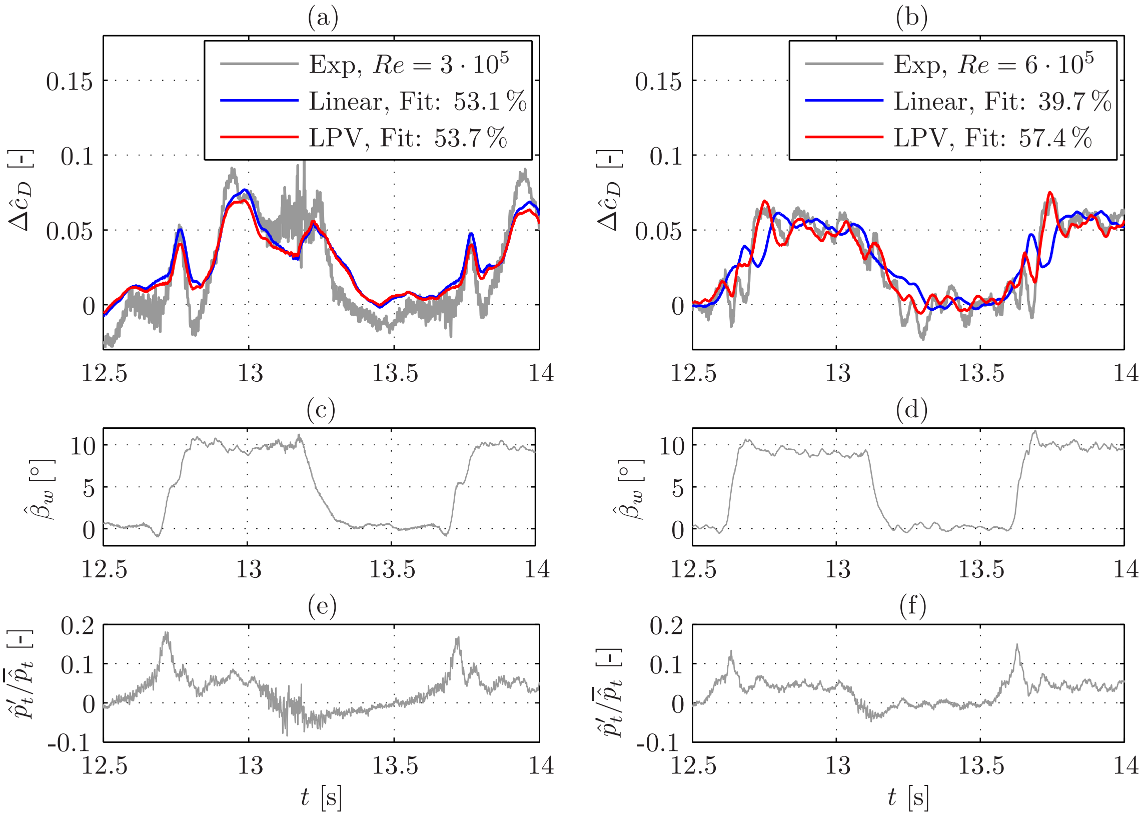

Figure 4.6: Simulated output of the identified linear and LPV models for the drag coefficient in comparison with the measured response for a cross-validation experiment with cross-wind gusts at $Re_L = 3 \cdot 10^5$ (left column) and $Re_L = 6 \cdot 10^5$ (right column).

dynamics are too slow to accurately capture the wake dynamics, whereas the LPV model is still able to provide a similar fit to that at the lower free-stream velocity.
The dimensional frequency and step responses of the LPV model to changes in cross-wind angle and normalized total pressure are plotted in Fig. 4.7. One can clearly see how the frequency response changes to faster dynamics as the Reynolds number increases. The response to excitation by changes in cross-wind angle corresponds to a low-pass behavior with a small overshoot of the drag coefficient, as shown by Fig. 4.7 (a) and (c). Changes in total pressure affect the drag coefficient mostly in a medium frequency range, see Fig. 4.7 (b) and (e), which results in a step response that settles almost back to zero.

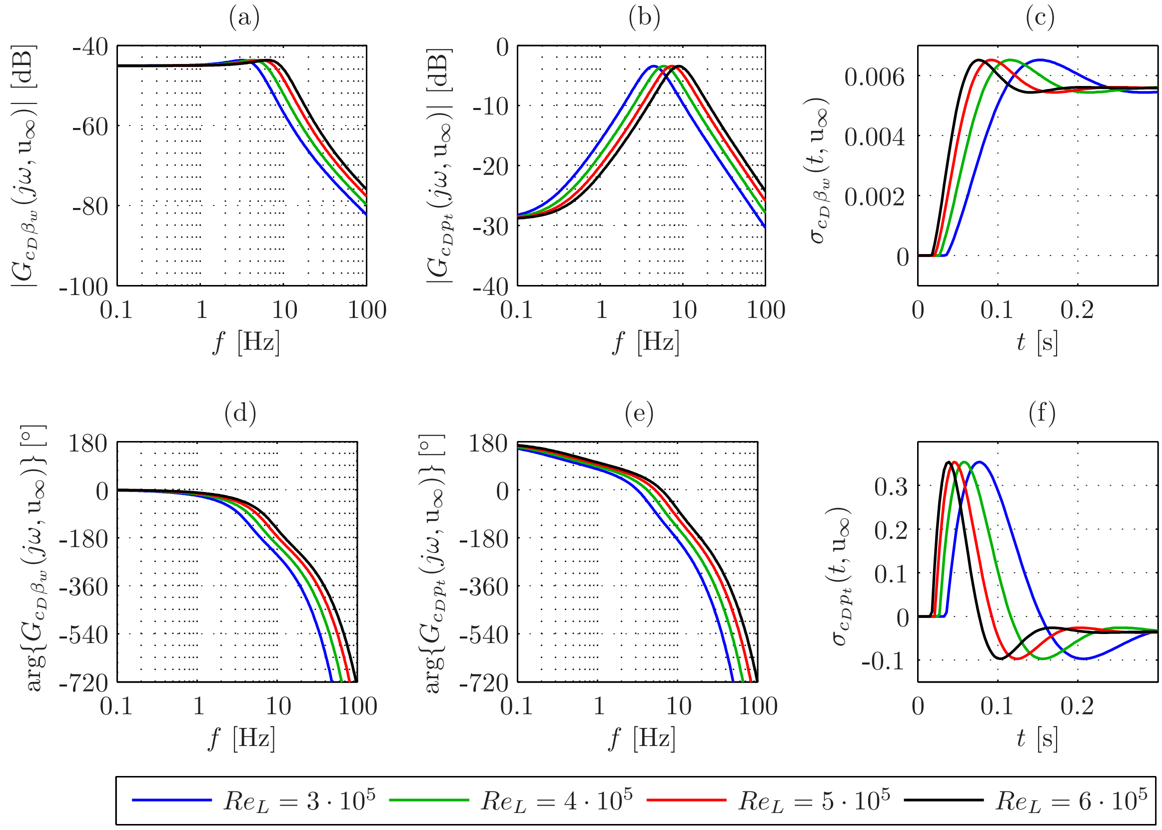

Figure 4.7: Dimensional frequency response of the LPV model for the drag coefficient to changes in cross-wind angle (a, d) and changes in normalized total pressure (b, e), evaluated at four different free-stream velocities corresponding to $3 \cdot 10^5 \leq Re_L \leq 6 \cdot 10^5$. Plots (c) and (d) show the step responses in dimensional time.

Side-force and yaw-moment dynamics

Like the model for the drag coefficient, separate MISO models are identified for the dynamics of side-force and yaw-moment coefficients. Again, a model order $n_x = 2$ is sufficient to capture the main characteristics, but no time delay is necessary, since the gust affects the sides of the bluff body almost immediately. Therefore, the structure of the LPV models is chosen as

$$\dot{\underline{x}}(t) = \underbrace{\frac{\mathrm{u}_\infty(t)}{L}\boldsymbol{A}^*}_{\boldsymbol{A}(\theta)}\,\underline{x}(t) + \underbrace{\frac{\mathrm{u}_\infty(t)}{L}\boldsymbol{E}^*}_{\boldsymbol{E}(\theta)}\,\underline{d}^*(t), \tag{4.9}$$

$$y^*(t) = \underbrace{\underline{c}^{*T}}_{\underline{c}^T}\,\underline{x}(t), \tag{4.10}$$

$$\theta(t) = \mathrm{u}_\infty(t), \tag{4.11}$$

respectively. Fig. 4.8 shows the simulated output of the initial linear models for the surrogate side-force coefficient $\hat{c}_S$ and for the yaw-moment coefficient $\hat{c}_N$ in comparison with the output of corresponding LPV models and the measured cross-wind gust response. As already observed for the wake response, the LPV models are able to provide a very good fit for the entire range of Reynolds numbers, whereas the linear models can only capture the dynamics well at a single operating condition, in this case $Re_L = 3 \cdot 10^5$.

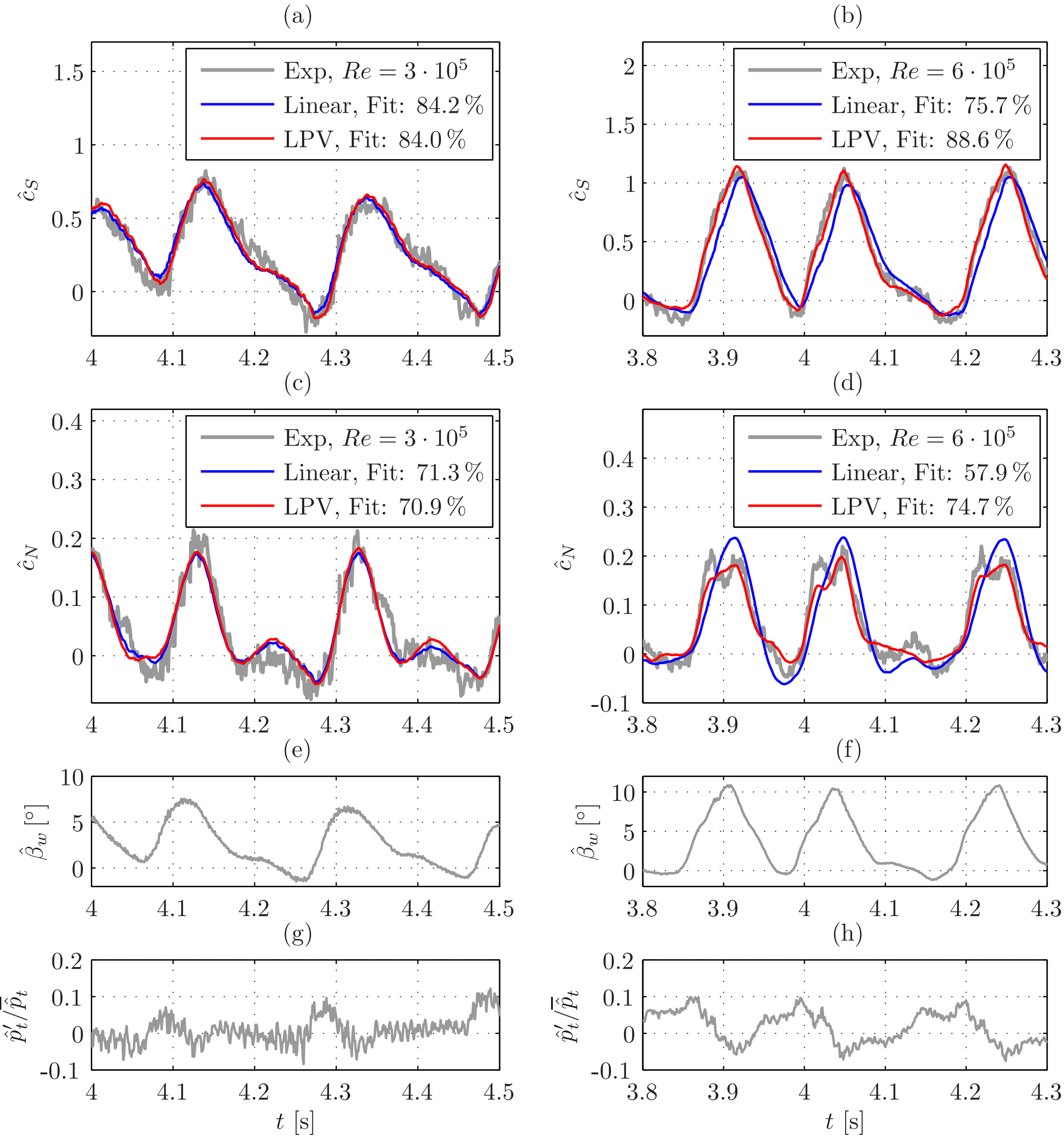

Figure 4.8: Simulated output of the identified linear and LPV models for the side-force and yaw-moment coefficients in comparison with the measured response for a cross-validation experiment with cross-wind gusts at $Re_L = 3 \cdot 10^5$ (left column) and $Re_L = 6 \cdot 10^5$ (right column).

Nondimensional frequency and step response of the identified LPV models

Since the coefficients of the LPV models are identified in nondimensional form, they allow a direct evaluation of the transient characteristics of the respective dimensionless state-space models

$$\frac{d\underline{x}^*}{dt^*} = \boldsymbol{A}^* \underline{x}^* + \boldsymbol{E}^* \underline{d}^*, \tag{4.12}$$

$$y^* = \underline{c}^{*T} \underline{x}^*, \tag{4.13}$$

which describe the dynamics of the gust response in convective time. Converting these state-space models to the frequency domain results in dimensionless transfer functions denoted by $G^*(j\omega^*)$ in the following, with the nondimensional radial frequency $\omega^* = 2\pi f^* = 2\pi f L/\mathrm{u}_\infty$. The corresponding nondimensional bode plots for the drag, side-force and yaw-moment coefficients are shown in Fig. 4.9. Here, the frequency response of the drag coefficient, see Fig. 4.9 (a),

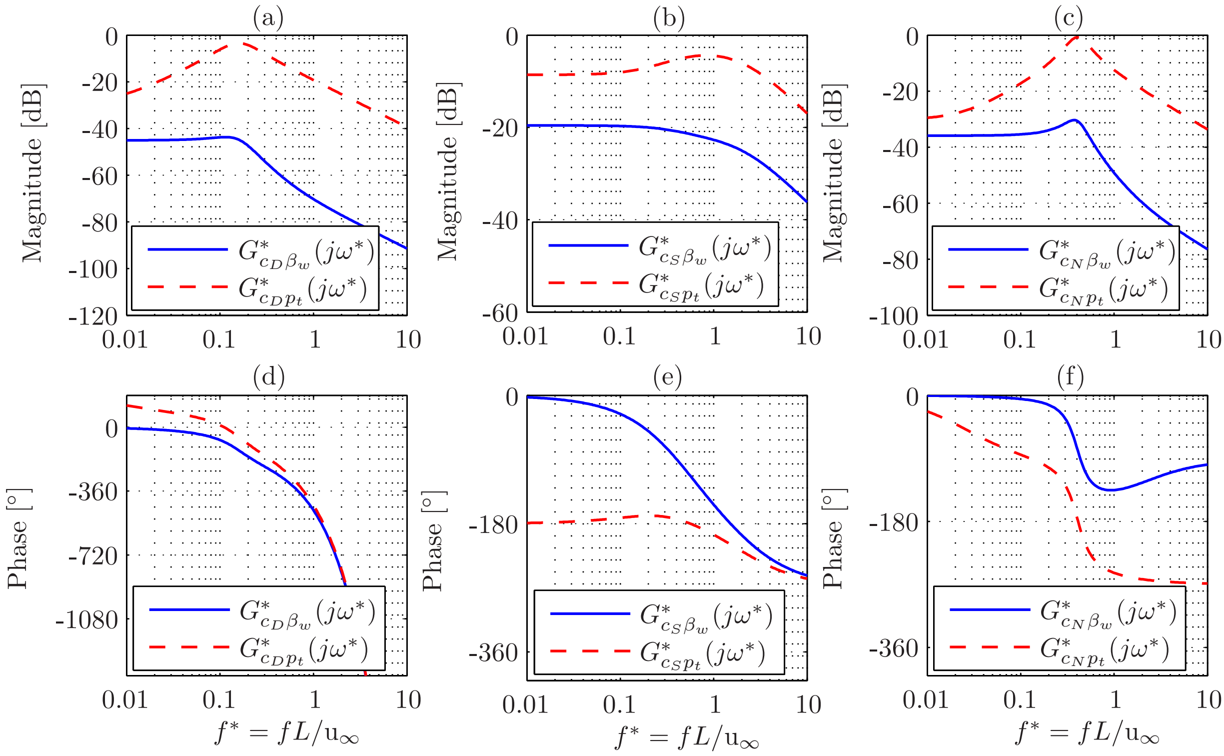

Figure 4.9: Nondimensional frequency response of drag, side-force and yaw-moment coefficients to changes in cross-wind angle β_w and to normalized total pressure fluctuations $p_t'/\overline{p}_t$.

shows a roll-off of the amplitude at rather slow frequencies $f^* \approx 0.2$. Its phase response, plotted in Fig. 4.9 (d), is dominated by the large convective time-delay $T_0^* = 1$.

By contrast, the amplitudes of side-force and yaw-moment coefficients shown in Fig. 4.9 (b) and (c), start to roll off only at significantly higher frequencies $f^* \approx 0.7$. Additionally, the frequency response of the yaw moment indicates a resonance peak for frequencies around $f^* \approx 0.4$.

In order to facilitate an easy comparison of the different time scales and transient characteristics of drag, side-force and yaw-moment coefficients, their nondimensional step responses $\sigma(t^*)$ to changes in cross-wind angle β_w are depicted in Fig. 4.10. The amplitude is normalized by the respective steady-state value y_s. The drag coefficient starts to increase after a convective time-delay $T_0^* = 1$ with rather slow dynamics. It overshoots by about 20% and settles to its steady-state value only very late, at $t^* \approx 7$.

By contrast, the side-force step response is characterized by a time constant in the order of $t^* \approx 1$, which equals the time it takes for the entire vehicle to enter the gust. The non-minimum phase behavior at the beginning of the simulated step response is probably due to an unmodeled time-delay. This may arise from the fact that the first pressure sensor used for the side-force

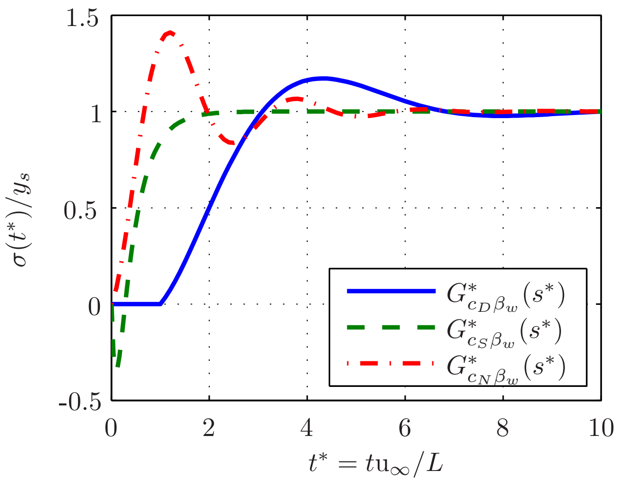

Figure 4.10: Normalized step response to cross-wind excitation of the identified nondimensional models for drag, side-force and yaw-moment coefficients.

calculation is located at a small distance downstream from the vehicle's front.
The yaw moment shows an even faster step response than the side force, with a significant overshoot by roughly 40%. This can easily be explained since pressure changes around the front, where the vehicle enters the gust first, increase the yaw moment, while the later pressure changes around the back of the vehicle decrease the yaw moment again when the gust has convected downstream.

4.3 Actuated flow characteristics

4.3.1 Symmetric actuation by continuous blowing

As already published in previous studies with the same bluff body [103, 102], the most efficient drag reduction at zero yaw is achieved with symmetric actuation with the same jet velocity at all four actuation slots for an overall momentum coefficient of $c_\mu \approx 0.02$. Due to the Coanda effect the blown air stays attached to the rounded surfaces at the actuator exit slots and deflects high-momentum free-stream fluid towards the base. This increases the base-pressure coefficient and therefore reduces drag, as can be seen from the steady-state maps in Fig. 4.11. The maps

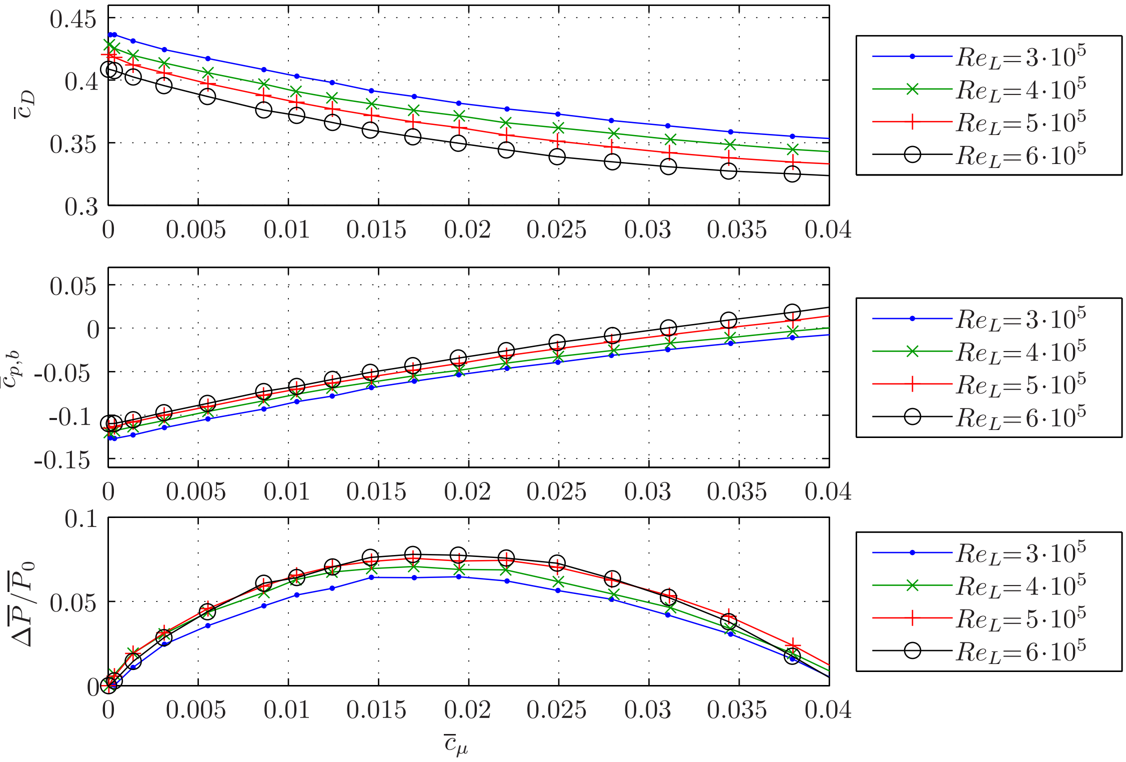

Figure 4.11: Steady-state maps of drag coefficient $\overline{c}_D$, base-pressure coefficient $\overline{c}_{p,b}$ and time-averaged, normalized power savings $\Delta\overline{P}/\overline{P}_0$ for symmetric blowing at $\overline{\beta}_w = 0°$ at several Reynolds numbers.

slightly depend on the Reynolds number, but the difference between actuated and natural flow is similar for all investigated flow speeds. Small to medium actuation amplitudes yield the most significant drag reduction. Increasing the momentum coefficient beyond 0.04 provides only small further savings, mostly due to the thrust of the actuation jets. Since this effect would also be present in an application to a real vehicle, the AFC efficiency is rated here by calculating the net power savings $\Delta P/P_0$, as suggested by Krentel et al. [73]. For the baseline case without actuation the power

$$P_0 = D_0 \mathrm{u}_\infty = \frac{\rho}{2} c_{D_0} A_B \mathrm{u}_\infty^3 \tag{4.14}$$

is necessary to overcome the aerodynamic drag D_0 at driving speed u_∞. Here, c_{D_0} denotes the drag coefficient for the natural flow. The power of each actuator jet i

$$P_{a,i} = \frac{1}{2}\dot{m}_{a,i}\mathrm{u}_{a,i}^2 = \frac{\rho}{2} A_{act,i}\mathrm{u}_{a,i}^3 \tag{4.15}$$

has to be subtracted from the power savings due to the drag reduction Δc_D achieved by AFC. This yields the overall normalized net power savings

$$\frac{\Delta P}{P_0} = \frac{\Delta c_D}{c_{D_0}} - \frac{P_{a,r}}{P_0} - \frac{P_{a,l}}{P_0} - \frac{P_{a,ul}}{P_0}, \tag{4.16}$$

with the baseline drag coefficient c_{D_0} and the powers $P_{a,r}$, $P_{a,l}$ and $P_{a,ul}$ of the right, left, upper and lower actuator jets, respectively. In the experiments in the cross-wind tunnel with an open test section the most efficient mean drag reduction is about $\Delta\overline{c}_D \approx 0.06$ or 15% under straight flow conditions, which corresponds to maximum normalized net power savings of about 8%, as is shown in the graph at the bottom of Fig. 4.11. Earlier experiments (not shown here) in an Eiffel-type wind tunnel with a closed test section indicate larger possible net power savings of up to 15% [103]. These differences suggest that a higher free-stream turbulence adversely influences the achievable drag reduction and AFC efficiency.

4.3.2 Symmetric actuation by pulsed blowing

Many authors report that unsteady actuation is more efficient than steady blowing in AFC applications due to the fact that this enables the amplification or suppression of natural instabilities in the flow. This is mostly the case for:

- Separated shear layers: Amplifying natural instabilities by pulsed or unsteady actuation, which increases mixing of the shear layer with high-momentum free-stream fluid. This can be used to reattach separated flows to airfoils at high angles of attack, see e.g. [49], or to the rear slant of vehicle models such as the Ahmed body, see e.g. [27, 73, 46]. However, this requires a suitable body shape with a surface that the flow can be reattached to. This is not case for 3D bluff bodies with a square back, unless a reattachment surface is added via extensions at the back such as boat tails or flaps [111].

- Two-dimensional bluff body wakes: Cylinders or 2D bluff bodies exhibit strong wake instabilities which form the well-known von Kármán vortex street. Open-loop pulsed actuation at certain frequencies or closed-loop control with phase-matched unsteady actuation is effective at suppressing these large-scale, alternating vortices and thus at synchronizing the wake [100].

In order to test if there exist actuation frequencies that are more beneficial than steady blowing for drag reduction of the 3D bluff body, a wide range of actuation amplitudes and frequencies was tested under straight flow conditions. Here, pulsed blowing is performed by solenoid valves with a maximum frequency of 200 Hz, see also section 4.1. Since the flow resistance of the valves changes with switching frequency, a look-up table for the effective blowing velocity for pulsed actuation was determined from hot-wire measurements at the exit of the actuator slots. This allows for adjusting the supply pressure such that a constant momentum coefficient is achieved for varying actuation frequencies.
Fig. 4.12 shows the results of a parameter study carried out for a variation of the actuation frequency, which is nondimensionalized here in terms of the actuation Strouhal number $St_{a,W}$ based on the vehicle's width W. The momentum coefficient was kept constant at $\overline{c}_\mu = 0.02$, which results in the most efficient drag reduction for steady blowing, as discussed in the previous section. The steady-state maps in Fig. 4.12 for the normalized drag coefficient $\overline{c}_D/\overline{c}_{D_0}$ show the same trend for the Reynolds numbers $3 \cdot 10^5 \leq Re_L \leq 5 \cdot 10^5$. Small to medium actuation frequencies $St_{a,W} < 0.25$ lead to a drag reduction of only about 5%, which is significantly smaller than the reduction of about 15% achieved by steady blowing. Pulsed actuation with $St_{a,W} \approx 0.38$ results in a drag increase indicating the excitation of wake instabilities in this frequency range. Increasing actuation frequency further decreases the drag coefficient significantly. For very high Strouhal numbers $St_{a,W} > 1$ its value slowly approaches the one achieved by steady blowing.
However, no case was found within the studied parameter range in which pulsed actuation is more efficient than steady blowing for the given bluff body shape and actuation system. Hence, continuous blowing is used throughout the remaining investigations presented in this thesis.

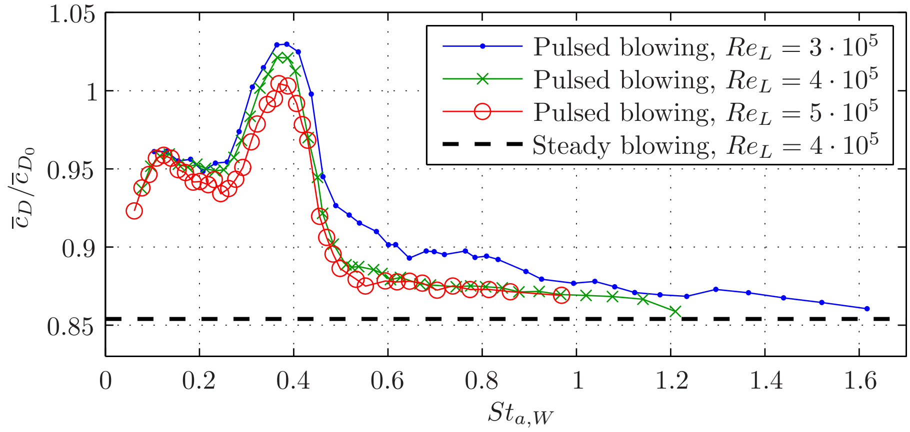

Figure 4.12: Time-averaged, normalized drag coefficient $\overline{c}_D/\overline{c}_{D_0}$ for symmetric, pulsed blowing for a variation of the actuation frequency $St_{a,W}$ with a fixed momentum coefficient $\overline{c}_\mu = 0.02$, at $\overline{\beta}_w = 0°$ for several Reynolds numbers compared with steady blowing.

4.3.3 Asymmetric actuation by continuous blowing

As stated already in an earlier publication [103], steady blowing through the Coanda actuators accelerates the flow along the rear sides of the bluff body, which leads to lower pressure in this region. This means that asymmetric actuation can be used to create a pressure difference between the rear wind- and leeward sides to influence not only drag or base pressure, but also side force and yaw moment. This is depicted in Fig. 4.13 for straight flow conditions and a cross-wind angle of $\overline{\beta}_w = 10°$. Here, the normalized blowing velocities $u^*_{a,r} = u_{a,r}/\overline{u}_\infty$ and $u^*_{a,l} = u_{a,l}/\overline{u}_\infty$ are varied at the right (windward) and left (leeward) actuators, respectively. This choice of input variables reduces the nonlinearities in the steady-state maps relative to using the momentum coefficients for nondimensionalization.

Side-force and yaw-moment coefficient depend almost linearly on the actuation amplitude. Exposing the bluff body to cross-wind only shifts the maps upwards, but does not affect their

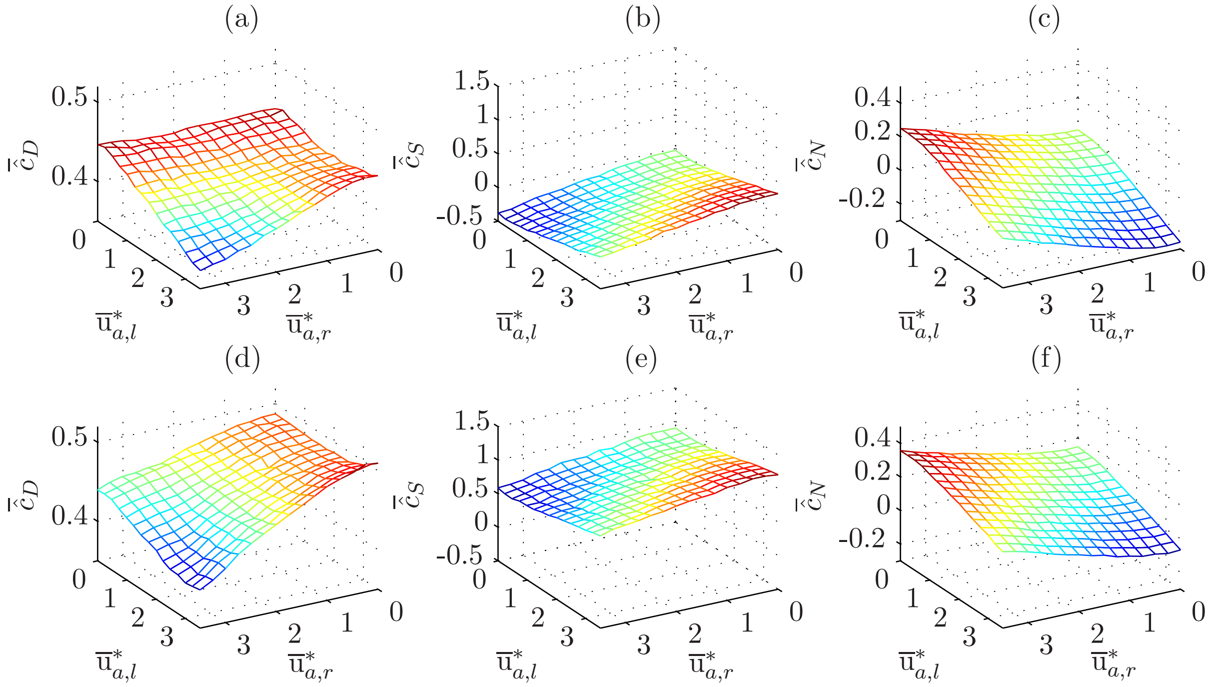

Figure 4.13: Steady-state maps of the coefficients for drag $\overline{\hat{c}}_D$, side force $\overline{\hat{c}}_S$ and yaw moment $\overline{\hat{c}}_N$ for asymmetric blowing at a cross-wind angle $\overline{\beta}_w = 0°$ (a-c) and $\overline{\beta}_w = 10°$ (d-f), $Re_L = 4 \cdot 10^5$.

behavior with respect to the actuation. Note that side-force and yaw-moment coefficients change in adverse directions, however. This is due to the pressure difference created between the wind- and leeward rear sides of the bluff body by asymmetric actuation. Reducing the yaw moment under cross-wind conditions requires a higher blowing velocity $u^*_{a,l}$ at the leeward (i.e. left) actuator, as can be seen in Fig. 4.13 (f). However, this slightly increases the side force acting on the bluff body as shown in Fig. 4.13 (e), and does not reduce the drag coefficient, see Fig. 4.13 (d). In contrast to side-force and yaw-moment coefficients, the map of the drag coefficient shows a significant number of nonlinearities. The degree of base-pressure increase and thus drag decrease not only depends on the ratio of the actuation amplitudes to each other, but also on the cross-wind angle. Whereas symmetric actuation leads to the largest base-pressure recovery for straight oncoming flow, it is more efficient to use stronger blowing at the right, windward actuator under side-wind conditions.

The boundary layer profiles measured with a hot-wire at the actuation slot exits on the wind- and leeward sides give some insight into the reasons for these characteristics. Fig. 4.14 (a) shows a comparison between the natural and symmetrically actuated flow with $\overline{u}^*_{a,r} = \overline{u}^*_{a,l} = \overline{u}^*_{a,ul} = 1.5$ at zero yaw. One can clearly see how the Coanda jets accelerate the flow in proximity to the wall

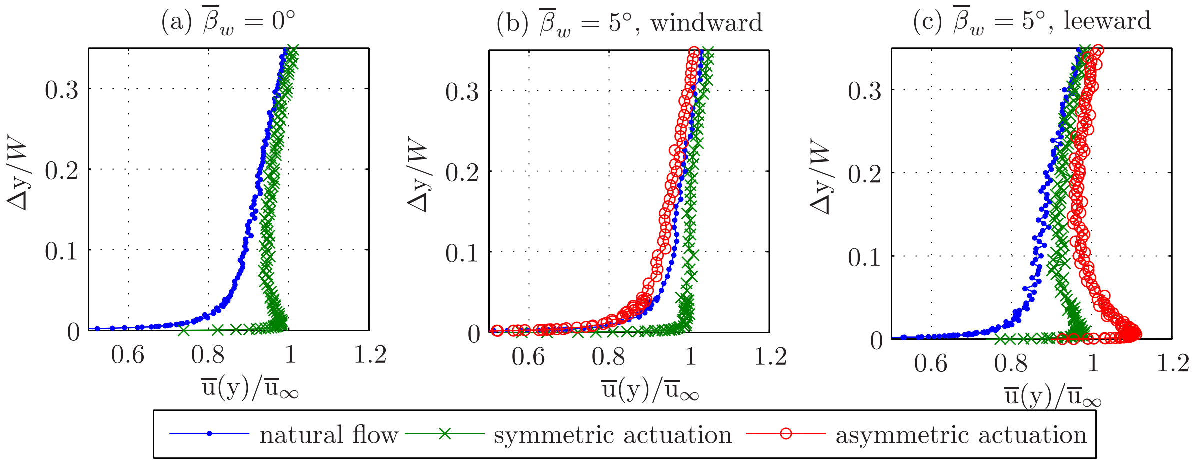

Figure 4.14: Boundary layer profiles for $Re_L = 4 \cdot 10^5$ at the rear edges of the bluff body. Plot (a) shows the natural flow and symmetrically actuated flow with $\overline{u}^*_{a,r} = \overline{u}^*_{a,l} = \overline{u}^*_{a,ul} = 1.5$ (most efficient drag reduction) at $\overline{\beta}_w = 0°$; plots (b) and (c) give the profiles at the wind- and leeward sides for $\overline{\beta}_w = 5°$ for natural flow, symmetric actuation as in (a) and asymmetric actuation with $\overline{u}^*_{a,r} = 0$, $\overline{u}^*_{a,l} = 2.3$, $\overline{u}^*_{a,ul} = 1.5$ (zero yaw moment).

which helps to deflect high-momentum fluid towards the wake and thus increase base pressure. In the cross-wind case the natural boundary layer on the leeward side is slightly thicker than on the windward side, as can be seen in Fig. 4.14 (b) and (c). Again, symmetric actuation leads to an acceleration of the boundary layer on both sides, providing an efficient drag reduction without affecting side force or yaw moment significantly. Switching the right, windward actuator off and increasing the blowing velocity at the left, leeward actuator to $\overline{u}^*_{a,l} = 2.3$ accelerates the leeward boundary layer and decelerates the windward flow. The higher velocity at the rear lee side leads to a lower pressure in this region, and vice versa at the rear luv side. This creates a counter moment around the z-axis that reduces the yaw moment created mainly by the asymmetric pressure distribution around the vehicle's front under cross-wind conditions. However, the lower pressure on the rear leeward side due to the asymmetric actuation also results in a small increase in side force. This is the effect mentioned above in the discussion of the steady-state maps in Fig. 4.13 (e) and (f).

All of these partly opposing dependencies have to be taken into account in the control design to provide an efficient drag reduction in changing flow conditions while simultaneously improving the vehicle's cross-wind sensitivity.

4.4 Actuated flow dynamics

Designing a feedback controller requires a dynamic plant model. The identification experiments are carried out for a range of Reynolds numbers $3 \cdot 10^5 \leq Re_L \leq 6 \cdot 10^5$ and constant cross-wind angles $0° < \beta_w < 10°$ by applying multiple input pseudo-random binary signals (PRBS) for the desired normalized blowing velocity $\underline{\mathrm{u}}^*_{a,des}$ to the actuators. The PRBS bandwidth is adjusted within a range of $15\,\mathrm{Hz} < f_{PRBS} < 30\,\mathrm{Hz}$ proportional to the Reynolds number, since larger free-stream velocities correspond to faster flow dynamics and thus require excitation at sufficiently high frequencies. Furthermore, several different actuation amplitudes are applied at each Reynolds number and cross-wind angle, so that the expected closed-loop operating regime is sufficiently covered. Each identification experiment is repeated 10 times with identical parameters. All measured variables are phase-averaged to reduce the influence of random disturbances and to improve the signal-to-noise ratio. From the measured data, separate models are identified for the dynamics of the actuators and the actuated flow, as depicted in Figure 4.15. The desired

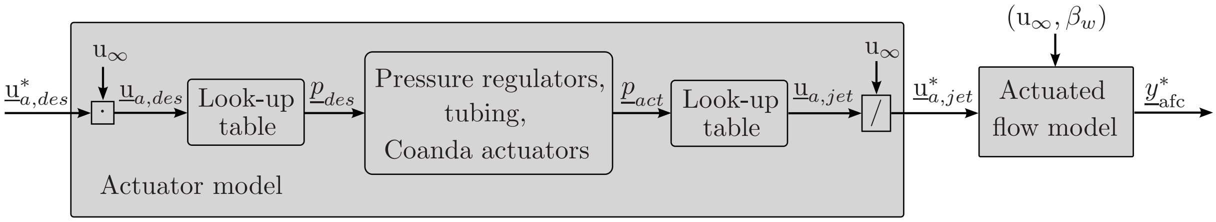

Figure 4.15: Schematic model structure for the actuators and the actuated flow dynamics.

normalized blowing velocities

$$\underline{\mathrm{u}}^*_{a,des} = \begin{bmatrix} \mathrm{u}_{a_1,des}/\mathrm{u}_\infty & \mathrm{u}_{a_2,des}/\mathrm{u}_\infty & \mathrm{u}_{a_3,des}/\mathrm{u}_\infty \end{bmatrix}^T \tag{4.17}$$

are chosen as the input vector for the actuator submodel. Here, actuators 1 and 2 correspond to the right and left Coanda slots, whereas index 3 designates the upper and lower slots, which are driven as a single actuator. The vector

$$\underline{\mathrm{u}}^*_{a,jet} = \begin{bmatrix} \mathrm{u}_{a_1,jet}/\mathrm{u}_\infty & \mathrm{u}_{a_2,jet}/\mathrm{u}_\infty & \mathrm{u}_{a_3,jet}/\mathrm{u}_\infty \end{bmatrix}^T \tag{4.18}$$

consists of the actual instantaneous nondimensional blowing velocities at the actuator slot exits and serves as the output vector of the actuator submodel. During the experiments the blowing velocities are normalized for $\mathrm{u}_\infty = \overline{\mathrm{u}}_{\infty,j}$, with the mean free-stream velocity $\overline{\mathrm{u}}_{\infty,j}$ at the current operating point j.

In the wind-tunnel implementation, the desired, dimensional blowing velocities $\underline{\mathrm{u}}_{a,des}$ are converted via a set of look-up tables to the corresponding pressure setpoints $\underline{p}_{des}$, which are then commanded to the pressure regulators. As described in section 4.1.2, piezo pressure transducers are installed near the outlet of each Coanda actuator duct. Another set of look-up tables is generated from a series of steady-state measurements for each actuator by mapping the measured pressures $\underline{p}_{act}$ inside the ducts to the blowing velocities as determined by the respective flow meters. These look-up tables allow for a time-resolved assessment of the instantaneous blowing velocity $\mathrm{u}_{a_i,jet}$ at each actuator slot i. All of these conversions are lumped together with the dynamics of the pressure regulators, the tubing and the coanda ducts in an overall linear MIMO actuator model, whose structure and identification are described in the next section 4.4.1.

The actuated flow model describes the response of the output variables

$$\underline{y}^*_{\mathrm{afc}} = \begin{bmatrix} \hat{c}_D & \hat{c}_S & \hat{c}_N \end{bmatrix}^T \tag{4.19}$$

to changes in nondimensional jet velocities $\underline{\mathrm{u}}^*_{a,jet}$ at the actuator exits. Here, the same kind of pressure transducers are used to measure the output variables $\hat{c}_D$, $\hat{c}_S$ and $\hat{c}_N$ and the input variables $\underline{\mathrm{u}}^*_{a,jet}$. This avoids potential errors in the identification of the aerodynamic part of the plant model, which could arise from varying sensor dynamics when measuring the input/output variables. For the identification of the actuated flow models, two different approaches are presented. One is based on a set of linear black-box models, which describe the dynamics at individual operating points. Thus, all nonlinearities and parameter-dependencies have to be subsequently modeled via an uncertainty description. The second approach is based on a linear parameter-varying model structure to capture the parameter-dependent behavior of the actuated flow with respect to free-stream velocity u_∞ and cross-wind angle β_w. The identification of these models is discussed in sections 4.4.2 and 4.4.3, respectively.

4.4.1 Actuator dynamics

The actuator models describe the dynamic input/output relationship between the desired and the actual nondimensional blowing velocities $u^*_{a_i,des}(t)$ and $u^*_{a_i,jet}(t)$ for each actuator i. Static nonlinearities are compensated prior to the identification via look-up tables, as described in the previous section. Furthermore, the recorded data sets suggest that the dynamics of the pressure regulators and tubing system do not change significantly over the relevant operating regime. Therefore, all identification experiments are merged into a single data set, from which linear discrete-time SISO models are identified separately for each of the three actuators with the Prediction-Error-Method (PEM) implemented in `MATLAB` [84]. These models have the structure

$$\underline{x}(k+1) = \boldsymbol{A}\underline{x}(k) + \underline{b}u(k-n_0), \tag{4.20}$$

$$y(k) = \underline{c}^T\underline{x}(k), \tag{4.21}$$

with $\underline{x} \in \mathbb{R}^3$ at a sampling time $T_s = 1\,\text{ms}$. Here, a model order of $n_x = 3$ and an input delay of $n_0 = 7$ samples is chosen.
The resulting linear models G_{a_i} describe the dynamics between desired and actual nondimensional blowing velocities $u^*_{a_i,des}$ and $u^*_{a_i,jet}$ for the three actuators $i = 1\ldots3$ with sufficient accuracy over the entire range of operating points. The corresponding frequency responses are shown in Fig. 4.16. All three actuators have a similar bandwidth of about $f_{bw,-3dB} \approx 20\text{Hz}$, above which their magnitude response rolls off with 20dB/decade. The phase response is dominated by the input time-delay of 7 ms, which causes important limitations for the achievable closed-loop bandwidth, as discussed in section 4.6.

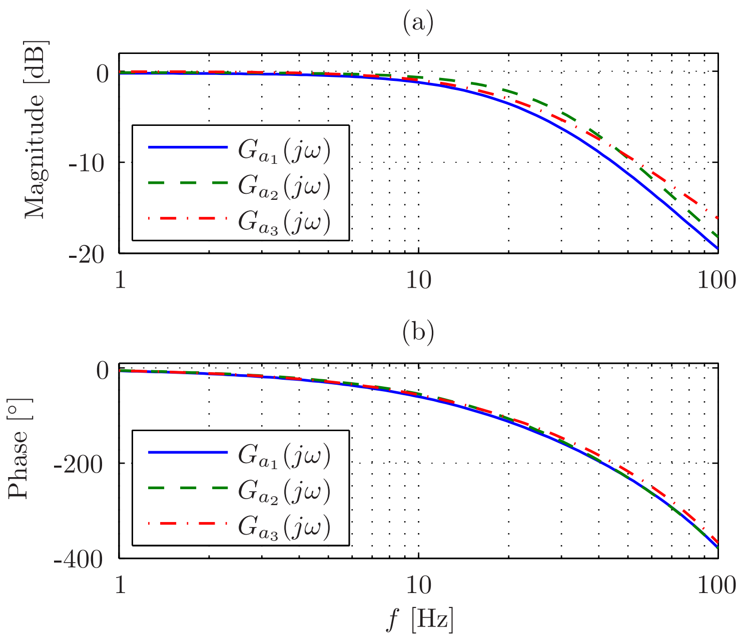

Figure 4.16: Magnitude (a) and phase (b) response of the identified actuator models.

For use in combination with the linear black-box models of the actuated flow, the actuator models are kept in discrete time and merged into a MIMO model. By contrast, the linear parameter-varying model is identified in continuous time. The identified actuator models must thus be converted to continuous time. This is carried out here with Tustin's method via a bilinear approximation of the derivative as described in the `Matlab`-documentation for the command `d2c` [84]. The respective models are subsequently reduced to the 5th order by balanced truncation as implemented in the `Matlab`-command `balred` [84]. This helps keep the order of the overall LPV plant model low, thus reducing the computational effort during the LPV control synthesis.

4.4.2 Linear black-box model identification of the actuated flow

A standard approach to capture the dynamics of the actuated flow consists of identifying a set of linear black-box models from experimental data. It has been used successfully in many previous applications of closed-loop AFC, e.g. Pastoor et al. [100] or Pfeiffer and King [103, 101]. Here, the input variables are chosen as

$$\underline{u}^*_{\text{afc}} = \underline{\mathrm{u}}^*_{a,jet} = \begin{bmatrix} \mathrm{u}^*_{a_1,jet} & \mathrm{u}^*_{a_2,jet} & \mathrm{u}^*_{a_3,jet} \end{bmatrix}^T, \tag{4.22}$$

where $\mathrm{u}^*_{a_i,jet} = \mathrm{u}_{a_i,jet}/\mathrm{u}_\infty$ denotes the instantaneous nondimensional blowing velocity at the exit of actuator i. The output variable vector

$$\underline{y}^*_{\text{afc}} = \begin{bmatrix} \hat{c}_D & \hat{c}_S & \hat{c}_N \end{bmatrix}^T \tag{4.23}$$

consists of the surrogate output variables for drag, side-force and yaw-moment coefficients, which are calculated from a weighted sum of pressure coefficients as described in Appendix C. Using nondimensional input/output variables mostly compensates for dependencies of the steady-state model gain on free-stream velocity. The remaining nonlinearities and parameter dependencies are taken into account by identifying individual models at each operating point, in this case at various Reynolds numbers, cross-wind angles and actuation amplitudes. The MIMO steady-state maps shown in Fig. 4.13 indicate an almost linear relationship between normalized blowing velocities and side-force and yaw-moment coefficients, signifying independence of cross-wind angle. However, during cross-wind the drag coefficient is more sensitive to actuation at the windward side than at the leeward side. Thus, for positive cross-wind angles blowing at the right, windward actuator leads to a large drag reduction, whereas the left, leeward actuator has little or no effect. Accordingly, for negative cross-wind angles the left actuator, which is now on the windward side, is expected to have a stronger effect on the drag coefficient. Although the experimental setup only allows side wind to be generated from one direction, the closed-loop control strategy has to work for an entire range from negative to positive cross-wind angles. Thus, the described characteristics of the drag coefficient have to be taken into account during the model identification. In order to mimic the effect of negative cross-wind angles, additional data sets were created from those recorded at positive angles by switching the right and left actuator input channels for the identification of the drag coefficient, but not for the side-force and yaw-moment coefficients since they have linear characteristics that do not depend on the cross-wind angle.
In total, a set of 181 models was identified using the Prediction-Error-Method. For more information on this standard approach, see e.g. Ljung [79]. All models have the same structure in discrete state-space form

$$\underline{x}(k+1) = \boldsymbol{A}\underline{x}(k) + \boldsymbol{B}\underline{u}^*_{\text{afc}}(k), \tag{4.24}$$

$$\underline{y}^*_{\text{afc}}(k) = \boldsymbol{C}\underline{x}(k), \tag{4.25}$$

with $\underline{x} \in \mathbb{R}^4$, $\underline{u}^*_{\text{afc}} \in \mathbb{R}^3$ and $\underline{y}^*_{\text{afc}} \in \mathbb{R}^3$ at a sampling time $T_s = 1\,\text{ms}$. A model order $n_x = 4$ is sufficient to capture the dynamics of the actuated flow with satisfactory accuracy. The characteristics of the identified models are discussed in the next section compared with those of linear parameter-varying models.

4.4.3 Linear parameter-varying model identification of the actuated flow

Similar to the models identified for the transient aerodynamic cross-wind gust response presented in section 4.2.3, a linear parameter-varying model structure lends itself well to capture the parameter-dependencies of the actuated flow dynamics. Again, separate multiple-input single-output (MISO) LPV models in continuous time are identified for the dynamics of drag, side-force and yaw-moment coefficients, respectively. The nondimensional input vector

$$\underline{u}^*(t) = \underline{\mathrm{u}}^*_{a,jet} = \begin{bmatrix} \mathrm{u}^*_{a1,jet} & \mathrm{u}^*_{a2,jet} & \mathrm{u}^*_{a3,jet} \end{bmatrix}^T \tag{4.26}$$

is the same as for the identification of the linear black-box models. It corresponds to the instantaneous normalized blowing velocities at the exits of the three actuators, respectively. For each model, the same LPV structure

$$\dot{\underline{x}}(t) = \underbrace{\mathrm{u}_\infty(t)\frac{1}{L}\boldsymbol{A}^*_1}_{\boldsymbol{A}(\underline{\theta})}\underline{x}(t) + \underbrace{\mathrm{u}_\infty(t)\frac{1}{L}\left(\boldsymbol{B}^*_1 + \hat{\beta}_w(t)\boldsymbol{B}^*_2\right)}_{\boldsymbol{B}(\underline{\theta})}\underline{u}^*(t), \tag{4.27}$$

$$y^*(t) = \underbrace{\underline{c}^{*T}}_{\underline{c}^T}\underline{x}(t), \tag{4.28}$$

$$\underline{\theta}(t) = \begin{bmatrix} \mathrm{u}_\infty(t) & \mathrm{u}_\infty(t)\hat{\beta}_w(t) \end{bmatrix}^T, \tag{4.29}$$

where $y^*(t)$ denotes the output variable of the respective MISO model for $\hat{c}_D$, $\hat{c}_S$ and $\hat{c}_N$. For the actuated flow dynamics a dependency on two parameters is considered.
Analogous to the models for the transient cross-wind gust response, the first parameter $\theta_1(t) = \mathrm{u}_\infty(t)$ is used to describe how the dynamics of the respective output variable scales with free-stream velocity. In the wind tunnel experiments for identification and control, the nominal, mean free-stream velocity $\overline{\mathrm{u}}_{\infty,i}$ of experiment i is used instead of the instantaneous free-stream velocity $\mathrm{u}_\infty(t)$. This is equivalent to using the driving speed of the vehicle as the scaling parameter for the actuated flow dynamics. Variations of the flow speed due to wind gusts or wakes of other cars or trucks are interpreted as disturbances at the nominal operating point defined by the current cruising speed of the vehicle. The second parameter $\theta_2(t) = \mathrm{u}_\infty(t)\hat{\beta}_w(t)$ is introduced here to model the varying sensitivities of the drag coefficient to wind- and leeward actuation under side-wind conditions, as discussed below.

Drag coefficient

The steady-state maps for the actuated flow of the drag coefficient indicate a nonlinear, parameter-dependent behavior as shown in Fig. 4.13 in section 4.3.3. A change in the slope of the steady-state map corresponds to a gain variation of the LPV state-space model. The actuated flow can only respond to changes in the actual instantaneous blowing velocity at the actuator exits and not to changes in desired blowing velocities commanded to the actuators. This gain dependency is thus modeled here by a parameter-dependent input matrix $\boldsymbol{B}^*(\underline{\theta}) = \boldsymbol{B}^*_1 + \hat{\beta}_w\boldsymbol{B}^*_2$ in the nondimensional model for the aerodynamic part of the actuated flow, see also section 2.2.2 for more details. Converting to the LPV model in Eq. (4.27-4.29) in dimensional time results in the second parameter $\theta_2(t) = \mathrm{u}_\infty(t)\hat{\beta}_w(t)$ with mixed dependency on free-stream velocity and cross-wind angle.
Apart from the change in sensitivity, the identification experiments do not indicate a variation of the frequency response of the actuated flow for changing cross-wind angles. Hence, only dependencies of the state matrix $\boldsymbol{A}(\underline{\theta})$ on one parameter $\theta_1 = \mathrm{u}_\infty$ are considered in Eq. (4.27). This also helps keep the number of model coefficients low.
A model order $n_x = 2$ was found sufficient to capture the dynamics of the drag coefficient. The identification is carried out based on the algorithm for LPV identification introduced in section 2.2.3. The coefficients are initialized based on an initial linear black-box model identified with

the standard Prediction-Error-Method from a single experiment. Subsequently, the coefficients of the LPV model are obtained by nonlinear optimization over the entire set of experiments, as used for the linear black-box model identification described in the previous section. These experiments comprise a range of Reynolds numbers $3 \cdot 10^5 \leq Re_L \leq 6 \cdot 10^5$ and constant cross-wind angles $0° \leq \beta_w \leq 10°$. Again, additional "virtual" data sets are generated by switching the left and right actuator channels to take the effect of negative cross-wind angles into account. The state-space matrices of the identified LPV model for the drag coefficient are listed in appendix C.2.2.

In contrast to the individual linear black-box models, which capture only the local plant behavior at the respective operating point, the LPV model has to represent the actuated flow dynamics for the entire operating regime as closely as possible. Fig. 4.17 shows the frequency response of the LPV model for the drag coefficient in comparison with the entire set of identified linear black-box models. Evaluating the LPV model at frozen parameter values $\theta_1 = \overline{\mathrm{u}}_{\infty,i}$ and

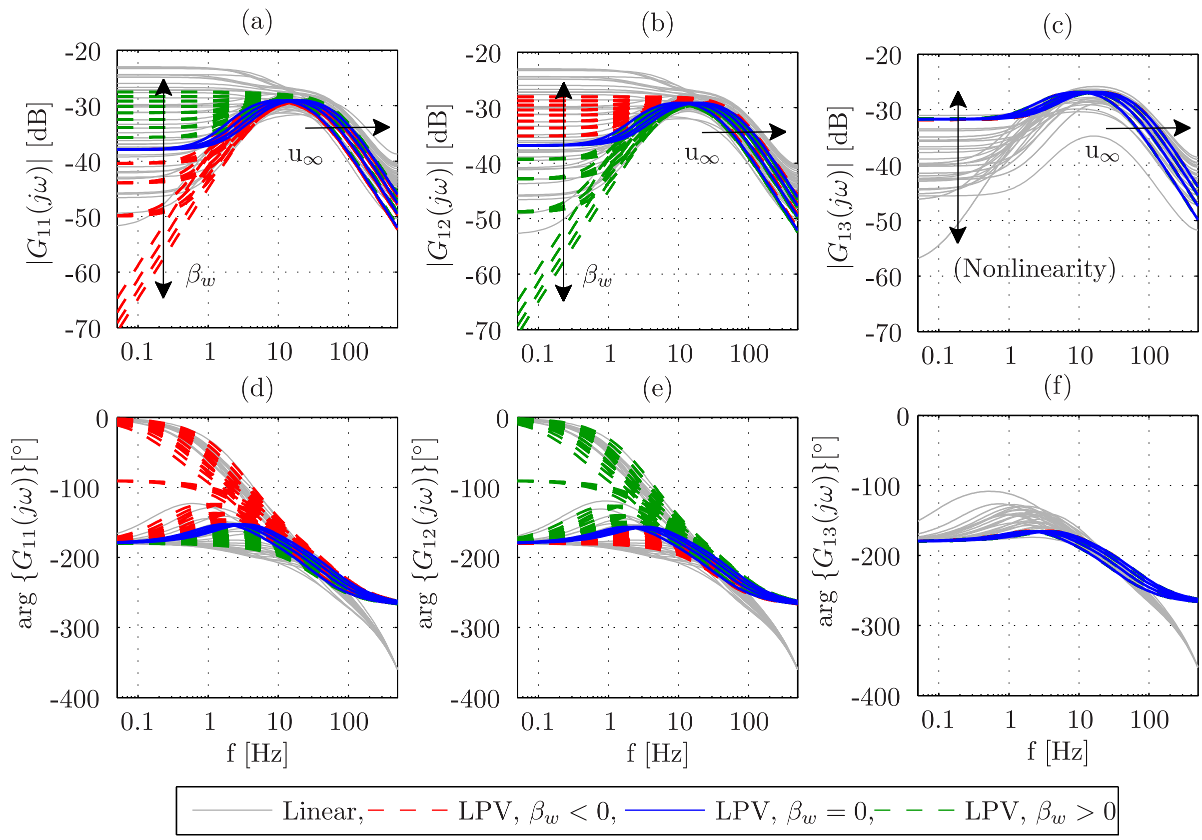

Figure 4.17: Frequency response of the LPV model for the drag coefficient to blowing at the right, left and upper/lower actuators (from left to right), evaluated at frozen parameter values for u_∞ and β_w covering the entire operating regime. The frequency response of the entire set of identified linear black-box models is shown in gray for comparison.

$\theta_2 = \overline{\mathrm{u}}_{\infty,i}\overline{\beta}_{w,i}$ yields local linear models $G_{11}(s)$, $G_{12}(s)$ and $G_{13}(s)$, which describe the response of the drag coefficient at the operating point of experiment i to actuation at the right, left and upper/lower slots, respectively. This allows for an easy comparison with the respective linear black-box model. As can be seen from Fig. 4.17 (a) and (b) the LPV models represents the magnitude variation in dependency of the cross-wind angle β_w for the wind- and leeward actuators very well. At low frequencies the phase response for these actuator channels, Fig. 4.17 (d) and (e), switches from $-180°$ to $0°$ when a certain positive or negative cross-wind angle is exceeded. Representing this behavior by the LPV model is crucial to reduce uncertainty and achieve an improvement in LPV control performance over conventional robust controllers.

Additionally, the LPV model captures the dependency of the frequency response to changes in

free-stream velocity very well. This suggests that the identified LPV model represents the underlying nondimensional flow characteristics correctly. Thus, scaling to different flow speeds and realistic vehicle dimensions should give at least a qualitatively correct estimate of the expected frequency response.
However, the variation of the amplitude response to actuation at the upper and lower Coanda slots is not represented by the LPV model, as seen in Fig. 4.17 (c). This is attributed to unmodeled nonlinearities. Attempts with different model structures not shown here indicate that the gain for the upper and lower actuator input channel increases with stronger actuation on the lee- and windward sides. This leads to a bilinear model structure that can be recast into a so-called Quasi-LPV model in which state or input variables are used as pseudo-parameters. However, stability or performance cannot be guaranteed for these models with the LPV control synthesis algorithms employed here. Hence, this modeling approach is not pursued further here, although it better approximates actuated flow dynamics.

Side-force and yaw-moment coefficient

For the dynamics of side-force and yaw-moment coefficients, the same LPV model structure as for the drag coefficient is chosen, see Eq. (4.27-4.29). However, their steady-state maps shown in Fig. 4.13 indicate an almost perfectly linear, parameter-independent response to constant actuation. Therefore, the input matrix $\boldsymbol{B}_2^*$ in Eq. (4.27) is set to zero for the identification of their dynamics. Only the dependency of the frequency characteristics on changes in free-stream velocity is considered. Nevertheless, the same model structure as in the identification for the drag coefficient is kept to facilitate the formulation of the overall MIMO LPV model from the individual MISO LPV models. The identification procedure follows the same procedure as discussed for the drag coefficient in the previous section. Again, a model order of $n_x = 2$ was found to be sufficient to capture the dynamics of side-force and yaw-moment coefficients with satisfactory accuracy, respectively. The values identified for the state-matrices of the LPV models are given in appendix C.2.2.
Figure 4.18 shows a comparison of the frequency response of the LPV models evaluated at frozen parameter values for u_∞ with the set of linear black-box models. Here, only the response to wind- and leeward actuation is plotted, since the influence of upper/lower actuation on side-force and yaw-moment coefficients is negligible. The amplitude response variation for different free-stream velocities is captured reasonably well by the respective LPV models for side-force and yaw-moment coefficients, as shown in Fig. 4.18 (a) and (b). However, the roll-off at higher frequencies for the LPV model does not match that for the linear models. This is likely due to the fact that the frequency response of the linear SISO submodels shown here is derived from linear black-box MIMO models with an overall model order $n_x = 4$. The order of the linear SISO submodels appears to be too low to accurately represent the system behavior at higher frequencies. By contrast, the three LPV MISO submodels have a model order of $n_x = 2$ each, resulting in an overall model order of 6. A cross-validation of the LPV models also yields better fits than the linear models, which suggests a superior approximation of the frequency response for the actuated flow.
The phase responses shown in Fig. 4.18 (c) and (d) indicate that side force and yaw moment react to actuation at right and left actuators in adverse directions. For instance, leeward blowing reduces the yaw moment during cross-wind but increases the side force. As a consequence, these two coefficients cannot be controlled independently for the given actuator configuration. Since both have an impact on lateral vehicle dynamics, a suitable surrogate variable is composed by a weighted sum of both coefficients. The approach is presented in more detail in section 4.5.4 after discussing the characteristics of the lateral vehicle dynamics.

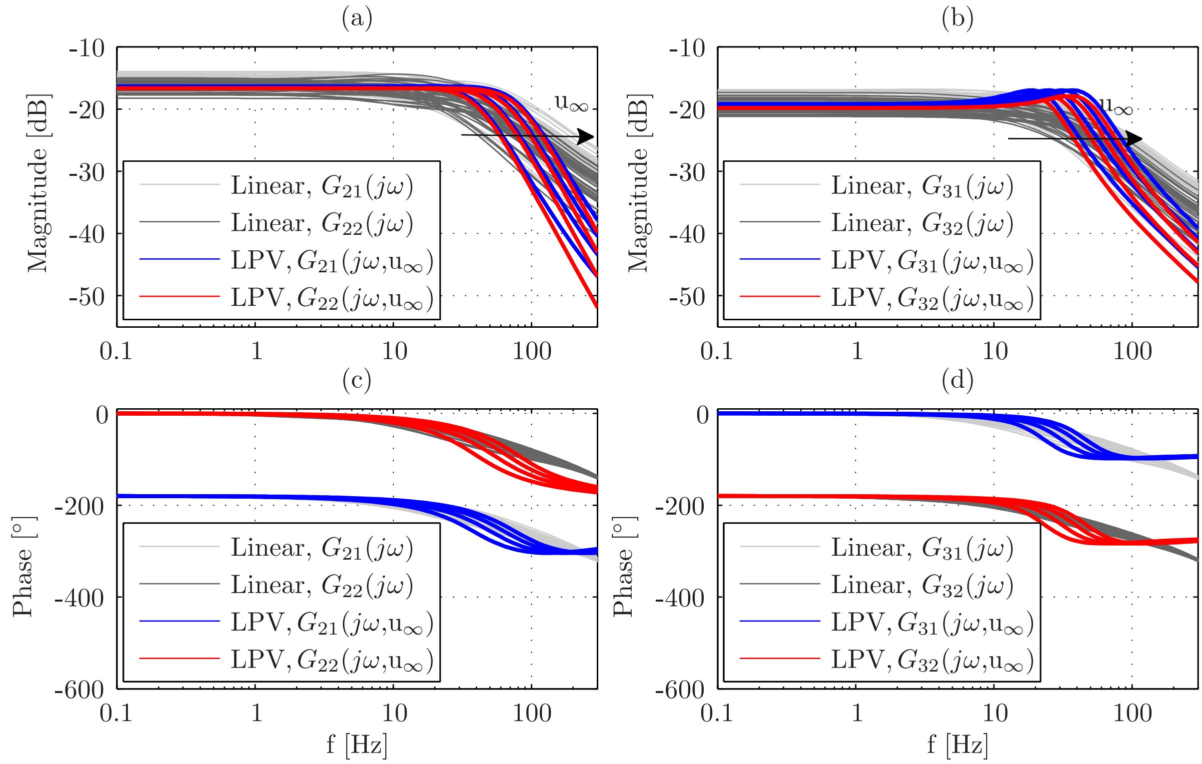

Figure 4.18: Frequency response of the LPV models for side-force and yaw-moment coefficients to wind- and leeward blowing, evaluated at four frozen parameter values for the free-stream velocity in the range $11.4\,\mathrm{m/s} \leq u_\infty \leq 22.8\,\mathrm{m/s}$. The frequency response of the set of identified linear black-box models is shown in gray for comparison.

Cross-validation of the identified LPV models

Figure 4.19 shows two cross-validation experiments for the identified models of the actuated flow. The left column results from a Reynolds number $Re_L = 3 \cdot 10^5$ for straight oncoming flow, whereas the experiment in the right column is conducted at $Re_L = 6 \cdot 10^5$ at a mean cross-wind angle of $\overline{\beta}_w = 10°$. The normalized jet velocities at the three actuators were varied with a different MIMO pseudo-random binary signal than the one used for the model identification. For each experiment, the measured surrogate output variables for drag, side-force and yaw-moment coefficients are compared with the simulated outputs of a linear MIMO model and of the LPV model, which consists of the three MISO submodels described in the previous sections. Only the deviations $\Delta\hat{c}_D$, $\Delta\hat{c}_S$ and $\Delta\hat{c}_N$ from the corresponding steady-state values of the respective operating point are plotted.

The linear model was identified at $Re_L = 3{\cdot}10^5$ and $\beta_w = 0°$ at the operating point corresponding to the left column of Fig. 4.19. Both the linear and the LPV model replicate the measured output data for this Reynolds number and cross-wind angle with similar accuracy. Due to unmodeled nonlinearities for the dynamics of the drag coefficient, the corresponding fits achieved by both models with regards to Variance Accounted For (VAF) are rather low, as seen in Fig. 4.19 (a). The models for side-force coefficient, Fig. 4.19 (c), and yaw-moment coefficient, Fig. 4.19 (e), are more accurate, with slightly better fits with the LPV model due to its higher order.

At the higher Reynolds number $Re_L = 6{\cdot}10^5$ the actuated flow has a significantly faster response to the actuation input. This is captured well by the LPV model, especially for side-force and yaw-moment coefficients, as can be seen in Fig. 4.19 (d) and (f). By contrast, the transient response of the linear model is considerably too slow and is unable to represent the gain variation of the drag coefficient under cross-wind conditions, see Fig. 4.19 (b), whereas the LPV model achieves a very high fit of 67.7 %.

All in all, these results suggest that the identified LPV model is well suited to describe the parameter dependency of the actuated flow dynamics over a large range of free-stream velocities and cross-wind angles. Capturing these effects by a set of linear black-box models which cover the entire operating range only allows all nonlinearities and parameter-dependencies to be lumped under an uncertainty description. Though some uncertainties due to nonlinear effects remain for the LPV approach as well, it shows increased model accuracy and an ability to capture and explain the flow physics to a greater degree than the linear black-box setting. In particular, this allows predictions to be made for differently scaled vehicles and higher free-stream velocities.

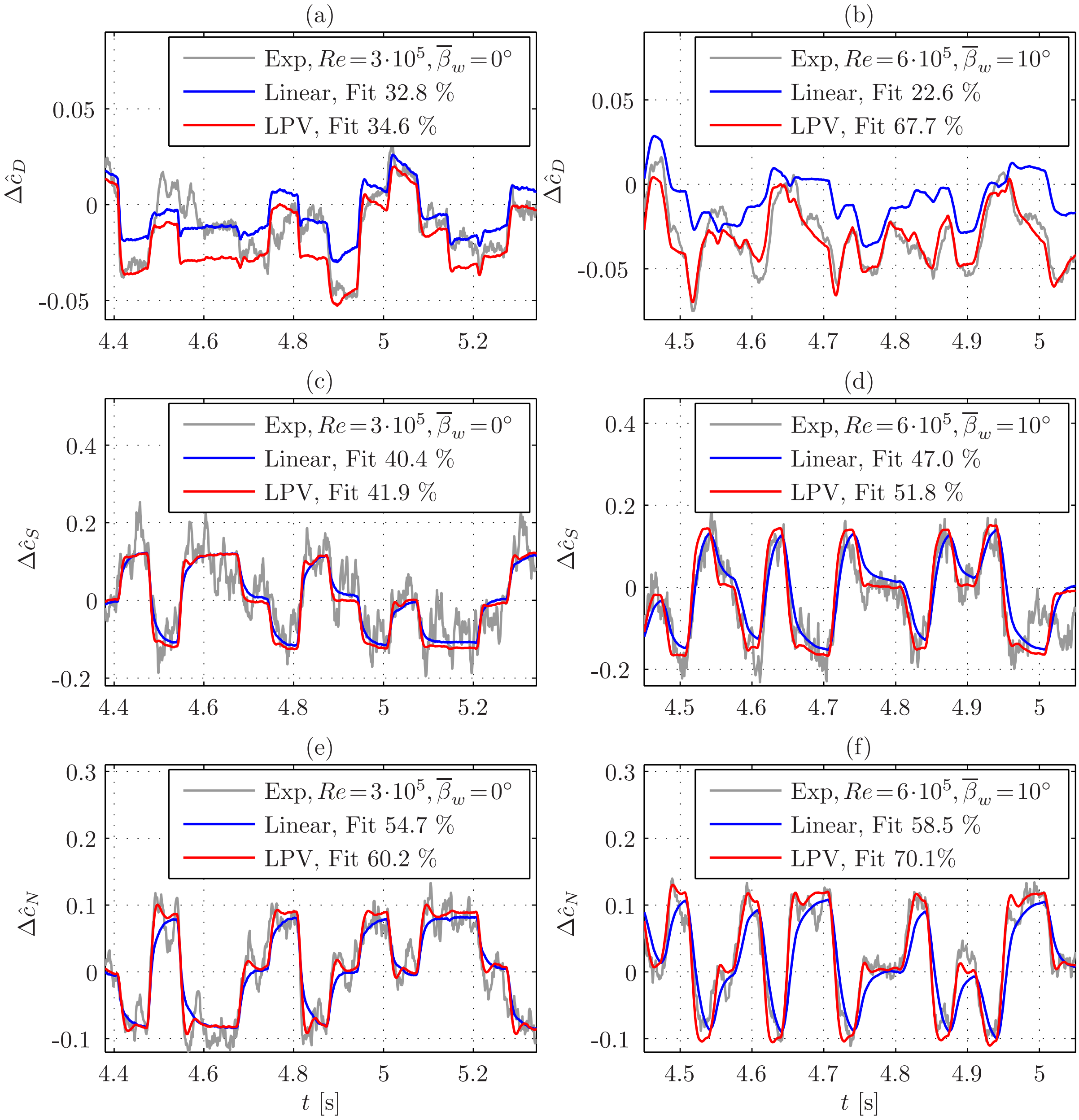

Figure 4.19: Simulated response of the LPV model and of a linear black-box model in comparison with the measured response from two cross-validation experiments for actuated flow dynamics at $Re_L = 3 \cdot 10^5, \overline{\beta}_w = 0°$ (left column) and $Re_L = 6 \cdot 10^5, \overline{\beta}_w = 10°$ (right column).

Nondimensional frequency response of the actuated flow model

Combining the three individual MISO models for the dynamics of drag, side-force and yaw-moment coefficients into an overall MIMO LPV model and converting it to convective time yields

$$\frac{d\underline{x}^*(t^*)}{dt^*} = \boldsymbol{A}_1^*\underline{x}^*(t^*) + \underbrace{\left(\boldsymbol{B}_1^* + \hat{\beta}_w(t^*)\boldsymbol{B}_2^*\right)}_{\boldsymbol{B}^*(\theta^*(t^*))}\underline{u}^*(t^*), \tag{4.30}$$

$$\underline{y}^*(t^*) = \boldsymbol{C}^*\underline{x}^*(t^*), \tag{4.31}$$

with the nondimensional input/output vectors

$$\underline{u}^*(t^*) = \left[\mathrm{u}^*_{a1,jet}(t^*) \quad \mathrm{u}^*_{a2,jet}(t^*) \quad \mathrm{u}^*_{a3,jet}(t^*)\right]^T, \ \underline{y}^*(t^*) = \left[\hat{c}_D(t^*) \quad \hat{c}_S(t^*) \quad \hat{c}_N(t^*)\right]^T. \tag{4.32}$$

Since the dependency of the dynamics on free-stream velocity u_∞ is eliminated for the representation in convective time, this model depends only on one parameter $\theta^*(t^*) = \beta_w(t^*)$. Evaluating the LPV state-space equations (4.30,4.31) at different frozen parameter values results in linear, nondimensional models that are valid at their corresponding operating point characterized by constant cross-wind angles $\hat{\beta}_w$. Transferring each of these models to the nondimensional frequency domain results in

$$\underline{y}^*(s^*) = \begin{bmatrix} G^*_{11}(s^*) & G^*_{12}(s^*) & G^*_{13}(s^*) \\ G^*_{21}(s^*) & G^*_{22}(s^*) & G^*_{23}(s^*) \\ G^*_{31}(s^*) & G^*_{32}(s^*) & G^*_{33}(s^*) \end{bmatrix} \underline{u}^*(s^*), \tag{4.33}$$

with a matrix of dimensionless transfer functions. Their frequency responses are shown in Fig. 4.20. Here, the amplitude and phase responses of G^*_{11} and G^*_{12} change with cross-wind angle

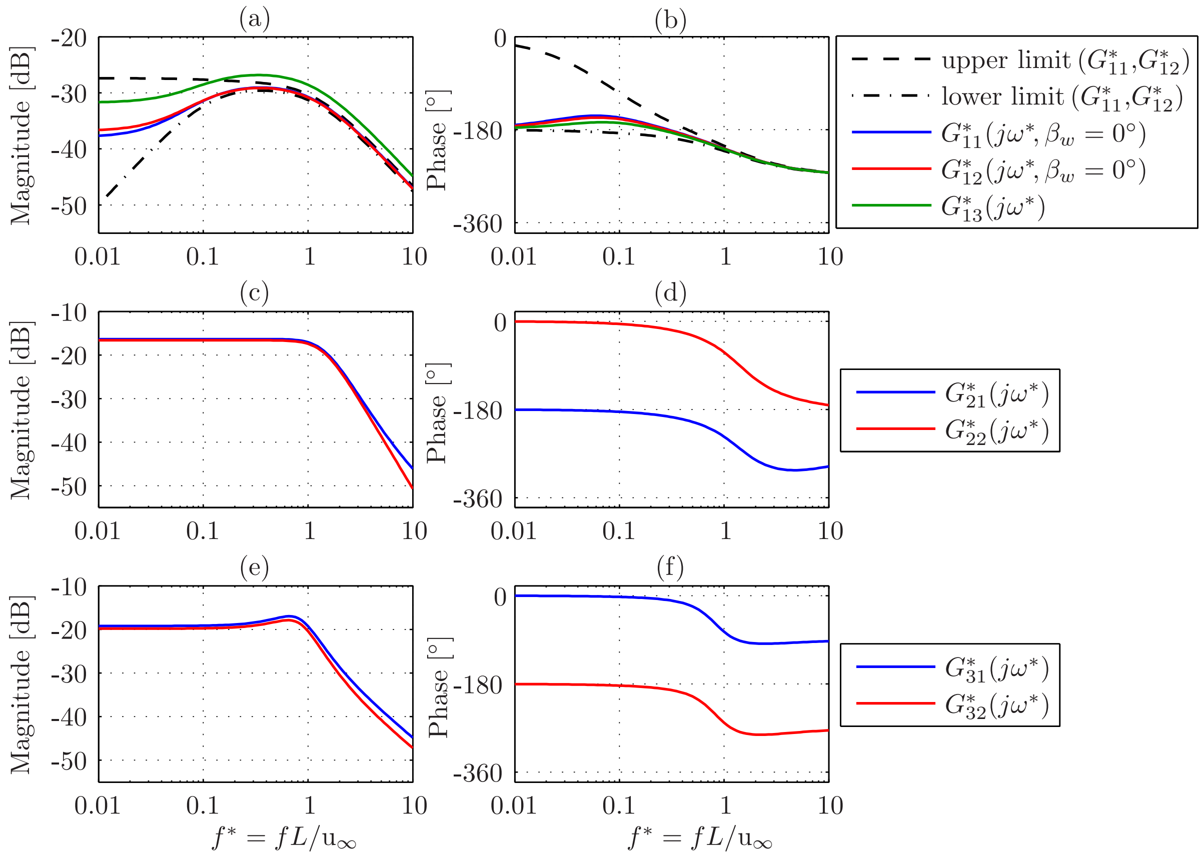

Figure 4.20: Nondimensional frequency response of the LPV model for the actuated flow dynamics of the drag coefficient (a,b), side-force coefficient (c,d) and yaw-moment coefficient (e,f).

β_w according to the varying sensitivity of the drag coefficient to wind- and leeward actuation. The corresponding range is marked by the dashed lines in Fig. 4.20 (a) and (b), whereas the colored lines denote their frequency response for straight flow conditions. The third actuator, corresponding to blowing at the upper/lower slots, has a significant, but parameter-independent influence on the drag coefficient, as seen in the frequency response of G^*_{13} in Fig. 4.20 (a, b).
The nondimensional dynamics of side-force and yaw-moment coefficients are shown in Fig. 4.20 (c-f). They do not vary with cross-wind angle β_w. The impact of the third actuator is negligible and is therefore not shown. As mentioned before, actuators 1 and 2 on the right and left sides have an opposing influence on $\hat{c}_S$ and $\hat{c}_N$, as shown in the phase responses in Fig. 4.20 (d, f). All magnitude responses start to roll off for frequencies $f^* > 1$. The drag coefficient shows the aforementioned gain variation at low frequencies, whereas the side-force coefficient has the fastest dynamics. The frequency response of the yaw-moment coefficient indicates a small resonance peak for frequencies $f^* \approx 0.8$.
Comparing these results with the nondimensional cross-wind gust response identified in section 4.2.3, see Fig. 4.9, reveals a significantly faster response of the actuated flow, especially for yaw-moment and drag coefficients. This is attributed to the fact that the actuation has the largest impact on the pressure distribution in the nearby regions along the rear sides and on the base of the vehicle, which results in a relatively fast response of the output variables. In comparison, it takes longer for the entire vehicle to enter the cross-wind gust. This indicates that it is in principle possible to suppress disturbances caused by cross-wind gusts with a feedforward or feedback active flow control system. However, additional limitations of the actuation system need to be taken into account. These are addressed in the following section.

Influence of actuator dynamics

The overall plant model for the control design consists of the submodels for the actuator and the actuated flow dynamics. The corresponding state-space equations for the LPV case are given in appendix C.2.2. Figure 4.21 shows a comparison of the dimensional frequency response of the actuator models, plots (a) and (c), with the actuated flow LPV model and the overall LPV

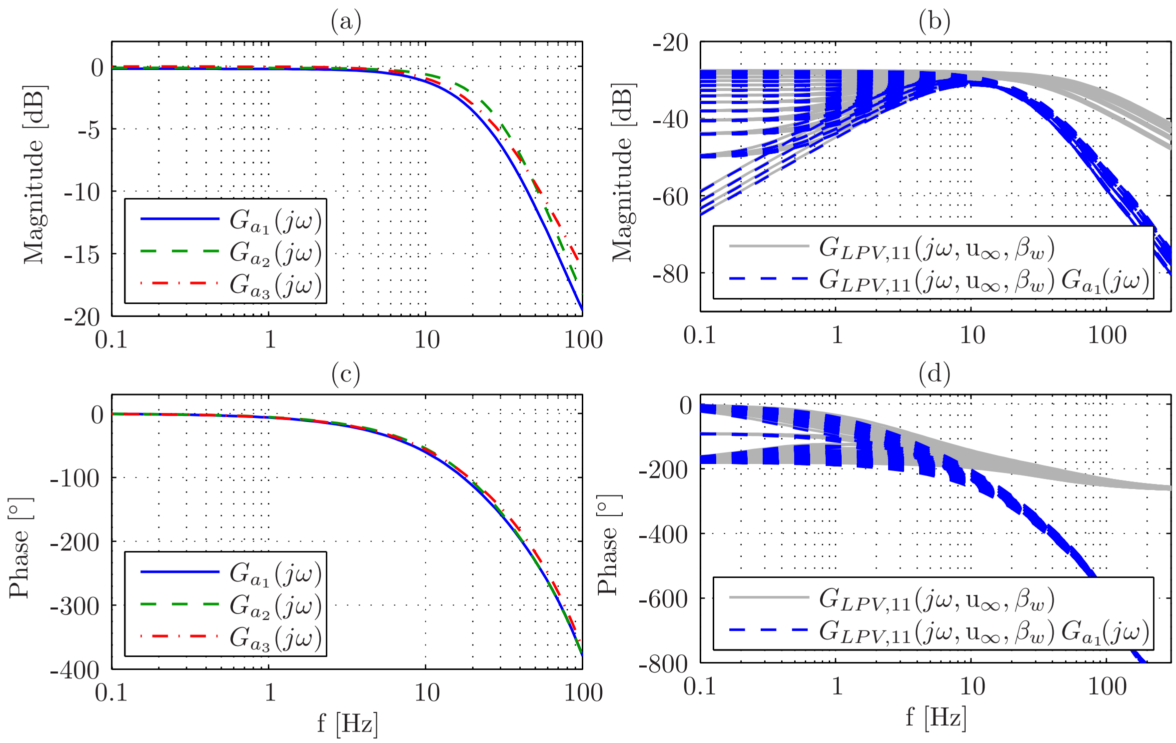

Figure 4.21: Dimensional frequency response of the actuator models (a, c) and of the LPV model for the drag coefficient to windward blowing with and without actuator dynamics (b, d).

model for a range of free-stream velocities $11.4\,\mathrm{m/s} \leq u_\infty \leq 22.8\,\mathrm{m/s}$ and cross-wind angles $-10° \leq \beta_w \leq 10°$, see plots (b) and (d). Here, only the response of the drag coefficient to blowing with actuator 1 on the rear right side is given. Whereas the LPV submodel of the actuated flow captures the variation with free-stream velocity at higher frequencies very well, the limited actuator bandwidth leads to roll-off at significantly lower frequencies. Furthermore, the input time-delay of the actuator models results in a large phase shift. Together, these effects limit the achievable closed-loop bandwidth in the wind tunnel experiment.
However, scaling of the aerodynamic part of the model suggests significantly slower actuated flow dynamics for a real-sized vehicle at realistic driving speeds, whereas similar or even faster dimensional actuator dynamics are likely to be achieved. The ratio of actuator bandwidth to fluid dynamic response time thus improves. Since also the transient cross-wind gust characteristics are shifted to lower frequencies as well, a better controller performance can be expected when applied to a real vehicle.

4.5 Lateral dynamics and virtual driver

The single-track and virtual driver model described in sections 2.3.1 and 2.3.2 form the basis for a real-time simulation of the lateral vehicle dynamics during the cross-wind gust experiments. This approach allows the lateral motion of arbitrary vehicles at any desired, user-defined driving velocity to be studied and replicated in the wind tunnel. Figure 4.22 shows a sketch of the single-

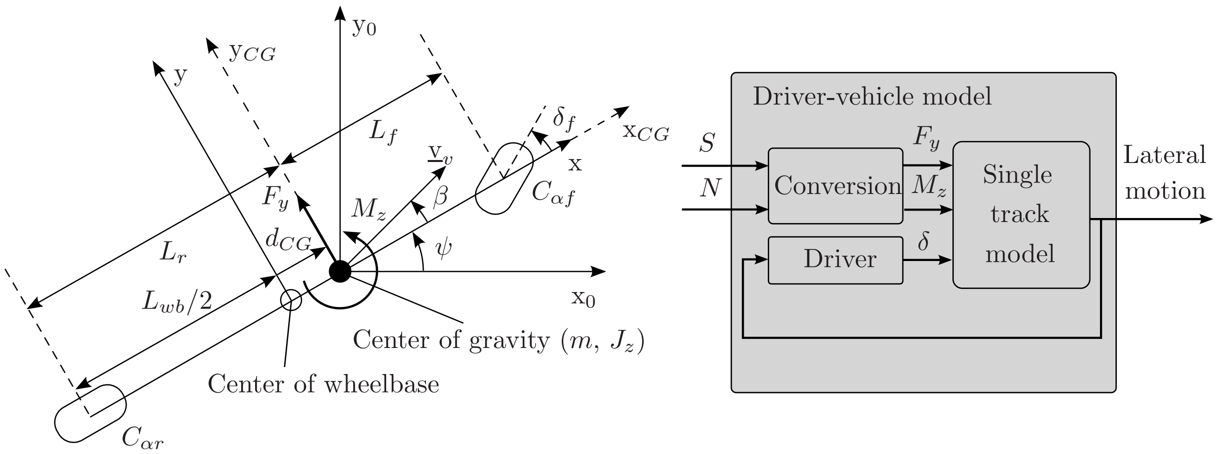

Figure 4.22: Single-track model (left) and driver-vehicle control loop for disturbance compensation (right), adapted from Risse [105] and Mitschke and Wallentowitz [85].

track model and the definitions of the various parameters. The measured aerodynamic side force S and yaw moment N serve as input variables for the simulation of the driver-vehicle model. Since they are defined for the x-y-coordinate system located at the geometric center of the wheelbase as is common in vehicle aerodynamics [56], they have to be transformed to the x_{CG}-y_{CG}-coordinate system used in lateral vehicle dynamics. It is located at the vehicle's center of gravity, at a position $x = d_{CG}$ away from the center of the wheelbase. This yields the side force $F_y = S$ and yaw moment $M_z = N - d_{CG}S$ acting on the center of gravity.
For a correct real-time replication of the lateral vehicle motion, the coefficients of vehicle and driver models have to be scaled to wind tunnel dimensions and free-stream velocity. Additionally, the measured side force and yaw moment have to be compensated for inertial forces arising from the model motion. Care must also be taken that the resulting effective cross-wind angle seen by the vehicle matches as closely as possible between on-road driving and the wind tunnel experiment. The approaches applied here for scaling, inertial compensation and correct vehicle motion replication are described in more detail in the following sections.

4.5.1 Replication of the lateral vehicle motion in the wind tunnel

In order to correctly replicate the lateral vehicle motion in the wind tunnel, the various velocity components of the oncoming flow experienced by the vehicle have to be taken into account. Fig. 4.23 shows a comparison of the differing cases for the approaching flow on-road and in the wind tunnel. Without any cross-wind the real car sees an oncoming flow $\underline{v}_v^-$ in the opposite

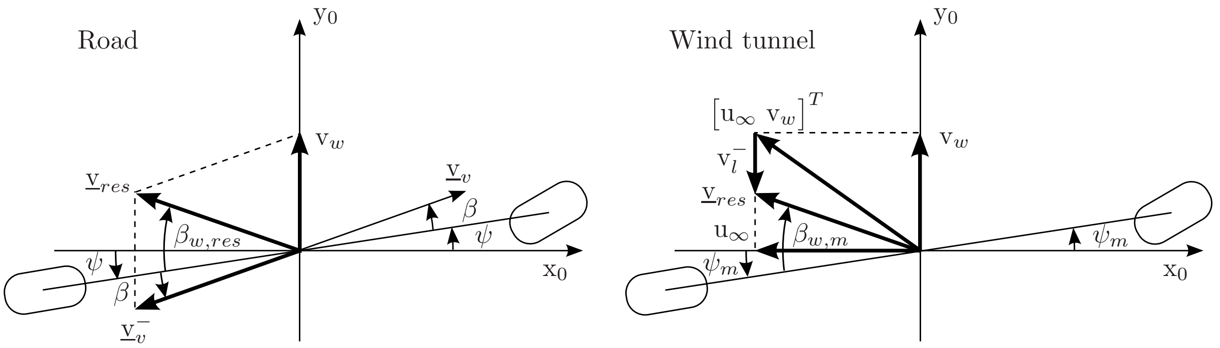

Figure 4.23: Comparison of the on-road flow conditions during cross-wind (left) with those in the wind tunnel (right).

direction of its driving velocity vector $\underline{v}_v$. It is inclined by the side-slip angle β relative to the longitudinal vehicle axis and turns with the vehicle when the latter is rotated by the yaw angle ψ. Subjecting the vehicle to a cross-wind v_w facing in y_0-direction results in an overall vector $\underline{v}_{res}$ of the oncoming flow. The effective cross-wind angle $\beta_{w,res}$ experienced by the vehicle can be calculated by

$$\beta_{w,res} = \psi + \tan^{-1}\left(\frac{v_w - \sin(\psi+\beta)v_v}{\cos(\psi+\beta)v_v}\right), \quad \text{with } v_v = |\underline{v}_v| = |\underline{v}_v^-|. \tag{4.34}$$

It corresponds to the angle between the flow vector $\underline{v}_{res}$ and the longitudinal vehicle axis. Here $\beta_{w,res}$ is defined in clockwise direction such that a positive angle results during cross-wind.
In the wind-tunnel situation the free-stream velocity u_∞ for nominal, straight flow conditions faces in a negative x_0-direction, whereas the cross-wind component v_w points in a positive y_0-direction. Superimposing these velocities with the component v_l^- due to lateral vehicle motion yields the flow vector $\underline{v}_{res}$. Thus, the wind tunnel model experiences an effective cross-wind angle

$$\beta_{w,m} = \psi_m + \tan^{-1}\left(\frac{v_w - v_l^-}{u_\infty}\right), \tag{4.35}$$

when exposed to side-wind gusts with combined lateral vehicle motion. Differences between the arc tangent terms in Eq. 4.34 and 4.35 are negligible, considering that the lateral vehicle velocity is calculated by

$$v_l = \sin(\psi+\beta)v_v, \tag{4.36}$$

and that the free-stream velocity u_∞ is approximately equal to

$$u_\infty \approx \cos(\psi+\beta)v_v, \tag{4.37}$$

for small angles ψ and β. This means that the model must be rotated during gusts by the angle

$$\psi_m = \psi, \tag{4.38}$$

so that the effective cross-wind angles $\beta_{w,res}$ and $\beta_{w,m}$ become approximately equal for on-road and wind tunnel flow conditions.
As already pointed out in the description of the experimental setup in section 4.1.3, the transient forces and moments measured by the 6-component balance during vehicle motion have to

be compensated for the model's inertia. This is done via two 3-axial accelerometers that are installed at the front and rear axle location to monitor the model's angular and lateral acceleration. The necessary coefficients for converting the accelerometer readings to inertial forces and moments are determined from identification experiments in the switched-off wind tunnel, see also section 4.1.3.

Fig. 4.24 shows the raw, uncompensated side-force and yaw-moment coefficients $c_{S,raw}$ and $c_{N,raw}$ during a cross-wind gust with simultaneous lateral vehicle motion in comparison with their compensated values. Additionally, the plot includes the surrogate variables $\hat{c}_S$ and $\hat{c}_N$ calculated entirely from surface-pressure measurements as described in section 4.2.2. The transient evolution of the compensated values from the direct force and moment measurements coincides well with that of the surrogate variables. This suggests that both methods yield a correct estimate of the external transient aerodynamic forces and moments during gusts, even during dynamic model motion.

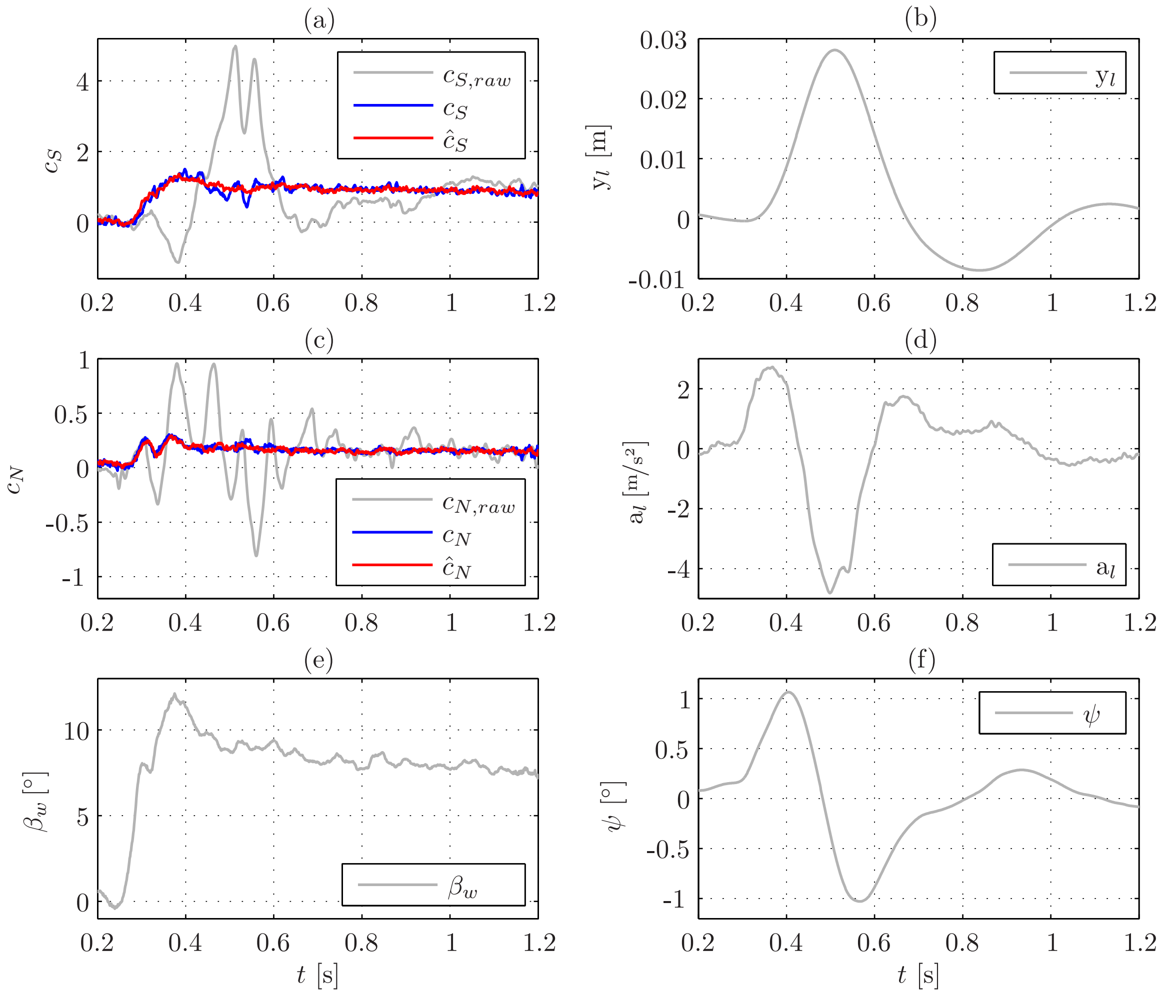

Figure 4.24: Comparison of the transient evolution of the side-force coefficient (a) and the yaw-moment coefficient (c) for a gust with a maximum cross-wind angle $\beta_w \approx 11°$ (e) and simultaneous lateral vehicle motion (b, d, f) at $Re_L = 4 \cdot 10^5$. The raw, uncompensated data is plotted in gray; the blue lines show the coefficients that are compensated for to reduce the effects of the model's inertia; the red lines represent the surrogate coefficients calculated from surface-pressure measurements.

4.5.2 Scaling to wind tunnel dimensions

The cross-wind gust experiments are carried out for a range of Reynolds numbers $3 \cdot 10^5 \leq Re_L \leq 6 \cdot 10^5$ as listed in Table 4.1. The values of the coefficients for single-track model and virtual driver are given in Table 4.2. They describe a typical delivery van of the European 3.5t-class with

Wind tunnel	Re_L	$3 \cdot 10^5$	$4 \cdot 10^5$	$5 \cdot 10^5$	$6 \cdot 10^5$
	$\mathrm{v}_v = \overline{\mathrm{u}}_\infty$ [m/s]	11.4	15.2	19.0	22.8
Real vehicle	$\mathrm{v}_{v,\mathrm{real}}$ [km/h]	90	120	150	180

Table 4.1: Driving speeds and wind tunnel free-stream velocities applied for the scaling of single-track and virtual driver coefficients.

medium load, which is similar in shape and dimensions to the generic 3D bluff body studied in this thesis. In order to match the smaller model dimensions and the current free-stream velocity in the wind tunnel, these coefficients have to be scaled. This is done according to their respective units such that nondimensional time $t^* = t_{\mathrm{real}}\mathrm{v}_{v,\mathrm{real}}/L_{\mathrm{real}} = t\mathrm{v}_v/L$ and nondimensional length $\mathrm{x}^* = \mathrm{x}_{\mathrm{real}}/L_{\mathrm{real}} = \mathrm{x}/L$ remain equal for the real van and the model vehicle. Here, the simulated driving speed v_v of the wind tunnel model corresponds to the mean axial free-stream velocity $\overline{\mathrm{u}}_\infty$ in the test section. The resulting scaling factors for the coefficients of the single-track model and the virtual driver are given in Table 4.2, along with their respective values for the real vehicle and the wind tunnel model. In principle, the scaling approach allows the lateral vehicle dynamics to be simulated and replicated for arbitrary driving velocities, even at a fixed wind tunnel free-stream velocity. However, in the cross-wind experiments the simulated driving speed v_v of the model vehicle is changed proportionally to the actual free-stream velocity $\overline{\mathrm{u}}_\infty$ in the wind tunnel, as listed in Table 4.1. Thus, the closed-loop control strategy has to be able to cope with simultaneously changing frequency characteristics of vehicle dynamics and transient aerodynamics as would be the case in a real on-road application. This also means that the ratio between simulated, unscaled driving speed $\mathrm{v}_{v,\mathrm{real}}$ and free-stream velocity $\overline{\mathrm{u}}_\infty$ in the test section remains constant throughout all experiments, as do the scaled values for the coefficients of the driver-vehicle simulation given in the right column of Table 4.2.

For the implementation in the wind tunnel the scaled driver-vehicle system is represented by a state-space model

$$\begin{bmatrix} \underline{\dot{x}}_v \\ \underline{\dot{x}}_{drv} \end{bmatrix} = \underbrace{\begin{bmatrix} \boldsymbol{A}_v & \boldsymbol{B}_v\boldsymbol{C}_{drv} \\ \boldsymbol{B}_{drv}\boldsymbol{C}_{drv} & \boldsymbol{A}_{drv} + \boldsymbol{B}_{drv}\boldsymbol{D}_v\boldsymbol{C}_{drv} \end{bmatrix}}_{\boldsymbol{A}_{vd}} \begin{bmatrix} \underline{x}_v \\ \underline{x}_{drv} \end{bmatrix} + \underbrace{\begin{bmatrix} \boldsymbol{E}_v \\ \boldsymbol{B}_{drv}\boldsymbol{F}_v + \boldsymbol{E}_{drv} \end{bmatrix}}_{\boldsymbol{E}_{vd}} \underline{d}_{vd}, \tag{4.39}$$

$$\underline{y}_{vd} = \underbrace{\begin{bmatrix} \boldsymbol{C}_v & \boldsymbol{D}_v\boldsymbol{C}_{drv} \end{bmatrix}}_{\boldsymbol{C}_{vd}} \begin{bmatrix} \underline{x}_v \\ \underline{x}_{drv} \end{bmatrix} + \underbrace{\boldsymbol{F}_v}_{\boldsymbol{F}_{vd}} \underline{d}_{vd}, \tag{4.40}$$

which is described more detailed in Appendix A. Equations (4.39, 4.40) describe the response $\underline{y}_{vd} = \begin{bmatrix} \mathrm{y}_l & \mathrm{v}_l & \mathrm{a}_l \end{bmatrix}^T$ of the driver-vehicle feedback loop to disturbance inputs $\underline{d}_{vd} = \begin{bmatrix} F_y & M_z \end{bmatrix}^T$. The measured aerodynamic side force S and yaw moment N have to be transformed from the geometric center of the wheelbase to the vehicle's center of gravity via

$$F_y = S \quad \text{and} \quad M_z = N - d_{CG}S, \tag{4.41}$$

as explained above. This results in the disturbance input vector

$$\underline{d}_{vd} = \begin{bmatrix} F_y \\ M_z \end{bmatrix} = \begin{bmatrix} 1 & 0 \\ -d_{CG} & 1 \end{bmatrix} \begin{bmatrix} S \\ N \end{bmatrix}, \tag{4.42}$$

which is equivalent to the equations implemented on the digital signal processor in the wind tunnel application.

	Description	Unit	Scaling factor	Variables	Real value	Scaled value
Vehicle	Length	[m]	$\frac{L}{L_{\text{real}}}$	L	5.6	0.4065
				L_{wb}	3.2	0.232
				L_f	1.71	0.124
				L_r	1.49	0.108
				d_{CG}	-0.107	-0.0077
	Mass	[kg]	$\frac{L^3}{L^3_{\text{real}}}$	m	3000	1.148
	Inertial moment	[kg m²]	$\frac{L^5}{L^5_{\text{real}}}$	J_z	7300	0.0147
	Stiffness	[N/m]	$\frac{L^2 \mathrm{v}_v^2}{L^2_{\text{real}} \mathrm{v}^2_{v,\text{real}}}$	$C_{\alpha f}$	157500	172.57
				$C_{\alpha r}$	302500	331.47
	Steering ratio	[-]	1	i_s	17.5	17.5
Driver	Time	[s]	$\frac{L}{L_{\text{real}}} \frac{\mathrm{v}_{v,\text{real}}}{\mathrm{v}_v}$	τ	0.2	0.032
				T_I	0.2	0.032
				T_S	0.7	0.111
	Frequency	[Hz]	$\frac{L_{\text{real}}}{L} \frac{\mathrm{v}_v}{\mathrm{v}_{v,\text{real}}}$	f_c	0.35	2.2
	Angle	[°]	1	ϕ_r	35	35

Table 4.2: Scaling factors from real-sized vehicle to wind tunnel model dimensions for the coefficients of single-track model and virtual driver.

The effect of scaling to wind tunnel dimensions on the frequency response of the driver-vehicle system can be depicted by calculating the transfer function $G_{\mathrm{a}_l\beta_w}(s)$, which describes the response of the lateral vehicle acceleration a_l to changes in cross-wind angle β_w. Hereby, S and N are replaced by their non-dimensional coefficients using

$$S = \frac{\rho}{2}\overline{\mathrm{u}}_\infty^2 A_B c_S \quad \text{and} \quad N = \frac{\rho}{2}\overline{\mathrm{u}}_\infty^2 A_B L_{wb} c_N. \tag{4.43}$$

Assuming quasi-steady aerodynamics and linearizing, c_S and c_N can be approximated by

$$c_S \approx \left.\frac{\partial c_S}{\partial \beta_w}\right|_S \beta_w \quad \text{and} \quad c_N \approx \left.\frac{\partial c_N}{\partial \beta_w}\right|_S \beta_w. \tag{4.44}$$

Note that the partial derivatives with respect to the cross-wind angle β_w correspond to the steady-state gains of the model identified in section 4.2.3 for the transient aerodynamic cross-wind gust response of the 3D bluff body. The dynamic part of this model is neglected here for now, but its impact on the driver-vehicle system for varying driving velocities is discussed later in section 4.5.3. Replacing the disturbance vector $\underline{d}_{vd}$ by

$$\underline{d}_{vd,quasi\text{-}steady} = \frac{\rho}{2}\overline{\mathrm{u}}_\infty^2 A_B \begin{bmatrix} \left.\frac{\partial c_S}{\partial \beta_w}\right|_S \\ -d_{CG} \left.\frac{\partial c_S}{\partial \beta_w}\right|_S + L_{wb} \left.\frac{\partial c_N}{\partial \beta_w}\right|_S \end{bmatrix} \beta_w, \tag{4.45}$$

assuming quasi-steady aerodynamics, and transferring Eq. (4.39) and (4.40) for the third output variable a_l into the Laplace domain yields the transfer function $G_{\mathrm{a}_l\beta_w}(s)$.

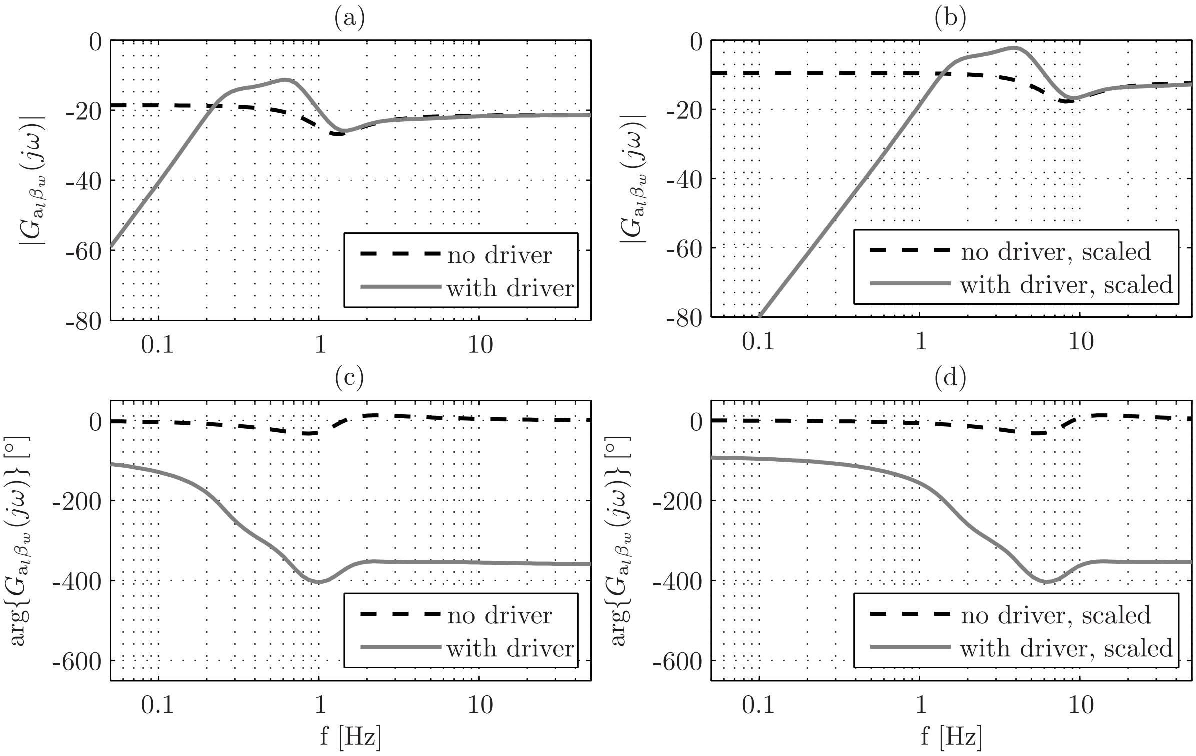

Figure 4.25: Comparison of the magnitude and phase response of the lateral vehicle acceleration a_l for the single-track model with and without driver in the unscaled and scaled cases, assuming a quasi-steady aerodynamic response to changes in cross-wind angle β_w. Plots (a) and (c) show the frequency response for the unscaled driver-vehicle model for real dimensions at a driving speed $v_{v,\text{real}} = 120\,\text{km/h} \approx 33.3\,\text{m/s}$, whereas plots (b) and (d) correspond to the model scaled to wind tunnel dimensions at a mean free-stream velocity $\overline{u}_\infty = v_v = 15.2\,\text{m/s}$.

Its frequency response is shown in Fig. 4.25 for the unscaled case of the real vehicle (a and c) and scaled case of the wind tunnel model (b and d). For comparison, the plots also include the frequency response of the vehicle model without driver. As can be seen from Fig. 4.25 (a) for the original, unscaled driver-vehicle model, the driver regulates slow disturbances of the lateral acceleration due to cross-wind gusts to zero. However, disturbances at frequencies $f > 0.2\,\text{Hz}$ are amplified by the driver relative to the frequency response of the uncontrolled vehicle without driver. This is due to the so-called "waterbed effect", a well-known consequence of feedback control for plants with time-delays or positive zeros, see e.g. Skogestad and Postlethwaite [121]. The scaling of the driver-vehicle model to the smaller wind tunnel dimensions and slower speed results in a shift to higher frequencies by a factor of about 6.3 and a larger amplitude of the acceleration response, as can be seen in Fig. 4.25 (b) and (d).

4.5.3 Interaction of transient aerodynamics and vehicle motion for various driving velocities

In automotive driving dynamics the aerodynamic forces and moments arising from cross-wind are usually taken into account via a quasi-steady approach [85]. This is done by determining the derivatives of side-force and yaw-moment coefficients c_S and c_N with respect to cross-wind angle β_w from a series of steady-state measurements in which the vehicle is installed on a turntable to evaluate the forces and moments at several, constant yaw angles [56].
However, this approach completely neglects all transient effects that may arise from the unsteady aerodynamic gust response itself and from possible effects of lateral vehicle motion on unsteady aerodynamics. The relative importance of these phenomena is discussed in the following sections.

Influence of the transient aerodynamic gust response on lateral vehicle dynamics

The dynamic models identified in section 4.2.2, Eq. (4.9) and (4.10), permit an analysis of how the transient aerodynamic cross-wind gust response affects lateral vehicle dynamics. In order to do so, the separate LPV models for c_S and c_N are combined into one LPV state-space model

$$\underline{\dot{x}}_{c_S c_N}(t) = \underbrace{\frac{\mathrm{u}_\infty(t)}{L}\boldsymbol{A}^*_{c_S c_N}}_{\boldsymbol{A}_{c_S c_N}(\theta_1)}\underline{x}_{c_S c_N}(t) + \underbrace{\frac{\mathrm{u}_\infty(t)}{L}\boldsymbol{E}^*_{c_S c_N}}_{\boldsymbol{E}_{c_S c_N}(\theta_1)} d_{c_S c_N}(t), \tag{4.46}$$

$$\underline{y}_{c_S c_N}(t) = \underbrace{\boldsymbol{C}^*_{c_S c_N}}_{\boldsymbol{C}_{c_S c_N}}\underline{x}_{c_S c_N}(t), \tag{4.47}$$

with $\theta_1 = \mathrm{u}_\infty$, $d_{c_S c_N} = \hat{\beta}_w$ and $\underline{y}_{c_S c_N} = \begin{bmatrix}\hat{c}_S & \hat{c}_N\end{bmatrix}^T$. Here only the input channel for disturbances from cross-wind angle changes is taken into account, whereas the influence of the total pressure fluctuation during gusts is neglected. Note that the quasi-steady aerodynamic derivatives $\left.\frac{\partial c_S}{\partial \beta_w}\right|_S$ and $\left.\frac{\partial c_N}{\partial \beta_w}\right|_S$ in Eq. 4.45 correspond to the steady-state gains of the unsteady aerodynamic model from Eq. 4.46 and 4.47.

Evaluating the LPV model at various frozen parameter values $p = \overline{\mathrm{u}}_{\infty,i}$ for $i = 1 \dots 4$, according to Table 4.1, yields individual linear models $G_{c_S c_N,\beta_w}(j\omega, \overline{\mathrm{u}}_{\infty,i})$ for the four driving speeds investigated here. The output vector $\underline{y}_{c_S c_N}(t)$ is used to replace the input disturbance vector $\underline{d}_{vd}$ of the driver-vehicle model given by Eq. (4.39, 4.40) by the unsteady aerodynamic disturbance vector

$$\underline{d}_{vd,unsteady}(t) = \frac{\rho}{2}\overline{\mathrm{u}}_\infty^2 A_B \begin{bmatrix} 1 & 0 \\ -d_{CG} & L_{wb}\end{bmatrix} \underline{y}_{c_S c_N}(t). \tag{4.48}$$

The scaled coefficients of driver and vehicle models are constant for the chosen fixed ratio between simulated unscaled driving velocity v and wind tunnel free-stream velocity u_∞, see Table 4.2. However, the state-space equations of the single-track model and those of the overall driver-vehicle model depend on the driving velocity v, as can be seen from Eq. (A.7, A.8) and (A.14, A.15) in Appendix A. Evaluating the scaled driver-vehicle model at the scaled driving speeds v_m according to Table 4.1 yields a set of four models for the lateral vehicle dynamics. Combining them with the unsteady aerodynamic input disturbance vector given in Eq. 4.48 and with the corresponding transient aerodynamic models, results in a set of models $G_{\mathrm{a}_l\beta_w}(j\omega, \overline{\mathrm{u}}_{\infty,i})$. They describe the lateral vehicle acceleration response to cross-wind angle disturbances β_w at the driving speeds $v_{m,i} = \overline{\mathrm{u}}_{\infty,i},\ \forall i = 1 \dots 4$ when taking unsteady aerodynamics into account. Figure 4.26 (a) and (b) shows their frequency responses in comparison with those of driver-vehicle models obtained based on the quasi-steady aerodynamic assumption in Eq. (4.45). In the lower plots (c) and (d) of Fig. 4.26 the magnitude and phase of the individual unsteady aerodynamic disturbance models for side-force coefficient $G_{c_S\beta_w}(j\omega, \overline{\mathrm{u}}_{\infty,i})$ and yaw-moment coefficient $G_{c_N\beta_w}(j\omega, \overline{\mathrm{u}}_{\infty,i})$ are given.

The bode plot of the quasi-steady models indicates that increasing driving speed mostly leads to a larger acceleration response to gusts with the same magnitude of cross-wind angle disturbances, whereas the frequency characteristics and the relevant bandwidth of the driver-vehicle model changes very little, since the driver adapts to the changing vehicle behavior. When taking transient aerodynamic disturbances into account, significant differences in magnitude and phase response arise. This is particularly the case for slow driving speeds. Whereas the frequency response of the driver-vehicle system changes very little, the frequency above which transient aerodynamic effects start to be relevant decreases more and more as free-stream velocity drops. Here the yaw-moment coefficient has the most significant impact. As shown in Fig. 4.26 (c), its frequency response is characterized by a peak in magnitude at relatively low frequencies. Therefore, the lateral vehicle acceleration response to unsteady aerodynamic disturbances exceeds the simplified case for quasi-steady aerodynamics in the range of about 5 to 10 Hz, as can be seen from the dashed and straight lines in Fig. 4.26 (a).

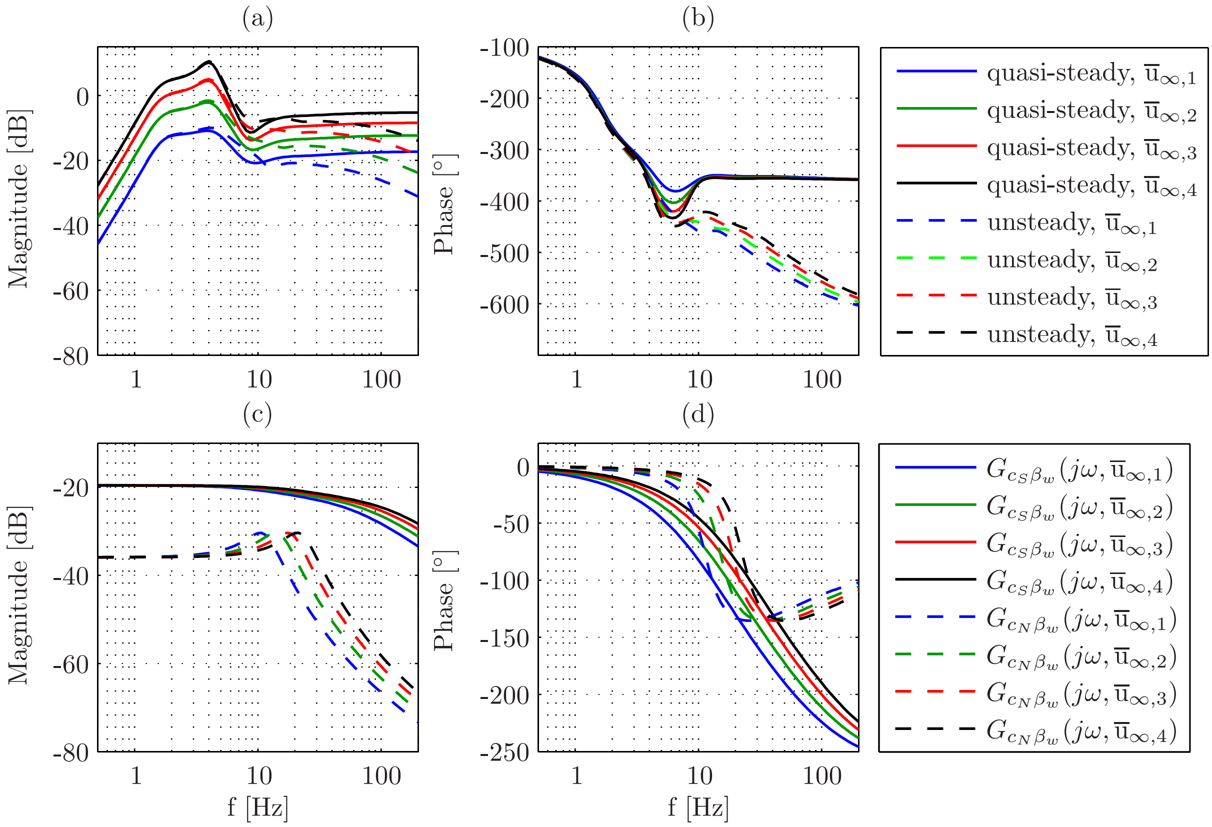

Figure 4.26: Influence of unsteady aerodynamics on the frequency response of lateral vehicle acceleration a_l to cross-wind disturbances β_w (a and b), evaluated for the scaled driver-vehicle model at increasing mean free-stream velocities $\overline{u}_{\infty,1} \dots \overline{u}_{\infty,4}$. The frequency response of the corresponding unsteady aerodynamic models for side-force and yaw-moment coefficients is given in the lower plots (c and d).

However, these differences are only significant at slow to medium driving velocities, at which the magnitude response of lateral vehicle dynamics is relatively insensitive to cross-wind disturbances. Therefore, the simple quasi-steady aerodynamic approach appears to be sufficient for the vehicle design process, at least for the vehicle type investigated here.

Influence of the lateral vehicle motion on transient aerodynamic characteristics

As discussed in the previous section, the unsteady aerodynamic characteristics of side-force and yaw-moment coefficients do have a measurable influence on the lateral vehicle dynamics. This poses the question whether the lateral vehicle motion itself has a "feedback" influence on transient aerodynamic forces and moments.

During wind tunnel experiments the unsteady aerodynamic response of side-force and yaw-moment coefficients to the gust is always present, since their real-time measurements are used as input variables for the driver-vehicle simulation. By contrast, the replication of the lateral vehicle motion in the wind tunnel test section can be switched on and off, thus allowing an easy qualitative test of its influence. Figure 4.27 shows the measured transient force and moment coefficients and the resulting lateral vehicle response from an experiment with pure driver-vehicle simulation without wind tunnel model motion, and compares them with those obtained for full real-time motion replication. These results also serve as an example for a typical lateral vehicle response to cross-wind gusts.

When the vehicle front enters the gust with a maximum cross-wind angle $\beta_w \approx 11°$, as in Fig. 4.27 (g), the side-force coefficient (a) and especially the yaw-moment coefficient (d) increase rapidly. This results in a large lateral deviation y_l (b), and significant peaks in lateral velocity

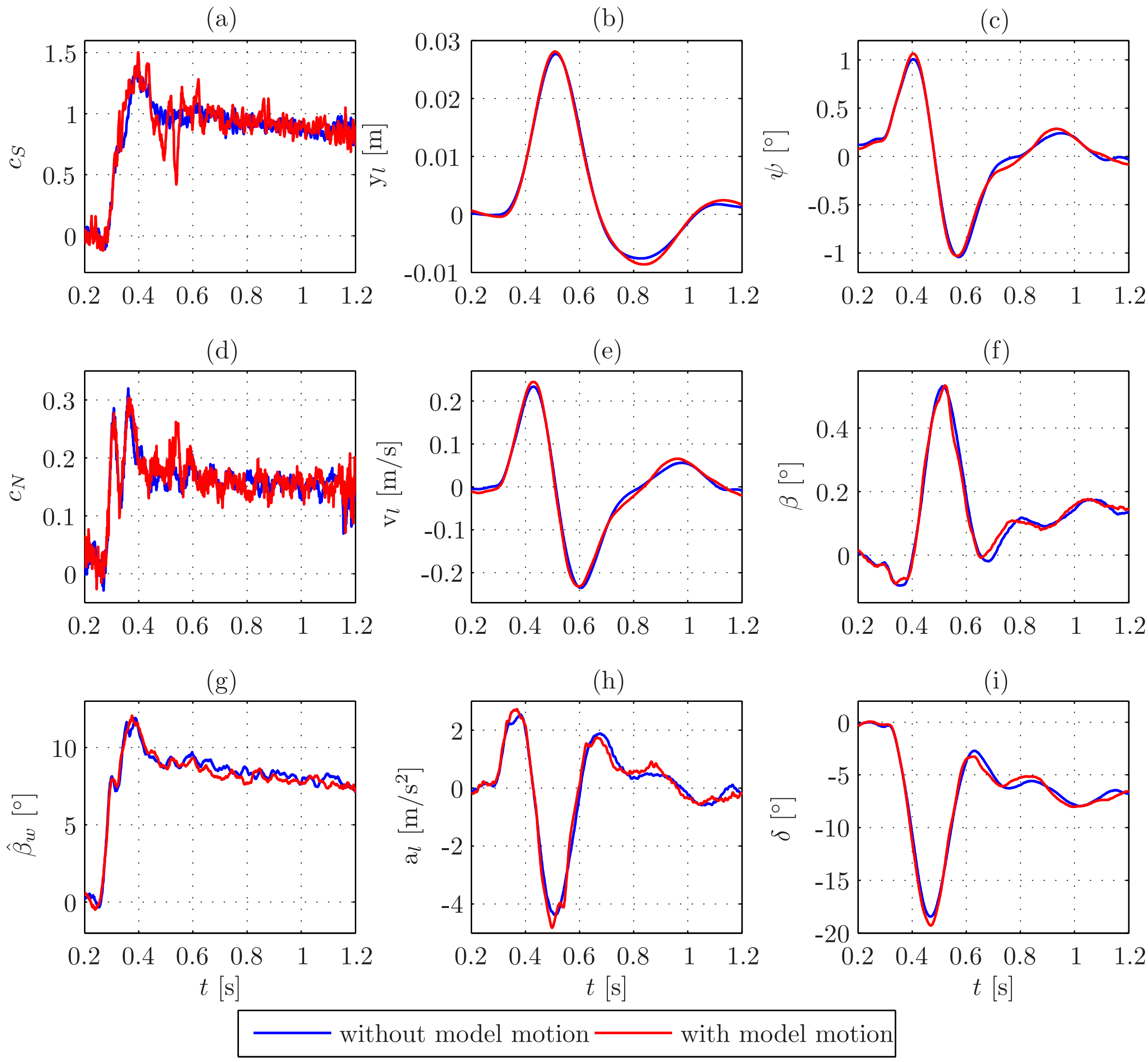

Figure 4.27: Comparison of experimental results without (blue) and with (red) model motion. Depicted are the phase-averaged time series of transient force and moment coefficients (left column) and of the simulated lateral vehicle and driver response (middle and right column) for similar gusts with a maximum cross-wind angle $\beta_w \approx 11°$ at $Re_L = 4 \cdot 10^5$.

v_l (e), acceleration a_l (h), yaw angle ψ (c) and side-slip angle β (f). The driver reacts by turning the steering wheel very far with a peak angle $\delta \approx -19°$ in an effort to compensate for the disturbance. It takes more than 0.7 s until the driver-vehicle system reaches its new steady-value. During constant cross-wind the lateral deviation, velocity and acceleration, as well as the yaw angle return to zero, while the steering wheel angle and the side-slip angle remain at values $\delta \approx -7°$ and $\beta \approx 0.17°$ for this specific gust such that the tires generate the necessary forces and moments to counter the influence of the gust.
The results obtained with and without model motion coincide very well and produce only minor differences. These may be due to insufficient compensation for the inertial forces and moments during the model motion, as can be seen by the small peaks in the side-force coefficient plotted in red in Fig. 4.27 (a). All in all, these results suggest that the feedback influence of the lateral vehicle motion on the transient aerodynamics is negligible.

4.5.4 Surrogate output variable for control synthesis

The lateral vehicle response is affected by two input disturbance variables, c_S and c_N. In order to suppress the impact of cross-wind gusts entirely, it would be desirable to regulate both variables to zero by closed-loop active flow control. However, as discussed in section 4.3, the side-force and yaw-moment coefficients cannot be controlled independently with the given actuator configuration. Asymmetric actuation with stronger blowing on the rear leeward side leads to flow acceleration in this region, which reduces the yaw moment significantly but increases the side force slightly.

For this reason a surrogate output variable is used that represents the combined effect of c_S and c_N on lateral vehicle dynamics by weighting both variables adequately. Transferring the state-space equations of the driver-vehicle system (4.39, 4.40) with the unsteady aerodynamic disturbance vector $\underline{d}_{vd,unsteady}$ from Eq. (4.48) into the Laplace domain yields

$$\mathrm{a}_l(s) = G_{\mathrm{a}_l c_S}(s) c_S(s) + G_{\mathrm{a}_l c_N}(s) c_N(s) \tag{4.49}$$

for the response of lateral vehicle acceleration to disturbances in terms of side-force and yaw-moment coefficient variations. Fig. 4.28 (a) shows the amplitude response of these two transfer functions $G_{\mathrm{a}_l c_S}(s)$ and $G_{\mathrm{a}_l c_N}(s)$ for the scaled driver-vehicle system at a free-stream velocity $\overline{\mathrm{u}}_\infty = 15.2\,\mathrm{m/s}$. The surrogate variable $y_{w_{c_S c_N}}$ should mimic the effect of both disturbance variables on the lateral vehicle response as closely as possible. Thus, demanding

$$\mathrm{a}_l(s) = G_{\mathrm{a}_l c_S}(s)\, c_S(s) + G_{\mathrm{a}_l c_N}(s)\, c_N(s) \overset{!}{=} \left(G_{\mathrm{a}_l c_S}(s) + G_{\mathrm{a}_l c_N}(s)\right) y_{w_{c_S c_N}}(s), \tag{4.50}$$

and solving for $y_{w_{c_S c_N}}$ results in

$$y_{w_{c_S c_N}} \overset{!}{=} \underbrace{\left(G_{\mathrm{a}_l c_S}(s) + G_{\mathrm{a}_l c_N}(s)\right)^{-1} G_{\mathrm{a}_l c_S}(s)}_{W_{c_S}(s)} c_S(s) + \underbrace{\left(G_{\mathrm{a}_l c_S}(s) + G_{\mathrm{a}_l c_N}(s)\right)^{-1} G_{\mathrm{a}_l c_N}(s)}_{W_{c_N}(s)} c_N(s). \tag{4.51}$$

Here $W_{c_S}(s)$ and $W_{c_N}(s)$ can be interpreted as frequency-dependent weighting factors for the effect of c_S and c_N on the lateral vehicle acceleration. Fig. 4.28 (b) shows their respective amplitude responses. Up to a frequency of approximately $f < 7\,\mathrm{Hz}$ the weighting factors remain almost constant, with the yaw-moment coefficient providing the dominant influence. For larger frequencies the side-force coefficient gains more and more importance, since its transfer function has a direct feedthrough part on lateral acceleration. However, the transfer function $G_{\mathrm{a}_l \beta_w}(j\omega)$ for the lateral vehicle response to side-wind gusts is relatively insensitive to cross-wind angle

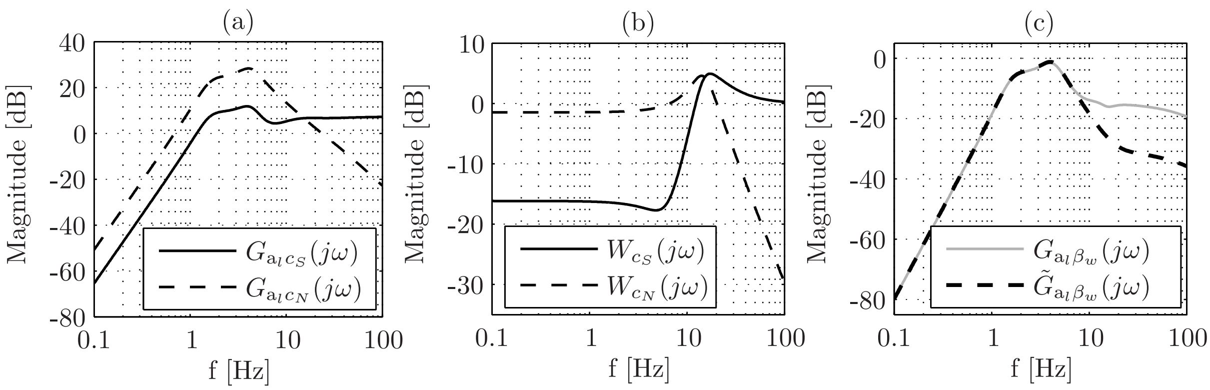

Figure 4.28: Frequency response of the transfer functions $G_{\mathrm{a}_l c_S}(s)$ and $G_{\mathrm{a}_l c_N}(s)$ for the lateral vehicle acceleration due to changes in side-force and yaw-moment coefficients (a), frequency dependent weighting factors $W_{c_S}(s)$ and $W_{c_N}(s)$ for the relative effect of c_S and c_N on lateral acceleration a_l (b), and the actual lateral acceleration response $G_{\mathrm{a}_l \beta_w}(s)$ to changes in cross-wind angle in comparison with the approximated transfer function $\tilde{G}_{\mathrm{a}_l \beta_w}(s)$ (c).

changes at frequencies $f > 7\,\mathrm{Hz}$, as in Fig. 4.28 (c). For simplicity's sake the side-force and yaw-moment coefficients are weighted with constant factors in the equation

$$y_{w_{c_S c_N}}(t) = w_{c_S} c_S(t) + w_{c_N} c_N(t), \text{ with } w_{c_S} = W_{c_S}(0) = 0.156, \text{ and } w_{c_N} = W_{c_N}(0) = 0.844. \tag{4.52}$$

The factors represent the steady-state gains of $W_{c_S}(s)$ and $W_{c_N}(s)$. Thus, the acceleration response to cross-wind gusts is approximated by

$$\mathrm{a}_l(s) \approx \underbrace{\left(G_{\mathrm{a}_l c_S}(s) + G_{\mathrm{a}_l c_N}(s)\right) \begin{bmatrix} w_{c_S} & w_{c_N} \end{bmatrix} \begin{bmatrix} G_{c_S \beta_w}(s) \\ G_{c_N \beta_w}(s) \end{bmatrix}}_{\tilde{G}_{\mathrm{a}_l \beta_w}(s)} \beta_w(s). \tag{4.53}$$

The error arising from this simplified weighting approach can be evaluated by calculating the amplitude response of the transfer function $\tilde{G}_{\mathrm{a}_l \beta_w}(s)$, as shown by the dashed line in Fig. 4.28 (c). As expected, it coincides very well with the frequency response of the actual transfer function $G_{\mathrm{a}_l \beta_w}(s)$ for frequencies $f < 7\,\mathrm{Hz}$. As will be discussed in the following section, this is slightly above the bandwidth that can be achieved by closed-loop control for the actuated flow in this specific problem. Therefore, the simplified weighting approach applied here yields a sufficient degree of accuracy for the calculation of the surrogate output variable $y_{w_{c_S c_N}}(t)$.

4.6 Control design

An efficient active flow control strategy must be designed in a way such that it is able to cope with the unsteady on-road flow conditions typically experienced by the vehicle. Here, the principal control objective is to ensure an efficient drag reduction not only for low-turbulent, straight oncoming flow, but also during cross-wind gusts. Additionally, the effects of side-wind disturbances on the lateral vehicle dynamics should ideally be suppressed to increase safety and comfort for the passengers. These goals can be achieved by a suitable MIMO control design. Two different approaches are presented and compared in the following sections. The first one is based on a robust feedback controller, which is synthesized in section 4.6.1 for the set of identified linear black-box models. The second approach is presented in section 4.6.2 and uses linear parameter-varying modeling and control synthesis methods in an effort to better take the parameter-dependent dynamics of the actuated flow into account.

Figure 4.29 shows the general controller architecture that applies to both approaches. During side-wind gusts, the changing cross-wind angle β_w and total pressure fluctuation $p_t'/\overline{p}_t$ create unsteady aerodynamic disturbances, which deviate drag, side-force and yaw-moment coefficients, c_D, c_S and c_N, from their respective nominal values. These effects are captured by the LPV model for the transient aerodynamic cross-wind gust response, whose identification is discussed in section 4.2.3. From a control theory point of view they correspond to a disturbance model, as indicated by the gray box in Fig. 4.29.

The measured side-force and yaw-moment coefficients c_S and c_N are converted to force F_y and moment M_z, which act on the center of gravity of the vehicle. They serve as input variables for the real-time simulation of the driver-vehicle model, which is scaled to wind tunnel dimensions and free-stream velocity as described in section 4.5. The calculated lateral motion is replicated via the pair of linear servo-actuators. The motion of the 3D bluff body in turn influences the unsteady aerodynamic response, as indicated by the dashed line. Although this effect is present in the wind tunnel experiments, its influence is found to be small for the relevant range of lateral vehicle motions, as discussed in section 4.5.3. It is thus omitted from the disturbance LPV model presented here.

The plant model, consisting of submodels for the actuators and for the actuated flow dynamics, forms the basis for the feedback control design. Here, the drag, side-force, and yaw-moment coefficients, c_D, c_S, and c_N, enter a block for the output calculation. This corresponds to weighting side-force and yaw-moment coefficients by their relative importance for the lateral vehicle

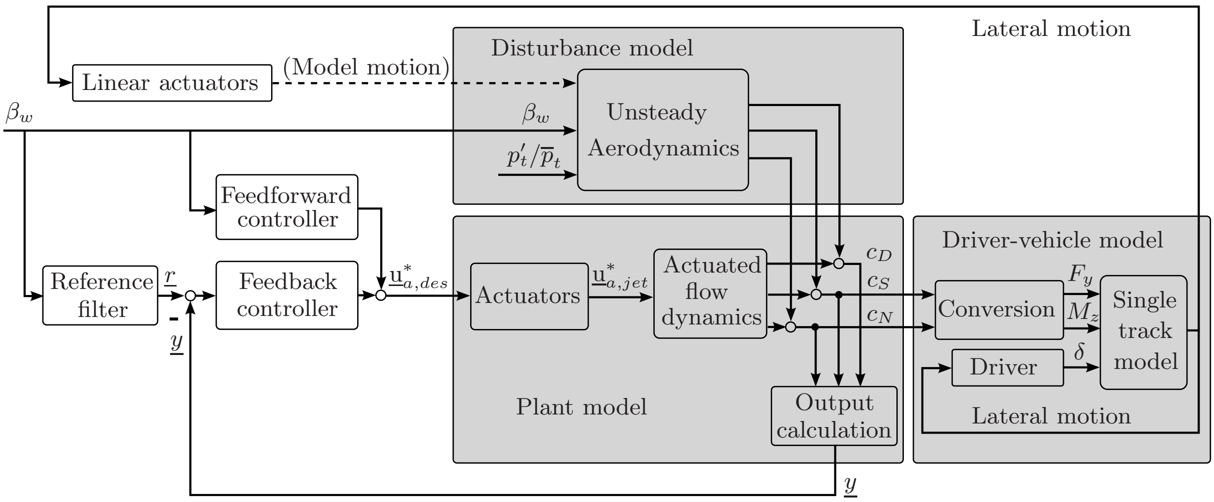

Figure 4.29: Controller architecture for the 3D bluff body. The models used for the control design and for the real-time driver-vehicle simulation are indicated by the gray boxes.

response to cross-wind gusts, as described in section 4.5.4. The output vector $\underline{y}$ is fed back and compared with the reference vector $\underline{r}$, which is determined via a reference filter to achieve an efficient drag reduction under all flow conditions. Its design is presented in section 4.6.3. The task of the feedback controller is thus to achieve good reference tracking and disturbance suppression by adjusting the values for the desired blowing velocity ratios $\underline{\mathrm{u}}^*_{a,des}$, which are commanded to the actuators. The corresponding design of the robust H_∞ controller is discussed in the next section; it is followed by the synthesis of the LPV feedback controller in section 4.6.2. Additionally, in section 4.6.4 an LPV feedforward controller is presented that uses measurements of the instantaneous cross-wind angle to further improve the bandwidth for disturbance suppression.

4.6.1 Robust H_∞ control

Nominal model and uncertainty description

The design of the robust H_∞ controller is carried out based on the actuator models and the set of black-box models of the actuated flow identified in section 4.4.2. To form the plant model for control design the three actuator models are connected in series with the inputs of each of the black-box models for actuated flow dynamics. This yields a set of 181 linear models with the same structure in discrete state-space form

$$\underline{x}(k+1) = \boldsymbol{A}\underline{x}(k) + \boldsymbol{B}\underline{u}(k-n_0), \tag{4.54}$$

$$\underline{y}(k) = \boldsymbol{C}\underline{x}(k), \tag{4.55}$$

with an input delay of $n_0 = 7$ time steps at each of the inputs at a sampling time $T_s = 1\,\mathrm{ms}$. Here, the input vector

$$\underline{u} = \begin{bmatrix}\mathrm{u}^*_{a1,des} & \mathrm{u}^*_{a2,des} & \mathrm{u}^*_{a3,des}\end{bmatrix}^T \tag{4.56}$$

corresponds to the desired blowing ratios at the three actuators, whereas the output vector

$$\underline{y} = \begin{bmatrix}\hat{c}_D & w_{c_S}\hat{c}_S + w_{c_N}\hat{c}_N\end{bmatrix}^T \tag{4.57}$$

consists of the surrogate variable for the drag coefficient and the weighted sum of estimated side-force and yaw-moment coefficients. All force and moment coefficients are estimated based on surface-pressure measurements. The weighting factors w_{c_S} and w_{c_N} are used here to form the second output variable, which approximates the combined effect of side-force and yaw-moment coefficients on the lateral dynamic vehicle response, as described in section 4.5.4. The identified MIMO state-space models are transferred into matrices of discrete transfer functions $\boldsymbol{G}_p(z)$.

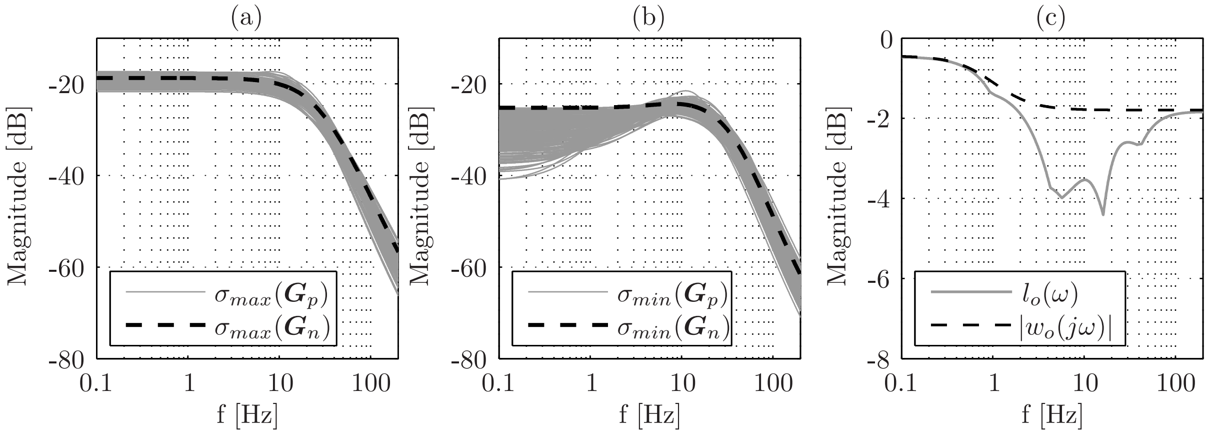

Figure 4.30: Maximal (a) and minimal (b) singular values of the set of models $\boldsymbol{G}_p$ and of the nominal model $\boldsymbol{G}_n$, and multiplicative output uncertainty $l_o(\omega)$ with the amplitude response of its upper bound $w_o(j\omega)$ (c).

Setting $z = e^{j\omega T_s}$ yields the frequency response of a discrete transfer function at a given angular frequency $\omega = 2\pi f$. This is shown in Fig. 4.30 (a) and (b) for the entire set of models $\boldsymbol{G}_p$ in terms of their maximum and minimum singular values σ_{max} and σ_{min}, which represent the largest and smallest gain of a MIMO model, respectively. For the synthesis of an H_∞ controller a nominal model $\boldsymbol{G}_n$ is necessary. However, there is no formal way of determining a suitable nominal model [121]. The primary goal is to achieve a small uncertainty, which is calculated here in in terms of the multiplicative output uncertainty

$$l_o(\omega) = \max_{\boldsymbol{G}_p \in \Pi_o} \overline{\sigma}\Big(\big(\boldsymbol{G}_p(e^{j\omega T_s}) - \boldsymbol{G}_n(e^{j\omega T_s})\big)\boldsymbol{G}_n^{-1}(e^{j\omega T_s})\Big). \tag{4.58}$$

It describes the maximal deviation of the frequency responses of all models $\boldsymbol{G}_p$ from the one of the nominal plant model $\boldsymbol{G}_n$. Additionally, the nominal model should have a low order and describe the real plant behavior well enough at the most common operating points.
As a starting point one of the identified models was chosen that yields an uncertainty $l_o(\omega) < 1$ for a large as possible frequency range. This model corresponds to the plant behavior at $Re_L = 4 \cdot 10^5$ at a steady cross-wind angle $\beta_w = 5°$. However, selecting this model as the nominal one would not be ideal, because it would result in an asymmetrical deterioration of the control performance at off-design conditions. This would particularly be the case for negative cross-wind angles, since the gains for the drag coefficient with respect to the right and left actuators change under side-wind conditions.
Therefore, the larger gain of the windward actuator is mirrored to the leeward actuator channel to obtain the nominal model. Although this model does not exactly capture the actual plant behavior at any of the individual operating conditions, it represents a good approximation of its average characteristics and ensures symmetric control performance for negative and positive cross-wind angles. As can be seen from Fig. 4.30 (c), the multiplicative output uncertainty resulting for this nominal model is below unity for all frequencies f. An upper bound for the uncertainty is chosen here as a scalar transfer function

$$w_o(s) = 0.95 \frac{\frac{1}{\omega_{o_2}} s + 1}{\frac{1}{\omega_{o_1}} s + 1}, \tag{4.59}$$

with $\omega_{o_1} = 0.95 \cdot 2\pi \frac{rad}{s}$ and $\omega_{o_2} = 1.11 \cdot 2\pi \frac{rad}{s}$, such that

$$|w_o(j\omega)| \geq l_o(\omega), \quad \forall \omega. \tag{4.60}$$

Based on an unstructured multiplicative output uncertainty $\boldsymbol{E}_o$ with a normalized uncertainty $\boldsymbol{\Delta}_o$, the complete set of models Π_o can be described by

$$\Pi_o : \boldsymbol{G}_p = (\boldsymbol{I} + \boldsymbol{E}_o)\boldsymbol{G}_n, \quad \boldsymbol{E}_o = w_o \boldsymbol{\Delta}_o, \quad \|\boldsymbol{\Delta}_o\|_\infty \leq 1. \tag{4.61}$$

More information concerning this approach is provided by Skogestad and Postlethwaite [121].

Control synthesis

The H_∞ controller $\boldsymbol{K}$ is designed based on the nominal model with an uncertainty description. This guarantees robust stability for the entire set of models. The output of the controlled plant in the nominal, unsaturated case is given by

$$\underline{y} = \boldsymbol{T}\underline{r} + \boldsymbol{S}\underline{d} - \boldsymbol{T}\underline{n}. \tag{4.62}$$

The complementary sensitivity

$$\boldsymbol{T} = (\boldsymbol{I} + \boldsymbol{G}_n\boldsymbol{K})^{-1}\boldsymbol{G}_n\boldsymbol{K} \tag{4.63}$$

represents the closed-loop transfer function with respect to the reference variable $\underline{r}$ and measurement noise $\underline{n}$, whereas the sensitivity

$$\boldsymbol{S} = (\boldsymbol{I} + \boldsymbol{G}_n\boldsymbol{K})^{-1} \tag{4.64}$$

relates to the performance at suppressing disturbances $\underline{d}$ acting on the output $\underline{y}$, such as deviations in drag, side-force and yaw-moment coefficients during cross-wind gusts. Requirements

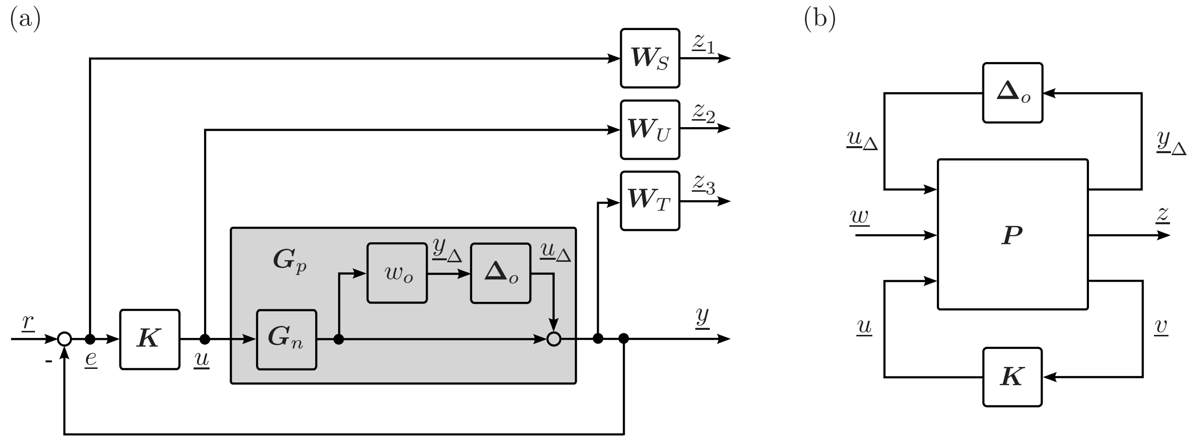

Figure 4.31: Controller architecture with the uncertain plant $\boldsymbol{G}_p$ and weights $\boldsymbol{W}_S$, $\boldsymbol{W}_U$ and $\boldsymbol{W}_T$ for the mixed sensitivity H_∞ control design (a) and generalized plant $\boldsymbol{P}$ (b) mapping the input signals $\underline{u}_\Delta$, $\underline{w} = \underline{r}$ and $\underline{u}$ to the output signals $\underline{y}_\Delta$, $\underline{z}$ and $\underline{v} = \underline{e}$.

for these closed-loop transfer functions and for the control effort $\boldsymbol{KS}$ are specified via adequate frequency-dependent weights [121]. Fig. 4.31 (a) shows the architecture of the controlled uncertain plant $\boldsymbol{G}_p$ augmented with the weights $\boldsymbol{W}_S$, $\boldsymbol{W}_U$ and $\boldsymbol{W}_T$. Here, a diagonal matrix of transfer functions

$$\boldsymbol{W}_S(s) = \begin{bmatrix} 1 & 0 \\ 0 & 1 \end{bmatrix} w_S(s), \quad \text{with } w_S(s) = \frac{\frac{1}{M_S}s + \omega_S}{s + \omega_S A_S}, \tag{4.65}$$

and $M_S = 2$, $\omega_S = 7 \cdot 2\pi \frac{rad}{s}$ and $A_S = 1 \cdot 10^{-4}$ is used to shape the sensitivity $\boldsymbol{S}$ such that disturbances are suppressed at low frequencies. The weight

$$\boldsymbol{W}_U = \begin{bmatrix} 1 & 0 & 0 \\ 0 & 1 & 0 \\ 0 & 0 & 1 \end{bmatrix} w_u(s), \quad \text{with } w_u(s) = 0.03\,\frac{s + \omega_u}{0.01s + \omega_u}, \tag{4.66}$$

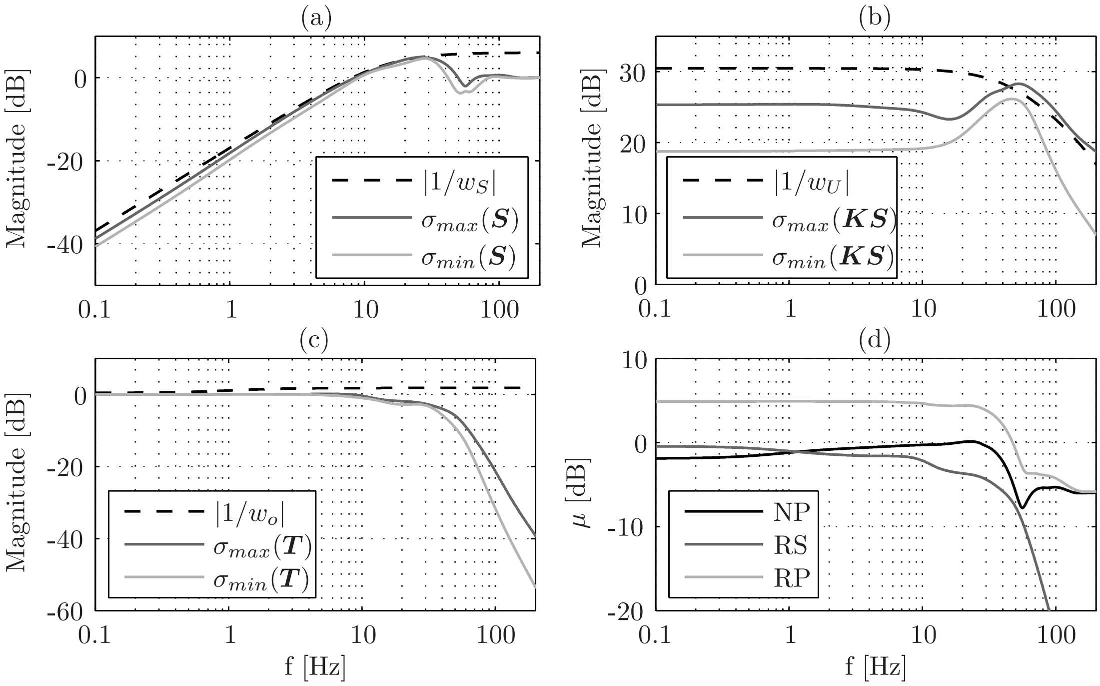

Figure 4.32: Maximum and minimum singular values of the sensitivity $\boldsymbol{S}$ (a), the control effort $\boldsymbol{KS}$ (b) and the complementary sensitivity function $\boldsymbol{T}$ (c) together with the magnitude of the inverse of the corresponding scalar weights used for the mixed-sensitivity synthesis of the H_∞ controller. The criteria for nominal performance (NP), robust stability (RS) and robust performance (RP) are shown in plot (d).

is chosen with $\omega_u = 50 \cdot 2\pi \frac{rad}{s}$ to limit the control effort $\boldsymbol{KS}$ at high frequencies. Finally, a loopshaping weight

$$\boldsymbol{W}_T = \begin{bmatrix} 1 & 0 \\ 0 & 1 \end{bmatrix} w_o(s) \tag{4.67}$$

is used for the complementary sensitivity function $\boldsymbol{T}$ with the scalar transfer function $w_o(s)$ representing an upper bound for the model uncertainty l_o. All loopshaping weights are converted to discrete-time transfer functions to facilitate the handling of the time delays at the inputs of the identified model. The controller is obtained by finding

$$\min_{\boldsymbol{K}} \|\boldsymbol{N}(\boldsymbol{K})\|_\infty, \text{ with } \boldsymbol{N}(\boldsymbol{K}) = \begin{bmatrix} \boldsymbol{W}_S\boldsymbol{S} \\ \boldsymbol{W}_U\boldsymbol{KS} \\ \boldsymbol{W}_T\boldsymbol{T} \end{bmatrix}. \tag{4.68}$$

For more details on the design of robust H_∞ controllers see [121]. Fig. 4.32 shows the result of the mixed-sensitivity controller synthesis with the frequency response of the chosen weights. With regard to disturbance suppression a nominal bandwidth of $\omega_{y_1} \approx 5.6\,\text{Hz}$ is obtained for the drag coefficient and $\omega_{y_2} \approx 6.4\,\text{Hz}$ for the weighted sum of side-force and yaw-moment coefficients. The H_∞ controller guarantees robust stability for the entire set of identified models, because the corresponding criterion

$$||w_o\boldsymbol{T}||_\infty < 1 \tag{4.69}$$

for a scalar bound of the multiplicative output uncertainty according to [121] is fulfilled. This can be seen in Fig. 4.32 (c), since the maximal singular value $\sigma_{max}(\boldsymbol{T})$ of the complementary sensitivity is smaller than the magnitude of the inverse of the upper bound $|1/w_o|$ for the uncertainty l_o at all frequencies.

Another way to evaluate whether the specifications for performance and stability of the closed control loop are met uses the structured singular value μ. A detailed discussion of the relevant theory is given by Skogestad and Postlethwaite in [121]; here the main idea is only briefly

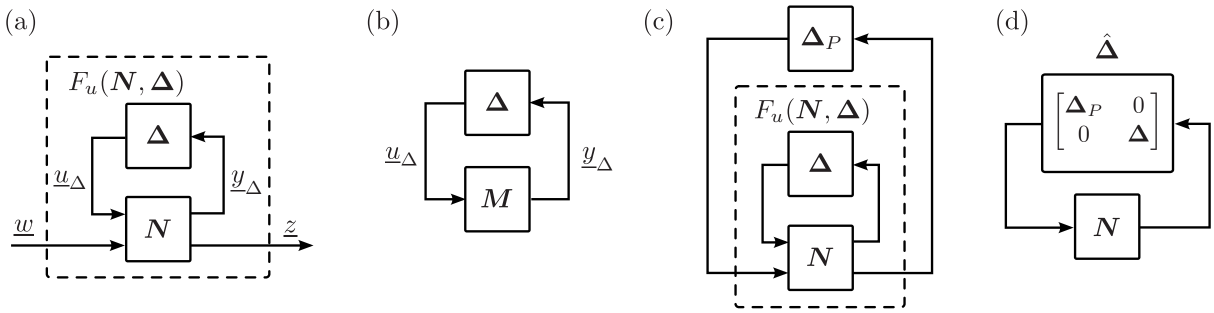

Figure 4.33: $F_u(\boldsymbol{N},\boldsymbol{\Delta})$-structure (a), $\boldsymbol{M\Delta}$-structure (b), $F_u(\boldsymbol{N},\boldsymbol{\Delta})\boldsymbol{\Delta}_P$-structure (c) and $\boldsymbol{N}\hat{\boldsymbol{\Delta}}$-structure (d) for μ-analysis of robust stability and performance.

outlined. Pulling out the uncertainty $\boldsymbol{\Delta}_o$ and the controller $\boldsymbol{K}$ as in Fig. 4.31 (b) results in the generalized plant $\boldsymbol{P}$. It maps the input signals u_Δ, $\underline{w} = \underline{r}$ and $\underline{u}$ to the output signals $\underline{y}_\Delta$, $\underline{z} = \begin{bmatrix}\underline{z}_1 & \underline{z}_2 & \underline{z}_3\end{bmatrix}^T$ and $\underline{v}$ and can be partitioned as

$$\begin{bmatrix}\underline{y}_\Delta \\ \underline{z}\end{bmatrix} = \boldsymbol{P}_{11}\begin{bmatrix}\underline{u}_\Delta \\ \underline{w}\end{bmatrix} + \boldsymbol{P}_{12}\underline{u}, \tag{4.70}$$

$$\underline{v} = \boldsymbol{P}_{21}\begin{bmatrix}\underline{u}_\Delta \\ \underline{w}\end{bmatrix} + \boldsymbol{P}_{22}\underline{u}. \tag{4.71}$$

Using $\underline{u} = \boldsymbol{K}\underline{v}$ to close a lower loop around $\boldsymbol{P}$ results in

$$\begin{bmatrix}\underline{y}_\Delta \\ \underline{z}\end{bmatrix} = \underbrace{\left(\boldsymbol{P}_{11} + \boldsymbol{P}_{12}\boldsymbol{K}(\boldsymbol{I} - \boldsymbol{P}_{22}\boldsymbol{K})^{-1}\boldsymbol{P}_{21}\right)}_{\boldsymbol{N}=F_l(\boldsymbol{P},\boldsymbol{K})}\begin{bmatrix}\underline{u}_\Delta \\ \underline{w}\end{bmatrix} = \underbrace{\begin{bmatrix}\boldsymbol{N}_{11} & \boldsymbol{N}_{12} \\ \boldsymbol{N}_{21} & \boldsymbol{N}_{22}\end{bmatrix}}_{\boldsymbol{N}}\begin{bmatrix}\underline{u}_\Delta \\ \underline{w}\end{bmatrix}. \tag{4.72}$$

The nominal system $\boldsymbol{N}$ shown in Fig. 4.33 (a) is thus related to $\boldsymbol{P}$ and $\boldsymbol{K}$ by a lower linear fractional transformation (LFT) $F_l(\boldsymbol{P},\boldsymbol{K})$. Similarly, the uncertain closed-loop transfer function from $\underline{w}$ to $\underline{z}$ is obtained by an upper LFT

$$\boldsymbol{F} = F_u(\boldsymbol{N},\boldsymbol{\Delta}) = \boldsymbol{N}_{22} + \boldsymbol{N}_{21}\boldsymbol{\Delta}(\boldsymbol{I} - \boldsymbol{N}_{11}\boldsymbol{\Delta})^{-1}\boldsymbol{N}_{12}. \tag{4.73}$$

Setting external signals to zero yields the $\boldsymbol{M\Delta}$-structure with $\boldsymbol{M} = \boldsymbol{N}_{11}$, as shown in Fig. 4.33 (b). For unstructured uncertainties $||\boldsymbol{\Delta}||_\infty \leq 1$ robust stability is achieved if $||\boldsymbol{M}||_\infty < 1$, or equivalently

$$\sigma_{max}\left(\boldsymbol{M}(j\omega)\right) < 1, \forall\omega. \tag{4.74}$$

Robust performance is achieved if the closed-loop transfer function of the uncertain system shown in Fig. 4.33 (a) satisfies

$$||F_u(\boldsymbol{N},\boldsymbol{\Delta})||_\infty < 1. \tag{4.75}$$

This condition cannot be easily evaluated as it would involve testing for all possible uncertainties $||\boldsymbol{\Delta}||_\infty \leq 1$. Instead, it is reformulated based on a fictitious feedback loop with a fictitious unstructured uncertainty $\boldsymbol{\Delta}_P$ as in Fig. 4.33 (c). Combining $\boldsymbol{\Delta}_P$ and $\boldsymbol{\Delta}$ into a single matrix yields the $\boldsymbol{N}\hat{\boldsymbol{\Delta}}$-system shown in Fig. 4.33 (d) with a block-diagonal, structured uncertainty matrix $\hat{\boldsymbol{\Delta}}$. As discussed by Skogestad and Postlethwaite in [121], the controlled uncertain plant $F_u(\boldsymbol{N},\boldsymbol{\Delta})$ achieves robust performance if the $\boldsymbol{N}\hat{\boldsymbol{\Delta}}$-system is robustly stable for the block-diagonal, structured uncertainty $\hat{\boldsymbol{\Delta}}$. This can be tested via the structured singular value μ. In contrast to the maximum singular value σ_{max}, μ also takes the structure of the uncertainty into account. It can also be used to test for nominal performance and robust stability of the closed control loop. This is shown in Figure 4.32 (d) for the 3D bluff body for the criteria

$$\text{Nominal performance (NP)} \quad \leftrightarrow \quad \sigma_{max}(\boldsymbol{N}_{22}) = \mu_{\boldsymbol{\Delta}_P}(\boldsymbol{N}_{22}) < 1, \quad \forall\omega, \tag{4.76}$$

$$\text{Robust stability (RS)} \quad \leftrightarrow \quad \mu_{\boldsymbol{\Delta}}(\boldsymbol{N}_{11}) < 1, \quad \forall\omega, \tag{4.77}$$

$$\text{Robust performance (RP)} \quad \leftrightarrow \quad \mu_{\hat{\boldsymbol{\Delta}}}(\boldsymbol{N}) < 1, \quad \forall\omega, \tag{4.78}$$

derived by Skogestad and Postlethwaite in [121]. Whereas nominal performance (NP) and robust stability (RS) are guaranteed by the H_∞ controller $\boldsymbol{K}$, robust performance (RP) is not achieved for the controlled uncertain plant. This means that disturbances acting on the controlled plant at certain off-design operating conditions cannot be suppressed with the same performance as in the nominal case.
The performance of the robust controller $\boldsymbol{K}$ was also tested in wind tunnel experiments. To account for actuator saturation, the control loop was augmented by a dynamic anti-reset windup compensator following the method proposed by Park and Choi [98]. Figure 4.34 shows sample results for the controlled flow in comparison with the natural flow for similar gusts with a maximum cross-wind angle $\beta_w \approx 10°$ at $Re_L = 4 \cdot 10^5$. The trajectories of the reference

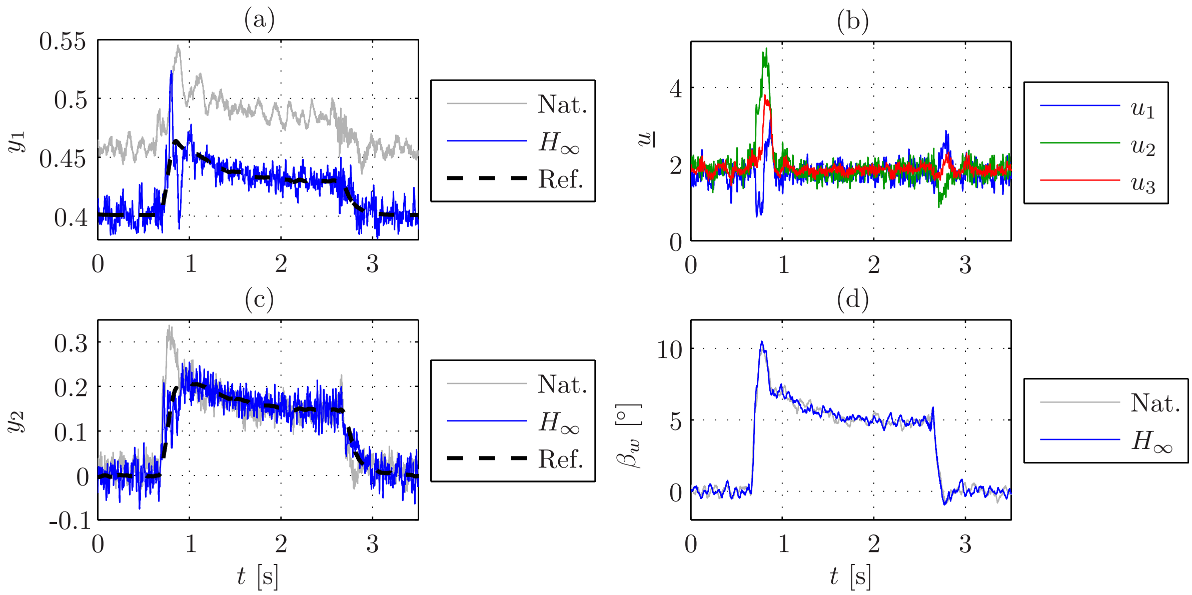

Figure 4.34: Experimental results obtained with the robust H_∞ controller in comparison with the natural flow for similar gusts with a maximum cross-wind angle $\beta_w \approx 10°$ at $Re_L = 4 \cdot 10^5$.

variables are calculated online based on measurements of the instantaneous cross-wind angle $\hat{\beta}_w(t)$ as estimated from pressure readings at the vehicle's front. A look-up table is used for the setpoint r_1 to achieve an efficient reduction of the drag coefficient shown in plot (a). A dynamic reference filter is applied for r_2 – see plot (c) – such that y_2 is slowly increased to the steady-state value of the natural flow, giving the driver enough time to react to the cross-wind gust. The setpoint calculation and the dynamic reference filter are described in more detail in section 4.6.3.
Fig. 4.34 (b) shows the actuating variables. All three of them are adjusted simultaneously by the robust H_∞ controller to regulate y_1 and y_2 to their desired time-varying reference values. Although a significant peak occurs in the controlled drag coefficient at the beginning of the gust, as in plot (a), the controller achieves a satisfactory overall performance in setpoint tracking and disturbance suppression. In section 4.7 this performance is compared with that of LPV feedback and feedforward control. Also included is a discussion of the effects of closed-loop AFC on the lateral vehicle response to cross-wind gusts.

4.6.2 LPV feedback control

LPV plant model

The LPV models identified in section 4.4.3 capture the actuated flow dynamics of drag, side-force and yaw-moment coefficients. Connecting these models in series with the linear actuator models yields an overall LPV plant model

$$\underline{\dot{x}}_{\text{afc}} = \underbrace{(\boldsymbol{A}_{\text{afc},0} + \theta_1 \boldsymbol{A}_{\text{afc},1} + \theta_2 \boldsymbol{A}_{\text{afc},2})}_{\boldsymbol{A}_{\text{afc}}(\underline{\theta})} \underline{x}_{\text{afc}} + \boldsymbol{B}_{\text{afc}} \underline{u}^*, \tag{4.79}$$

$$\underline{y}^*_{\text{afc}} = \boldsymbol{C}_{\text{afc}}\, \underline{x}_{\text{afc}}, \tag{4.80}$$

with

$$\underline{u}^* = \begin{bmatrix} \mathrm{u}^*_{a_1,des} \\ \mathrm{u}^*_{a_2,des} \\ \mathrm{u}^*_{a_3,des} \end{bmatrix} = \begin{bmatrix} \mathrm{u}_{a_1,des}/\mathrm{u}_\infty \\ \mathrm{u}_{a_2,des}/\mathrm{u}_\infty \\ \mathrm{u}_{a_3,des}/\mathrm{u}_\infty \end{bmatrix}, \quad \underline{y}^*_{\text{afc}} = \begin{bmatrix} \hat{c}_D \\ w_{c_S}\hat{c}_S + w_{c_N}\hat{c}_N \end{bmatrix}, \quad \underline{\theta} = \begin{bmatrix} \mathrm{u}_\infty \\ \beta_w \mathrm{u}_\infty \end{bmatrix}. \tag{4.81}$$

Here, the constant matrix $\boldsymbol{B}_{\text{afc}}$ corresponds to the input matrices of the actuator models. The dynamics of the actuators, as well as the parameter-dependent dynamics of drag, side-force and yaw-moment coefficients are captured by the varying state-matrix $\boldsymbol{A}_{\text{afc}}(\underline{\theta})$.
The output variable vector $\underline{y}^*_{\text{afc}}$ is calculated from the state variables via the constant output matrix $\boldsymbol{C}_{\text{afc}}$ and consists of the drag coefficient and the weighted sum of side-force and yaw-moment coefficients. All values of the LPV state-space matrices are given in Appendix C.2.2.

LPV control synthesis

For the synthesis of the LPV controller the LPV plant model (4.79, 4.80), denoted here by $\boldsymbol{G}(\underline{\theta})$, is augmented by frequency-dependent weights $\boldsymbol{W}_S(s)$ and $\boldsymbol{W}_U(s)$ as shown in Fig. 4.35 (a). For the sensitivity $\boldsymbol{S}(\underline{\theta})$ of the controlled LPV plant, the same diagonal matrix of transfer functions

$$\boldsymbol{W}_S(s) = \begin{bmatrix} 1 & 0 \\ 0 & 1 \end{bmatrix} w_S(s), \qquad \text{with } w_S(s) = \frac{\frac{1}{M_S}s + \omega_S}{s + \omega_S A_S}, \tag{4.82}$$

and $M_S = 2$, $\omega_S = 7 \cdot 2\pi \frac{rad}{s}$ and $A_S = 1 \cdot 10^{-4}$ is used as in the linear H_∞ controller synthesis. By contrast, the weighting function for the LPV control effort is specified slightly differently from the linear case, with

$$\boldsymbol{W}_U = \begin{bmatrix} 1 & 0 & 0 \\ 0 & 1 & 0 \\ 0 & 0 & 1.4 \end{bmatrix} w_u(s), \tag{4.83}$$

and a scalar transfer function

$$w_u(s) = 0.02\, \frac{s + \omega_u}{0.01s + \omega_u}, \tag{4.84}$$

with $\omega_u = 50 \cdot 2\pi \frac{rad}{s}$. Since two output variables are to be controlled with three input variables, there is an additional degree of freedom when regulating the plant to given reference values, i.e. the same drag coefficient can be achieved with different combinations of control input amplitudes. Therefore, the relative usage of the three actuators has to be adjusted via adequate weights for the control effort. Compared with the robust control design, a larger penalty is applied for the weighting of the third control input in the LPV design, but a smaller penalty for the overall LPV control effort. This is due to the different gains of the LPV model for the drag coefficient relative to the linear nominal model. The chosen values were obtained by tuning the weights experimentally so that all three control inputs are used at approximately equal amplitudes when controlling the drag coefficient under nominally straight flow conditions. This corresponds to the most efficient actuation determined in open-loop experiments, see section 4.3.

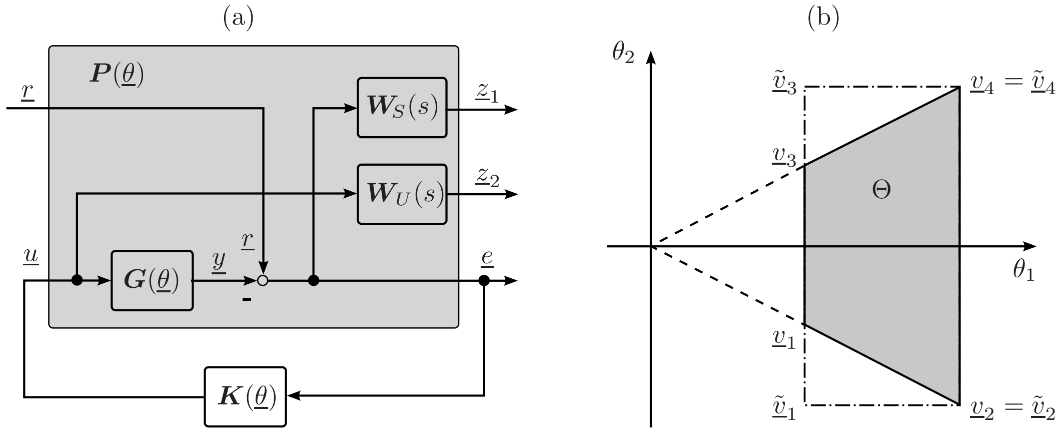

Figure 4.35: Generalized plant for LPV feedback control synthesis (a) and parameter polytope (b)

Augmenting the LPV plant (4.79, 4.80) with the weights $\boldsymbol{W}_S(s)$ and $\boldsymbol{W}_U(s)$ yields the generalized plant $\boldsymbol{P}(\underline{\theta})$ as shown in Fig. 4.35 (a). In the state-space form given by Eq. (2.16 - 2.18) it becomes

$$\boldsymbol{P}(\underline{\theta}) := \left\{ \begin{bmatrix} \dot{\underline{x}} \\ \underline{z} \\ \underline{y} \end{bmatrix} = \begin{bmatrix} \boldsymbol{A}(\underline{\theta}) & \boldsymbol{B}_1 & \boldsymbol{B}_2 \\ \boldsymbol{C}_1 & \boldsymbol{D}_{11} & \boldsymbol{D}_{12} \\ \boldsymbol{C}_2 & \boldsymbol{D}_{21} & 0 \end{bmatrix} \begin{bmatrix} \underline{x} \\ \underline{w} \\ \underline{u} \end{bmatrix} \right., \tag{4.85}$$

with the exogenous and the control inputs

$$\underline{w} = \begin{bmatrix} r_1 \\ r_2 \end{bmatrix}, \quad \text{and} \quad \underline{u} = \begin{bmatrix} \mathrm{u}_{a_1,des}/\mathrm{u}_\infty \\ \mathrm{u}_{a_2,des}/\mathrm{u}_\infty \\ \mathrm{u}_{a_3,des}/\mathrm{u}_\infty \end{bmatrix}, \tag{4.86}$$

respectively, and the weighted and the measured outputs

$$\underline{z} = \begin{bmatrix} \underline{z}_1 & \underline{z}_2 \end{bmatrix}^T = \left[\begin{array}{cc:ccc} z_{e_1} & z_{e_2} & z_{u_1} & z_{u_2} & z_{u_3} \end{array} \right]^T, \quad \text{and} \quad \underline{y} = \begin{bmatrix} \hat{c}_D \\ w_{c_S}\hat{c}_S + w_{c_N}\hat{c}_N \end{bmatrix}, \tag{4.87}$$

respectively. Here, only the state matrix $\boldsymbol{A}(\underline{\theta})$ depends on the parameter $\underline{\theta}$, and the LPV plant does not have a direct feedthrough from $\underline{u}$ to $\underline{y}$. Furthermore, the pairs $(\boldsymbol{A}(\underline{\theta}), \boldsymbol{B}_2)$ and $(\boldsymbol{A}(\underline{\theta}), \boldsymbol{C}_2)$ are quadratically stabilizable and detectable for all admissible parameter trajectories Θ, respectively. Thus, the assumptions (A1) - (A3) in section 2.1.1 are fulfilled and an LPV controller can be synthesized with the algorithm by Apkarian et al. [14].
To this end, the generalized plant $\boldsymbol{P}(\underline{\theta})$ is subsequently converted to polytopic form

$$\mathcal{P} := Co \left\{ \begin{bmatrix} \boldsymbol{A}_i & \boldsymbol{B}_1 & \boldsymbol{B}_2 \\ \boldsymbol{C}_1 & \boldsymbol{D}_{11} & \boldsymbol{D}_{12} \\ \boldsymbol{C}_2 & \boldsymbol{D}_{21} & 0 \end{bmatrix}, i = 1 \ldots 4 \right\}. \tag{4.88}$$

Here, $\boldsymbol{A}_i$ denotes the values of $\boldsymbol{A}(\underline{\theta})$ at the vertices $\underline{v}_1 \ldots \underline{v}_4$ of the parameter polytope Θ shown in Fig. 4.35 (b). In the LPV synthesis approach, usually a rectangular parameter box is applied, with corners $\tilde{v}_1 \ldots \tilde{v}_4$ corresponding to the extremal values of the parameter vector $\underline{\theta} = \begin{bmatrix} \mathrm{u}_\infty & \mathrm{u}_\infty \beta_w \end{bmatrix}^T$. Here this would result in an overbounding of the parameter space, since a correct LPV representation of the actuated flow dynamics requires a second parameter $\theta_2 = \mathrm{u}_\infty \beta_w$ with mixed dependency on two independent physical variables. However, the corners $\tilde{v}_1$ and $\tilde{v}_3$ cannot be reached by the physical plant, since they correspond to $\tilde{v}_1 = \begin{bmatrix} \mathrm{u}_{\infty,min} & \mathrm{u}_{\infty,max}\beta_{w,min} \end{bmatrix}^T$ and $\tilde{v}_3 = \begin{bmatrix} \mathrm{u}_{\infty,min} & \mathrm{u}_{\infty,max}\beta_{w,max} \end{bmatrix}^T$. This would introduce unnecessary conservatism in the design of the LPV controller.
The actual upper and lower limits due to the coupling between θ_1 and θ_2 are marked by the dashed lines in Fig. 4.35 (b). Together with admissible range $\mathrm{u}_{\infty,min} < \theta_1 < \mathrm{u}_{\infty,max}$, this results

in a trapezoidal polytope Θ with corners $\underline{v}_1 \ldots \underline{v}_4$. Using these vertices in the polytopic plant description (4.88) helps narrow the conservatism in the LPV control design. However, as pointed out by Apkarian et al. [14], it is still somewhat conservative, since the LMI conditions guarantee quadratic stability and performance for infinitely fast parameter variations. This assumption certainly does not apply to the 3D bluff body, as the free-stream velocity, corresponding to the driving velocity, changes only at a limited rate. Taking the variation rates into account as well would require more advanced control synthesis methods, such as those proposed by Apkarian et al. in [11]. This approach is not examined further in this thesis, but it represents an interesting possibility for extending the presented work.
Here, the control synthesis is carried out with the algorithm by Apkarian et al. [14] as implemented in the MATLAB-command "`hinfgs.m`". For all possible parameter trajectories, the resulting controller $K(\underline{\theta})$ guarantees global stability of the closed-loop LPV system and limits the $\mathcal{L}_2$-gain of the input/output map between $\underline{w}$ and $\underline{z}$ by

$$\|\underline{z}\|_2 < \gamma \, \|\underline{w}\|_2 \,. \tag{4.89}$$

Here, a value of $\gamma = 1.17$ is achieved. The frequency response in terms of the minimal and maximal singular values of the closed-loop transfer functions at the polytope corners is shown together with the weighting transfer functions in Fig. 4.36. Only vertices 3 and 4 are evaluated in this plot, since the controlled plant has symmetric characteristics at negative cross-angles that correspond to vertices 1 and 2. The specifications for sensitivity and control effort are fulfilled satisfactorily, with a slightly better performance at higher free-stream velocities due to the faster response of the actuated flow, as can be seen in Fig. 4.36 (d-f).

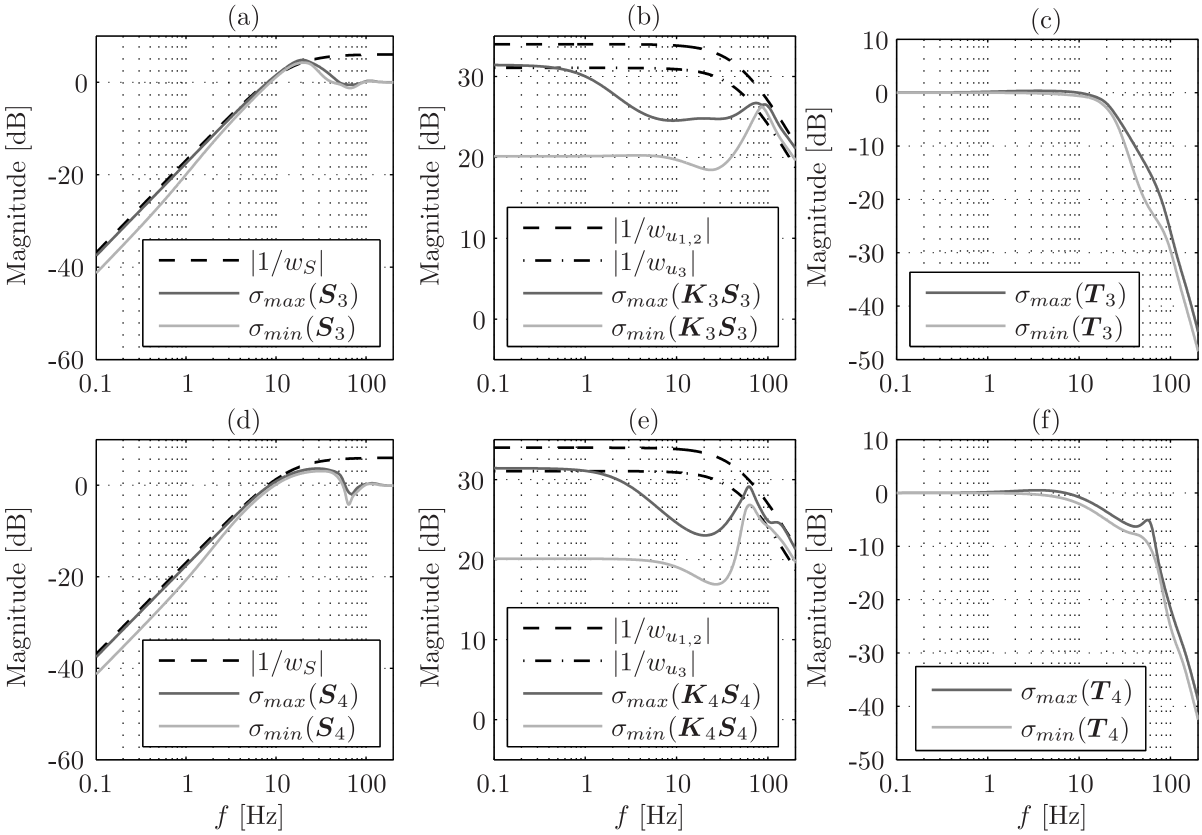

Figure 4.36: Frequency response of the weighting filters with the upper and lower singular values of the closed-loop LPV transfer functions for sensitivity, control effort and complementary sensitivity at vertices 3 (plots a-c) and 4 (plots e-f), respectively.

Implementation

Several steps are involved in implementing the synthesized LPV controller on the digital signal processor (DSP) for the real-time application in the wind tunnel experiments. First, the instantaneous controller matrices of $\boldsymbol{K}(\underline{\theta})$ resulting from the measured parameter vector $\underline{\theta}$ are calculated by interpolating online between the vertex controllers by

$$\boldsymbol{K}(\underline{\theta}) = \sum_{i=1}^{4} \alpha_i \boldsymbol{K}_i, \text{ with } \boldsymbol{K}_i = \begin{bmatrix} \boldsymbol{A}_{K_i} & \boldsymbol{B}_{K_i} \\ \boldsymbol{C}_{K_i} & \boldsymbol{D}_{K_i} \end{bmatrix}, i = 1 \dots 4, \tag{4.90}$$

with the polytopic coordinates α_i as defined by the polytope

$$\Theta = Co \left\{ \sum_{i=1}^{4} \alpha_i \underline{v}_i : \quad \alpha_i \geq 0; \quad \sum_{i=1}^{4} \alpha_i = 1 \right\}. \tag{4.91}$$

Due to fast controller modes the continuous-time state-space equations of the LPV controller

$$\dot{\underline{x}}_K(t) = \boldsymbol{A}_K(\underline{\theta}(t))\underline{x}_K(t) + \boldsymbol{B}_K(\underline{\theta}(t))\underline{e}(t), \tag{4.92}$$

$$\underline{u}(t) = \boldsymbol{C}_K(\underline{\theta}(t))\underline{x}_K(t) + \boldsymbol{D}_K(\underline{\theta}(t))\underline{e}(t), \tag{4.93}$$

cannot be solved directly by numerical integration on the DSP, as this would result in an unstable behavior at the chosen sampling rate of 1 kHz. Therefore, the controller state-space equations are discretized online via the LPV counterpart of the bilinear transformation proposed by Apkarian [10]. More details on this approach are given in section 2.1.2. The trapezoidal approximation scheme preserves the stability of the original continuous-time state-space system. However, the bilinear transformation involves a computationally costly matrix inversion. Hence, following the proposition by Apkarian [10], the update of the discrete-time controller matrices on the DSP is carried out only every second sampling step to enable a real-time application in the wind tunnel experiment.

Experimental results for a typical cross-wind gust with LPV feedback control are shown in Fig. 4.37 in comparison with the natural, uncontrolled gust response. The reference values are calculated based on a look-up table for r_1 and a dynamic reference filter for r_2. The exact approach is presented and discussed in the following section 4.6.3. The LPV feedback controller is able to regulate y_1 and y_2 very close to their respective reference trajectories by adjusting the three actuating variables simultaneously, as can be seen in plot (e). This ensures an efficient drag reduction relative to the natural flow, as in Fig. 4.37 (a). Fast variations of y_2 due to cross-wind gust disturbances are successfully suppressed. The relative contribution of the four vertex controllers is shown in Fig. 4.37 (f) for the polytopic coordinates α_i, $i = 1 \dots 4$. A comparison of the LPV feedback control performance with robust H_∞ control and a discussion of the resulting lateral vehicle response are given in section 4.7.

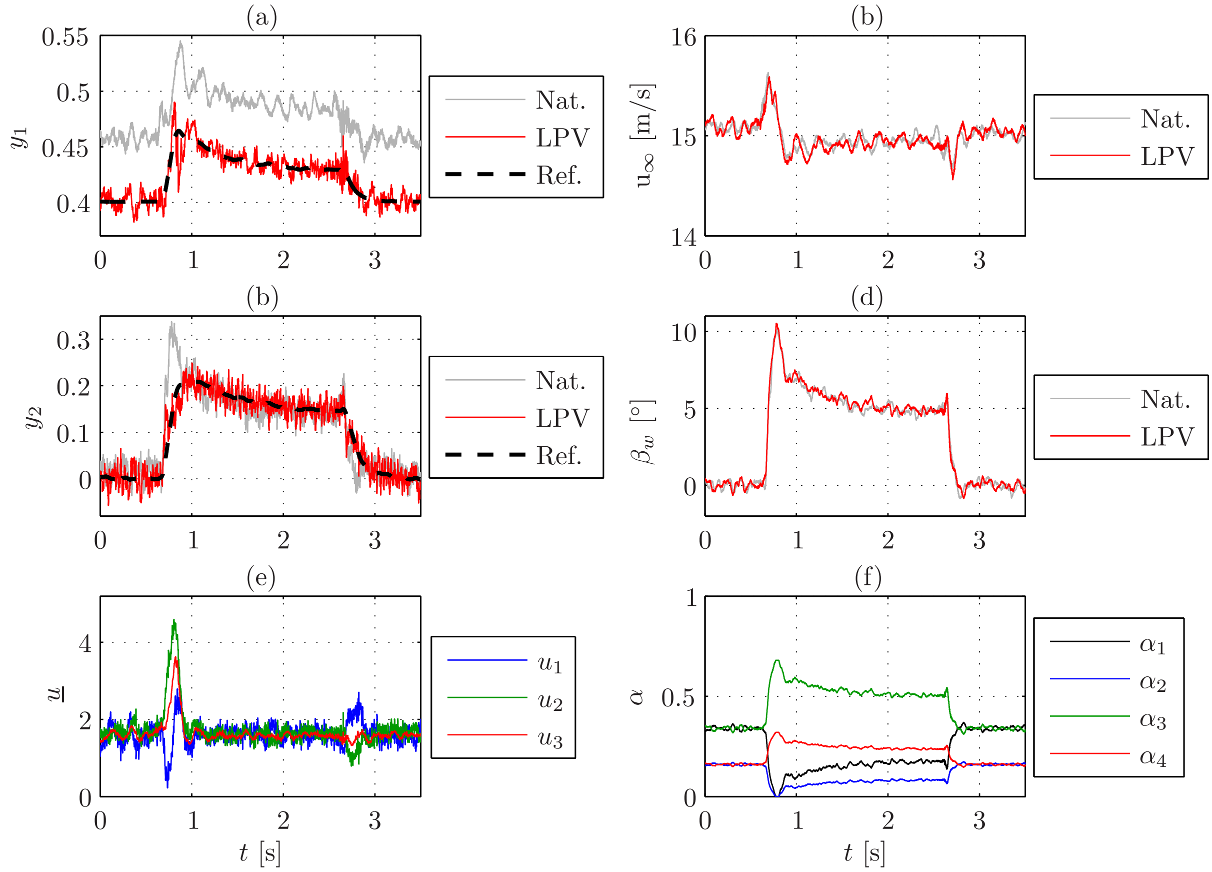

Figure 4.37: Experimental results obtained with the LPV feedback controller in comparison with the natural flow for similar gusts with a maximum cross-wind angle of $\beta_w \approx 10°$ at $Re_L = 4 \cdot 10^5$.

4.6.3 Setpoint calculation and dynamic reference filter

For closed-loop control of the flow around the 3D bluff body, adequate reference values r_1 and r_2 must be chosen to achieve an efficient reduction of the drag coefficient while improving the vehicle's cross-wind sensitivity. To this end, two different alternatives are studied.

The first version corresponds to regulating the second output variable y_2 to zero in an effort to completely suppress the influence of cross-wind gusts on the lateral dynamics. In order to create a look-up table with suitable values for the setpoint r_1, the bluff body was subjected to a range of constant cross-wind angles $0° \leq \beta_w \leq 7°$. At each angle, the flow was controlled to several drag coefficients while keeping y_2 at zero. Evaluating the net power savings $\Delta P/P_0$ for each of these steady-state experiments yields a map for the most efficient setpoint $r_1 = f(\beta_w)$ as a function of cross-wind angle.

Figure 4.38 shows the resulting look-up tables for the reference values. Only for small cross-wind angles can the drag coefficient be efficiently reduced to values below those of the natural flow, see plot (a). The output variable y_2 corresponds to the weighted sum of side-force and yaw-moment coefficients. Regulating it to zero under side-wind conditions means reducing the yaw-moment coefficient to values below zero to compensate for the effect of the side force increase on the lateral vehicle response. As already discussed in section 4.3.3 for the actuated flow characteristics, this requires large blowing velocities at the right, windward actuator, which leads to an additional increase in drag coefficient, see the steady-state map (d) in Fig. 4.13. Therefore, the complete suppression of the steady-state effect of larger cross-wind angles on the lateral vehicle response comes at the price of increasing the overall power consumption of the vehicle.

To circumvent this drawback, a second version of the setpoint calculation is applied. A human driver can easily compensate for slow variations of the cross-wind angle by turning the steering

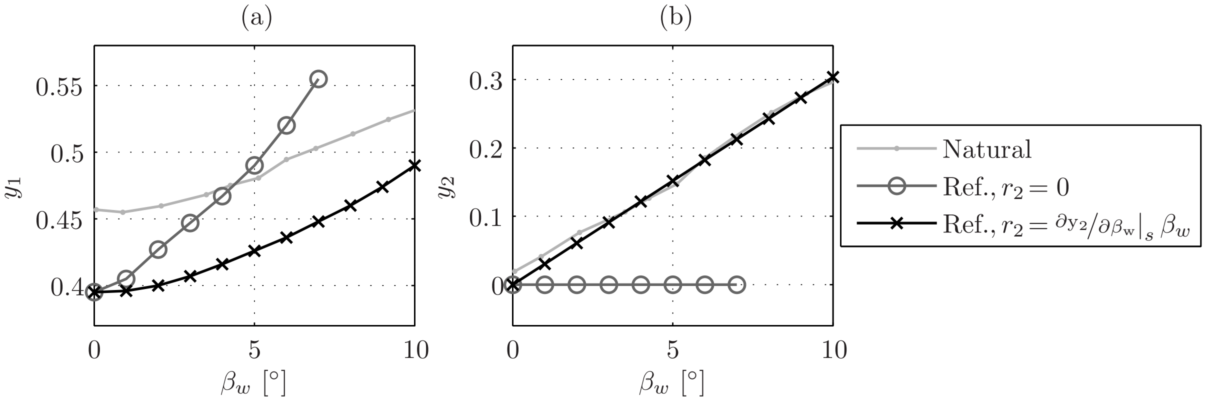

Figure 4.38: Reference values for the controllers.

wheel. For the driver-vehicle system considered here, this corresponds to a closed-loop bandwidth of $f_{bw} \approx 0.2\,\mathrm{Hz}$ for the real-sized case, and $f_{bw,m} \approx 1.5\,\mathrm{Hz}$ for the case scaled to wind tunnel dimensions, as in section 4.5, Fig. 4.25. Thus, the closed-loop active flow control strategy only has to suppress disturbances acting on lateral vehicle dynamics at frequencies above the bandwidth already achieved by the driver.

Therefore, the calculation of the reference value r_2 is carried out via a first-order dynamic reference filter

$$r_2 = F(s)\beta_w = \frac{k}{T_1 s + 1}\beta_w, \quad \text{with } T_1 = \frac{1}{\omega_F}. \tag{4.94}$$

The angular roll-off frequency is set to $\omega_F = 1.2 \cdot 2\pi\frac{\mathrm{rad}}{\mathrm{s}}$ for the wind-tunnel case, such that frequencies above 1.2 Hz are to be suppressed by feedback AFC, whereas slower disturbances are compensated for by the driver. The chosen gain is equal to the steady-state derivative of y_2 with respect to β_w of the natural flow, i.e.

$$k = \left.\frac{\partial y_2}{\partial \beta_w}\right|_S, \tag{4.95}$$

so that the vehicle response to constant cross-wind disturbances remains unaffected by AFC. Figure 4.39 shows the frequency response of the reference filter $F(s)$ in comparison with the response of the disturbance transfer function from β_w to y_2, which is evaluated here for three different cases. For the natural flow, the transient aerodynamic gust response of side-force and yaw-moment coefficients to changes in cross-wind angle β_w is described by the MISO LPV

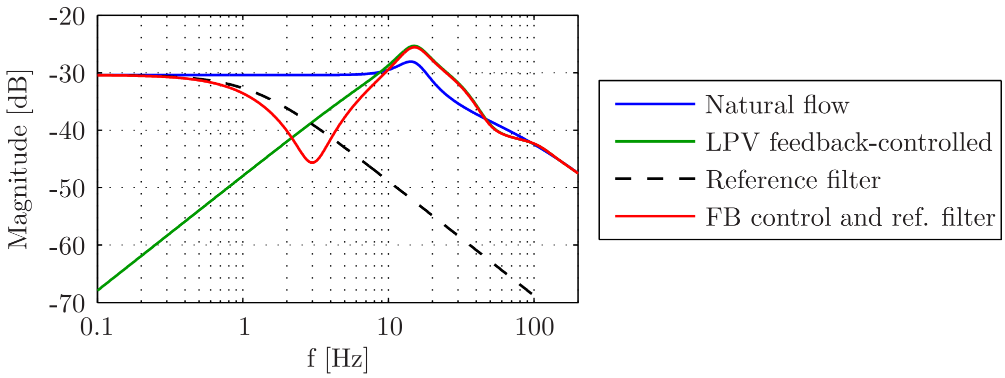

Figure 4.39: Frequency response of the reference filter $F(s)$ and of the disturbance transfer function at $Re_L = 4 \cdot 10^5$ and $\beta_w = 0°$ for the natural flow and the LPV feedback-controlled flow without and with reference filter.

models identified in section 4.2.3. Combining them into a single model with disturbance input variable $d_{c_S c_N} = \beta_w$ yields the LPV state-space equations

$$\underline{\dot{x}}_{c_S c_N} = \underbrace{\frac{\mathrm{u}_\infty}{L}\boldsymbol{A}^*_{c_S c_N}}_{\boldsymbol{A}_{c_S c_N}(\theta_1)} \underline{x}_{c_S c_N} + \underbrace{\frac{\mathrm{u}_\infty}{L}\boldsymbol{E}^*_{c_S c_N}}_{\boldsymbol{E}_{c_S c_N}(\theta_1)} d_{c_S c_N}, \tag{4.96}$$

$$\underline{y}_{c_S c_N} = \underbrace{\boldsymbol{C}^*_{c_S c_N}}_{\boldsymbol{C}_{c_S c_N}} \underline{x}_{c_S c_N} = \begin{bmatrix} 0 & 1 & 0 & 0 \\ 0 & 0 & 0 & 1 \end{bmatrix} \underline{x}_{c_S c_N}, \tag{4.97}$$

with $\theta_1 = \mathrm{u}_\infty$, $d_{c_S c_N} = \beta_w$ and $\underline{y}_{c_S c_N} = \begin{bmatrix} \hat{c}_S & \hat{c}_N \end{bmatrix}^T$. An LPV model for the weighted sum $y_2 = y_{w_{c_S c_N}} = w_{c_S} c_S + w_{c_N} c_N$ is then simply obtained from Eq. (4.97) by

$$y_2 = \begin{bmatrix} w_{c_S} & w_{c_N} \end{bmatrix} \begin{bmatrix} c_S \\ c_N \end{bmatrix} = \frac{1}{L} \begin{bmatrix} 0 & w_{c_S} & 0 & w_{c_N} \end{bmatrix} \underline{x}_{c_S c_N}, \tag{4.98}$$

with state variable $\underline{x}_{c_S c_N}$ governed by Eq. (4.96). Evaluating these LPV state-space equations for a frozen parameter value $\theta_1 = 15.2\,\mathrm{m/s}$ corresponding to $Re_L = 4 \cdot 10^5$ and transferring them into the Laplace domain yields the disturbance transfer function $G_d(s, \theta_1)$ for the natural, uncontrolled flow.
Similarly, the sensitivity of the closed-loop to output disturbances is given by

$$\boldsymbol{S}(s, \underline{\theta}) = \begin{bmatrix} S_{11}(s, \underline{\theta}) & S_{12}(s, \underline{\theta}) \\ S_{21}(s, \underline{\theta}) & S_{22}(s, \underline{\theta}) \end{bmatrix} = \left(\boldsymbol{I} + \boldsymbol{G}(s, \underline{\theta})\boldsymbol{K}(s, \underline{\theta})\right)^{-1}, \tag{4.99}$$

and the complementary sensitivity for reference tracking by

$$\boldsymbol{T}(s, \underline{\theta}) = \begin{bmatrix} T_{11}(s, \underline{\theta}) & T_{12}(s, \underline{\theta}) \\ T_{21}(s, \underline{\theta}) & T_{22}(s, \underline{\theta}) \end{bmatrix} = \left(\boldsymbol{I} + \boldsymbol{G}(s, \underline{\theta})\boldsymbol{K}(s, \underline{\theta})\right)^{-1} \boldsymbol{G}(s, \underline{\theta})\boldsymbol{K}(s, \underline{\theta}), \tag{4.100}$$

where $\boldsymbol{G}(s, \underline{\theta})$ and $\boldsymbol{K}(s, \underline{\theta})$ denote the transfer functions of the LPV plant Eq. (4.79, 4.79) and LPV feedback controller Eq. (4.92, 4.93) at frozen parameter values $\underline{\theta} = \begin{bmatrix} \mathrm{u}_\infty & \beta_w \mathrm{u}_\infty \end{bmatrix}^T = \begin{bmatrix} 15.2\,\mathrm{m/s} & 0 \end{bmatrix}^T$, respectively. The response of y_2 to disturbances $d = \beta_w$ of the feedback loop without reference filter is thus given by

$$y_2 = S_{22}(s, \underline{\theta}) G_d(s, \underline{\theta}) d. \tag{4.101}$$

Extending Eq. (4.101) by the dynamic reference filter $F(s)$ yields

$$y_2 = \left(S_{22}(s, \underline{\theta}) G_d(s, \underline{\theta}) + T_{22}(s, \underline{\theta}) F(s)\right) d. \tag{4.102}$$

As depicted in Fig. 4.39, the LPV feedback controller suppresses all disturbances acting on y_2 due to changes is cross-wind angle β_w up to a bandwidth of approximately 7 Hz. Because of a waterbed effect arising from the input time-delays of the actuators, disturbances above 10 Hz are slightly amplified relative to the natural flow.
The reference filter relaxes the disturbance suppression at low frequencies $f < 1.2\,\mathrm{Hz}$, where the driver has effective control over the vehicle. Due to the additional transfer function $T_{22}(s, \underline{\theta})$ related to reference tracking of the controller, disturbances in the range $2\,\mathrm{Hz} < f < 7\,\mathrm{Hz}$ are suppressed more strongly by the feedback controller with the reference filter than by the one without.
Of course, these frequency characteristics could also be directly achieved by specifying different loopshaping weights during control synthesis. However, the approach followed here gives more freedom in the design process from a practical point of view. First, the feedback controller is designed to provide a maximum bandwidth at disturbance suppression and reference tracking. In a second step, the steady-state side-wind sensitivity of the vehicle and the cross-over bandwidth

between closed-loop active flow control and driver can be adjusted via the parameters of the reference filter $F(s)$, independent of the synthesized feedback controller.
The disturbance suppression range $1.2\,\mathrm{Hz} < f < 7\,\mathrm{Hz}$ of the combined feedback AFC strategy with reference filter coincides well with the range of frequencies $1\,\mathrm{Hz} < f < 10\,\mathrm{Hz}$ at which lateral vehicle dynamics are sensitive to cross-wind gusts, see Fig. 4.26 in section 4.5.3. However, a better suppression at higher frequencies $f > 7\,\mathrm{Hz}$ would be desirable to further improve the vehicle's cross-wind sensitivity by AFC. This can be achieved by an additional feedforward controller, whose synthesis is discussed in the following section.

4.6.4 LPV feedforward control

As presented in section 4.2.2 for the transient gust response, the time-varying cross-wind angle $\beta_w(t)$ can be estimated from instantaneous pressure measurements with two sensors located at the vehicle's front. Based on the LPV disturbance model $G_d(\underline{\theta})$ with input $d = \beta_w$ and an LPV plant model $\tilde{\boldsymbol{G}}(\underline{\theta})$, a feedforward LPV controller $\boldsymbol{K}_d(\underline{\theta})$ can be designed to improve the performance of the AFC strategy. The synthesis is carried out with the same methods as the LPV H_∞ feedback control design described in sections 2.1.1 and 4.6.2.
Figure 4.40 (a) shows the feedforward control architecture. Changes in cross-wind angle $d = \beta_w$ cause disturbances acting on the output y_2 with parameter-dependent dynamics represented by $G_d(\underline{\theta})$. The feedforward controller $\boldsymbol{K}_d(\underline{\theta})$ counteracts these disturbances by adjusting the reduced actuating variable $\underline{\tilde{u}} = \begin{bmatrix} u_1 & u_2 \end{bmatrix}^T$ based on measurements of the disturbance input variable $d = \beta_w$. Since the LPV control synthesis algorithm by Apkarian et al. [14] requires parameter-independent feedthrough matrices of the generalized LPV plant, a fast prefilter $\boldsymbol{G}_f(s)$ is added at the plant input. A preliminary feedforward LPV controller $\boldsymbol{K}'_d(\underline{\theta})$ is then designed based on the augmented LPV plant $\tilde{\boldsymbol{P}}(\underline{\theta})$ shown in Fig. 4.40 (b).
The objective is to further reduce the cross-wind sensitivity of the vehicle by suppressing disturbances acting on y_2 in a frequency range where LPV feedback is no longer effective. The focus

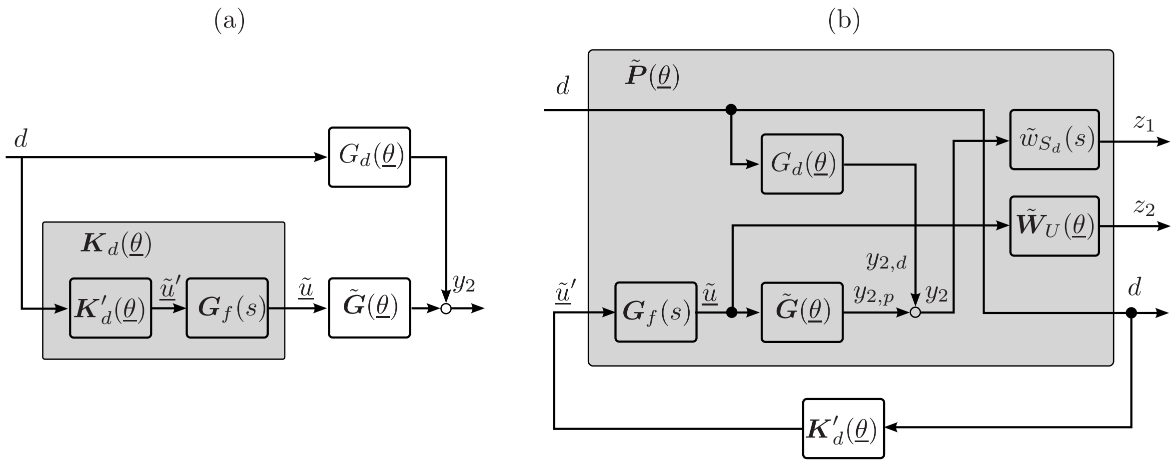

Figure 4.40: Feedforward controller architecture (a) and generalized plant for feedforward LPV H_∞ control synthesis (b).

lies on improving the lateral vehicle response, whereas a large bandwidth for control of the drag coefficient is of minor importance for the overall power consumption. Of course, the design could be extended to a "full" feedforward controller to suppress disturbances acting on the drag coefficient as well, based on measurements of the entire disturbance input vector $\underline{d} = \begin{bmatrix} \beta_w & p'_t/\overline{p}_t \end{bmatrix}$. Here, the feedforward design is carried out based on submodels for disturbance and plant to keep the controller order low. This reduces the computational effort for real-time control. The SISO model $G_d(\underline{\theta})$ introduced in the previous section describes the gust response of the weighted sum $y_2 = w_{c_S} c_S + w_{c_N} c_N$ to changes in cross-wind angle $d = \beta_w$. It corresponds to the LPV disturbance model for the feedforward design. The influence of the total pressure fluctuation

$p_t'/\overline{p}_t$ during gusts is neglected here, since it mostly affects the wake, not so much the side-force and yaw-moment coefficients.
Similarly, a submodel $\tilde{\boldsymbol{G}}(\underline{\theta})$ is derived from the overall LPV plant model $\boldsymbol{G}(\underline{\theta})$ by taking into account only the input and state variables that affect the output variable y_2. As discussed with respect to the LPV identification of actuated flow dynamics, see section 4.4.3, only wind- and leeward actuation influence side-force and yaw-moment coefficients. Hence, the third input variable u_3 and the corresponding actuator state variables have been removed from the submodel $\tilde{\boldsymbol{G}}(\underline{\theta})$. Furthermore, all states corresponding to the dynamics of the drag coefficient are omitted here. This yields a DISO LPV plant model $\tilde{\boldsymbol{G}}(\underline{\theta})$ with 14 states, instead of the original 2×3 MIMO LPV model of order $n_x = 21$.
The generalized structure of the augmented plant is shown in Fig. 4.40 (b). Specifications for the feedforward performance and control effort are taken into account via the weights $\tilde{w}_{S_d}(s)$ and $\tilde{\boldsymbol{W}}_U(\underline{\theta})$, respectively. The disturbance sensitivity $S_d(\underline{\theta})$ of the feedforward controlled plant is given by

$$y_2 = \underbrace{\left(G_d(\underline{\theta}) + \tilde{\boldsymbol{G}}(\underline{\theta})\boldsymbol{K}_d(\underline{\theta})\right)}_{S_d(\underline{\theta})} d, \tag{4.103}$$

and the corresponding weight is specified as a first order transfer function

$$\tilde{w}_{S_d}(s) = \frac{1}{k}\frac{s + \omega_{S_d}}{A_{S_d}s + \omega_{S_d}}. \tag{4.104}$$

The frequency response of its inverse $1/\tilde{w}_{S_d}(s)$ is shown in Fig. 4.41 (a) and (c). The coefficients k, ω_{S_d} and A_{S_d} are adjusted such that the feedforward controller only provides supplementary disturbance suppression and does not interfere with the feedback LPV controller. To this end,

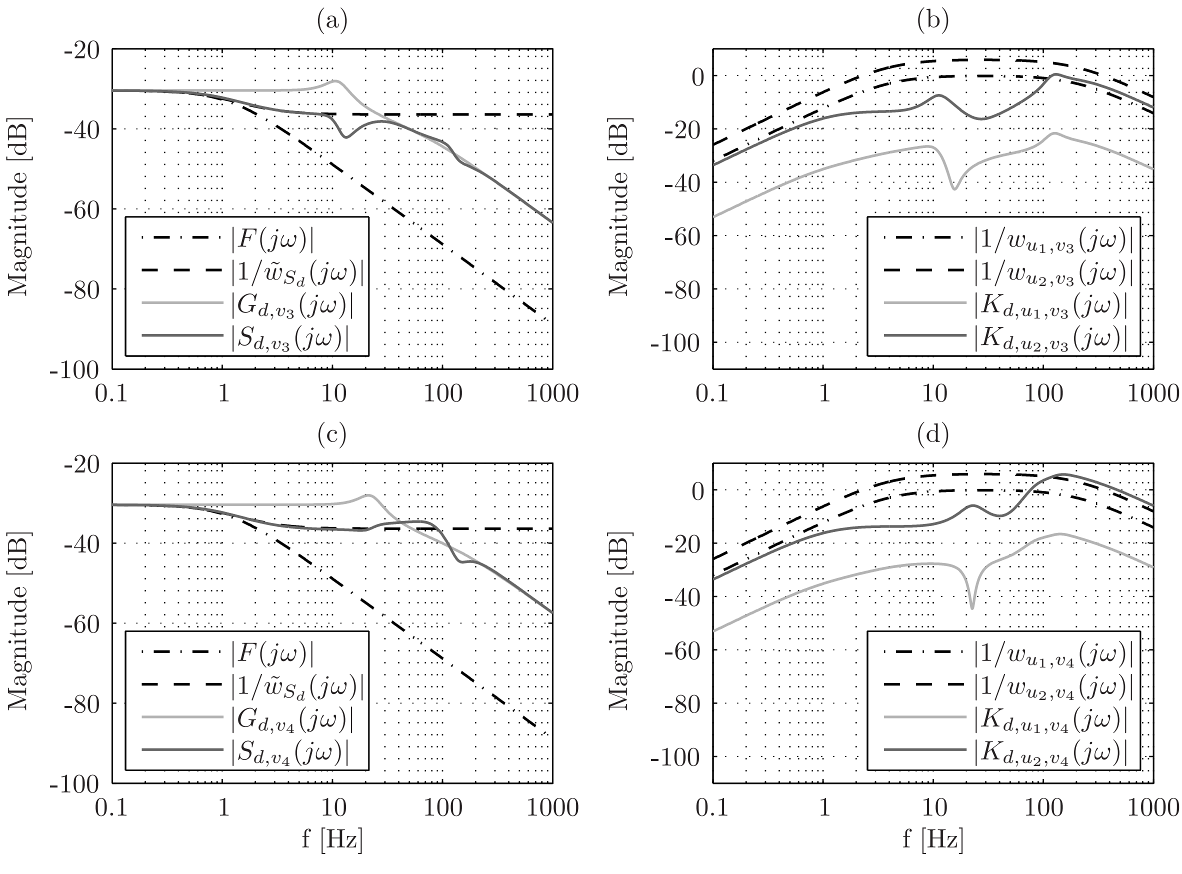

Figure 4.41: Frequency response of the weighting filters and of the LPV transfer functions for disturbance sensitivity and control effort of the feedforward controlled plant at vertices 3 (a, b) and 4 (c, d), respectively.

the frequency $\omega_{S_d} = 1 \cdot 2\pi\frac{\text{rad}}{\text{s}}$ is chosen such that the feedforward controller is active in a frequency range above the cut-off frequency of the reference filter $F(s)$. Disturbances at lower frequencies are to be passed through to the plant output with the same gain

$$k = \left.\frac{\partial y_2}{\partial \beta_w}\right|_S \tag{4.105}$$

as that of the disturbance model $G_d(\underline{\theta})$ for the natural, uncontrolled flow, whereas the coefficient $A_{S_d} = 0.5$ specifies the desired disturbance suppression at higher frequencies. An upper limit is put on the control effort via a parameter-dependent weight

$$\tilde{\boldsymbol{W}}_U(\underline{\theta}) = \sum_{i=1}^{4} \alpha_i \tilde{\boldsymbol{W}}_{U,v_i}, \text{ with } \tilde{\boldsymbol{W}}_{U,v_i} = \begin{bmatrix} \boldsymbol{A}_{\tilde{W}_{U,v_i}} & \boldsymbol{B}_{\tilde{W}_{U,v_i}} \\ \boldsymbol{C}_{\tilde{W}_{U,v_i}} & \boldsymbol{D}_{\tilde{W}_{U,v_i}} \end{bmatrix}, i = 1 \ldots 4, \tag{4.106}$$

and polytopic coordinates α_i as defined by the polytope

$$\Theta = \left\{ \sum_{i=1}^{4} \alpha_i \underline{v}_i : \quad \alpha_i \geq 0; \quad \sum_{i=1}^{4} \alpha_i = 1 \right\}. \tag{4.107}$$

Here, the same vertices are used as for the feedback controller design described in section 4.6.2. The LTI systems $\tilde{W}_{u,v_i}$ at the vertices $\underline{v}_1 \ldots \underline{v}_4$ correspond to the state-space representation of the frequency dependent matrices

$$\tilde{\boldsymbol{W}}_{U,v_1}(s) = \begin{bmatrix} w_{u_1,v_1}(s) & 0 \\ 0 & w_{u_2,v_1}(s) \end{bmatrix} = \begin{bmatrix} 0.5 & 0 \\ 0 & 1 \end{bmatrix} \tilde{w}_u(s), \tag{4.108}$$

$$\tilde{\boldsymbol{W}}_{U,v_2}(s) = \begin{bmatrix} w_{u_1,v_2}(s) & 0 \\ 0 & w_{u_2,v_2}(s) \end{bmatrix} = \begin{bmatrix} 0.5 & 0 \\ 0 & 1 \end{bmatrix} \tilde{w}_u(s), \tag{4.109}$$

$$\tilde{\boldsymbol{W}}_{U,v_3}(s) = \begin{bmatrix} w_{u_1,v_3}(s) & 0 \\ 0 & w_{u_2,v_3}(s) \end{bmatrix} = \begin{bmatrix} 1 & 0 \\ 0 & 0.5 \end{bmatrix} \tilde{w}_u(s), \tag{4.110}$$

$$\tilde{\boldsymbol{W}}_{U,v_4}(s) = \begin{bmatrix} w_{u_1,v_4}(s) & 0 \\ 0 & w_{u_2,v_4}(s) \end{bmatrix} = \begin{bmatrix} 1 & 0 \\ 0 & 0.5 \end{bmatrix} \tilde{w}_u(s), \tag{4.111}$$

$$\text{with } \tilde{w}_u(s) = \frac{\frac{1}{M_1}s + \omega_1}{s + \omega_1 A_1} \cdot \frac{s + \frac{1}{M_2}\omega_2}{A_2 s + \omega_2}, \tag{4.112}$$

and $\omega_1 = 4 \cdot 2\pi\frac{\text{rad}}{\text{s}}$, $\omega_2 = 200 \cdot 2\pi\frac{\text{rad}}{\text{s}}$, $M_1 = M_2 = 1$, $A_1 = A_2 = 1 \cdot 10^{-3}$. The coefficients of the scalar transfer function $\tilde{w}_u(s)$ are chosen here such that control input is only allowed in the medium frequency range of $4\,\text{Hz} < f < 200\,\text{Hz}$. This penalizes the control effort at low frequencies and forces the steady-state response of the feedforward disturbance sensitivity $S_d(\underline{\theta})$ to be equal to the gain k of the natural disturbance transfer function $G_d(\underline{\theta})$.
Identical weighting matrices $\tilde{\boldsymbol{W}}_{U,v_1}(s) = \tilde{\boldsymbol{W}}_{U,v_2}(s)$ are specified at the corners 1 and 2 of the polytope Θ that correspond to negative cross-wind angles. Here, a lower penalty is put on u_1. Conversely, u_2 is penalized less for positive cross-wind angles via the weights $\tilde{\boldsymbol{W}}_{U,v_3}(s) = \tilde{\boldsymbol{W}}_{U,v_4}(s)$. This way, the feedforward controller always applies an asymmetrically larger control input on the leeward side, which helps avoid actuator saturation when the vehicle enters a sharp edged gust. At $\beta_w = 0$ both actuators u_1 and u_2 are used to the same extent, because the asymmetric vertex controllers contribute equal amounts. Figure 4.41 (b) and (d) show the frequency response of the inverse weights for the control effort at vertices 3 and 4, corresponding to a positive cross-wind angle $\beta_w = 10°$ at minimum and maximum free-stream velocity, respectively.
One of the prerequisites for the applicability of the LPV H_∞ control synthesis algorithm by Apkarian et al. [14] is a parameter-independent feedthrough matrix $\boldsymbol{D}_{21}$ from control input $\underline{u}$ to weighted output $\underline{z}$. Therefore, a fast prefilter

$$\underline{\tilde{u}} = \underbrace{\begin{bmatrix} 1 & 0 \\ 0 & 1 \end{bmatrix} \frac{1}{Ts + 1}}_{\boldsymbol{G}_f(s)} \underline{\tilde{u}}', \text{ with } T = 0.001\,\text{s}, \tag{4.113}$$

is added at input of the plant $\tilde{G}(\underline{\theta})$. The generalized plant $\tilde{P}(\underline{\theta})$ is obtained in a similar way as in the LPV feedback control design. Here, it maps the external input d and the control input $\underline{\tilde{u}}'$ to the weighted outputs $\underline{z}$ and measured outputs d. A preliminary controller $K'_d(\underline{\theta})$ is synthesized by solving the LMIs (2.35 - 2.37) as implemented in the `MATLAB`-function "`hinfgs.m`", such that the upper limit of the $\mathcal{L}_2$ gain γ in

$$\|\underline{z}\|_2 < \gamma \|d\|_2 \tag{4.114}$$

is minimized. Here, a value of $\gamma = 1.69$ is achieved. The output of the preliminary controller $\boldsymbol{K}'_d(\underline{\theta})$ is multiplied with the low-pass filter $\boldsymbol{G}_f(s)$ to obtain the final controller

$$\boldsymbol{K}_d(\underline{\theta}) = \boldsymbol{G}_f(s)\boldsymbol{K}'_d(\underline{\theta}). \tag{4.115}$$

Fig. 4.41 shows the result of the feedforward control design in terms of the frequency response of the disturbance sensitivity $S_d(\underline{\theta})$ and the control effort $\boldsymbol{K}_d(\underline{\theta})$ in comparison with their weights, the natural disturbance transfer function $G_d(\underline{\theta})$ and the reference filter $F(s)$. At vertex 3, which corresponds to the lowest free-stream velocity $\mathrm{u}_\infty = 11.4\,\mathrm{m/s}$ and a cross-wind angle $\beta_w = 10°$, all specifications are fulfilled, see Fig. 4.41 (a) and (b). The lower row, plots (c) and (d), shows the frequency responses at vertex 4, for $\mathrm{u}_\infty = 22.8\,\mathrm{m/s}$ and $\beta_w = 10°$. Due to faster disturbance dynamics, but limited actuator bandwidth, the specifications are harder to meet and slightly exceeded for higher frequencies. Vertices 1 and 2 are not shown here, as they correspond to the same free-stream velocities at a negative cross-wind angle $\beta_w = -10°$. There the feedforward controlled plant has the same characteristics as at vertices 3 and 4; only the control channels corresponding to u_1 and u_2 are switched. All in all, a good disturbance suppression by -6 dB at a reasonable control effort is achieved for the feedforward control design.
The final controller $\boldsymbol{K}_d(\underline{\theta})$ is implemented on the DSP with the same online interpolation and trapezoidal LPV discretization technique as applied in the LPV feedback controller, see sections 2.1.2 and 4.6.2.
Figure 4.42 shows an example of a cross-wind gust experiment with feedforward control in comparison with the natural gust response. Here, the control input is calculated by

$$\underline{u}(t) = \begin{bmatrix} u_1(t) & u_2(t) & u_3(t) \end{bmatrix}^T = \begin{bmatrix} \overline{u}_1 + \tilde{u}_1(t) & \overline{u}_2 + \tilde{u}_2(t) & 0 \end{bmatrix}^T \tag{4.116}$$

with a constant offset of $\overline{u}_1 = \overline{u}_2 = 1.8$. The contribution of the feedforward controller to the actuating variables corresponds to $\tilde{u}_1(t)$ and $\tilde{u}_2(t)$. At $t \approx 0.6\,\mathrm{s}$ the cross-wind gust with a peak angle of $\beta_w \approx 10°$ reaches the front of the bluff body, see Fig. 4.42 (d). For the natural, uncontrolled flow, this results in a large increase in both output variables y_1 and y_2, corresponding to drag coefficient and weighted sum of side-force and yaw-moment coefficients shown in plots (a) and (c), respectively. As intended by the choice of parameter-dependent weights for the control effort, the feedforward controller uses mostly the leeward actuating variable u_2 to counteract the disturbances acting on y_2, see Fig. 4.42 (e). This reduces the peak of y_2 at the beginning of the cross-wind gust significantly. Plot (f) shows the relative contribution of the four vertex controllers in terms of the polytopic coordinates α_i for $i = 1 \ldots 4$. The drag coefficient is only slightly reduced by the feedforward controller. This could also be achieved by a suitable MIMO feedforward control design, but this is not the objective here, since this task is already fulfilled satisfactorily by the feedback LPV loop.
The impact of feedforward control on the lateral vehicle dynamics during cross-wind gusts, as well as a comparison with the performance of the LPV feedback controller, is discussed in the next section.

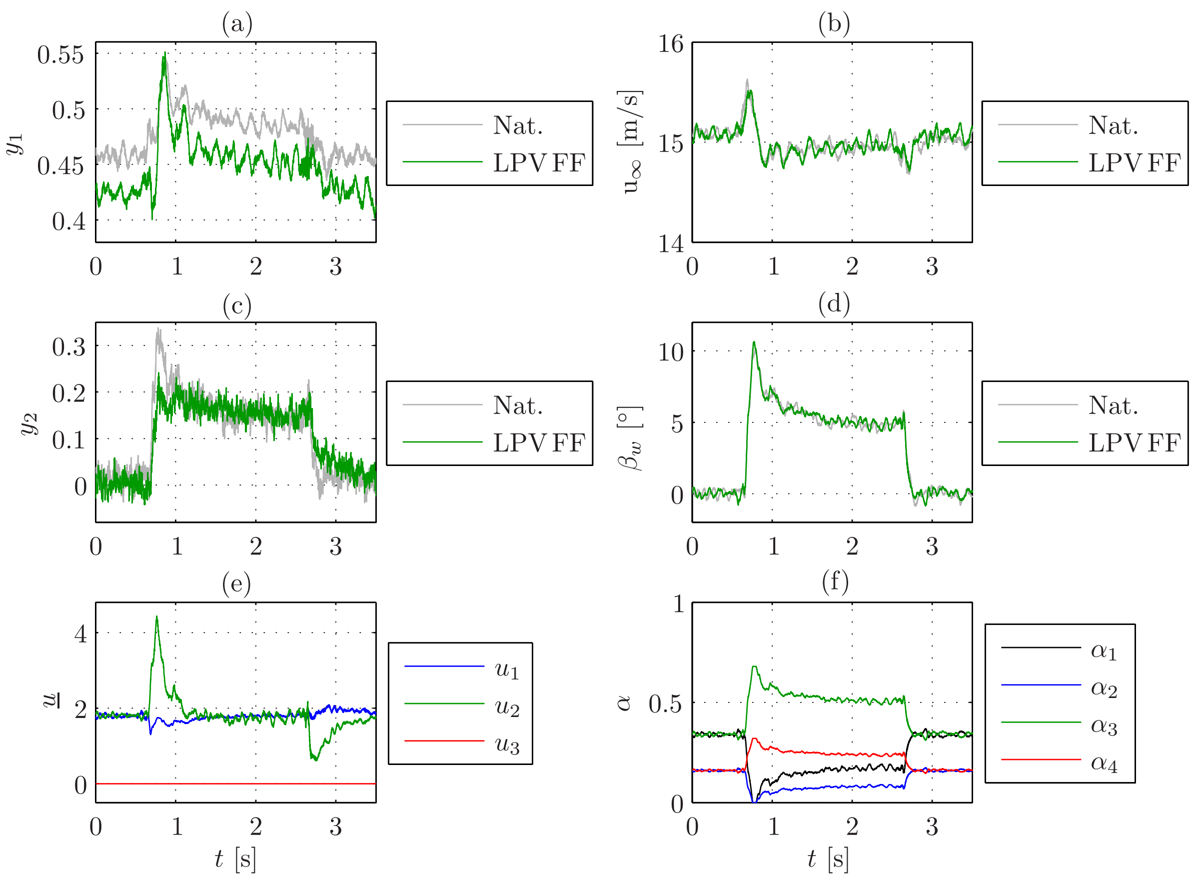

Figure 4.42: Experimental results obtained with LPV feedforward control (LPV FF) in comparison with the natural flow (Nat.) for similar gusts with a maximum cross-wind angle $\beta_w \approx 10°$ at $Re_L = 4 \cdot 10^5$.

4.7 Results and discussion

4.7.1 Control performance and lateral vehicle response

The performance of the various controllers and their effect on the lateral vehicle response are evaluated in cross-wind gust experiments. Here, the lateral vehicle motion is replicated in the wind tunnel in real-time with the method described in section 4.5. A sample result obtained with combined feedback and feedforward LPV control is shown in Fig. 4.43. For comparison, the response of the natural flow is also depicted for a similar cross-wind gust with a maximum cross-wind angle $\beta_w \approx 10°$ at the same Reynolds number $Re_L = 4 \cdot 10^5$.
The reference values r_1 and r_2 are calculated online from the current estimated cross-wind angle $\hat{\beta}_w$ with the method presented in section 4.6.3. It relies on a look-up table to determine the current setpoint r_1 for the drag coefficient, which yields the most efficient drag reduction at a given cross-wind angle. For the weighted sum y_2 of side-force and yaw-moment coefficients a dynamic reference filter is applied, which slowly increases the setpoint r_2 to a value that corresponds to the natural flow.
As can be seen in Fig. 4.43 (a) and (b) the combined feedback and feedforward LPV controller successfully regulates the outputs $\underline{y}$ so that they follow their setpoint trajectories $\underline{r}$. This provides a significant drag reduction relative to the natural, uncontrolled flow. Only at the beginning of the gust is a larger deviation of y_1 from its setpoint r_1 visible. As discussed with regard to the LPV control design in section 4.6, the bandwidth of the closed loop is limited to frequencies $f < 7\,\text{Hz}$. Due to a waterbed effect arising from the input time-delay of the actuators, disturbances at higher frequencies are slightly amplified by the feedback loop. This may explain the overshoot

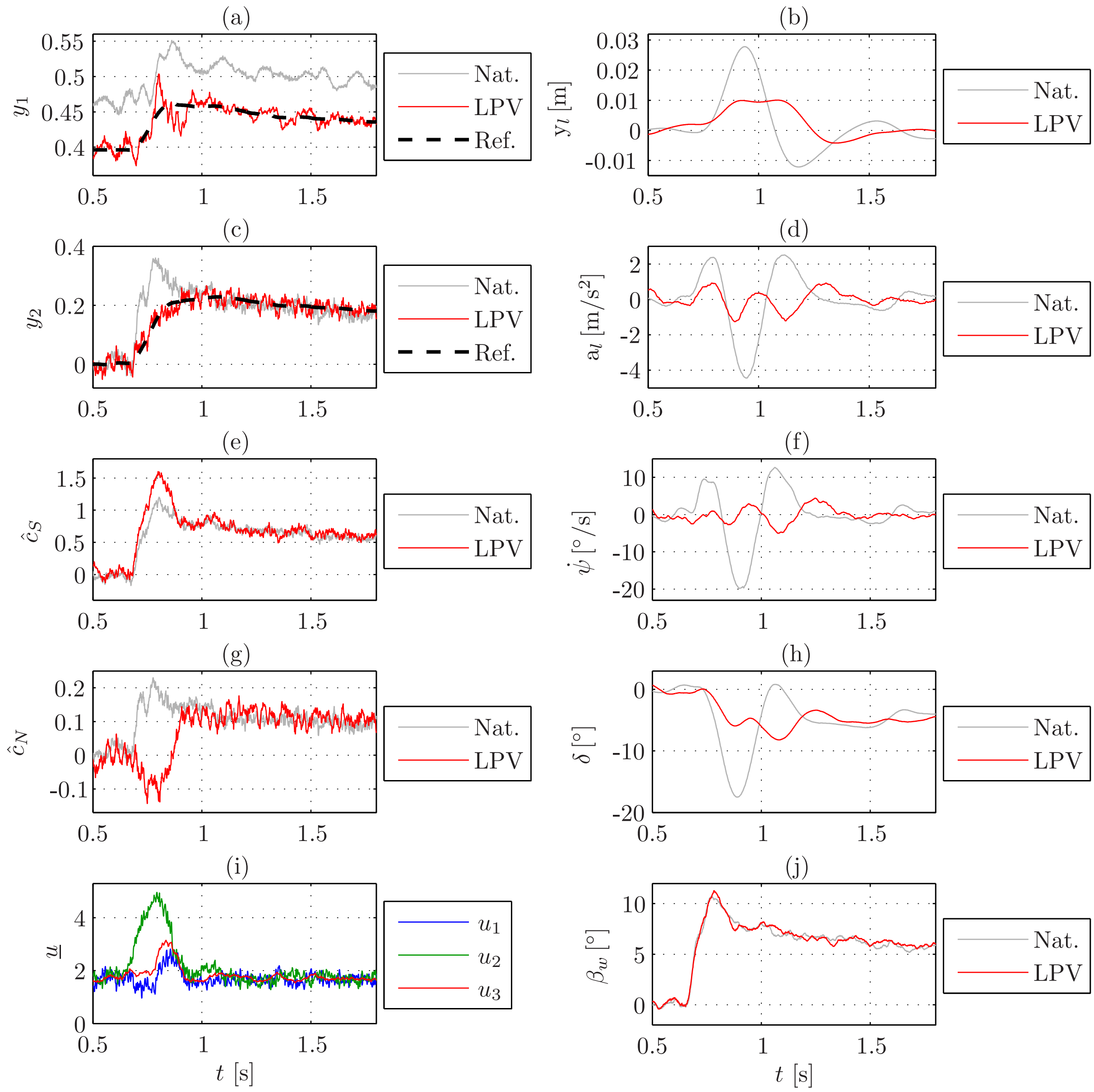

Figure 4.43: Experimental results obtained with combined feedback and feedforward LPV active flow control in comparison with the natural flow for similar gusts with a maximum cross-wind angle $\beta_w \approx 10°$ at $Re_L = 4 \cdot 10^5$. The resulting lateral vehicle response is simulated online and replicated in the wind tunnel during the experiment, with scaled parameters corresponding to a driving speed $v = 120$km/h of a full-sized vehicle.

observed for the drag coefficient y_1.
For the second output variable y_2, the LPV controller performs better in reference tracking and disturbance suppression. This is partially due to the additional feedforward control applied for this output channel. Control of y_2 is also easier because of the almost perfectly linear dynamics of side-force and yaw-moment coefficients, which only vary with free-stream velocity as discussed in section 4.4.3 with regard to LPV model identification.
The slow increase of the controlled output variable y_2 has several benefits. First of all, only fast variations are suppressed by the controller. This effectively gives the driver enough time to react to a gust and he can easily compensate for the remaining constant and slowly varying effects of cross-wind on lateral vehicle dynamics. Second, a larger control input is only needed during fast changes of the cross-wind angle β_w, as in plot (i). This enables an efficient drag reduction even during cross-wind gusts.

As pointed out earlier, the surrogate variable y_2 represents the weighted sum of side-force and yaw-moment coefficients and approximates their combined effect on the lateral vehicle response. Controlling y_2 to its reference trajectory r_2 results in a small increase in side force during the cross-wind transient, see plot (e). By contrast, the yaw moment shown in Fig. 4.43 (g) is first reduced to negative values to compensate for the effect of the side force increase on the lateral vehicle response. When the cross-wind angle β_w approaches a steady value, both the side-force and yaw-moment coefficients reach values similar to those from the natural flow.
Thus, the controller suppresses disturbances acting on y_2 only in a frequency range where the driver is not able to react. This results in a significantly smaller lateral deviation y_l of the vehicle and in a larger reduction of the peaks in lateral acceleration a_l and yaw rate $\dot{\psi}$, see Fig. 4.43 (b), (d) and (f), respectively. The driver thus needs less steering effort to compensate for the remaining effect of the cross-wind on lateral vehicle dynamics.

4.7.2 Performance of LPV versus robust feedback control

As discussed in section 4.4, the actuated flow dynamics exhibit a nonlinear, parameter-dependent behavior. For the robust control design, these characteristics are taken into account by identifying a large set of linear black-box models at several operating points for different cross-wind angles, free-stream velocities and actuation amplitudes. All nonlinearities and parameter-dependencies are described by an uncertainty model that encompasses all possible deviations of the plant dynamics from a nominal model. The uncertainty description is taken into account via adequate weights in the mixed-sensitivity design of the robust feedback controller presented in section 4.6.1. Whereas robust stability of the closed-loop is guaranteed with regard to the chosen unstructured multiplicative output certainty, robust performance is not achieved by the robust H_∞ controller, see section 4.6.1, Fig. 4.32 (d).
By contrast, the LPV feedback control design takes the parameter-dependent plant characteristics explicitly into account. The dynamics of the actuated flow vary proportionally with the free-stream velocity. Additionally, the gain of the drag coefficient with respect to wind- and leeward actuation depends on the current cross-wind angle to which the vehicle is exposed. Of course, some nonlinearities of the actuated flow are not captured, but the LPV models identified in section 4.4.3 describe the flow characteristics over the entire operating regime significantly better than linear models.
In order to assess the advantages achieved by LPV control over robust H_∞ control, the worst case sensitivities $\boldsymbol{S}_{p,H_\infty}$ and $\boldsymbol{S}_{LPV}$ for each controller are determined by evaluating the closed-loop transfer functions based on the LPV model for the range of free-stream velocities $11.4\,\mathrm{m/s} \leq \mathrm{u}_\infty \leq 22.8\,\mathrm{m/s}$ and cross-wind angles $-10° \leq \beta_w \leq 10°$. The maximum singular values of the

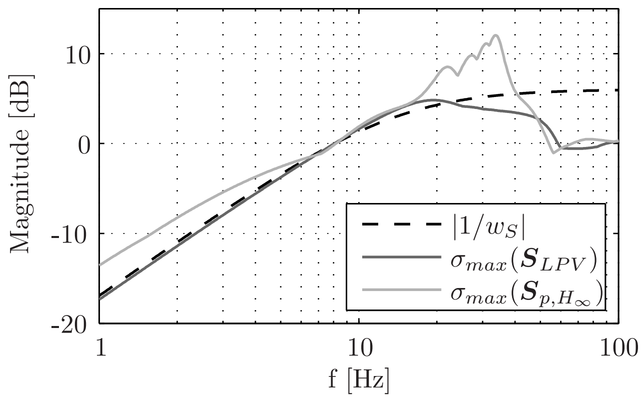

Figure 4.44: Maximum singular values of the worst case sensitivities $\boldsymbol{S}_{p,H_\infty}$ and $\boldsymbol{S}_{LPV}$ for the robust H_∞ and LPV feedback controller, respectively, in comparison with the magnitude of the inverse of the sensitivity weight w_S.

worst case sensitivities are shown in Fig. 4.44 in comparison with the magnitude $|1/w_S|$ of the inverse of the sensitivity weight. Here, the LPV controller fulfills the specification very well and achieves a worst case bandwidth of about 5.5 Hz. The upper bound for the sensitivity is only slightly exceeded in the range $10\,\mathrm{Hz} < f < 20\,\mathrm{Hz}$. Compared with the LPV controller, an inferior performance of the robust controller is to be expected, with a worst case bandwidth of about 4.6 Hz and large peak of the sensitivity at higher frequencies.

The performance of both feedback controllers is tested in the cross-wind gust experiments shown in Fig. 4.45. For the experiment with the robust H_∞ controller, a large peak followed by an undershoot occurs in the drag coefficient at the beginning of the gust, see plot (a). As expected from the evaluation of the worst case sensitivity, the LPV controller performs better, especially in terms of suppressing disturbances acting on the drag coefficient. This is attributed to the fact that the LPV controller takes the gain variation of the actuated flow under side-wind conditions explicitly into account. Furthermore, the LPV feedback controller tracks the reference variable r_2 slightly better than the robust H_∞ controller. This results in a smaller lateral deviation y_l and in reduced oscillations of the lateral acceleration a_l and of the steering angle δ.

These results show the advantages of the LPV approach for active flow control, although the performance gains are not large when compared with robust control. However, the time and effort for identifying an LPV model and synthesizing an LPV controller are comparable to the robust approach, which requires extensive experiments to identify a large enough set of models to capture all nonlinearities and parameter-dependencies within the uncertainty description. Furthermore, the LPV "gray-box" approach gives more insight by modeling the underlying nondimensional flow physics more accurately. This makes predictions for other free-stream velocities and vehicle dimensions possible.

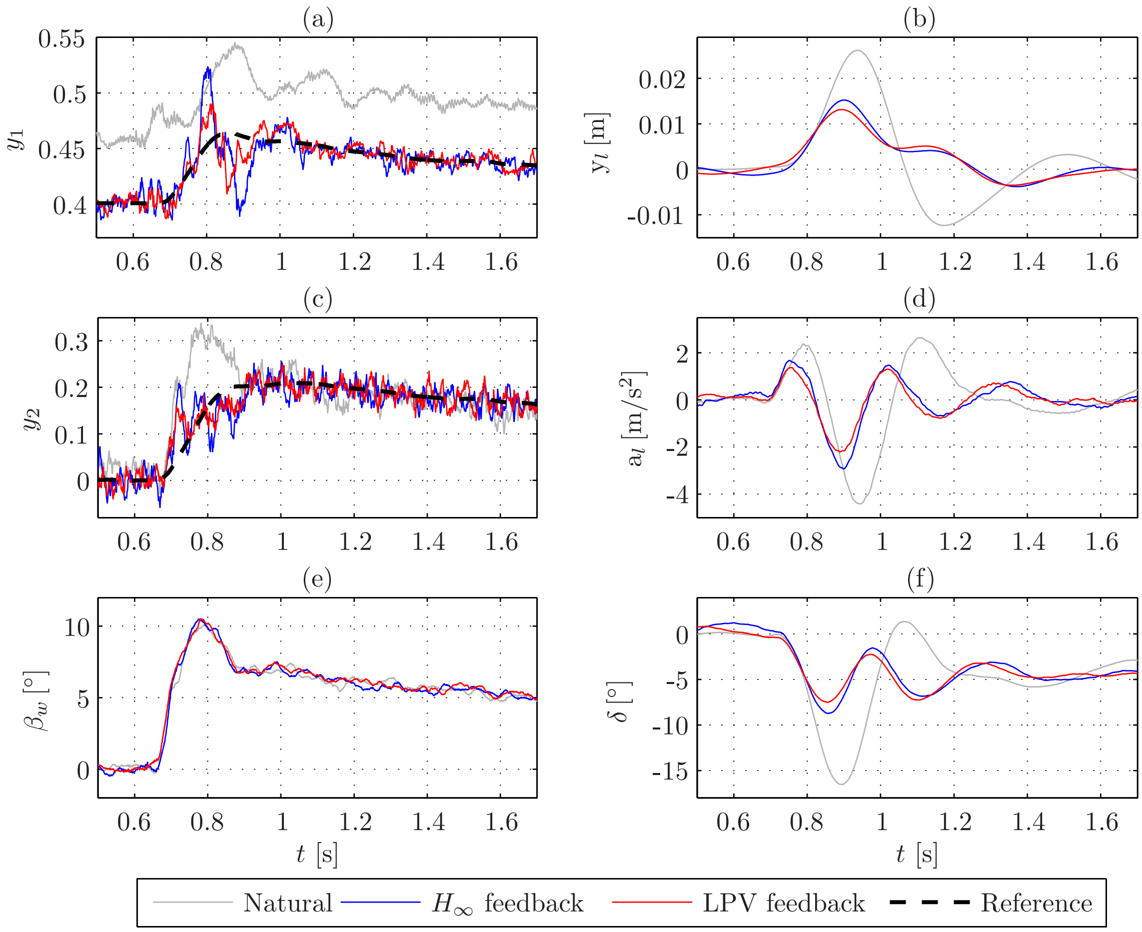

Figure 4.45: Experimental results obtained with robust H_∞ and LPV feedback control in comparison with the natural cross-wind gust response at $Re_L = 4 \cdot 10^5$.

4.7.3 Performance of LPV feedback versus LPV feedforward control

Feedback control generally offers the benefit of suppressing unmodeled disturbances and of being able to compensate for inaccuracies between plant model and actual process. However, this usually comes at the price of amplifying disturbances in a certain frequency range, especially if time delays or positive zeros are present in the plant transfer function [121], as it is the case here for the actuated flow dynamics. This drawback can be partially alleviated by an additional feedforward control component.

The feedforward LPV controller presented in section 4.6.4 is designed to suppress disturbances acting on y_2 such that it supports the LPV feedback controller in a frequency range where the latter is not effective or may even amplify disturbances. In the following, the performance of LPV feedback control, LPV feedforward control and combined LPV control is evaluated by their closed-loop frequency response and by their effect on the lateral vehicle response in cross-wind gust experiments.

Fig. 4.46 (a) shows the frequency response of y_2 to cross-wind disturbances β_w for the three different cases of controlled flow in comparison with the natural flow characteristics. The corre-

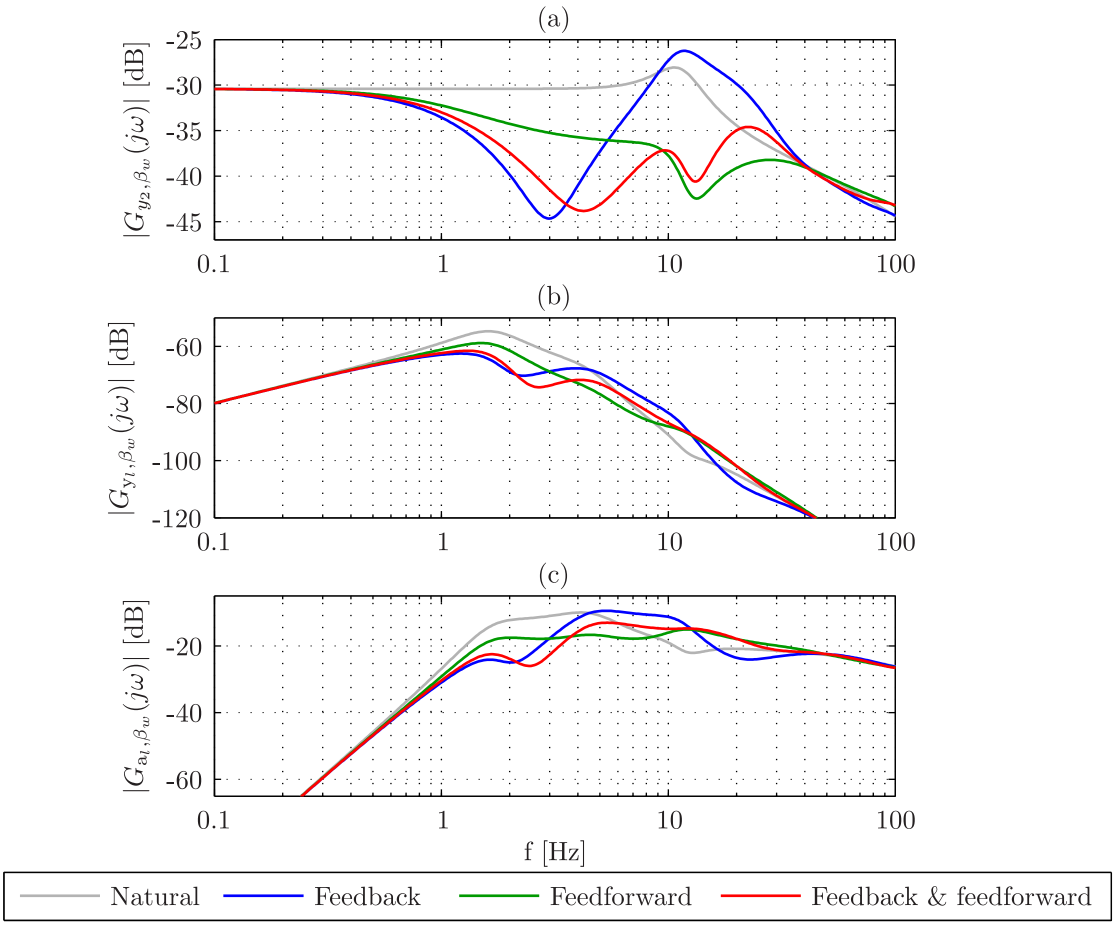

Figure 4.46: Comparison of the natural and the controlled frequency response of the output variable y_2 (a), the lateral displacement y_l (b) and the lateral acceleration a_l (c) to cross-wind gusts β_w at $Re_L = 4 \cdot 10^5$.

sponding frequency response of the lateral vehicle dynamics is shown in Fig. 4.46 (b) and (c). When only LPV feedback control is applied in combination with the dynamic reference filter disturbances are well suppressed in the frequency range $1\,\mathrm{Hz} < f < 7\,\mathrm{Hz}$. However, a waterbed effect occurs due to the input time-delays of the actuators, resulting in a disturbance amplification for the frequencies $f > 10\,\mathrm{Hz}$. In the case of exclusive LPV feedforward control a slightly smaller disturbance suppression is achieved than with LPV feedback control, but over a signif-

icantly larger frequency range. What is more, the disturbances are not amplified. However, feedforward control can suppress only disturbances that are detected based on the measured changes of the cross-wind angle β_w. The combined feedforward and feedback LPV control strategy shows good disturbance suppression over the entire frequency range. The feedforward part reduces the frequency response to disturbances in the range where feedback control is no longer effective, thus decreasing the waterbed effect.
These advantages are also clearly visible in the frequency response of the lateral deviation y_l and of the lateral acceleration a_l to cross-wind gusts β_w, see Fig. 4.46 (b, c). However, the weighting approach for the surrogate variable y_2 approximates the effect of c_S and c_N on lateral vehicle response only for a frequency range up to about 7 Hz as discussed in section 4.5.4. This leads to an inaccurate suppression of disturbances at higher frequencies, less than optimal for the lateral vehicle response. For this reason the frequency characteristics of the driver-vehicle system with AFC exhibit a slightly worse performance than what would be expected from the disturbance transfer functions shown in Fig. 4.46 (a). This drawback from the relatively simple weighting approach for y_2 could be potentially circumvented by a more sophisticated LPV H_∞ control synthesis that includes the driver-vehicle system in the generalized plant.
A comparison of the transient response for the three cases with feedback, feedforward and combined LPV control is shown in Fig. 4.47 for similar cross-wind gust experiments at $Re_L = 4\cdot 10^5$. The feedforward controller alone performs quite well at reducing the peak in y_2 at the beginning of the gust, see plot (c). This results in a smaller lateral vehicle response relative to the uncontrolled case, as shown in the right column of Fig. 4.47. However, the feedforward controller is only designed for suppressing disturbances acting on y_2. Only a small drag reduction is thus achieved. By contrast, LPV feedback control provides the benefit of reference tracking and

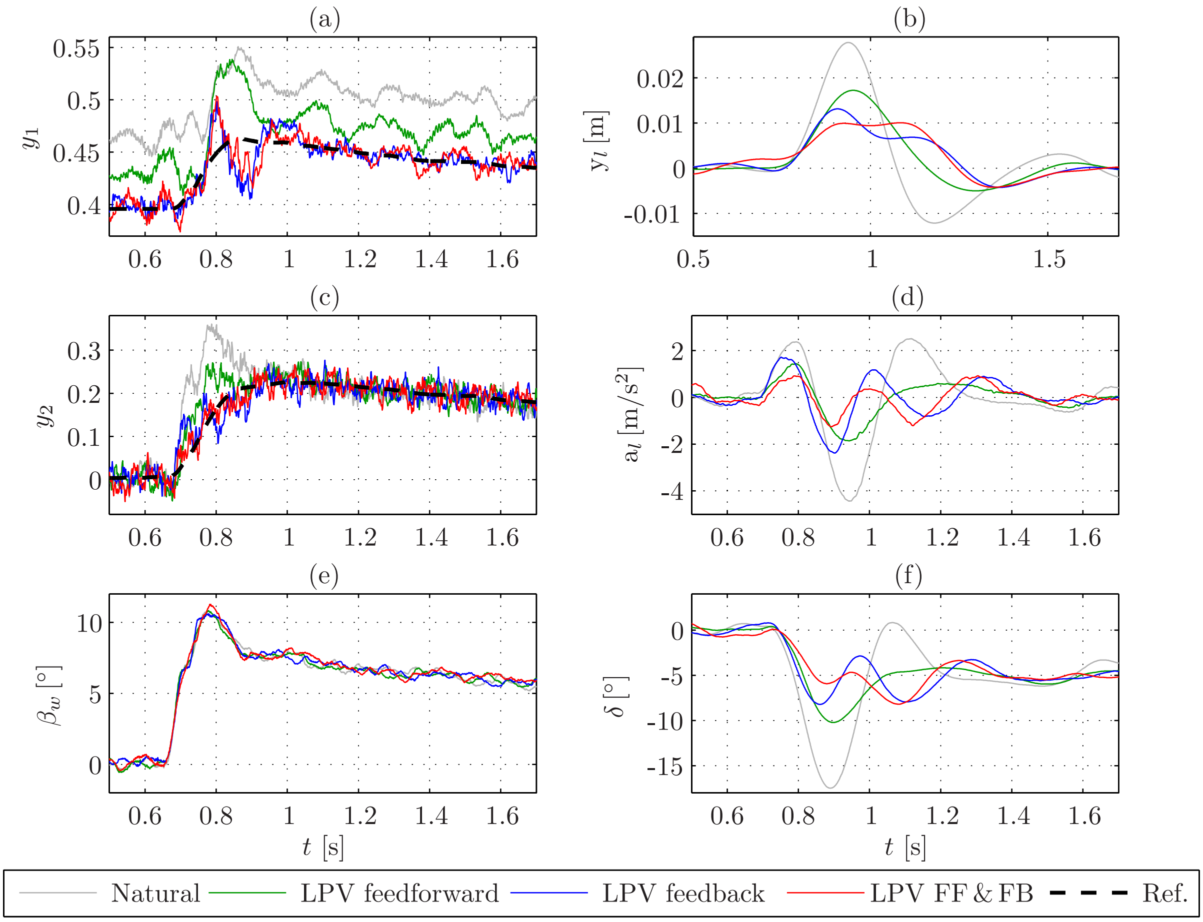

Figure 4.47: Experimental results obtained with feedforward (FF), feedback (FB) and combined FF & FB LPV control, in comparison with the natural cross-wind gust response at $Re_L = 4\cdot 10^5$.

disturbance suppression for both output variables, even for unmodeled disturbances. As shown in Fig. 4.47 (a) and (c), the drag coefficient y_1 and the weighted sum y_2 of the side-force and yaw-moment coefficients follow their reference trajectories well, with a better performance with regard to the second output variable. In terms of the response of the driver-vehicle system, the lateral deviation y_l during the gust is smaller than in the case with pure feedforward control. The lateral acceleration a_l is reduced in amplitude when compared with the uncontrolled case, but less than by feedforward control. Furthermore, the oscillations in a_l are shifted to a higher frequency by feedback control due to the waterbed effect. These observations coincide with the projected frequency response shown in Fig. 4.46 (b) and (c).
Applying additional feedforward control in the combined strategy improves reference tracking and disturbance suppression of y_2, which also translates into a further reduction of the lateral vehicle deviation y_l and especially of the lateral acceleration a_l, see Fig. 4.47 (b) and (d). As expected, the transient response of the drag coefficient is almost identical for the cases with pure feedback LPV control and combined LPV control, since the additional feedforward controller is only designed to suppress disturbances acting on y_2.
These results demonstrate that LPV feedback control alone already performs very well with AFC for bluff bodies. If fewer sensors are available and no reference tracking with zero steady-state error is required, feedforward control alone may yield sufficient performance. However, the combined LPV control strategy yields the benefits of both approaches, and their respective contribution to the overall control performance can be easily adjusted via the weights applied during the LPV H_∞ control synthesis. This way, drawbacks of feedback control - such as disturbance amplification at higher frequencies - can be alleviated by additional feedforward control.

4.7.4 LPV control performance and lateral vehicle response for various free-stream velocities

In this section the performance of the combined LPV control strategy is discussed for various free-stream velocities corresponding to different simulated driving speeds in the model for lateral vehicle dynamics. Again, both the predicted frequency characteristics and the transient response to cross-wind gusts in wind tunnel experiments are considered here.
The LPV models identified in sections 4.2.3 and 4.4.3 take into account the parameter-dependent dynamics of the cross-wind gust response and of the actuated flow characteristics with regard to varying free-stream velocity. The corresponding LPV feedback and feedforward control design guarantees stability and performance for a range of free-stream velocities $11.4\,\mathrm{m/s} \leq \mathrm{u}_\infty \leq 22.8\,\mathrm{m/s}$, corresponding to Reynolds numbers $3 \cdot 10^5 \leq Re_L \leq 6 \cdot 10^5$. To evaluate the effect of LPV control on the lateral vehicle response, the driving speed of the real-time simulation of the driver-vehicle model is coupled proportionally to free-stream velocity. This corresponds to a simulated range of driving velocities $90\,\mathrm{km/h} \leq \mathrm{v}_v \leq 180\,\mathrm{km/h}$ of the real vehicle.
Figure 4.48 shows the frequency response of the output variable y_2, which corresponds to the weighted sum of side-force and yaw-moment coefficients, as well as of the lateral deviation y_l and of the acceleration a_l to changes in cross-wind angle β_w for three Reynolds numbers $Re_{L,1} = 3 \cdot 10^5$, $Re_{L,2} = 4 \cdot 10^5$ and $Re_{L,3} = 5 \cdot 10^5$. To this end, the LPV model and controllers are evaluated at frozen parameter values in terms of a nominal cross-wind angle $\overline{\beta}_w = 0°$ and free-stream velocities $\overline{\mathrm{u}}_{\infty,1} = 11.4\,\mathrm{m/s}$, $\overline{\mathrm{u}}_{\infty,2} = 15.2\,\mathrm{m/s}$ and $\overline{\mathrm{u}}_{\infty,3} = 19.0\,\mathrm{m/s}$. The frequency responses shown in Fig. 4.48 (a-c) suggest a good suppression of disturbances acting on y_2 by the combined LPV control strategy over the entire range of free-stream velocities. Also, the lateral displacement and acceleration are reduced significantly by closed-loop AFC at all examined driving speeds, but improvements are only achieved for frequencies up to $\approx 7\,\mathrm{Hz}$. In the case of the lateral vehicle displacement this does not represent a disadvantage, since its frequency response rolls off in this range anyway. However, the acceleration response is slightly increased for $f > 7\,\mathrm{Hz}$ when compared with the natural flow. This behavior is not observed to the same degree in the frequency response of the controlled output y_2 to cross-wind gusts. Further improvements may be achieved by a more advanced control design, such as by integrating the driver-vehicle

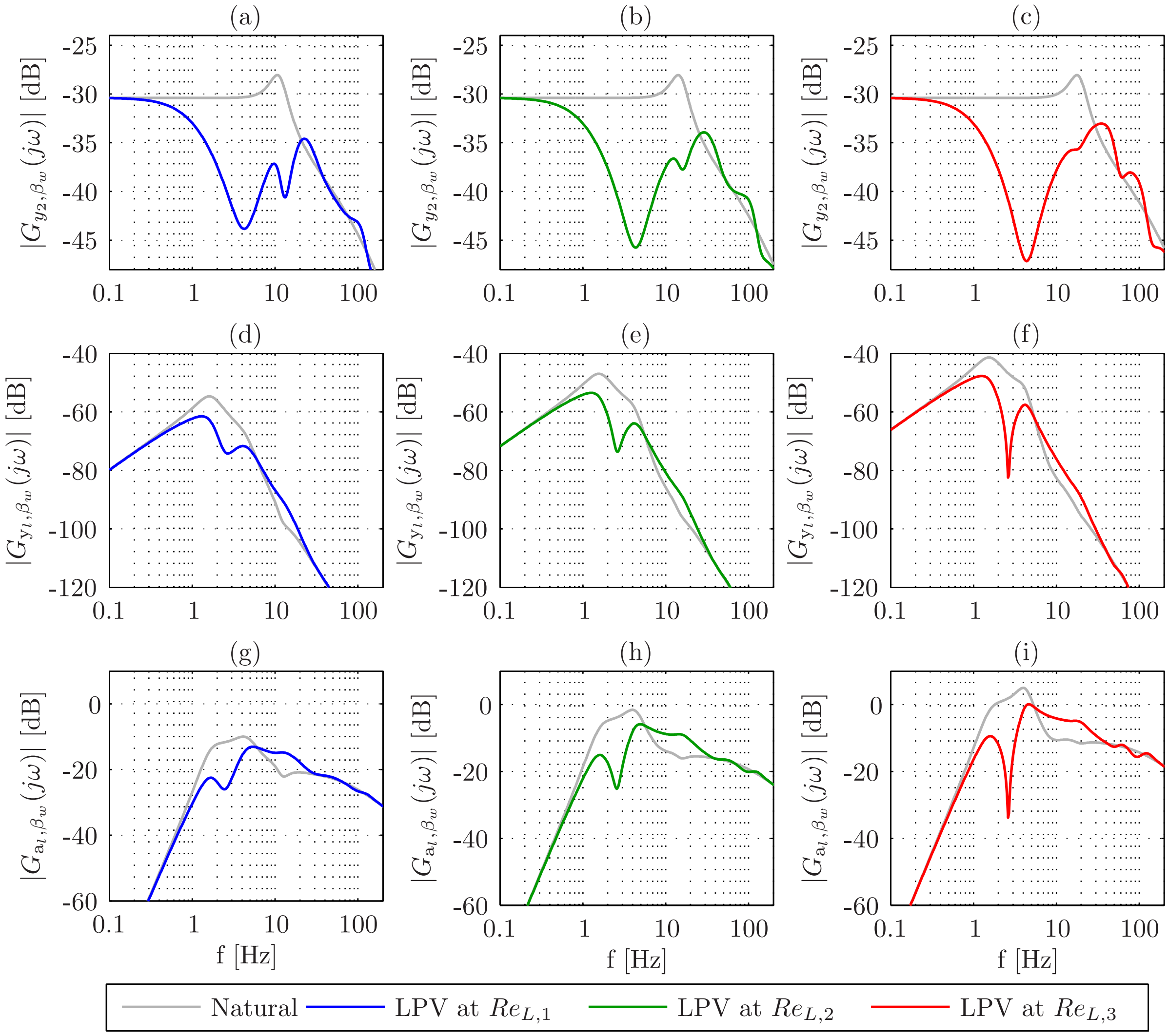

Figure 4.48: Frequency response of the output variable y_2 (a-c), the lateral displacement y_l (d-f) and the lateral acceleration a_l (g-i) for cross-wind gusts β_w at three Reynolds numbers $Re_{L,1} = 3 \cdot 10^5$, $Re_{L,2} = 4 \cdot 10^5$ and $Re_{L,3} = 5 \cdot 10^5$. The colored lines correspond to the flow controlled by the combined feedback and forward LPV strategy; the gray lines indicate the natural gust response.

model in the augmented LPV plant used for control synthesis. This would better capture the effect of AFC on lateral vehicle dynamics than the fixed weighting approach of side-force and yaw-moment coefficients in the calculation of the surrogate variable y_2.
As expected from the frequency response of the disturbance transfer functions for the controlled flow, the combined feedback and feedforward LPV control strategy achieves a good performance in wind tunnel experiments with cross-wind gusts at varying free-stream velocities. The corresponding results are shown in Fig. 4.49. At all three Reynolds numbers studied here, the LPV controller is able to regulate the output variables very well to their reference trajectories. Only the peaks observed in the drag coefficient at the beginning of the gust become larger with increasing free-stream velocities, see plots (a-c). Since the cross-wind gust also elapses faster as shown in Fig. 4.49 (p-r), the disturbances also occur in a higher frequency range. Thus, they are harder to suppress by the feedback part of the LPV controller, whose bandwidth is limited by a waterbed effect caused by the input time-delay of the actuators. The performance in terms of disturbance suppression for the drag coefficient could also be improved by an additional feedforward part, similar to the design carried out for the second output variable y_2. Here, an almost perfect tracking of the reference trajectories r_2 is achieved by the combined LPV controller, as

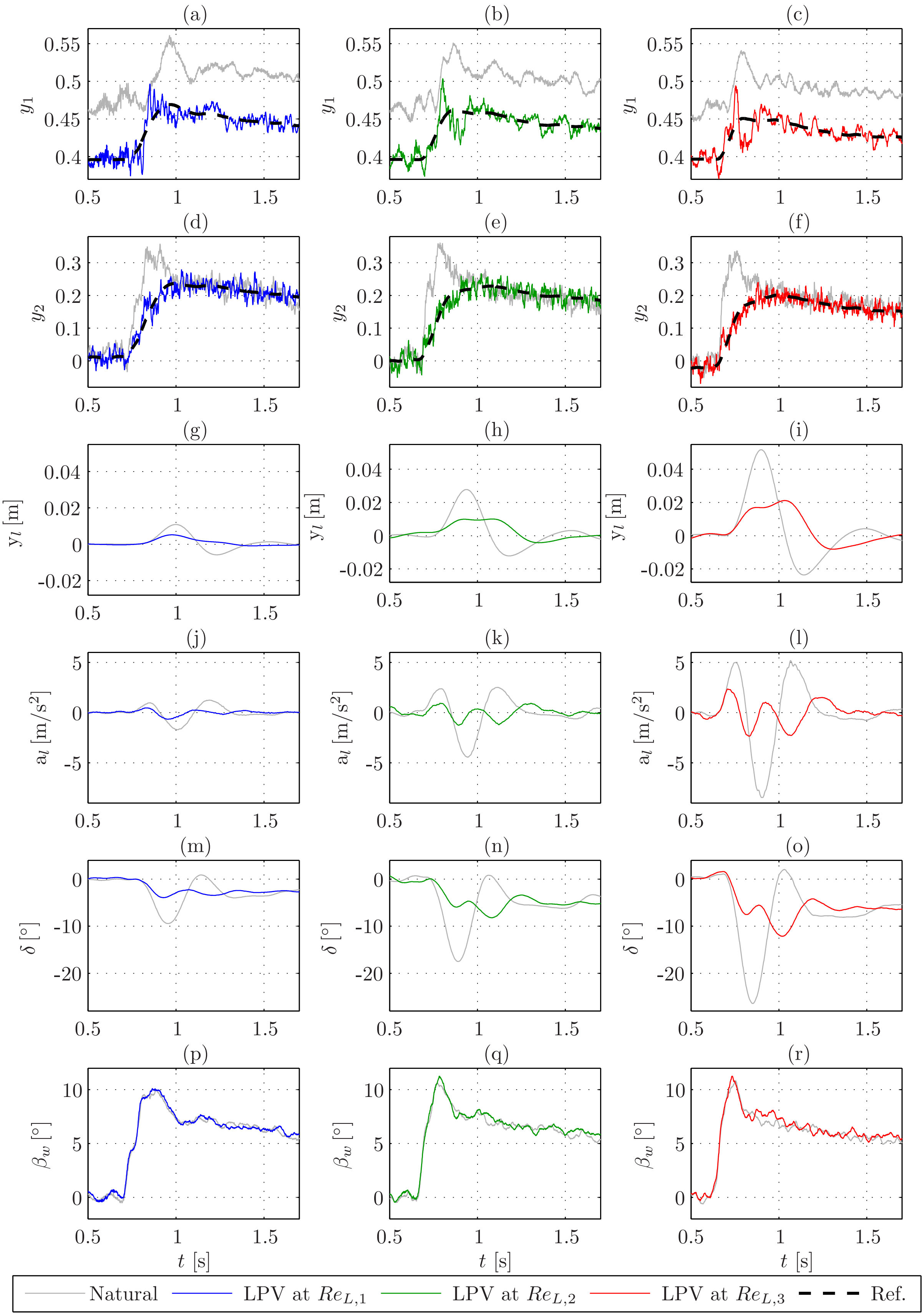

Figure 4.49: Comparison of the natural and the controlled cross-wind gust response with combined LPV feedback & feedforward control at three Reynolds nubmers $Re_{L,1} = 3 \cdot 10^5$ (left column), $Re_{L,2} = 4 \cdot 10^5$ (middle column) and $Re_{L,3} = 5 \cdot 10^5$ (right column).

shown in Fig. 4.49 (d-f). At all three free-stream velocities studied here, this results in a significantly improved lateral vehicle response in terms of reduced lateral displacement (g-i), smaller lateral acceleration (j-l) and less steering effort for the driver (m-o) when compared with the natural, uncontrolled case without AFC.

As mentioned above, improvements on the presented control strategy may be achieved by integrating the driver-vehicle model into the generalized plant to avoid the drawbacks associated with the fixed weighting approach of side-force and yaw-moment coefficients. Furthermore, the presented calculation of the reference values for the drag coefficient is based on a look-up table with setpoints that are only optimal under steady-state conditions with constant side wind. This does not represent the most energy-efficient possibility under the influence of transient, time-varying gusts. To improve on this point, an AFC strategy based on economic model predictive control could be applied to calculate optimal control inputs that minimize the overall power consumption of the vehicle under the presence of cross-wind disturbances. However, the required computational effort may be prohibitive for its real-time application to AFC. Instead, a mixed H_2/H_∞-LPV control approach may be applied, and could be designed in such a way that the H_2-norm of the transfer function from cross-wind disturbances to the overall power consumption of the vehicle is minimized while taking H_∞-constraints into account to guarantee performance of the closed-loop in disturbance suppression, reference tracking and control effort.

All in all, the experimental results demonstrate that the cross-wind sensitivity can be significantly improved by closed-loop AFC while efficiently reducing the drag coefficient, even under unsteady flow conditions. The presented LPV modeling and control methods are well suited to take into account the parameter-dependencies of the actuated flow. This results in a better performance than that of robust control methods. Furthermore, the LPV approach provides the possibility of predicting the performance and frequency characteristics for other vehicle dimensions and free-stream velocities than the ones used in the wind tunnel experiments. This is carried out and discussed in the following section for a full-sized vehicle at realistic driving speeds velocities.

4.7.5 Estimated transient aerodynamic characteristics and closed-loop LPV control performance for a full-sized vehicle

The LPV structure of the identified models for the unsteady cross-wind gust response and for the actuated flow dynamics – see sections 4.2.3 and 4.4.3, respectively – provides the possibility of estimating the expected transient aerodynamic characteristics and control performance for a full-sized vehicle at realistic driving velocities.

To this end, the corresponding LPV models are evaluated for a vehicle length $l = 5.6\,\mathrm{m}$ and a range of free-stream velocities $20\,\mathrm{m/s} \leq \mathrm{u}_\infty \leq 50\,\mathrm{m/s}$ and cross-wind angles $-10° \leq \beta_w \leq 10°$, whereas the dynamics of the actuator system are assumed to remain identical to those of the experimental setup. This supposition is realistic, since the same or smaller tube length should be applicable in a real vehicle, and the utilized pressure regulators can provide enough mass flow for the full-sized vehicle.

The frequency responses of these models are shown in the left column of Fig. 4.50 for a sample driving speed of $120\,\mathrm{km/h}$ and a nominal cross-wind angle $\beta_w = 0°$. As can be seen from plot (a), the unsteady response of the drag coefficient c_D to cross-wind angle disturbances β_w starts to roll off at very low frequencies around $f \approx 1\,\mathrm{Hz}$. By contrast, the dynamics of the coefficients for side force and yaw moment are significantly faster, with cut-off frequencies around $20\,\mathrm{Hz}$ and $4\,\mathrm{Hz}$, respectively. In particular, the magnitude response of the yaw moment coefficient shows a small amplification peak for disturbances in the range $1\,\mathrm{Hz} \leq f \leq 3\,\mathrm{Hz}$. These characteristics lead to a transient overshoot of the yaw moment, as reported in many publications, see e.g. [120, 106, 114, 133]. Furthermore, the peak in the magnitude response overlaps with the range of frequencies $1.0\,\mathrm{Hz} \leq f \leq 1.5\,\mathrm{Hz}$ in which a significant amount of lateral turbulence is present for high-way driving in gusty cross-wind conditions, as described by Wojciak [145]. Hence, transient effects should be taken into account when assessing the characteristics of drag

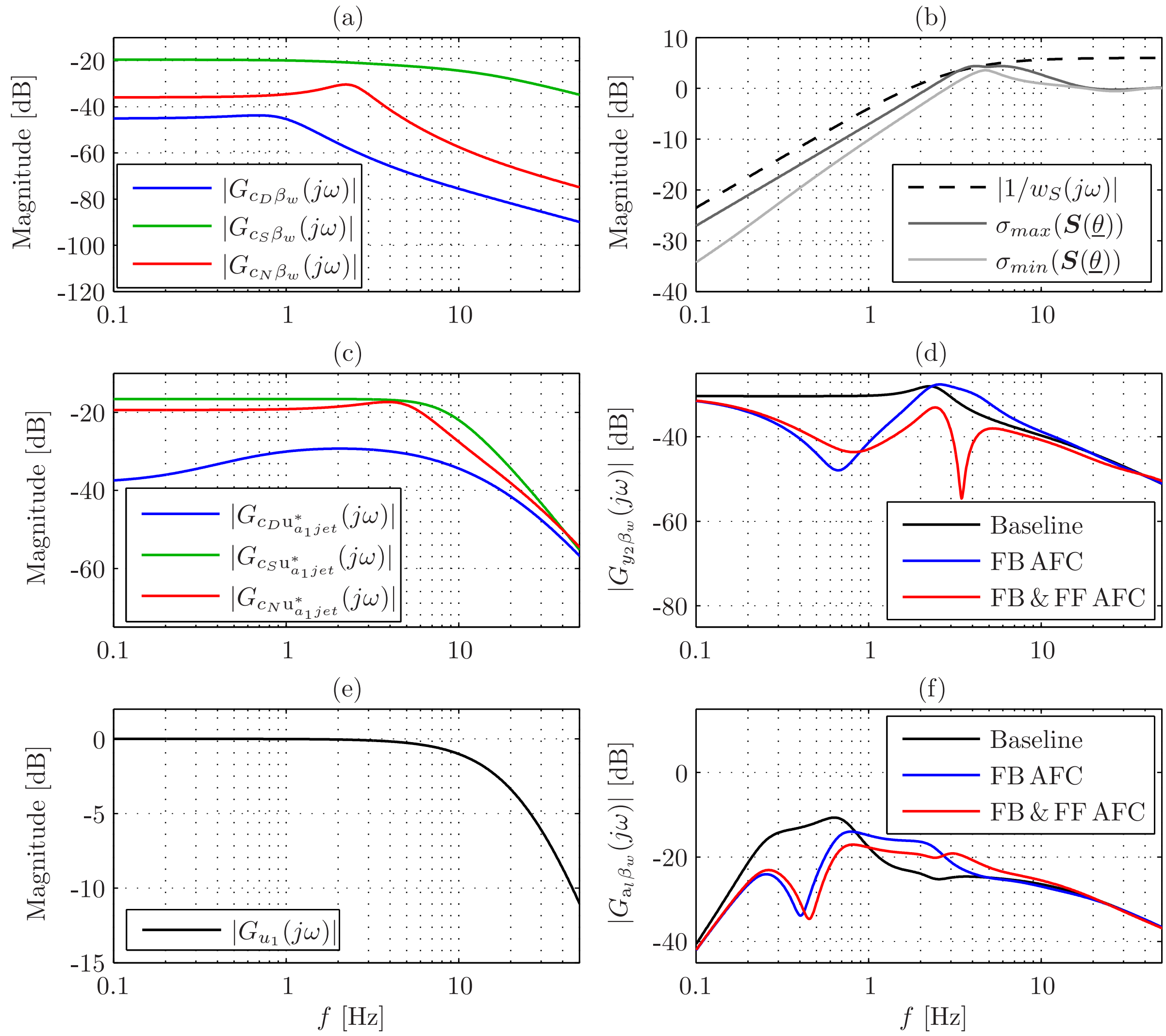

Figure 4.50: Predicted frequency responses for a full-sized vehicle with length $L_{\text{real}} = 5.6\,\text{m}$ at a driving speed $\text{v}_{v,\text{real}} = 120\,\text{km/h}$ and a nominal cross-wind angle $\beta_w = 0°$, based on the identified LPV models for the unsteady aerodynamic cross-wind gust response (a), the actuated flow dynamics (c) and the linear actuator dynamics (e). The right column shows the sensitivity with LPV feedback control (b), and the magnitude responses of the transfer functions for cross-wind angle disturbances β_w to output variable y_2 (d) and to the lateral vehicle acceleration a_l (f) for the baseline case relative to feedback LPV control and to combined feedback and feedforward LPV control, respectively.

and yaw-moment coefficients, whereas the side-force coefficient may well be approximated by a quasi-steady approach.

The frequency characteristics of the force and moment coefficients for the actuated flow are shown in Fig. 4.50 (c). Here, only the response to the instantaneous jet blowing ratio $\text{u}^*_{a_1 jet} = \text{u}_{a_1 jet}/\overline{\text{u}}_\infty$ for a nominal cross-wind angle $\beta_w = 0°$ is given, since the characteristics for the other actuator channels are similar. With the exception of the side-force coefficient, the magnitude responses indicate that the dynamics of the actuated flow are faster than the transient effects associated with the unsteady cross-wind gust response. Provided that the bandwidth of the actuator system is sufficient, estimated here to be approximately 20 Hz, this makes possible an effective suppression of the unsteady aerodynamic effects by closed-loop AFC.

To this end, LPV feedback and feedforward controllers are designed here with the methods described in section 4.6. For the LPV controller synthesis for the full-sized vehicle, the same structure of the weights for sensitivity and the control effort is applied as for the wind tunnel

model, but their time constants are chosen five times longer to account for the slower dynamics of the upscaled LPV models. The result of the LPV H_∞ control design is shown in Fig. 4.50 (b) for the maximum and minimum singular values of the closed-loop sensitivity for a driving velocity $\mathrm{v}_{v,\mathrm{real}} = 120\,\mathrm{km/h}$ at a nominal cross-wind angle $\overline{\beta}_w = 0°$. For these conditions, a bandwidth of approximately 1.6 Hz is achieved by LPV closed-loop AFC. This is sufficient to ensure an efficient reduction of the drag coefficient whose response to cross-wind disturbances rolls off for frequencies $f \geq 1\,\mathrm{Hz}$ as shown in plot (a). However, the sensitivity of the closed-loop shows a waterbed effect with a small amplification of disturbances in the frequency range $2\,\mathrm{Hz} \leq f \leq 20\,\mathrm{Hz}$. Analogous to the wind-tunnel case, this stems from the time delay at the input of the pressure regulators in the actuator system.
The combined effect of side-force and yaw-moment coefficients on lateral vehicle dynamics is approximated by the second output variable y_2. Its frequency response to cross-wind angle disturbances is depicted in Fig. 4.50 (d) for the baseline case in comparison with LPV feedback control (FB AFC) and combined LPV feedback and feedforward control (FB & FF AFC). Following the design presented in section 4.6.3, a dynamic reference filter is taken into account, which lets slow disturbances at frequencies $f < 0.2\,\mathrm{Hz}$ pass through, as these can be easily compensated for by the driver. Above this frequency, feedback LPV AFC provides an effective suppression of disturbances up to the closed-loop bandwidth of about 1.6 Hz. In the higher frequency range, the disturbance response can be improved by additional feedforward LPV control. As can be seen from Fig. 4.50 (f), combined feedback and feedforward LPV control results in a significantly reduced lateral vehicle acceleration response to cross-wind when compared with the baseline case. However, the performance obtained for the output variable y_2 is not achieved to the same degree for lateral vehicle acceleration. As mentioned in the previous section, this is due to the fixed weighting of side-force and yaw-moment coefficients and may be improved by integrating the driver-vehicle model in the generalized plant for LPV control synthesis. Nevertheless, the LPV controller presented here provides a significant improvement in the overall cross-wind sensitivity and a sufficient bandwidth for an efficient drag reduction in unsteady flow conditions.

Chapter 5

Conclusion

Road vehicles encounter various unsteady flow conditions, of which transient cross-wind has an especially large impact not only on driving safety, but also on fuel consumption due to an increased drag coefficient. Here, Active Flow Control technology can provide a substantial improvement, as it is able to adapt to changing flow conditions. This can be achieved via a suitable multivariable closed-loop flow control strategy, as demonstrated by the experimental results presented in this thesis.

Coanda blowing as proposed by Englar [34, 35] represents an effective and robust way to actuate the bluff body wake. In the case of the 2D and 3D bluff bodies investigated here, the drag coefficient can be efficiently reduced by 35 % and by 15 %, respectively. Although this requires rather high momentum coefficients with blowing velocities above the free-stream velocity, overall net power savings of up to 25 % and 8 % are achieved for the 2D and 3D bluff bodies, respectively. Furthermore, side-force and yaw-moment coefficients can be manipulated by asymmetric Coanda blowing to counter cross-wind effects.

The design of a corresponding closed-loop AFC strategy requires a model of the actuated flow. Its typically nonlinear dynamics can be captured with well-established approaches based on a set of linear black-box models identified from experiments at different operating points. Based on these models, a linear robust controller can be designed that provides a satisfactory performance in the multivariable case for AFC in cross-wind conditions, as shown by the wind tunnel results obtained with the 2D and 3D bluff bodies.

Yet unsteady aerodynamic phenomena usually show a parameter-dependent behavior, with dynamics that vary with free-stream velocity and other parameters such as cross-wind angle. These dependencies can be better captured by linear parameter-varying (LPV) models than by linear black-box models. To this end, this thesis proposes and applies a novel, practical way to identify gray-box LPV models from experimental data. This also allows for the design of LPV H_∞ gain-scheduling controllers whose dynamics are adjusted online according to the current parameter value. LPV control thus delivers a superior performance relative to linear robust control, as is shown for the 3D bluff body studied here.

The same LPV identification approach can be applied to model the transient cross-wind gust response. This captures the dependency of unsteady aerodynamic characteristics on free-stream velocity, allowing an investigation of its interaction with the lateral vehicle response for various driving speeds. Here, this is carried out for the cross-wind gust response of the 3D bluff body and for a single-track and virtual driver model with coefficients corresponding to a typical delivery van. Mostly due to the transient overshoot of the yaw moment, the overall frequency response of the lateral vehicle dynamics is significantly different from that of a quasi-steady approach. This is most pronounced at low to medium driving velocities up to about 120 km/h, though the magnitude response of the lateral vehicle acceleration is fairly small at these driving velocities. At higher speeds, the cross-wind sensitivity increases, but unsteady aerodynamic effects have a negligible influence.

However, the dynamic lateral response of the vehicle and the driver behavior should always be taken into account when assessing cross-wind sensitivity. To this end, the novel dynamic model support system presented in this thesis permits an experimental investigation of the interaction between unsteady aerodynamics and lateral vehicle motion. The measured transient side force and yaw moment serve as input variables for a real-time simulation of a single-track model and a virtual driver, on whose basis the wind tunnel model is moved in the test section. This way, the lateral dynamics of arbitrary vehicles can be replicated and all transient aerodynamic effects are realistically captured during the experiment. The results confirm that the transient characteristics of the aerodynamic cross-wind gust response do have an important influence on the lateral vehicle response, whereas unsteady effects from the lateral motion on the aerodynamics are negligible.

The developed LPV controller for feedback AFC suppresses disturbances acting on side-force and yaw-moment coefficients during cross-wind gusts in a way which is beneficial for the lateral vehicle response. The corresponding requirements for the closed-loop transfer functions are specified via adequate frequency-dependent weights for sensitivity and control effort. In combination with a suitably designed dynamic reference filter, the closed control loop lets disturbances at low frequencies pass through. These can be easily compensated for by the driver, but the feedback controller suppresses them in a frequency range where the driver cannot react. This minimizes the required control effort and helps achieve an efficient drag reduction in unsteady flow conditions while simultaneously improving cross-wind sensitivity. The sensitivity of the closed loop can be further reduced by an additional feedforward LPV controller. It is designed based on the identified LPV disturbance models for the unsteady cross-wind gust response and takes parameter variations of free-stream velocity and cross-wind angle into account. The cross-wind gust experiments with online replication of the lateral vehicle dynamics demonstrate the effectiveness of the combined feedback and feedforward LPV controller. To this end, the lateral vehicle displacement during gusts is reduced by more than 50 % relative to the baseline case without AFC.

All in all, the results show how closed-loop AFC can be used to efficiently reduce the aerodynamic drag in realistic, unsteady flow conditions. Furthermore, additional benefits such as reduced cross-wind sensitivity make the application of this technology attractive, as it can also help increase driving safety and comfort for passengers.

Acknowledgment

This work was funded by the German Research Foundation (DFG) in the context of the research projects Ki 679/9-1 and Ki 679/9-2 “Regelung instationärer Strömungen um stumpfe Körper unter Berücksichtigung der Fahrzeugquerdynamik”.

References

[1] Ackermann, J., T. Bünte, and D. Odenthal: *Advantages Of Active Steering For Vehicle Dynamics Control.* In *Proc. 32nd International Symposium on Automotive Technology and Automation*, pages 263–270, Wien, 1999.

[2] Ackermann, J., J. Guldner, W. Sienel, R. Steinhauser, and V. I. Utkin: *Linear and Nonlinear Controller Design for Robust Automatic Steering.* Control System Technology, 3:132–143, 1995.

[3] Ahmed, S. R., R. Ramm, and G. Faltin: *Some salient features of the time-averaged ground vehicle wake.* SAE Paper 840300, 1984.

[4] Aider, J. L., J. F. Beaudoin, and J. E. Wesfreid: *Drag and lift reduction of a 3D bluff-body using active vortex generators.* Experiments in Fluids, 48(5):771–789, 2009.

[5] Aleksić, K., D.M. Luchtenburg, R. King, B.R. Noack, and J. Pfeiffer: *Robust nonlinear control versus linear model predictive control of a bluff body wake.* In *5th AIAA Flow Control Conference,* AIAA 2010-4833, Chicago, Illinois, USA, 2010.

[6] Aleksić-Roeßner, K., R. King, O. Lehmann, G. Tadmor, and M. Morzyński: *On the need of nonlinear control for efficient model-based wake stabilization.* Theoretical and Computational Fluid Dynamics, 28(1):23–49, 2014.

[7] Ali, M., S. S. Chughtai, and H. Werner: *An LPV Gain Scheduling Approach to Transition Control in Plane Poiseuille Flow.* In *Proceedings of the European Control Conference*, pages 2033–2038, Budapest, Hungary, 2009.

[8] Amitay, M., B. L. Smith, and A. Glezer: *Aerodynamic Flow Control Using Synthetic Jet Technology.* In *36th AIAA Aerospace Sciences Meeting and Exhibit,* AIAA 98-0208, Reno, Nevada, USA, 1998.

[9] Ammon, D.: *CO_2-mindernde Fahrwerk- und Fahrdynamiksysteme.* ATZ - Automobiltechnische Zeitschrift, 112(10):770–775, 2010.

[10] Apkarian, P.: *On the Discretization of LMI-Synthesized Linear Parameter-Varying Controllers.* Automatica, 33:655–661, 1997.

[11] Apkarian, P. and R.J. Adams: *Advanced gain-scheduling techniques for uncertain systems.* IEEE Transactions on Control Systems Technology, 6(1):21–32, 1998.

[12] Apkarian, P. and J. M. Biannic: *Self-scheduled H_∞ Control of Missile via Linear Matrix Inequalities.* Journal of Guidance, Control and Dynamics, 18(3):532–538, 1995.

[13] Apkarian, P. and P. Gahinet: *A Convex Characterization of Gain-Scheduled H_∞ Controllers.* IEEE Transactions on Automatic Control, 40(5):853–864, 1995.

[14] Apkarian, P., P. Gahinet, and G. Becker: *Self-Scheduled H_∞ Control of Linear Parameter-Varying Systems: A Design Example.* Automatica, 31(9):1251–1261, 1995.

[15] Apkarian, P., P. C. Pellanda, and H. D. Tuan: *Mixed H_2/H_∞ Multi-Channel Linear Parameter-Varying Control in Discrete Time.* System and Control Letters, 41:333–346, 2000.

[16] Aubrun, S., J. McNally, F. Alvi, and A. Kourta: *Separation flow control on a generic ground vehicle using steady microjet arrays.* Experiments in Fluids, 51:1177–1187, 2011.

[17] Bearman, P. W.: *Investigation of the flow behind a two-dimensional model with a blunt trailing edge and fitted with splitter plates.* Journal of Fluid Mechanics, 21:241–255, 1965.

[18] Bearman, P. W.: *The effect of base bleed on the flow behind a two-dimensional model with a blunt trailing edge.* Aeronautical Quarterly, 18:207–224, 1967.

[19] Bearman, P. W.: *Near wake flows behind two- and three-dimensional bluff bodies.* Journal of Wind Engineering and Industrial Aerodynamics, 69-71:33–54, 1997.

[20] Beaudoin, J. F., O. Cadot, J. L. Aider, and J. E. Wesfreid: *Drag reduction of a bluff body using adaptive control methods.* Physics of Fluids, 18(085107):1–10, 2006.

[21] Becker, A.: *Messungen im Nachlauf von Körpern mit stumpfen Heck mittels der Laser-Doppler-Anemometrie.* Fortschritt-Berichte VDI. VDI-Verlag, 1994.

[22] Becker, G. and A. Packard: *Robust performance of linear parametrically varying systems using parametrically-dependent linear feedback.* Systems & Control Letters, 23(3):205–215, 1994.

[23] Becker, R., R. King, R. Petz, and W. Nitsche: *Adaptive Closed-Loop Separation Control on a High-Lift Configuration Using Extremum Seeking.* AIAA Journal, 45(6):1382–1392, 2007.

[24] Boonto, S. and H. Werner: *Closed-Loop System Identification of LPV Input-Output Models - Application to an Arm-Driven Inverted Pendulum.* In *Proceedings of the 47th IEEE Conference on Decision and Control*, pages 2606–2611, 2008.

[25] Boyd, S., L. El Ghaoui, E. Feron, and V. Balakrishnan: *Linear Matrix Inequalities in System and Control Theory.* Society for Industrial and Applied Mathematics, 1994.

[26] Brunn, A., W. Nitsche, L. Henning, R. King, and L. Henning: *Application of Slope-Seeking to a Generic Car Model for Active Drag Control.* In *26th AIAA Applied Aerodynamics Conference,* AIAA 2008-6734, Honolulu, Hawaii, 2008.

[27] Brunn, A., E. Wassen, D. Sperber, W. Nitsche, and F. Thiele: *Active drag control for a generic car model.* In King, R. (editor): *Active Flow Control*, volume 95 of *Notes on Numerical Fluid Mechanics and Multidisciplinary Design*, pages 247–259. Springer, Berlin, Heidelberg, 2007.

[28] Caigny, J. De, J.F. Camino, R. C. L. F. Oliveira, P. L. D. Peres, and J. Sweres: *Gain-scheduled H_2 and H_∞ control of discrete-time polytopic time-varying systems.* IET Control Theory and Applications, 4(3):362–380, 2010.

[29] Choi, H.: *Active control of flows over bluff bodies for drag reduction.* In *Proceedings of the 4th Symposium on Smart Control of Turbulence*, pages 1–12, 2003.

[30] Choi, H., W. P. Jeon, and J. Kim: *Control of Flow Over a Bluff Body.* Annual Review of Fluid Mechanics, 40:113–139, 2008.

[31] Daimler AG: *The crosswind assist.* http://www.daimler.com/dccom/0-5-1210218-1-1577465-1-0-0-1210228-0-0-135-0-0-0-0-0-0-0-0.html, accessed March 10, 2015.

[32] Dominy, R. G.: *A technique for the investigation of transient aerodynamic forces on road vehicles in cross winds.* Proceedings of the Institute of Mechanical Engineers Part D: Journal of Automobile Engineering, 205(4):245–250, 1991.

[33] Dominy, R.G. and A. Ryan: *An Improved Wind Tunnel Configuration for the Investigation of Aerodynamic Cross Wind Gust Response.* SAE Technical Paper 1999-01-0808, 1999.

[34] Englar, R. J.: *Advanced Aerodynamic Devices to Improve the Performance Economics, Handling and Safety of Heavy vehicles*. SAE Technical Paper 2001-01-2072, 2001.

[35] Englar, R. J.: *Pneumatic Heavy Vehicle Aerodynamic Drag Reduction.* In *The Aerodynamics of Heavy Vehicles: Trucks, Buses, and Trains*, volume 19 of *Lecture Notes in Applied and Computational Mechanics*, pages 277–302. Engineering Conferences International, Springer, 2004.

[36] Englar, R. J., G. S. Jones, B. G. Allan, and J. C. Lin: *2-d circulation control airfoil benchmark experiments intended for cfd code validation.* In *47th AIAA Aerospace Sciences Meeting,* AIAA 2009-902, Orlanda, Florida, 2009.

[37] Felici, F., J. W. van Wingerden, and M. Verhaegen: *Subspace identification of MIMO LPV systems using a periodic scheduling sequence*. Automatica, 43(10):1684–1697, 2007.

[38] Ferrand, V.: *Forces and Flow Structures on a Simplified Car Model Exposed to an Unsteady Harmonic Crosswind*. Journal of Fluids Engineering, 136:1–8, 2013.

[39] Filippone, A.: *Unsteady Gust Response of Road Vehicles*. Journal of Fluids Engineering, 125:806–812, 2003.

[40] Fitzpatrick, K., Y. Feng, R. Lind, A. J. Kurdila, and D. W. Mikolaitis: *Flow Control in a Driven Cavity Incorporating Excitation Phase Differential*. Journal of Guidance, Control and Dynamics, 28:63–70, 2005.

[41] Fuller, J. B. and M. Passmore: *Unsteady Aerodynamics of an Oscillating Fastback Model*. SAE International Journal of Passenger Cars - Mechanical Systems, 6(1):403–413, 2013.

[42] Gahinet, P., A. Nemirovski, A. J. Laub, and M. Chilali: *LMI Control Toolbox*. Technical report, The MathWorks Inc., 1994.

[43] Gelbert, G., J.P. Moeck, M.R. Bothien, R. King, and C.O. Paschereit: *Model Predictive Control of Thermoacoustic Instabilities in a Swirl-Stabilized Combustor*. In *Proceedings of the 46th AIAA Aerospace Sciences Meeting and Exhibit,* AIAA 2008-1055, 2008.

[44] Gerhard, J., M. Pastoor, R. King, B. Noack, A. Dillmann, M. Morzyński, and G. Tadmor: *Model-based control of vortex shedding using low-dimensional galerkin models*. In *33rd AIAA Fluid Dynamics Conference and Exhibit,* AIAA 2003-4262, Orlando, Florida, 2003.

[45] Geropp, D. and H. J. Odenthal: *Drag reduction of motor vehicles by active flow control using the Coanda effect*. Experiments in Fluids, 28:74–85, 2000.

[46] Gilliéron, P. and A. Kourta: *Aerodynamic drag control by pulsed jets on simplified car geometry*. Experiments in Fluids, 54(1457):1–16, 2013.

[47] Goetz, H.: *Crosswind Facilities and Procedures*. SAE special publication SP-1109, Warrendale, USA, 1995.

[48] Goldin, N., R. King, A. Pätzold, W. Nitsche, D. Haller, and P. Woias: *Laminar flow control with distribute surface actuation: damping Tollmien-Schlichting waves with active surface displacement*. Experiments in Fluids, 54(1478):1–11, 2013.

[49] Greenblatt, D. and I. J. Wygnanski: *The control of flow seperation by periodic excitation.* Progress in Aerospace Science, 36:487–545, 2000.

[50] Guilmineau, E. and F. Chometon: *Experimental and Numerical Study of Unsteady Wakes Behind an Oscillating Car Model*. In *Proceedings of the IUTAM Symposium Unsteady Separated Flows and their Control*, Corfu, Greece, 2007.

[51] Hemida, H. and S. Krajnović: *Transient Simulation of the Aerodynamic Response of a Double-Deck Bus in Gusty Winds*. Journal of Fluids Engineering, 131(3):1–10, 2009.

[52] Henning, L.: *Regelung abgelöster Scherschichten durch aktive Beeinflussung.* PhD thesis, Technische Universität Berlin, 2008.

[53] Henning, L., R. Becker, G. Feuerbach, R. Muminović, R. King, R. Petz, A. Brunn, and W. Nitsche: *Extensions of adaptive slope-seeking for active flow control.* Journal of Systems and Control Engineering, 222(5):309–322, 2008.

[54] Henning, L. and R. King: *Drag reduction by closed-loop control of a separated flow over a bluff body with a blunt trailing edge.* In *Proceedings of the 44th IEEE Conference on Decision and Control, and the European Control Conference*, pages 494–499, Seville, Spain, 2005.

[55] Henning, L. and R. King: *Multivariable closed-loop control of the reattachment length downstream of a backward-facing step.* In *Proceedings of the 16th IFAC World Congress, IFAC*, Prague, Czechia, 2005.

[56] Hucho, W. H.: *Aerodynamik des Automobils.* Vieweg Verlag, 2008.

[57] Hucho, W. H.: *Aerodynamik der stumpfen Körper - Physikalische Grundlagen und Anwendungen in der Praxis.* Vieweg + Teubner Verlag, 2011.

[58] Huemer, J.: *Einfluss instationärer aerodynamischer Kräfte auf die Fahrdynamik von Personenkraftwagen.* PhD thesis, Technische Universität München, 2014.

[59] Huerre, P. and P. A. Monketwitz: *Local and global instabilities in spatially developing flows.* Annual Review of Fluid Mechanics, 22:473–537, 1990.

[60] Isermann, R. (editor): *Fahrdynamik-Regelung: Modellbildung, Fahrerassistenzsysteme, Mechatronik.* Vieweg-Verlag, 2006.

[61] Jones, G. S., J. C. Lin, B. G. Allan, W. E. Milholen, C. L. Rumsey, and R. C. Swanson: *Overview of cfd validation experiments for circulation control applications at nasa.* In *International Powered Lift Conference*, pages 22–24, 2008.

[62] Kalighi, B., S. Zhang, C. Koromilas, and S. R. Balkanyi: *Experimental and Computational Study of Unsteady Wake Flow Behind a Bluff Body with a Drag Reduction Device.* SAE Technical Paper 2001-01-1042, 2001.

[63] Kawakami, M., N. Sato, P. Aschwanden, J. Müller, Y. Kato, M. Nakagawa, and E. Ono: *Validation and Modeling of Transient Aerodynamic Loads Acting on a Simplified Passenger Car Model in Sinusoidal Motion.* SAE International Journal of Passenger Cars - Mechanical Systems, 5(1):340–357, 2012.

[64] Keppler, D., M. Rau, D. Ammon, J. Kalkkuhl, A. Suissa, M. Walter, L. Maack, K. D. Hilf, and C. Däsch: *Realisierung einer Seitenwind-Assistenzfunktion für PKW.* In *AAET 2010 Automatisierungssysteme, Assistenzsysteme und eingebettete Systeme für Transportmittel*, Braunschweig, Germany, 2010.

[65] Kerstens, W., J. Pfeiffer, D. Williams, R. King, and T. Colonius: *Closed-Loop Control of Lift for Longitudinal Gust Suppression at Low Reynolds Numbers.* AIAA Journal, 49(8):1721–1728, 2011.

[66] Kerstens, W., D. Williams, J. Pfeiffer, and R. King: *Closed Loop Control of a Wing's Lift for 'Gust' Suppression.* In *5th AIAA Flow Control Conference,* AIAA 2010-4969, Chicago, Illinois, USA, 2010.

[67] Kim, J., S. Hahn, J. Kim, D. K. Lee, J. Choi, W. P. Jeon, and H. Choi: *Active control of turbulent flow over a model vehicle for drag reduction.* Journal of Turbulence, 5(19), 2004.

[68] King, R., K. Aleksić, G. Gelbert, N. Losse, R. Muminovic, A. Brunn, W. Nitsche, M. R. Bothien, J. P. Moeck, C. O. Paschereit, and B. R. Noack: *Model predictive flow control.* In *4th AIAA Flow Control Conference,* AIAA 2008-3975, Seattle, Washington, USA, 2008.

[69] King, R., N. Heinz, M. Bauer, T. Grund, and W. Nitsche: *Flight and wind tunnel tests of closed-loop active flow control.* In *6th AIAA Flow Control Conference,* AIAA 2012-2801, 2012.

[70] King, R., L. Henning, R. Petz, W. Nitsche, O. Lemke, and W. Neise: *Adaptive flow control using slope seeking.* In *14th Mediterranean Conference on Control and Automation*, 2006.

[71] Krajnović, S., H. E. Hafsteinsson, E. Helgason, and B. Basara: *Shape optimization of a bus for crosswind stability.* In *Euromech Colloquium 509: Vehicle Aerodynamics*, pages 162–173, Berlin, 2009.

[72] Krantz, W.: *An Advanced Approach for Predicting and Assessing the Driver's Response to Natural Crosswind.* PhD thesis, Universität Stuttgart, 2011.

[73] Krentel, D.l, R. Muminović, A. Brunn, , W. Nitsche, and R. King: *Application of Active Flow Control on Generic 3D Car Models.* In King, R. (editor): *Active Flow Control II*, volume 108 of *Notes on Numerical Fluid Mechanics and Multidisciplinary Design*, pages 223–239. Springer, 2010.

[74] Küssner, H. G.: *Zusammenfassender Bericht über den instationären Auftrieb von Flügeln.* Luftfahrtforschung, 13(12):410–424, 1936.

[75] Leclerc, C., E. Levallois, P. Gilliéron, and A. Kourta: *Aerodynamic Drag Reduction by Synthetic Jet: A 2D Numerical Study Around a Simplified Car.* In *3rd AIAA Flow Control Conference,* AIAA 2006-3337, 2006.

[76] Leder, A.: *Abgelöste Strömungen: physikalische Grundlagen.* Grundlagen und Fortschritte der Ingenieurwissenschaften. Vieweg, 1992.

[77] Leishman, J. G.: *Principles of Helicopter Aerodynamics.* Cambridge University Press, 2006.

[78] Littlewood, R. P. and M. A. Passmore: *Aerodynamic drag reduction of a simplified square-back vehicle using steady blowing.* Experiments in Fluids, 53:519–529, 2012.

[79] Ljung, L.: *System Identification: Theory for the User.* Prentice Hall PTR, 1999.

[80] Luchtenburg, D. M., K. Aleksić, M. Schlegel, B. R. Noack, , R. King, G. Tadmor, B. Günther, and F. Thiele: *Turbulence Control Based on Reduced-Order Models and Nonlinear Control Design.* In King, R. (editor): *Active Flow Control II*, volume 108 of *Notes on Numerical Fluid Mechanics and Multidisciplinary Design*, pages 341–356. Springer, 2010.

[81] Luenberger, D. G.: *Canonical forms for linear multivariable systems.* IEEE Transactions on Automatic Control, AC-12(3):290–293, June 1967.

[82] Mankowski, O. A., D. B. Sims-Williams, and R. G. Dominy: *A Wind Tunnel Simulation Facility for On-Road Transients.* SAE International Journal of Passenger Cars - Mechanical Systems, 7(3):1087–1095, 2014.

[83] Mansor, S. and M.A. Passmore: *Estimation of bluff body transient aerodynamics using an oscillating model rig.* Journal of Wind Engineering and Industrial Aerodynamics, 96:1218–1231, 2008.

[84] MATLAB: *Release R2007b.* The MathWorks Inc., Natic, Massachusetts, 2007.

[85] Mitschke, Manfred and Henning Wallentowitz: *Dynamik der Kraftfahrzeuge.* Springer-Verlag, Berlin Heidelberg, 4th edition, 2004.

[86] Müller-Vahl, H. F., C. N. Nayeri, C. O. Paschereit, and D. Greenblatt: *Control of Unsteady Aerodynamic Loads Using Adaptive Blowing.* In *32nd AIAA Applied Aerodynamics Conference,* AIAA 2014-2562, Atlanta, Georgia, USA, 2014.

[87] Muminović, R., L. Henning, R. King, A. Brunn, and W. Nitsche: *Robust and Model Predictive Drag Control for a Generic Car Model.* In *4th AIAA Flow Control Conference,* AIAA 2008-3859, Seattle, Washington, USA, 2008.

[88] Muminović, R., J. Pfeiffer, N. Werner, and R. King: *Model Predictive Control for a 2D Bluff Body Under Disturbed Flow Conditions.* In King, R. (editor): *Active Flow Control II*, volume 108 of *Notes on Numerical Fluid Mechanics and Multidisciplinary Design*, pages 257–272. Springer, 2010.

[89] Muminović, R., N. Werner, J. Pfeiffer, and R. King: *Drag reduction of two 2D bluff bodies in a tandem arrangment through robust model predictice control.* In *5th AIAA Flow Control Conference,* AIAA 2010-4835, Chicago, Illinois, USA, 2010.

[90] Muminović, Rifet: *Modellprädiktive Regelung abgelöster Scherströmungen an stumpfen Körpern.* PhD thesis, Technische Universität Berlin, 2013.

[91] Nelles, O.: *Nonlinear System Identification.* Springer-Verlag, 2001.

[92] Nishino, T., S. Hahn, and K. Shariff: *Large-eddy simulations of a turbulent coanda jet on a circulation control airfoil.* Physics of Fluids, 22:1–15, 2010.

[93] Oettle, N., O. Mankowski, D. Sims-Williams, and R. Dominy: *Evaluation of the Aerodynamic and Aeroacoustic Response of a Vehicle to Transient Flow Conditions.* SAE International Journal of Passenger Cars - Mechanical Systems, 6(1):389–402, 2013.

[94] Okada, Y., T. Nouzawa, S. Okamoto, T. Fujita, T. Kamioka, and M. Tsubokura: *Unsteady vehicle aerodynamics during a dynamic steering action: 1st report, on-road analysis.* SAE Technical Paper 2012-01-0446, 2012.

[95] Packard, A.: *Gain scheduling via linear fractional transformations.* Systems & Control Letters, 22(2):79–92, 1994.

[96] Parezanović, V. and O. Cadot: *Experimental sensitivity analysis of the global properties of a two-dimensional turbulent wake.* Journal of Fluid Mechanics, 693:115–149, 2012.

[97] Park, H., D. Lee, W. P. Jeon, S. Hahn, J. Kim, J. Kim, J. Choi, and H. Choi: *Drag reduction in flow over a two-dimensional bluff body with a blunt trailing edge using a new passive device.* Journal of Fluid Mechanics, 563:389–414, 2006.

[98] Park, J. K. and C.H. Choi: *Dynamical Anti-Reset Windup Method for Discrete-Time Saturating Systems.* Automatica, 33(6):1055–1072, 1997.

[99] Passmore, M.A.: *An experimental study of unsteady vehicle aerodynamics.* Proceedings of the Institute of Mechanical Engineers Part D: Journal of Automobile Engineering, 215(7):779–788, 2001.

[100] Pastoor, M., L. Henning, B. Noack, R. King, and G. Tadmor: *Feedback shear layer control for bluff body drag reduction.* Journal of Fluid Mechanics, 608(1):161 – 196, 2008.

[101] Pfeiffer, J. and R. King: *Robust Closed-Loop Flow Control of Drag and Yaw Moment for a Bluff Body under Cross-Wind Conditions.* In Wiedemann, Jochen (editor): *Progress in Vehicle Aerodynamics and Thermal Management - Proceedings of the 8th FKFS-Conference*, pages 159–173. Expert Verlag, 2012.

[102] Pfeiffer, J. and R. King: *Linear parameter-varying active flow control for a 3D bluff body exposed to cross-wind gusts.* In *32nd AIAA Applied Aerodynamics Conference,* AIAA 2014-2406, 2014.

[103] Pfeiffer, Jens and Rudibert King: *Multivariable closed-loop flow control of drag and yaw moment for a 3d bluff body.* In *6th AIAA Flow Control Conference*, 2012. AIAA 2012-2802, DOI 10.2514/6.2012-2802.

[104] Prime, Z., B. Cazzolato, and C. Doolan: *A mixed $H2/H_\infty$ scheduling control scheme for a two degree-of-freedom aeroelastic system under varying airspeed and gust conditions.* In *AIAA Guidance, Navigation and Control Conference and Exhibit,* AIAA 2008-6787, Honolulu, Hawaii, 2008.

[105] Risse, H. J.: *Das Fahrerverhalten bei normaler Fahrzeugführung.* PhD thesis, Technische Universität Braunschweig, 1991.

[106] Ryan, A. and R. G. Dominy: *The Aerodynamic Forces Induced on a Passenger Vehicle in Response to a Transient Cross-Wind Gust at a Relative Incidence of* 30°. SAE Technical Paper 980392, (980392), 1998.

[107] Ryan, A. and R. G. Dominy: *Wake Surveys Behind a Passenger Car Subjected to a Transient Cross-Wind Gust.* SAE International Journal of Passenger Cars - Mechanical Systems, 109(6):1461–1469, 2000.

[108] Sackmann, M. and A. Trächtler: *Nichtlineare Fahrdynamikregelung mit einer aktiven Vorderachslenkung zur Verbesserung des Seitenwindverhaltens.* at - Automatisierungstechnik, 51(12):535–546, 2003.

[109] Scherer, C., P. Gahinet, and M. Chilali: *Multiobjective Output-Feedback Control via LMI-Optimization.* IEEE Transactions on Automatic Control, 42:896–911, 1997.

[110] Schlichting, H. and K. Gersten: *Boundary Layer Theory.* Springer-Verlag, Berlin Heidelberg, 2000.

[111] Schmidt, H. J., R. Woszidlo, C. N. Nayeri, and C. O. Paschereit: *Drag reduction on a rectangular bluff body with base flaps and fluidic oscillators.* Experiments in Fluids, 56(151):1–16, 2015.

[112] Schorn, M., J. Schmitt, U. Stählin, and R. Isermann: *Model Based Braking Control with Support by Active Steering.* In *16th IFAC World Congress*, pages 263–270, Prague, Czech Republic, 2005.

[113] Schröck, D.: *Eine Methode zur Bestimmung der aerodynamischen Eigenschaften eines Fahrzeugs unter böigem Seitenwind.* PhD thesis, Universität Stuttgart, 2012.

[114] Schröck, D., W. Krantz, N. Widdecke, and J. Wiedemann: *Unsteady Aerodynamic Properties of a Vehicle Model and their Effect on Driver and vehicle under Side Wind Conditions.* SAE International Journal of Passenger Cars - Mechanical Systems, 4(1):108–119, 2011.

[115] Seifert, A., O. Stalnov, D. Sperber, G. Arwatz, V. Palei, S. Palei, I. Dayan, and I. Fono: *Large Trucks Drag Reduction Using Active Flow Control.* In *46th AIAA Aerospace Sciences Meeting and Exhibit,* AIAA 2008-743, 2008.

[116] Shamma, J. S. and M. Athans: *Analysis of Gain Scheduled Control for Nonlinear Plants.* IEEE Transactions on Automatic Control, 35(8):898–907, 1990.

[117] Shamma, J. S. and M. Athans: *Guaranteed properties of gain scheduled control for linear parameter-varying plants.* Automatica, 27(3):559–564, 1991.

[118] Shamma, J. S. and M. Athans: *Gain scheduling: potential hazards and possible remedies.* IEEE Control Systems Magazine, 12(3):101–107, 1992.

[119] Siegel, S., K. Cohen, and T. McLaughlin: *Feedback control of a circular cylinder wake in experiment and simulation.* In *33rd AIAA Fluid Dynamics Conference and Exhibit,* AIAA 2003-3569, Orlando, Florida, 2003.

[120] Sims-Williams, D.: *Cross Winds and Transients: Reality, Simulation and Effects*. SAE International Journal of Passenger Cars - Mechanical Systems, 4(1):172–182, 2011.

[121] Skogestad, S. and I. Postlethwaite: *Multivariable Feedback Control - Analysis and Design (2nd Edition)*. John Wiley & Sons, Chichester, England, 2005.

[122] Sumitani, K. and M. Yamada: *Development of "Aero Slit" - Improvement of Aerodynamic Yaw Characteristics for Commercial Vehicles*. SAE Technical Paper 890372, 1989.

[123] Széchényi, Edmond: *Crosswind and its simulation*. In Wiedemann, J. and W. H. Hucho (editors): *Progress in Vehicle Aerodynamics: Advanced Experimental Techniques*, pages 83–96. Expert Verlag, Renningen, 2000.

[124] Theissen, P., J. Wojciak, K. Heuler, R. Demuth, T. Indinger, and N. Adams: *Experimental Investigation of Unsteady Vehicle Aerodynamics under Time-Dependent Flow Conditions - Part 1*. SAE Technical Paper 2011-01-0177, 2011.

[125] Theodorsen, T.: *General Theory of Aerodynamic Instability and the Mechanisms of Flutter*. Technical report, NACA Report 496, 1935.

[126] Tombazis, N. and P. W. Bearman: *A study of three-dimensional aspects of vortex shedding from a bluff body with a mild geometric disturbance*. Journal of Fluid Mechanics, 330:85–112, 1997.

[127] Troshin, Victor and Avraham Seifert: *Performance recovery of a thick turbulent airfoil using a distributed closed-loop flow control system*. Experiments in Fluids, 54(1443):1–19, 2013.

[128] Tsubokura, M., Y. Ikawa, T. Nakashima, Y. Okada, T. Kamioka, and T. Nouzawa: *Unsteady vehicle aerodynamics during a dynamic steering action: 2nd report, numerical analysis*. SAE International Journal of Passenger Cars - Mechanical Systems, 5(1):358–368, 2012.

[129] Tóth, Roland: *Modeling and Identification of Linear Parameter-Varying Systems*, volume 403 of *Lecture Notes in Control and Information Sciences*. Springer-Verlag, 2010.

[130] Verdult, V.: *Nonlinear System Identification: A State-Space Approach*. PhD thesis, University of Twente, 2002.

[131] Verdult, V. and M. Verhaegen: *Identification of Multivariable Linear Parameter-Varying Systems Based on Subspace Techniques*. In *Proceedings of the 39th IEEE Conference on Decision and Control*, pages 1567–1572, Sydney, Australia, 2000.

[132] Verdult, V. and M. Verhaegen: *Kernel methods for subspace identification of multivariable LPV and bilinear systems*. Automatica, 41(9):1557–1565, 2005.

[133] Volpe, R., V. Ferrand, A. Da Silva, and L. Le Moyne: *Forces and flow structures evolution on a car body in a sudden crosswind*. Journal of Wind Engineering and Industrial Aerodynamics, 5(128):114–125, 2015.

[134] Volpe, R., A. Da Silva, V. Ferrand, and L. Le Moyne: *Experimental and Numerical Validation of Wind Gust Facility*. Journal of Fluids Engineering, 135:1–9, 2013.

[135] V.Verdult, M. Verhaegen, and J. Scherpen: *Identification of Nonlinear Nonautonomous State-Space Systems from Input-Output Measurments*. In *Proceedings of IEEE International Conference on Industrial Technology*, volume 2, pages 410–414, 2000.

[136] Wagner, A.: *An Approach to Predict and Evaluate the Driver's Response to Crosswind*. In Wiedemann, J. and W. H. Hucho (editors): *Progress in Vehicle Aerodynamics III: Unsteady Flow Effects*, pages 107–120. Expert Verlag, Renningen, 2004.

[137] Wagner, H.: *über die Entstehung des dynamischen Auftriebs von Tragflügeln.* ZAMM - Journal of Applied Mathematics and Mechanics, 5(1):17–35, 1925.

[138] Watkins, S., S. Toksoy, and J.W. Saunders: *On the Generation of Tunnel Turbulence for Road Vehicles.* In *11th Australasian Fluid Mechanics Conference*, Hobart, Australia, 14-18 December 1992.

[139] Wetzel, D. A., J. Griffin, and L. N. Cattafesta: *Experiments on an elliptic circulation control airfoil.* Journal of Fluid Mechanics, 730:99–144, 2013.

[140] White, F. M.: *Fluid Mechanics.* McGraw-Hill, New York, USA, 7th edition, 2009.

[141] Williams, D., W. Kerstens, J. Pfeiffer, and R. King: *Unsteady Lift Suppression with a Robust Closed Loop Controller.* In King, R. (editor): *Active Flow Control II*, volume 108 of *Notes on Numerical Fluid Mechanics and Multidisciplinary Design*, pages 19–30. Springer, 2010.

[142] Wingerden, J. W. van and M. Verhaegen: *Subspace identification of Bilinear and LPV systems for open- and closed-loop data.* Automatica, 45:372–381, 2009.

[143] Wojciak, J., T. Indinger, N. Theissen, and P. R. Demuth: *Experimental study of on-road aerodynamics during crosswind gusts.* In *MIRA Vehicle Aerodynamics Conference*, Grove, UK, October 13-14 2010.

[144] Wojciak, J., P. Theissen, K. Heuler, T. Indinger, N. Adams, and R. Demuth: *Experimental Investigation of Unsteady Vehicle Aerodynamics under Time-Dependent Flow Conditions - Part2.* SAE Technical Paper 2011-01-0164, 2011.

[145] Wojciak, J. D.: *Quantitative Analysis of Vehicle Aerodynamics during Crosswind Gusts.* PhD thesis, Technische Universität München, 2012.

[146] Wood, G. D., P. J. Goddard, and K. Glover: *Approximation of Linear Parameter-Varying Systems.* In *Proc. of the 35th Conference on Decision and Control*, pages 406–411, Kobe, Japan, 1996.

[147] Wordley, S. and J. Saunders: *On-road Turbulence.* SAE International Journal of Passenger Cars - Mechanical Systems, 1(1):341–360, 2009.

[148] Wordley, S. and J. Saunders: *On-road turbulence: Part 2.* SAE International Journal of Passenger Cars - Mechanical Systems, 2(1):111–137, 2009.

[149] Wu, F., X. H. Yang, A. Packard, and G. Becker: *Induced L_2-norm control for LPV system with bounded parameter variation rates.* In *Proceedings of the American Control Conference*, volume 3, pages 2379–2383, 1995.

Appendix A

State-space equations of the driver-vehicle model

Single-track model

The single-track model presented in section 2.3.1 consists of two differential equations

$$\dot{\beta} = a_{11}\beta + a_{12}\dot{\psi} + b_1\delta + e_1 F_y, \tag{A.1}$$
$$\ddot{\psi} = a_{21}\beta + a_{22}\dot{\psi} + b_2\delta + e_2 M_z, \tag{A.2}$$

for the side-slip angle β and the yaw angle ψ, with the coefficients

$$\begin{aligned}
a_{11} &= -\frac{C_{\alpha r} + C_{\alpha f}}{m\mathrm{v}_v},\ a_{12} = \frac{C_{\alpha r}L_r - C_{\alpha f}L_f}{m\mathrm{v}_v^2} - 1, \\
a_{21} &= \frac{C_{\alpha r}L_r + C_{\alpha f}L_f}{J_z},\ a_{22} = -\frac{C_{\alpha r}L_r^2 + C_{\alpha f}L_f^2}{J_z\mathrm{v}_v}, \\
b_1 &= \frac{C_{\alpha f}}{i_s m\mathrm{v}_v},\ b_2 = \frac{C_{\alpha f}L_f}{i_s J_z},\ e_1 = \frac{1}{m\mathrm{v}_v},\ e_2 = \frac{1}{J_z}.
\end{aligned} \tag{A.3}$$

For small angles ψ and β, lateral velocity v_l and acceleration a_l can be approximated by

$$\mathrm{v}_l \approx (\psi + \beta)\mathrm{v}_v, \tag{A.4}$$
$$\mathrm{a}_l \approx (\dot{\psi} + \dot{\psi})\mathrm{v}_v. \tag{A.5}$$

Transferring Eq. (A.1,A.2,A.4,A.5) into the state-space domain using

$$\underline{x}_v = \begin{bmatrix}\beta & \psi & \dot{\psi} & y\end{bmatrix}^T, \quad u_v = \delta, \quad \underline{d}_v = \begin{bmatrix}F_y & M_z\end{bmatrix}^T, \quad \underline{y}_v = \begin{bmatrix}\mathrm{y}_l & \mathrm{v}_l & \mathrm{a}_l\end{bmatrix}^T, \tag{A.6}$$

results in

$$\underline{\dot{x}}_v = \underbrace{\begin{bmatrix} a_{11} & 0 & a_{12} & 0 \\ 0 & 0 & 1 & 0 \\ a_{21} & 0 & a_{22} & 0 \\ \mathrm{v}_v & \mathrm{v}_v & 0 & 0 \end{bmatrix}}_{\boldsymbol{A}_v} \underline{x}_v + \underbrace{\begin{bmatrix} b_1 \\ 0 \\ b_2 \\ 0 \end{bmatrix}}_{\boldsymbol{B}_v} u_v + \underbrace{\begin{bmatrix} e_1 & 0 \\ 0 & 0 \\ 0 & e_2 \\ 0 & 0 \end{bmatrix}}_{\boldsymbol{E}_v} \underline{d}_v, \tag{A.7}$$

$$\underline{y}_v = \underbrace{\begin{bmatrix} 0 & 0 & 0 & 1 \\ \mathrm{v}_v & \mathrm{v}_v & 0 & 0 \\ a_{11}\mathrm{v}_v & 0 & (a_{12}+1)\mathrm{v}_v & 0 \end{bmatrix}}_{\boldsymbol{C}_v} \underline{x}_v + \underbrace{\begin{bmatrix} 0 \\ 0 \\ b_1\mathrm{v}_v \end{bmatrix}}_{\boldsymbol{D}_v} u_v + \underbrace{\begin{bmatrix} 0 & 0 \\ 0 & 0 \\ e_1\mathrm{v}_v & 0 \end{bmatrix}}_{\boldsymbol{F}_v} \underline{d}_v, \tag{A.8}$$

for the lateral motion $\underline{y}_v$ of the vehicle in response to steering input u_v and cross-wind disturbance input $\underline{d}_v$.

Virtual driver model

As described in section 2.3.2, the control law of the virtual driver model proposed by Risse [105] and Mitschke and Wallentowitz [85] is given by

$$\delta = \begin{bmatrix} \frac{-V_M}{1+T_I s} & \frac{-V_M}{1+T_I s} T_P & \frac{-V_M}{1+T_I s}\frac{T_P^2}{2} \end{bmatrix} G_{delay}(s) \begin{bmatrix} \mathrm{y}_l \\ \mathrm{v}_l \\ \mathrm{a}_l \end{bmatrix} + \begin{bmatrix} \frac{k_{\delta F_y}}{1+T_S s} & \frac{k_{\delta M_z}}{1+T_S s} \end{bmatrix} G_{delay}(s) \begin{bmatrix} F_y \\ M_z \end{bmatrix}, \tag{A.9}$$

with

$$G_{delay}(s) = \frac{1 - \frac{\tau}{2}s + \frac{\tau^2}{12}s^2}{1 + \frac{\tau}{2}s + \frac{\tau^2}{12}s^2}. \tag{A.10}$$

Transferring Eq. A.9 and A.10 into the state-space domain with state vector $\underline{x}_{drv}$ and input, disturbance and output vectors

$$\underline{u}_{drv} = \underline{y}_v = \begin{bmatrix} \mathrm{y}_l & \mathrm{v}_l & \mathrm{a}_l \end{bmatrix}^T, \quad \underline{d}_{drv} = \underline{d}_v = \begin{bmatrix} F_y & M_z \end{bmatrix}^T, \quad y_{drv} = u_v = \delta, \tag{A.11}$$

respectively, results in the state-space model

$$\underline{\dot{x}}_{drv} = \underbrace{\begin{bmatrix} 0 & 1 & 0 & 0 \\ -\frac{12}{\tau^2} & -\frac{6}{\tau} & 1 & 1 \\ 0 & 0 & -\frac{1}{T_S} & 0 \\ 0 & 0 & 0 & -\frac{1}{T_I} \end{bmatrix}}_{\boldsymbol{A}_{drv}} \underline{x}_{drv} + \underbrace{\begin{bmatrix} 0 & 0 & 0 \\ 0 & 0 & 0 \\ 0 & 0 & 0 \\ -\frac{V_M}{T_I} & -\frac{V_M T_P}{T_I} & -\frac{V_M T_P^2}{2T_I} \end{bmatrix}}_{\boldsymbol{B}_{drv}} \underline{u}_{drv} + \underbrace{\begin{bmatrix} 0 & 0 \\ 0 & 0 \\ \frac{k_{\delta F_y}}{T_S} & \frac{k_{\delta M_z}}{T_S} \\ 0 & 0 \end{bmatrix}}_{\boldsymbol{E}_{drv}} \underline{d}_{drv}, \tag{A.12}$$

$$y_{drv} = \underbrace{\begin{bmatrix} 0 & -\frac{12}{\tau} & 1 & 1 \end{bmatrix}}_{\boldsymbol{C}_{drv}} \underline{x}_{drv} + \underbrace{\begin{bmatrix} 0 & 0 & 0 \end{bmatrix}}_{\boldsymbol{D}_{drv}} \underline{u}_{drv} + \underbrace{\begin{bmatrix} 0 & 0 \end{bmatrix}}_{\boldsymbol{F}_{drv}} \underline{d}_{drv}, \tag{A.13}$$

for the virtual driver's steering response to inputs $\underline{u}_{drv}$, which correspond to changes in lateral displacement, velocity and acceleration of the vehicle, as well as to disturbance inputs $\underline{d}_{drv}$ due to cross-wind.

Driver-vehicle model

Combining Eq. A.7 and A.8 for the lateral vehicle dynamics and Eq. A.12 and A.13 for the virtual driver dynamics into a single set of state-space equations results in the overall model

$$\begin{bmatrix} \underline{\dot{x}}_v \\ \underline{\dot{x}}_{drv} \end{bmatrix} = \underbrace{\begin{bmatrix} \boldsymbol{A}_v & \boldsymbol{B}_v \boldsymbol{C}_{drv} \\ \boldsymbol{B}_d \boldsymbol{C}_{drv} & \boldsymbol{A}_{drv} + \boldsymbol{B}_{drv} \boldsymbol{D}_v \boldsymbol{C}_{drv} \end{bmatrix}}_{\boldsymbol{A}_{vd}} \begin{bmatrix} \underline{x}_v \\ \underline{x}_{drv} \end{bmatrix} + \underbrace{\begin{bmatrix} \boldsymbol{E}_v \\ \boldsymbol{B}_{drv} \boldsymbol{F}_v + \boldsymbol{E}_{drv} \end{bmatrix}}_{\boldsymbol{E}_{vd}} \underline{d}_{vd}, \tag{A.14}$$

$$\underline{y}_{vd} = \underbrace{\begin{bmatrix} \boldsymbol{C}_v & \boldsymbol{D}_v \boldsymbol{C}_{drv} \end{bmatrix}}_{\boldsymbol{C}_{vd}} \begin{bmatrix} \underline{x}_v \\ \underline{x}_{drv} \end{bmatrix} + \underbrace{\boldsymbol{F}_v}_{\boldsymbol{F}_{vd}} \underline{d}_{vd}, \tag{A.15}$$

which describes the response $\underline{y}_{vd} = \begin{bmatrix} \mathrm{y}_l & \mathrm{v}_l & \mathrm{a}_l \end{bmatrix}^T$ of the driver-vehicle feedback loop to disturbance inputs $\underline{d}_{vd} = \begin{bmatrix} F_y & M_z \end{bmatrix}^T$.

Appendix B

2D bluff body

B.1 Estimation of force and moment coefficients from surface-pressure measurements

As described in section 3.4.3, the coefficients for drag, side force and yaw moment of the 2D bluff body can be estimated from a weighted sum of pressure coefficients. The corresponding weighting parameters ϑ_{c_D}, ϑ_{c_S} and ϑ_{c_N} are determined from a series of steady-state measurements at various free-stream velocities, cross-wind angles and actuation amplitudes via the standard linear least squares optimization as described by Nelles [91]. Here, the drag coefficient can be estimated by

$$\hat{c}_D = \begin{bmatrix} c_{p2} & c_{p24} & c_{p,b} & 1 \end{bmatrix} \underline{\vartheta}_{c_D}, \text{ with } \underline{\vartheta}_{c_D} = \begin{bmatrix} 0.3295 \pm 4.99 \cdot 10^{-3} \\ 0.3370 \pm 6.49 \cdot 10^{-3} \\ -0.5957 \pm 6.61 \cdot 10^{-3} \\ 0.1226 \pm 3.10 \cdot 10^{-3} \end{bmatrix}, \tag{B.1}$$

with a relative standard deviation of the estimation error of $\sigma_{e,c_D} / \max(c_D) = 3.31\,\%$. The weighting parameters for the side-force coefficient are determined as

$$\hat{c}_S = \begin{bmatrix} c_{p2} & c_{p11} & c_{p15} & c_{p24} \end{bmatrix} \underline{\vartheta}_{c_S}, \text{ with } \underline{\vartheta}_{c_S} = \begin{bmatrix} -1.0229 \pm 9.31 \cdot 10^{-3} \\ -2.9837 \pm 1.35 \cdot 10^{-2} \\ 3.2546 \pm 1.47 \cdot 10^{-2} \\ 0.6081 \pm 9.58 \cdot 10^{-3} \end{bmatrix}, \tag{B.2}$$

and for the yaw-moment coefficient as

$$\hat{c}_N = \begin{bmatrix} c_{p2} & c_{p11} & c_{p15} & c_{p24} \end{bmatrix} \underline{\vartheta}_{c_N}, \text{ with } \underline{\vartheta}_{c_N} = \begin{bmatrix} -0.3231 \pm 2.11 \cdot 10^{-3} \\ 0.8181 \pm 3.07 \cdot 10^{-3} \\ -0.8844 \pm 3.33 \cdot 10^{-3} \\ 0.3304 \pm 2.17 \cdot 10^{-3} \end{bmatrix}, \tag{B.3}$$

with $\sigma_{e,c_S} / \max(c_S) = 1.63\,\%$ and $\sigma_{e,c_N} / \max(c_N) = 2.72\,\%$, respectively. A comparison of measured and estimated coefficients is shown in Fig. B.1.

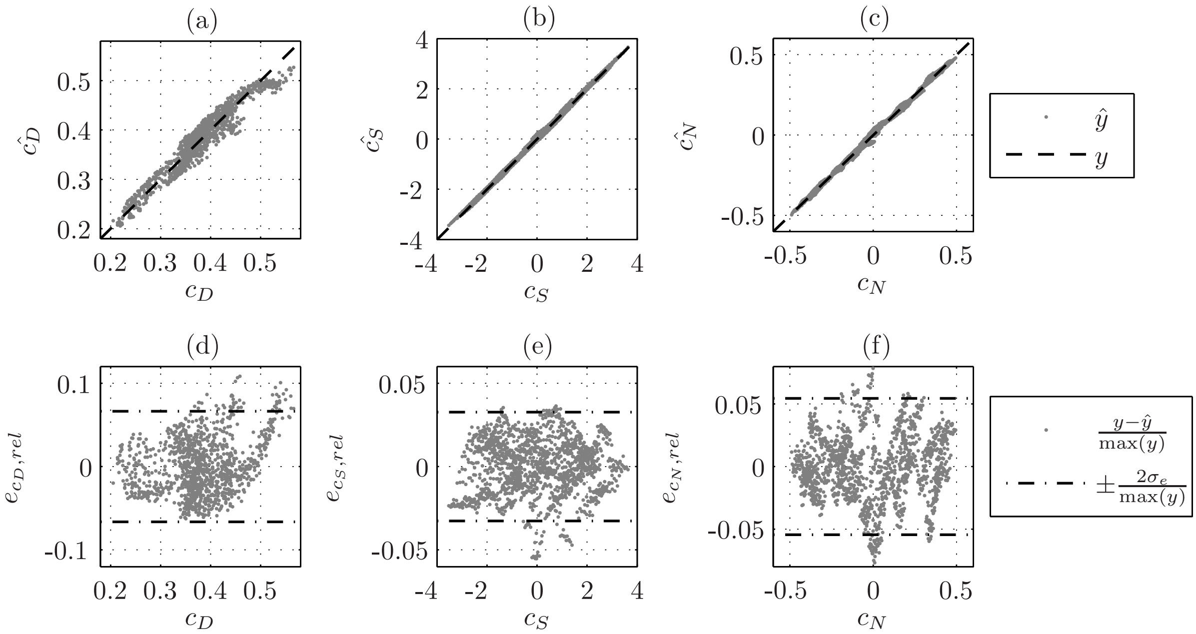

Figure B.1: Comparison of the measured coefficients for drag c_D (a), side force c_S (b) and yaw moment c_N (c), respectively, with their surrogate values $\hat{c}_D$, $\hat{c}_S$, $\hat{c}_N$ as estimated from surface-pressure measurements. Plots (d-f) show the relative errors and the confidence interval expressed in terms of the double relative standard deviation.

Appendix C

3D bluff body

C.1 Estimation of cross-wind angle, total pressure and force and moment coefficients from surface-pressure measurements

The cross-wind angle β_w, the total pressure p_t and the coefficients for drag, side force and yaw moment of the 3D bluff body, c_D, c_S and c_N, respectively, can be estimated from surface-pressure measurements as described in Sec. 4.2.2. To this end, the 3D bluff body was subjected to various constant cross-wind angles, free-stream velocities and actuation amplitudes. The corresponding weighting parameters $\underline{\vartheta}_{\beta_w}$, ϑ_{p_t}, $\underline{\vartheta}_{c_D}$, $\underline{\vartheta}_{c_S}$ and $\underline{\vartheta}_{c_N}$ are determined with the method for linear least squares optimization as described by Nelles [91]. The total pressure is estimated by

$$\hat{p}_t = (p_{13} + p_{15})\vartheta_{p_t}, \text{ with } \vartheta_{p_t} = 0.5852 \pm 2.9 \cdot 10^{-4}, \tag{C.1}$$

with a relative standard deviation of the estimation error $\sigma_{e,p_t}/\max(p_t) = 1.01\%$. The cross-wind angle can be approximated by

$$\hat{\beta} = \begin{bmatrix}(c_{p_{13}} - c_{p_{15}}) & 1\end{bmatrix} \underline{\vartheta}_{\beta_w}, \text{ with } \underline{\vartheta}_{\beta_w} = \begin{bmatrix} 31.927 \pm 5.2 \cdot 10^{-2} \\ 0.585 \pm 8.7 \cdot 10^{-3} \end{bmatrix} \tag{C.2}$$

with $\sigma_{e,\beta_w}/\max(\beta_w) = 1.16\,\%$. Estimates for the force and moment coefficients are given by

$$\hat{c}_D = \begin{bmatrix} c_{p,b} & 1 \end{bmatrix} \underline{\vartheta}_{c_{p,b}}, \text{ with } \underline{\vartheta}_{c_D} = \begin{bmatrix} -0.7148 \pm 1.04 \cdot 10^{-2} \\ 0.3575 \pm 1.54 \cdot 10^{-3} \end{bmatrix}, \tag{C.3}$$

$$\hat{c}_S = \begin{bmatrix} c_{p_4} & c_{p_{11}} & c_{p_{17}} & c_{p_{24}} \end{bmatrix} \underline{\vartheta}_{c_S}, \text{ with } \underline{\vartheta}_{c_S} = \begin{bmatrix} 1.2716 \pm 8.01 \cdot 10^{-3} \\ 1.2281 \pm 2.90 \cdot 10^{-3} \\ -1.1297 \pm 2.89 \cdot 10^{-3} \\ -1.2355 \pm 7.73 \cdot 10^{-3} \end{bmatrix}, \text{ and} \tag{C.4}$$

$$\hat{c}_N = \begin{bmatrix} c_{p_4} & c_{p_{11}} & c_{p_{17}} & c_{p_{24}} \end{bmatrix} \underline{\vartheta}_{c_N}, \text{ with } \underline{\vartheta}_{c_N} = \begin{bmatrix} -0.9991 \pm 6.36 \cdot 10^{-3} \\ 0.2773 \pm 2.30 \cdot 10^{-3} \\ -0.3316 \pm 2.29 \cdot 10^{-3} \\ 0.9664 \pm 6.13 \cdot 10^{-3} \end{bmatrix}, \tag{C.5}$$

with $\sigma_{e,c_D}/\max(c_D) = 2.29\,\%$, $\sigma_{e,c_S}/\max(c_S) = 0.93\,\%$ and $\sigma_{e,c_N}/\max(c_N) = 2.36\,\%$. A comparison of the measured and estimated values is shown in Fig. C.1 and C.2, respectively.

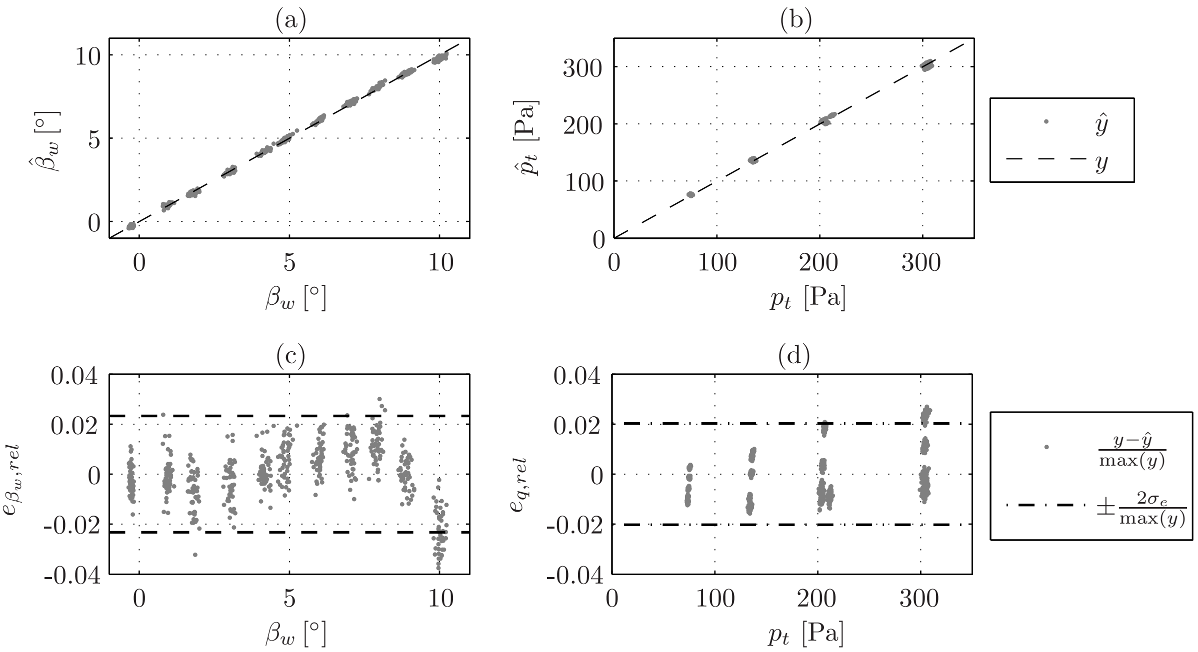

Figure C.1: Comparison of the cross-wind angle β_w (a) and the total pressure p_t (c) as measured by the five-hole probe with their respective surrogate values $\hat{\beta}_w$ and $\hat{p}_t$ as estimated from surface-pressure measurements. Plots (c-d) show the relative errors and the confidence interval expressed in terms of the double relative standard deviation.

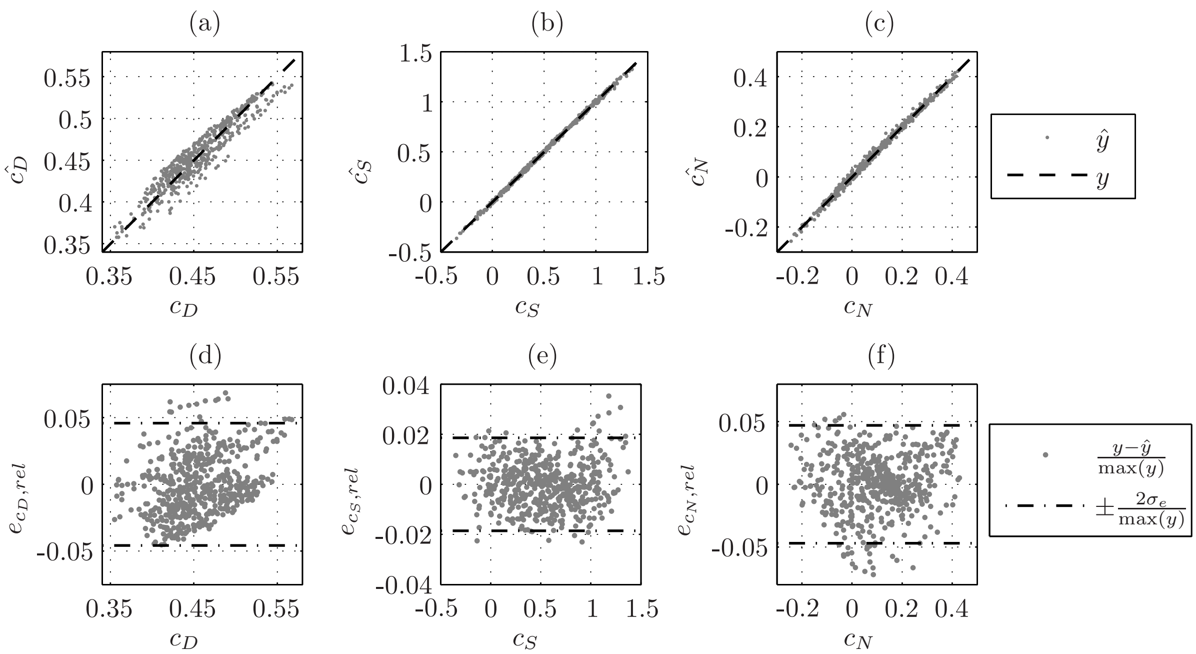

Figure C.2: Comparison of the measured coefficients for drag c_D (a), side force c_S (b) and yaw moment c_N (c) with their respective surrogate values $\hat{c}_D$, $\hat{c}_S$, $\hat{c}_N$ as estimated from surface-pressure measurements. Plots (d-f) show the relative errors and the confidence interval expressed in terms of the double relative standard deviation.

C.2 Linear parameter-varying unsteady aerodynamic models

C.2.1 LPV models for the cross-wind gust response

Section 4.2.3 describes the identification of linear parameter-varying models for the cross-wind gust response of the force and moment coefficients of the 3D bluff body. The disturbance input vector

$$\underline{d}^*(t) = \begin{bmatrix} \beta_w(t) & p_t'(t)/\overline{p}_t \end{bmatrix}^T \tag{C.6}$$

consists of the time-varying cross-wind angle $\beta_w(t)$ and the normalized total pressure fluctuation $p_t'(t)/\overline{p}_t$. For reasons of consistency the parameter vector

$$\underline{\theta}(t) = \begin{bmatrix} \mathrm{u}_\infty(t) & \mathrm{u}_\infty(t)\beta_w(t) \end{bmatrix}^T \tag{C.7}$$

is the same as that for the LPV models for the actuated flow, although no dependency on cross-wind angle was determined for the gust response.

Drag coefficient

For the dynamics of the drag coefficient the LPV state-space model

$$\dot{\underline{x}}_{c_D,\mathrm{cwg}}(t) = \underbrace{\mathrm{u}_\infty(t)\frac{1}{L}\boldsymbol{A}^*_{c_D,\mathrm{cwg},1}}_{\boldsymbol{A}_{c_D,\mathrm{cwg}}(\underline{\theta})}\underline{x}_{c_D,\mathrm{cwg}}(t) + \underbrace{\mathrm{u}_\infty(t)\frac{1}{L}\boldsymbol{E}^*_{c_D,\mathrm{cwg},1}}_{\boldsymbol{E}_{c_D,\mathrm{cwg}}(\underline{\theta})}\underline{d}^*\left(t - \frac{L}{\mathrm{u}_\infty(t)}T_0^*\right), \tag{C.8}$$

$$y^*_{c_D,\mathrm{cwg}}(t) = \underline{c}^{*T}_{c_D,\mathrm{cwg}}\underline{x}_{c_D,\mathrm{cwg}}(t), \tag{C.9}$$

is identified, with the matrices

$$\boldsymbol{A}^*_{c_D,\mathrm{cwg},1} = \begin{bmatrix} 0 & -0.9918 \\ 1 & -1.0084 \end{bmatrix}, \quad \boldsymbol{E}^*_{c_D,\mathrm{cwg},1} = \begin{bmatrix} 0.0055 & -0.0353 \\ 0.0017 & 0.6770 \end{bmatrix}, \quad \underline{c}^{*T}_{c_D,\mathrm{cwg}} = \begin{bmatrix} 0 & 1 \end{bmatrix}, \tag{C.10}$$

and a nondimensional input time-delay $T_0^* = 1$.

Side-force coefficient

The transient cross-wind gust response of the side-force coefficient is described by

$$\dot{\underline{x}}_{c_S,\mathrm{cwg}}(t) = \underbrace{\mathrm{u}_\infty(t)\frac{1}{L}\boldsymbol{A}^*_{c_S,\mathrm{cwg},1}}_{\boldsymbol{A}_{c_S,\mathrm{cwg}}(\underline{\theta})}\underline{x}_{c_S,\mathrm{cwg}}(t) + \underbrace{\mathrm{u}_\infty(t)\frac{1}{L}\boldsymbol{B}^*_{c_S,\mathrm{cwg},1}}_{\boldsymbol{E}_{c_S,\mathrm{cwg}}(\underline{\theta})}\underline{d}^*(t), \tag{C.11}$$

$$y^*_{c_S,\mathrm{cwg}}(t) = \underline{c}^{*T}_{c_S,\mathrm{cwg}}\underline{x}_{c_S,\mathrm{cwg}}(t), \tag{C.12}$$

with the dimensionless state-space matrices

$$\boldsymbol{A}^*_{c_S,\mathrm{cwg},1} = \begin{bmatrix} 0 & -34.1234 \\ 1 & -15.624 \end{bmatrix}, \quad \boldsymbol{E}^*_{c_S,\mathrm{cwg},1} = \begin{bmatrix} 3.5823 & -12.6537 \\ -0.9940 & -9.1167 \end{bmatrix}, \quad \underline{c}^{*T}_{c_S,\mathrm{cwg}} = \begin{bmatrix} 0 & 1 \end{bmatrix}. \tag{C.13}$$

Yaw-moment coefficient

The LPV model for the response of the yaw-moment coefficient to cross-wind gusts has the structure

$$\dot{\underline{x}}_{c_N,\mathrm{cwg}}(t) = \underbrace{\mathrm{u}_\infty(t)\frac{1}{L}\boldsymbol{A}^*_{c_N,\mathrm{cwg},1}}_{\boldsymbol{A}_{c_N,\mathrm{cwg}}(\underline{\theta})}\underline{x}_{c_N,\mathrm{cwg}}(t) + \underbrace{\mathrm{u}_\infty(t)\frac{1}{L}\boldsymbol{B}^*_{c_N,\mathrm{cwg},1}}_{\boldsymbol{E}_{c_N,\mathrm{cwg}}(\underline{\theta})}\underline{d}^*(t), \tag{C.14}$$

$$y^*_{c_N,\mathrm{cwg}}(t) = \underline{c}^{*T}_{c_N,\mathrm{cwg}}\underline{x}_{c_N,\mathrm{cwg}}(t), \tag{C.15}$$

with the nondimensional state-space matrices

$$\boldsymbol{A}^*_{c_N,\mathrm{cwg},1} = \begin{bmatrix} 0 & -6.4628 \\ 1 & -1.4282 \end{bmatrix}, \quad \boldsymbol{E}^*_{c_N,\mathrm{cwg},1} = \begin{bmatrix} 0.1038 & 0.2000 \\ 0.0094 & -1.3027 \end{bmatrix}, \quad \underline{c}^{*T}_{c_N,\mathrm{cwg}} = \begin{bmatrix} 0 & 1 \end{bmatrix}. \tag{C.16}$$

C.2.2 LPV models for the actuated flow dynamics

The identification of the LPV models for the actuated flow dynamics is described in section 4.4.3. For these models the input vector

$$\underline{u}^*_{\mathrm{afc}} = \underline{\mathrm{u}}^*_{a,jet}(t) = \begin{bmatrix}\mathrm{u}_{a_1,jet}/\mathrm{u}_\infty & \mathrm{u}_{a_2,jet}/\mathrm{u}_\infty & \mathrm{u}_{a_3,jet}/\mathrm{u}_\infty\end{bmatrix}^T \tag{C.17}$$

corresponds to the nondimensional instantaneous blowing velocities at the outlets of the three Coanda actuators. The parameter vector is set at

$$\underline{\theta}(t) = \begin{bmatrix}\mathrm{u}_\infty(t) & \mathrm{u}_\infty(t)\beta_w(t)\end{bmatrix}^T. \tag{C.18}$$

Drag coefficient

The response of the drag coefficient to Coanda blowing $\underline{u}^*_{\mathrm{afc}} = \underline{\mathrm{u}}^*_{a,jet}$ is captured by the LPV state-space model

$$\dot{\underline{x}}_{c_D,\mathrm{afc}}(t) = \underbrace{\mathrm{u}_\infty(t)\frac{1}{L}\boldsymbol{A}^*_{c_D,\mathrm{afc},1}}_{\boldsymbol{A}_{c_D,\mathrm{afc}}(\underline{\theta})}\,\underline{x}_{c_D,\mathrm{afc}}(t) + \underbrace{\mathrm{u}_\infty(t)\frac{1}{L}\left(\boldsymbol{B}^*_{c_D,\mathrm{afc},1} + \beta_w(t)\boldsymbol{B}^*_{c_D,\mathrm{afc},2}\right)}_{\boldsymbol{B}_{c_D,\mathrm{afc}}(\underline{\theta})}\,\underline{u}^*_{\mathrm{afc}}(t), \tag{C.19}$$

$$y^*_{c_D,\mathrm{afc}}(t) = \underline{c}^{*T}_{c_D,\mathrm{afc}}\,\underline{x}_{c_D,\mathrm{afc}}(t), \tag{C.20}$$

with the nondimensional matrices

$$\boldsymbol{A}^*_{c_D,\mathrm{afc},1} = \begin{bmatrix}0 & -5.0708\\ 1 & -7.9656\end{bmatrix}, \tag{C.21}$$

$$\boldsymbol{B}^*_{c_D,\mathrm{afc},1} = \begin{bmatrix}-0.0661 & -0.0715 & -0.1314\\ -0.2739 & -0.2759 & -0.3564\end{bmatrix}, \boldsymbol{B}^*_{c_D,\mathrm{afc},2} = \begin{bmatrix}-0.0146 & 0.0146 & 0\\ -0.0019 & 0.0019 & 0\end{bmatrix}, \tag{C.22}$$

$$\underline{c}^{*T}_{c_D,\mathrm{afc}} = \begin{bmatrix}0 & 1\end{bmatrix}. \tag{C.23}$$

Side-force coefficient

For the actuated flow dynamics of the side-force coefficient to input $\underline{u}^*_{\mathrm{afc}} = \underline{\mathrm{u}}^*_{a,jet}$ an LPV state-model

$$\dot{\underline{x}}_{c_S,\mathrm{afc}}(t) = \underbrace{\mathrm{u}_\infty(t)\frac{1}{L}\boldsymbol{A}^*_{c_S,\mathrm{afc},1}}_{\boldsymbol{A}_{c_S,\mathrm{afc}}(\underline{\theta})}\,\underline{x}_{c_S,\mathrm{afc}}(t) + \underbrace{\mathrm{u}_\infty(t)\frac{1}{L}\boldsymbol{B}^*_{c_S,\mathrm{afc},1}}_{\boldsymbol{B}_{c_S,\mathrm{afc}}(\underline{\theta})}\,\underline{u}^*_{\mathrm{afc}}(t), \tag{C.24}$$

$$y^*_{c_S,\mathrm{afc}}(t) = \underline{c}^{*T}_{c_S,\mathrm{afc}}\,\underline{x}_{c_S,\mathrm{afc}}(t), \tag{C.25}$$

is identified, with the nondimensional matrices

$$\boldsymbol{A}^*_{c_S,\mathrm{afc},1} = \begin{bmatrix}0 & -78.1260\\ 1 & -12.1596\end{bmatrix}, \quad \boldsymbol{B}^*_{c_S,\mathrm{afc},1} = \begin{bmatrix}-11.8633 & -11.4598 & -0.0158\\ -0.2464 & -0.0079 & -0.1891\end{bmatrix}, \quad \underline{c}^{*T}_{c_S,\mathrm{afc}} = \begin{bmatrix}0 & 1\end{bmatrix}. \tag{C.26}$$

Yaw-moment coefficient

The dynamics of the yaw-moment coefficient for inputs $\underline{u}^*_{\mathrm{afc}} = \underline{\mathrm{u}}^*_{a,jet}(t)$ in terms of Coanda blowing at the trailing edges of the 3D bluff body are described by the LPV state-space model

$$\dot{\underline{x}}_{c_N,\mathrm{afc}}(t) = \underbrace{\mathrm{u}_\infty(t)\frac{1}{L}\boldsymbol{A}^*_{c_N,\mathrm{afc},1}}_{\boldsymbol{A}_{c_N,\mathrm{afc}}(\underline{\theta})}\,\underline{x}_{c_N,\mathrm{afc}}(t) + \underbrace{\mathrm{u}_\infty(t)\frac{1}{L}\boldsymbol{B}^*_{c_N,\mathrm{afc},1}}_{\boldsymbol{B}_{c_N,\mathrm{afc}}(\underline{\theta})}\,\underline{u}^*_{\mathrm{afc}}, \tag{C.27}$$

$$y^*_{c_N,\mathrm{afc}}(t) = \underline{c}^{*T}_{c_N,\mathrm{afc}}\,\underline{x}_{c_N,\mathrm{afc}}(t), \tag{C.28}$$

for which the dimensionless matrices

$$\boldsymbol{A}^*_{c_N,\text{afc},1} = \begin{bmatrix} 0 & -27.5612 \\ 1 & -5.1489 \end{bmatrix}, \quad \boldsymbol{B}^*_{c_N,\text{afc},1} = \begin{bmatrix} 3.0172 & -2.8125 & 0.0313 \\ 0.3563 & -0.2693 & 0.0575 \end{bmatrix}, \quad \underline{c}^{*T}_{c_N,\text{afc}} = \begin{bmatrix} 0 & 1 \end{bmatrix}, \tag{C.29}$$

are identified.

Overall LPV plant model for the 3D bluff body

An overall plant model for the response of the aerodynamic coefficients of the 3D bluff body to Coanda actuation is obtained by combining the individual models for drag, side-force and yaw-moment coefficients and for the actuator dynamics in a MIMO LPV state-space model. The actuator dynamics are identified in section 4.4.1 and are described by a linear state-space model

$$\dot{\underline{x}}_a = \boldsymbol{A}_a \underline{x}_a + \boldsymbol{B}_a \underline{u}^*_a, \tag{C.30}$$

$$\underline{y}^*_a = \boldsymbol{C}_a \underline{x}_a, \tag{C.31}$$

with

$$\underline{u}^*_a = \underline{\mathrm{u}}^*_{a,des} = \begin{bmatrix} \mathrm{u}_{a1,des}/\mathrm{u}_\infty & \mathrm{u}_{a2,des}/\mathrm{u}_\infty & \mathrm{u}_{a3,des}/\mathrm{u}_\infty \end{bmatrix}^T, \tag{C.32}$$

$$\underline{y}^*_a = \underline{\mathrm{u}}^*_{a,jet} = \begin{bmatrix} \mathrm{u}_{a1,jet}/\mathrm{u}_\infty & \mathrm{u}_{a2,jet}/\mathrm{u}_\infty & \mathrm{u}_{a3,jet}/\mathrm{u}_\infty \end{bmatrix}^T. \tag{C.33}$$

The overall LPV plant model has the structure

$$\dot{\underline{x}}_\text{afc} = \underbrace{\left(\boldsymbol{A}_{\text{afc},0} + \theta_1 \boldsymbol{A}_{\text{afc},1} + \theta_2 A_{\text{afc},2}\right)}_{\boldsymbol{A}_\text{afc}(\underline{\theta})} \underline{x}_\text{afc} + \boldsymbol{B}_\text{afc} \underline{u}^*_a, \tag{C.34}$$

$$\underline{y}^*_\text{afc} = \boldsymbol{C}_\text{afc} \underline{x}_\text{afc}, \tag{C.35}$$

with the input, state, output and parameter vectors

$$\underline{u}^*_a = \begin{bmatrix} \mathrm{u}_{a1,des}/\mathrm{u}_\infty \\ \mathrm{u}_{a2,des}/\mathrm{u}_\infty \\ \mathrm{u}_{a3,des}/\mathrm{u}_\infty \end{bmatrix}, \quad \underline{x}_\text{afc} = \begin{bmatrix} \underline{x}_{c_D,\text{afc}} \\ \underline{x}_{c_S,\text{afc}} \\ \underline{x}_{c_N,\text{afc}} \\ \underline{x}_a \end{bmatrix}, \quad \underline{y}^*_\text{afc} = \begin{bmatrix} \hat{c}_D \\ w_{c_S}\hat{c}_S + w_{c_N}\hat{c}_N \end{bmatrix}, \quad \underline{\theta} = \begin{bmatrix} \mathrm{u}_\infty \\ \beta_w \mathrm{u}_\infty \end{bmatrix}, \tag{C.36}$$

respectively. The corresponding LPV state-space matrices are

$$\boldsymbol{A}_{\text{afc},0} = \begin{bmatrix} 0 & 0 & 0 & 0 \\ 0 & 0 & 0 & 0 \\ 0 & 0 & 0 & 0 \\ 0 & 0 & 0 & \boldsymbol{A}_a \end{bmatrix}, \tag{C.37}$$

$$\boldsymbol{A}_{\text{afc},1} = \begin{bmatrix} \frac{1}{L}\boldsymbol{A}^*_{c_D,\text{afc},1} & 0 & 0 & \frac{1}{L}\boldsymbol{B}^*_{c_D,\text{afc},1} C_a \\ 0 & \frac{1}{L}\boldsymbol{A}^*_{c_S,\text{afc},1} & 0 & \frac{1}{L}\boldsymbol{B}^*_{c_S,\text{afc},1} \boldsymbol{C}_a \\ 0 & 0 & \frac{1}{L}\boldsymbol{A}^*_{c_N,\text{afc},1} & \frac{1}{L}\boldsymbol{B}^*_{c_N,\text{afc},1} \boldsymbol{C}_a \\ 0 & 0 & 0 & 0 \end{bmatrix}, \tag{C.38}$$

$$\boldsymbol{A}_{\text{afc},2} = \begin{bmatrix} 0 & 0 & 0 & \frac{1}{L}\boldsymbol{B}^*_{c_D,\text{afc},2} \boldsymbol{C}_a \\ 0 & 0 & 0 & 0 \\ 0 & 0 & 0 & 0 \\ 0 & 0 & 0 & 0 \end{bmatrix}, \tag{C.39}$$

$$\boldsymbol{B}_\text{afc} = \begin{bmatrix} 0 \\ 0 \\ 0 \\ \boldsymbol{B}_a \end{bmatrix}, \quad \text{and} \quad \boldsymbol{C}_\text{afc} = \begin{bmatrix} \underline{c}^{*T}_{c_D,\text{afc}} & 0 & 0 & 0 \\ 0 & w_{c_S}\underline{c}^{*T}_{c_S,\text{afc}} & w_{c_N}\underline{c}^{*T}_{c_N,\text{afc}} & 0 \end{bmatrix}. \tag{C.40}$$